Erlend Magnus Viggen

The lattice Boltzmann method: Fundamentals and acoustics

Thesis for the degree of Philosophiae Doctor

Trondheim, February 2014

Norwegian University of Science and Technology
Faculty of Information Technology, Mathematics and Electrical Engineering
Department of Electronics and Telecommunications

NTNU – Trondheim
Norwegian University of
Science and Technology

NTNU
Norwegian University of Science and Technology

Thesis for the degree of Philosophiae Doctor

Faculty of Information Technology, Mathematics and Electrical Engineering
Department of Electronics and Telecommunications

ISBN 978-82-326-0036-6 (printed ver.)
ISBN 978-82-326-0037-3 (electronic ver.)
ISSN 1503-8181

Doctoral theses at NTNU, 2014:55

Printed by NTNU-trykk

Abstract

The lattice Boltzmann method has been widely used as a solver for incompressible flow, though it is not restricted to this application. More generally, it can be used as a compressible Navier-Stokes solver, albeit with a restriction that the Mach number is low. While that restriction may seem strict, it does not hinder the application of the method to the simulation of sound waves, for which the Mach numbers are generally very low. Even sound waves with strong nonlinear effects can be captured well. Despite this, the method has not been as widely used for problems where acoustic phenomena are involved as it has been for incompressible problems.

The research presented this thesis goes into three different aspects of lattice Boltzmann acoustics. Firstly, linearisation analyses are used to derive and compare the sound propagation properties of the lattice Boltzmann equation and comparable fluid models for both free and forced waves. The propagation properties of the fully discrete lattice Boltzmann equation are shown to converge at second order towards those of the discrete-velocity Boltzmann equation, which itself predicts the same lowest-order absorption but different dispersion to the other fluid models.

Secondly, it is shown how multipole sound sources can be created mesoscopically by adding a particle source term to the Boltzmann equation. This method is straightforwardly extended to the lattice Boltzmann method by discretisation. The results of lattice Boltzmann simulations of monopole, dipole, and quadrupole point sources are shown to agree very well with the combined predictions of this multipole method and the linearisation analysis. The exception to this agreement is the immediate vicinity of the point source, where the singularity in the analytical solution cannot be reproduced numerically.

Thirdly, an extended lattice Boltzmann model is described. This model alters the equilibrium distribution to reproduce variable equations of state while remaining simple to implement and efficient to run. To compensate for an unphysical bulk viscosity, the extended model contains a bulk viscosity correction term. It is shown that all equilibrium distributions that allow variable equations of state must be identical for the one-dimensional D1Q3 velocity set. Using such a D1Q3 velocity set and an isentropic equation of state, both mechanisms of nonlinear acoustics are captured successfully in a simulation, improving on previous isothermal simulations where only one mechanism could be captured. In addition, the effect of molecular relaxation on sound propagation is simulated using a model equation of state. Though the particular implementation used is not completely stable, the results agree well with theory.

Preface

There are a few things that I would like to tell you about this thesis before you dive in.

This thesis is split into two parts. Part I covers the underlying theory: Fluid mechanics, acoustics, the kinetic theory of gases, and finally the lattice Boltzmann method itself. Part II builds directly on this background, and covers the research that was done in the course of my ph.d. project.

Throughout this thesis you will occasionally see small notes in the margin. Whenever new and important terms are introduced, these margin notes give a short definition. Occasionally, these notes may be repeated for various reasons: Readers may have skipped past a previous definition in an earlier chapter, a different formulation might make more sense in light of the surrounding text, or I may simply have considered a concept critical enough to repeat.

At conferences I have surprisingly often met other students who tell me that they have used my Master's thesis to learn the lattice Boltzmann method. This has been tremendously inspiring, and has led me to take extra care to make Part I of the thesis thorough (though hopefully not *off-puttingly* thorough) and readable. As introductions to the lattice Boltzmann method that are easily readable, thorough, and *freely available* are thin on the ground, one of my goals has been to make Part I just such an introduction. I hope that I have succeeded in this goal, though this is of course up to you to decide.

While my Master's thesis will still offer a quicker and simpler introduction to the lattice Boltzmann method, Part I of this thesis puts more emphasis on the physical background of the method, which is in my opinion essential to truly understand it.

This thesis is submitted to the Norwegian University of Science and Technology (NTNU) in partial fulfilment of the requirements for the degree of Philosophiae Doctor *(ph.d.). The ph.d. project ran for four years, with one year spent on teaching duties. The work was carried out at the Acoustics Research Center at the Department of Electronics and Telecommunications, with Professor Ulf Kristiansen as supervisor.*

I hope you find it interesting.

Acknowledgements

Throughout these four years as a ph.d. student, there have been many people who have aided me in various ways. For this I am deeply grateful.

I would have had a much harder time early on if Joris Verschaeve had not spent many an hour helping me to understand the lattice Boltzmann method. Similarly, my later work would have been much more difficult if not for the occasional comment from Paul Dellar. His deep insight has been invaluable to me and my work.

There are many other researchers with whom I have had interesting and useful discussions on a wide variety of scientific topics. I would especially like to thank Timm Krüger, Jonas Lätt, Tim Reis, Tor Ytrehus, David Packwood, Manuel Hasert, Martin Schlaffer, and Guillaume Dutilleux. Also, I would like to thank all the other friendly people whose company I have enjoyed at conferences. Thanks to them, the non-scientific aspects of these conferences have never been dull.

I am grateful for the company and friendship of some of my fellow travellers through the ph.d. program at NTNU. While they are too many for me to start listing names, I would especially like to thank Anders Løvstad for being excellent company in the office throughout much of our time as ph.d. students, though I do not miss the roar of his computer.

Finally, I am very grateful to Ulf Kristiansen for being as available and affable an advisor as any ph.d. student could hope to have.

To all of you: *Thank you.*

Erlend Magnus Viggen
Trondheim, September 2013

Contents

Part I

Background

1 Introduction

Many scientific articles on the lattice Boltzmann method begin with a fairly dense paragraph on the method and its capabilities, which typically goes something like this:

> The lattice Boltzmann (LB) method is a recent advance in computational fluid dynamics (CFD). While traditional CFD methods directly discretise and solve the macroscopic equations of fluid mechanics, the LB method solves a discrete kinetic equation which reproduces the fluid mechanics equations in the macroscopic limit. It is straightforward to implement and parallelise efficiently, while being versatile enough to simulate multiphase flows, multicomponent flows, flows of complex fluids, flows in complex geometries such as porous media, thermal flows, and turbulent flows.

A paragraph this succinct can of course not give a full picture of the method. However, it *does* manage to paint much of this picture in broad strokes. Let us now paint some of the finer strokes by expanding on the three sentences of this paragraph.

Cellular automaton
A discrete model with very simple rules that can typically result in very complex behaviour

Lattice gas
A cellular automaton for simulating gases, based on particles moving around on a lattice, their collisions conserving mass and momentum

As the first sentence states, the LB method has not been around for as long as most other CFD methods. Historically, it grew out of the field of *cellular automata*, and specifically *lattice gases*, which we will look at briefly in section 1.1.2. The first lattice gas was described in 1973 [1], though it was not until 1986 that a lattice gas that could be used to correctly simulate fluid flow was proposed [2]. An article was published soon after in 1988 on a modification to lattice gases in order to avoid some of their problems when simulating fluid flow [3]. This article can be considered the first article on the lattice Boltzmann method.

The second sentence of the paragraph implies that the LB method solves the equations of fluid mechanics indirectly by solving something *else*, something *simpler*. While this may seem too good to be true, there is indeed a good physical reason why it works. The lattice Boltzmann method is a discretisation of the Boltzmann equation, an equation which describes gases at a more detailed level than the equations of fluid mechanics, while still having a simpler form. If we smooth away these details in the right way, we end up with the equations familiar from fluid mech-

anics. In section 1.1 we will look at the relation between the different descriptions of a gas.

As for the third sentence, it is a truth with modifications. It is indeed true that the basic LB method is both simple and fairly powerful. However, it is almost a truism that if you take something simple and bolt on something complex, the end product becomes complicated. LB models that are more accurate or that can capture more complex physics are indeed more difficult to understand and to implement. Even so, capturing complex physics using LB may still be simpler than when using more traditional CFD methods. Finally, while *parallelising* LB for simple cases is not difficult, such simple parallelisations can become quite inefficient for more complex cases; general and efficient parallelisation of LB is difficult [4].

Parallelising
Separating a computer program into pieces that can run in parallel, which may increase its speed as the pieces can be run simultaneously on several different processors

The rest of this introductory chapter is split into two sections. The first section introduces the different *scales*, or *levels of detail*, at which we can describe matter, and the connection between these scales for gases. A very simple lattice gas model for tracking the molecules of a gas is described, and the connection to the less detailed but more useful lattice Boltzmann method is hinted at. The discussion in this section is kept at as simple a level as possible. The second section describes this thesis, going into its aims, its structure, other publications by the author during the same research project, and its mathematical notation.

1.1 Microscopic, mesoscopic, and macroscopic scales

Consider a glass of water. To the human senses, the water seems continuous and uniform. If we were able to look at the fluid at size scales on the order of nanometers, though, we would see that the fluid is neither continuous nor uniform; it consists of invididual molecules which are constantly shifting around. We would be able to see that some areas of this cloud of molecules are denser than others, as sketched in Figure 1.1. However, since our eyesight is far from good enough to perceive this level of detail, this non-uniformity is evened out due to the law of large numbers, and we perceive the water as uniform.

We usually describe the properties and movement of the water using tangible terms like *density* and, if the glass of water is stirred, *fluid velocity*. This coarse level of detail which we can percieve directly, we call the *macroscopic scale*. The equations of fluid mechanics, which describe how these macroscopic variables evolve, are correspondingly equations for the macroscopic scale.

Mass density, ρ
Mass per physical volume in $\mathrm{kg/m^3}$

Fluid velocity, u
The local velocity of the fluid in $\mathrm{m/s}$

Macroscopic scale
Where we use tangible terms to describe physical systems

In the *microscopic scale*, we look at a much more complete (and probably overwhelming!) level of detail. Instead of regarding the fluid as a smooth continuum, we look at all the different molecules of which it consists. Each molecule, indexed by i, has a mass m_i, a position $\boldsymbol{x}_i = (x_i, y_i, z_i)$,

Microscopic scale
Where we describe a physical system through all its individual components

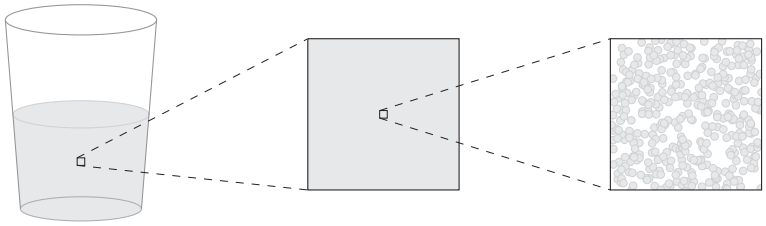

Figure 1.1: Molecules in a glass of water. When zooming in far enough, we see that the fluid is not quite uniform.

a velocity $\boldsymbol{\xi}_i$, in addition to additional variables to describe its internal state: typically its rotation and its vibration. The motion of each of these molecules can be described by Newton's laws of motion, though some quantum mechanics must also be applied if the internal configuration is considered.

1.1.1 Connection

Since the microscopic and macroscopic pictures describe the same physical system, it must be possible to link them somehow. Somehow, the wildly fluctuating microscopic world must tell us something about the smooth and continuous macroscopic world.

Expectation value, $\mathsf{E}(\dots)$
For a random variable, the expectation value is what we would find if we could measure it an infinite amount of times and average the results. In that sense, it is an idealised average.

To link them, we must consider the *expectation values* of the microscopic system. Thus, the macroscopic mass density $\rho(\boldsymbol{x}, t)$ at position $\boldsymbol{x}$ and time t is found by adding up the mass m_i of the particles that we would *expect to find* in a tiny volume V at $\boldsymbol{x}$, such as the rightmost volume in Figure 1.1. Mathematically,

$$\rho(\boldsymbol{x}, t) = \lim_{V \to 0} \mathsf{E}\left(\frac{1}{V} \sum_{\boldsymbol{x}_i \in V} m_i \right). \tag{1.1a}$$

Momentum density, $\rho \boldsymbol{u}$
Momentum per physical volume in $\mathrm{kg/s\,m^2}$

Similarly, the *momentum density* can be found from adding the momentum $m_i \boldsymbol{\xi}_i$ of each particle in the volume,

$$\rho \boldsymbol{u}(\boldsymbol{x}, t) = \lim_{V \to 0} \mathsf{E}\left(\frac{1}{V} \sum_{\boldsymbol{x}_i \in V} m_i \boldsymbol{\xi}_i \right). \tag{1.1b}$$

Energy density, ρE
Kinetic energy per physical volume in $\mathrm{J/m^3}$

Finally, the *energy density* can be found by adding the kinetic energy $\frac{1}{2} m_i |\boldsymbol{\xi}_i|^2$ of each particle,

$$\rho E(\boldsymbol{x}, t) = \lim_{V \to 0} \mathsf{E}\left(\frac{1}{2V} \sum_{\boldsymbol{x}_i \in V} m_i |\boldsymbol{\xi}_i|^2 \right). \tag{1.1c}$$

If we know the density and the momentum density, then we can obviously directly find the fluid velocity as $\boldsymbol{u} = \rho \boldsymbol{u} / \rho$.

If the fluid is at rest with $\boldsymbol{u} = 0$, the particles are still in motion at the microscale. However, their directions of velocity are equally distributed, so that the vector sum in (1.1b) is zero. The energy density (1.1c) is not zero; it measures the *intensity* of the internal particle motion in the gas. We shall later see in Chapter 3 that it is related to the temperature.

Mesoscopic scale
A statistical description in between the microscopic and macroscopic scale

There is also the *mesoscopic scale*, where the level of detail is somewhere between the extremely detailed microscopic scale and the tangible macroscopic scale. Instead of tracking every particle, we track the *distribution* of particles. While this is a fairly abstract concept, we will give an example of this at the end of section 1.1.2 and go on to describe the theory of gases at the mesoscopic scale, known as the *kinetic theory of gases*, in Chapter 3.

On the microscopic and mesoscopic scales, ideal gases are by far the simplest type of fluid to deal with. In a gas which is not too dense, the molecules are far enough apart that their interaction is approximately always through one-on-one collisions. For a very dense gas, the molecules are much closer together and the assumption that collisions are always one-on-one is no longer a sufficient approximation. Things are even more difficult in liquids, where the molecules are held close to each other by intermolecular attracting forces, meaning that there is a continuous interaction between the molecules. The field of kinetic theory is therefore most well-developed for dilute gases; the kinetic theory of liquids is a much more difficult topic [5].

On the macroscopic scale, though, the difference between gases and liquids is much less clear, as the same equations hold for both. The difference is manifested mainly by a difference in material parameters. For instance, liquids tend to have a significantly higher speed of sound than gases.

For a gas which is not too dense, then, the different levels of description are connected as shown in Figure 1.2. The most detailed description is on the microscopic scale, and this can be approximated via mesoscopic kinetic theory to find the equations of macroscopic fluid mechanics.*

We can see the general equations of fluid mechanics as splintering into two different, incompatible descriptions, depending on which approximations are taken. For engineering fluid mechanics where fluid flows are the topic, the fluid is almost always assumed to be incompressible. Incompressibility means that the density is constant, which is incompatible with the compressible phenomenon of sound. For acoustics, the fluid is almost always assumed to be at rest or nearly so, with sound waves disturbing the fluid only very slightly.

In this thesis, we will only barely look into the microscopic description, and incompressible fluid mechanics will be mentioned only in passing. We will be looking primarily at *kinetic theory*, general *fluid mechanics*,

*We will look at the connection between kinetic theory and fluid mechanics in detail in section 3.8.

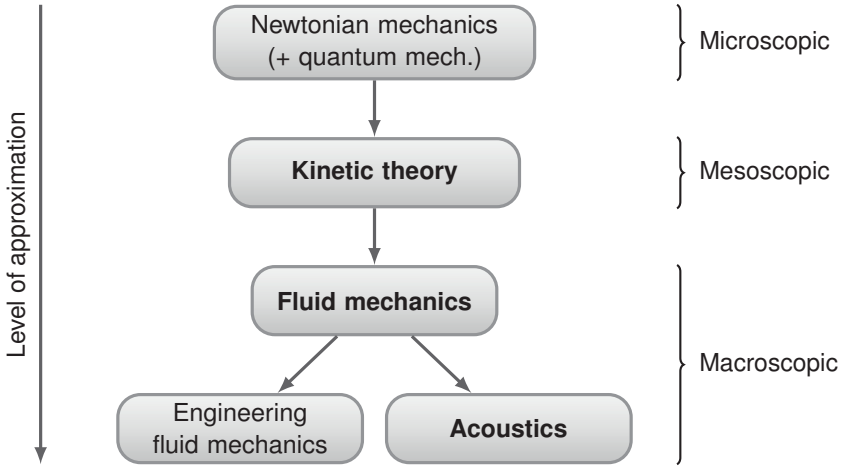

Figure 1.2: The hierarchy of descriptions of a gas. This thesis will focus on the three highlighted descriptions.

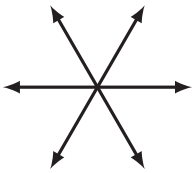

Figure 1.3: The six possible particle velocities in the FHP lattice gas

and *acoustics*. This will differentiate this thesis somewhat from most of the lattice Boltzmann literature, which is focused on applications in incompressible fluid mechanics.

1.1.2 A simple microscopic model: The FHP lattice gas

A lattice gas is a microscopic model which attempts to simulate the behaviour and interaction of the individual particles in a gas in as simple a fashion as possible. In the following, we will go briefly through the FHP model from 1986 [2], named after its inventors Frisch, Hasslacher, and Pomeau. This is the simplest possible lattice gas which can reproduce the behaviour of a fluid.

Rules

In a lattice gas, a large number of particles exist on a *lattice*, a regular grid of nodes. In the FHP model, this lattice is hexagonal; lattice gases

on square lattices turned out to be unable to reproduce correct fluid behaviour. Each particle has one out of six possible velocities shown in Figure 1.3, which point from the particle's current node to a neighbouring node. In each node, zero to six particles may be present simultaneously as long as they all have unique velocities.

Every time that the clock ticks forwards by one time step Δt, two rules are applied:

- **Streaming.** All particles move from their current node to the neighbouring node in the direction of their velocity vector.
- **Collision.** If two or three particles meet head on in a node, their outgoing velocities are changed from their incoming velocities. The two-particle case has two possible resolutions which are chosen at random with equal probability.

These rules are illustrated in Figure 1.4. After the streaming step, particles in each node may collide, and after the collision step, particles are prepared to stream to neighbouring nodes. Later versions of the FHP model introduced particles at rest (where $\boldsymbol{\xi}_i = 0$) and additional collision types, but we will not go into these here.

Both rules are in accordance with fundamental mechanical laws. The streaming rule embodies Newton's first law; the particles' velocities are constant until forces are applied to them in collisions. Within each node, these collisions obey the conservation of mass $\sum_i m_i$, momentum $\sum_i m_i \boldsymbol{\xi}_i$, and energy $\sum_i m_i |\boldsymbol{\xi}_i|^2/2$.

Macroscopic variables and statistical noise

Since a lattice gas is a microscopic model, the mass and momentum in the nodes of the system will always be fluctuating, even when the system is at an equilibrium.* While this *statistical noise* is a desired property if such fluctuations are the topic of study, they are highly undesired when trying to simulate nice and smooth fluid flows.

To use this model to predict anything on the macroscopic scale, we would need to approximate the expectation values in (1.1) somehow. Several methods may be used in order to do this. One such method utilises the law of large numbers by averaging over several nearby nodes, which can be compared with expanding the small volume V in (1.1). Another is averaging the results over several time steps. These two methods will indeed reduce the statistical noise, at the cost of smoothing out the macroscopic solution slightly. In order to reduce this smoothing, the simulation resolution could be increased, putting more nodes inside the

*There are two trivial exceptions to this. One, if the lattice contains *no* particles. Two, if the lattice is *completely stuffed* with particles, with no empty spaces.

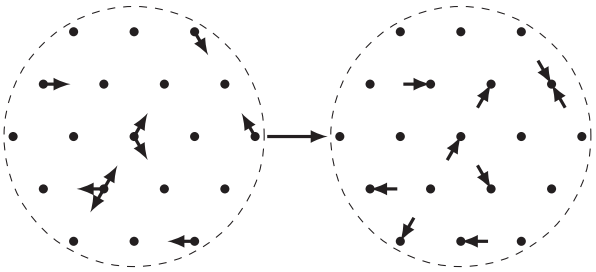

(a) Streaming rule

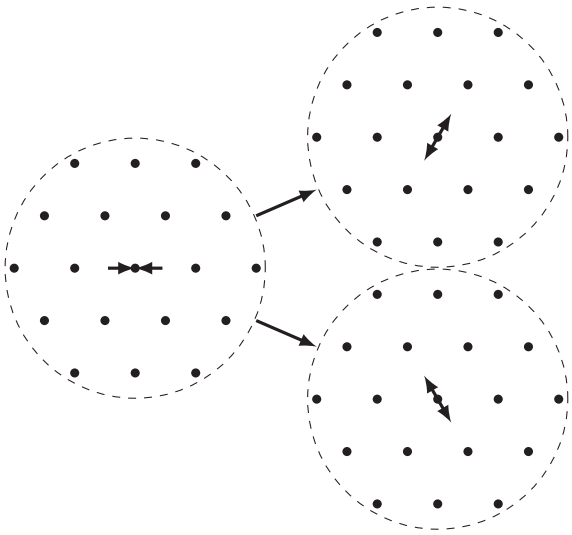

(b) Double collision rule; the resolutions are chosen randomly with equal probability

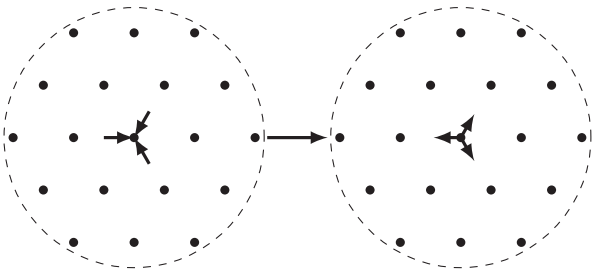

(c) Triple collision rule

Figure 1.4: Rules of the FHP model. *Incoming* and *outgoing* particles, i.e. particles *before* and *after* the collision step, are represented with arrows pointing *into* and *out of* nodes, respectively.

same physical space. A third, quite demanding, method is to simultaneously simulate several similar systems such that each system is initialised with the same macroscopic state but different microscopic states. The macroscopic variables can be estimated by averaging the results over this ensemble of systems.

Still, the problem of statistical noise can only ever be reduced in these ways, never entirely removed. Lattice gas simulations of fluid flow typically end up with a significant amount of noise in their results [6, 7], limiting their usefulness.

Towards the mesoscopic scale

A clever solution to the problem of statistical noise was found independently by different groups [3, 8]. Instead of tracking particles that are either *there* or *not there*, it is possible to track *particle distributions*; essentially the expectation value of the number of particles. If we hypothetically had an ensemble of infinitely many similar systems, the particle distribution can be seen as the average over the systems of the particle number in each state. In another sense, it is the *probability* of finding a particle in that state. For example, if the particle distribution is 0 for a certain position, time, and particle velocity, there is *never* a particle in that particular state. If the particle distribution is 1, there is *always* a particle in that state.

This particle distribution function is usually denoted as $f_i(\boldsymbol{x}, t)$. i now indexes the different possible velocities $\boldsymbol{\xi}_i$ (six for the FHP lattice gas) instead of different particles. Thus, $f_i(\boldsymbol{x}, t)$ can be seen as the probability of finding a particle with velocity $\boldsymbol{\xi}_i$ at position $\boldsymbol{x}$ and time t. We have now gone from the *microscale* lattice gas to a corresponding *mesoscale* description.

The lattice Boltzmann method was historically derived in this way, as a modification to lattice gases using the distribution function f_i. We could now proceed along these lines to fully derive the lattice Boltzmann method,* but there is also another, more physical, way to derive it from the kinetic theory of gases. This thesis will follow the latter type of derivation, as this gives a very valuable insight into the underlying physical aspects and their connection to the numerical method.

We will therefore stop here for now, and leave this discussion as an example of a mesoscale description of a gas. We will pick up this thread again in Chapter 3, where we will look at the kinetic theory of gases. In Chapter 4, the lattice Boltzmann method will be derived as a discretisation of the *Boltzmann equation*, a cornerstone equation of this kinetic theory.

*Indeed, that was what this author did in his Master's thesis [9].

1.2 This thesis

Let us now take a break from the theory to consider the purpose and the structure of this thesis.

1.2.1 Goals

There are two relevant sets of goals here. The first set is the goals of the ph.d. research project that underlies this thesis, and the second set is the goals of the thesis itself.

Project goals

The title of the research project was *Acoustic properties and methods of lattice Boltzmann*. The project had two goals. First, to improve the current understanding of the propagation of sound waves in LB simulations. Second, to find new and develop existing methods for LB acoustics.

Thesis goals

The primary goal of this thesis is of course to present the research that was done in the course of the research project. By exploiting the additional space afforded by a thesis, the idea is to present the research in a more *comprehensive* and *comprehensible* fashion than scientific articles allow for. The hope is to make this research as simple as possible to understand and to develop further.

The secondary goal is to attempt to give a clearly written, reasonably thorough, and freely available introduction to the lattice Boltzmann method. A fair amount of introduction would anyhow be necessary in this thesis as background for the research. Extending that introduction makes it more valuable for other people who are trying to learn the fundamentals of the lattice Boltzmann method.

1.2.2 Thesis structure

This thesis is divided into two main parts. Part I contains background material for Part II, including an introduction to the lattice Boltzmann method and its underlying physics. Part II describes the results of the research that was carried out in the course of the project. The structure of the thesis and the main information flow between the different chapters and parts is shown in Figure 1.5.

The thesis contains the following eight chapters:

Part I: Background

Ch. 1 **Introduction:** This chapter.

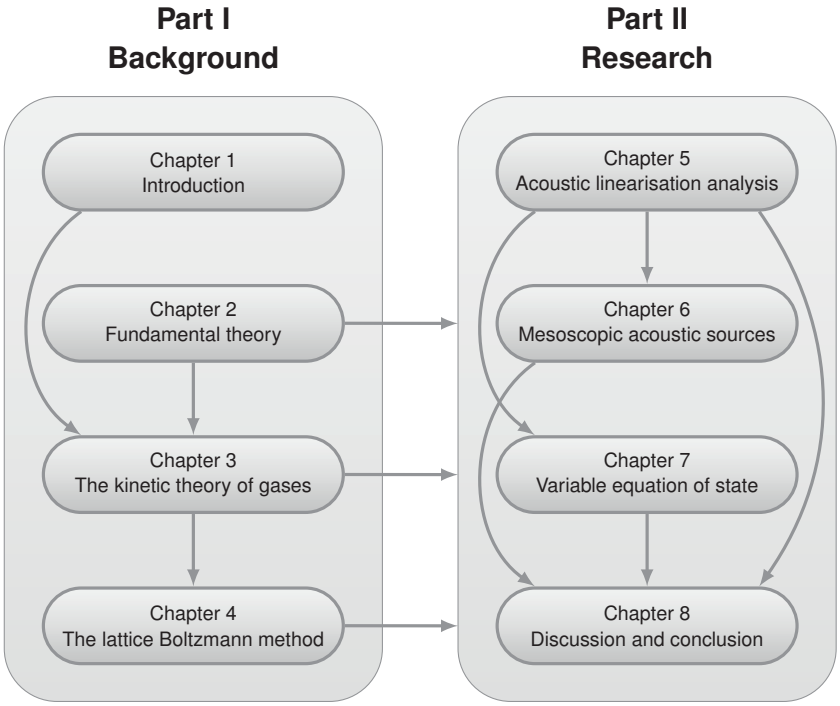

Figure 1.5: The structure of the thesis. The arrows represent the main flow of information.

Ch. 2 **Fundamental theory:** Introduction to index notation, fluid mechanics, and acoustics

Ch. 3 **The kinetic theory of gases:** The mesoscopic description of a gas and its connection to fluid mechanics

Ch. 4 **The lattice Boltzmann method:** Derivation of LB from kinetic theory and description of its basics

Part II: Research

Ch. 5 **Acoustic linearisation analysis:** Derivation and comparison of the sound propagation properties of various fluid models, including LB

Ch. 6 **Mesoscopic acoustic sources:** Derivation of mesoscopic sound sources that can be implemented in LB

Ch. 7 **Variable equation of state:** An extended LB model that allows changing the fluid's equation of state and bulk viscosity is applied to simulate nonlinear acoustics and molecular relaxation

Ch. 8 **Discussion and conclusion:** A summary of the research and some ideas on how it may be continued

1.2.3 Related published articles

In the course of this ph.d. project, five scientific articles have been published. All were written solely by this author, and all are freely and legally available online at this time of writing. In chronological order, they are:

The lattice Boltzmann method in acoustics (2010) [10]
Proceedings of the 33rd Scandinavian symposium on physical acoustics

Abstract: The lattice Boltzmann method, a method based in kinetic theory and used for simulating fluid behaviour, is presented with particular regard to usage in acoustics. A point source method of generating acoustic waves in the computational domain is presented, and simple simulation results with this method are analysed. The simulated waves' transient wavefronts in one dimension are shown to agree with analytical solutions from acoustic theory. The phase velocity and absorption coefficients of the waves and their deviations from theory are analysed. Finally, the physical time and space steps relating simulation units with physical units are discussed and shown to limit acoustic usage of the method to small scales in time and space.

Comments: This article uses the LB point source presented in [9] to simulate sound waves propagating in 1D, 2D, and 3D. This point source is inferior to the mesoscopic source method presented in Chapter 6, for reasons that will be explained in that chapter. Nevertheless, the article was a first step to some results that are given in Chapters 5 and 6. The limit described in the abstract's final sentence has turned out to be less bad than assumed; in Chapter 6 we will see that using another particle collision model softens the constraints causing this limit.

Viscously damped acoustic waves with the lattice Boltzmann method (2011) [11]
Philosophical Transactions of the Royal Society A **369**, pp. 2246–2254

Abstract: Acoustic wave propagation in lattice Boltzmann Bhatnagar-Gross-Krook simulations may be analysed using a linearization method. This method has been used in the past to study the propagation of waves that are viscously damped in time, and is here extended to also study waves that are viscously damped in space. Its validity is verified against simulations, and the results are compared with theoretical expressions. It is found in the infinite resolution limit $k \to 0$ that the absorption coefficients and phase differences between density and velocity waves match theoretical expressions for small values of $\omega\tau_\nu$, the characteristic number for viscous acoustic damping. However, the phase velocities and amplitude ratios between the waves increase incorrectly with $(\omega\tau_\nu)^2$, and agree with theory only in the inviscid limit $k \to 0$, $\omega\tau_\nu \to 0$. The

actual behaviour of simulated plane waves in the infinite resolution limit is quantified.

Comments: This article partially forms the basis of Chapter 5. The numerical results in this article are improved and given analytically in that chapter.

Sound propagation properties of the discrete-velocity Boltzmann equation (2013) [12]
Communications in Computational Physics **13**, pp. 671–684

Abstract: As the numerical resolution is increased and the discretisation error decreases, the lattice Boltzmann method tends towards the discrete-velocity Boltzmann equation (DVBE). An expression for the propagation properties of plane sound waves is found for this equation. This expression is compared to similar ones from the Navier-Stokes and Burnett models, and is found to be closest to the latter. The anisotropy of sound propagation with the DVBE is examined using a two-dimensional velocity set. It is found that both the anisotropy and the deviation between the models is negligible if the Knudsen number is less than 1 by at least an order of magnitude.

Comments: This article also partially forms the basis of Chapter 5.

Acoustic multipole sources for the lattice Boltzmann method (2013) [13]
Physical Review E **87**, p. 023306

Abstract: By including an oscillating particle source term, acoustic multipole sources can be implemented in the lattice Boltzmann method. The effect of this source term on the macroscopic conservation equations is found using a Chapman-Enskog expansion. In a lattice with q particle velocities, the source term can be decomposed into q orthogonal multipoles. More complex sources may be formed by superposing these basic multipoles. Analytical solutions found from the macroscopic equations and an analytical lattice Boltzmann wavenumber are compared with inviscid multipole simulations, finding very good agreement except close to singularities in the analytical solutions. Unlike the BGK operator, the regularized collision operator is proven capable of accurately simulating two-dimensional acoustic generation and propagation at zero viscosity.

Comments: This article partially forms the basis of Chapter 6.

Acoustic multipole sources from the Boltzmann equation (2013) [14]
Proceedings of the 36th Scandinavian symposium on physical acoustics

Abstract: By adding a particle source term in the Boltzmann equation

of kinetic theory, it is possible to represent particles appearing and disappearing throughout the fluid with a specified distribution of particle velocities. By deriving the wave equation from this modified Boltzmann equation via the conservation equations of fluid mechanics, multipole source terms in the wave equation are found. These multipole source terms are given by the particle source term in the Boltzmann equation. To the Euler level in the momentum equation, a monopole and a dipole source term appear in the wave equation. To the Navier-Stokes level, a quadrupole term with negligible magnitude also appears.

Comments: This is a companion article to the previous article, also partially forming the basis of Chapter 6. A preprint was published at arXiv.org [15], with identical content but different formatting.

Acoustic equations of state for simple lattice Boltzmann velocity sets
Submitted to *Communications in Computational Physics*

Abstract: The most widely used lattice Boltzmann (LB) method uses an isothermal equation of state. This is not sufficient to simulate a number of acoustic phenomena where the equation of state cannot be approximated as linear and constant. It is possible to implement variable equations of state by altering the LB equilibrium distribution. For simple velocity sets with velocity components $\xi_{i\alpha} \in \{-1, 0, 1\}$ for all i, these equilibria necessarily cause error terms in the momentum equation. These error terms are shown to be either correctable or negligible at the cost of weakening the compressibility further. For the D1Q3 velocity set the equilibrium distribution is shown to be unique. Its sound propagation properties are found for both forced and free waves with applicability beyond D1Q3. Finally, the equilibrium distribution is applied to a nonlinear acoustics simulation where both mechanisms of nonlinearity are simulated with good results, proving that the compressibility of the method is still sufficiently strong even for nonlinear acoustics.

Comments: This article covers several of the topics of Chapter 7, though in a more concise manner that allows for a clearer exposition.

1.2.4 Mathematical notation and list of symbols

In this thesis, some accents, subscripts and superscripts of symbols used in the matematical notation carry a certain meaning. These are shown in Table 1.1. Note that no notational difference is used between vectors, matrices, or higher-order tensors, as all are *tensors*.

This thesis makes extensive use of *index notation*, a style of notation commonly used in fluid mechanics as an alternative to vector and tensor notation. This style of notation will be explained in section 2.1.

Table 1.1: Accents, subscripts and superscipts, applied to the example symbol λ

Mark	Description
$\boldsymbol{\lambda}$	Vector or tensor
λ_α	Arbitrary element of a spatial first-order tensor (vector) $\boldsymbol{\lambda}$
$\lambda_{\alpha\beta}$	Arbitrary element of a spatial second-order tensor (matrix) $\boldsymbol{\lambda}$
$\lambda_{\alpha\beta\gamma}$	Arbitrary element of a spatial third-order tensor $\boldsymbol{\lambda}$
λ_0	Rest state value or ideal value of λ
λ'	Deviation from rest state; $\lambda = \lambda_0 + \lambda'$
$\lambda^\star$	Amplitude of the deviation λ'
$\lambda^{(0)}$	Equilibrium value
$\lambda^{(n)}$	nth order perturbation around equilibrium value
λ^{neq}	Nonequilibrium value $\lambda - \lambda^{(0)}$
λ_{ph}	Value of λ in physical units
λ_{la}	Value of λ in simplified lattice units
$\tilde{\lambda}$	Nondimensionalised value
$\hat{\lambda}$	Complex phasor or related quantity

Throughout a mathematical text of this size, a large number of mathematical symbols must necessarily be defined. In order to stay as consistent as possible with the literature, some symbols have received several different meanings, though an effort is made in the text to avoid confusion. For future reference, the symbols that are used repeatedly throughout this thesis are shown in Table 1.2.

Table 1.2: Regularly used symbols throughout this thesis

Symbol	Description
$\boldsymbol{A}$	Multipole transformation matrix
b	Bulk viscosity correction constant
$\boldsymbol{B}$	Particle source basis
$\mathcal{B}_i$	Bulk viscosity correction term
c	Speed of sound
c_0	Ideal, small-signal speed of sound
c_ξ	Velocity set constant (equals c_0 outside Chapter 7)
c_i	Isothermal speed of sound (equals c_0 outside Chapter 7)
c_V	Heat capacity at constant volume
c_p	Heat capacity at constant pressure
d	Number of spatial dimensions
d_i	Number of inner degrees of freedom
d_tot	Total number of degrees of freedom
e	Internal energy
E	Total energy
$\mathsf{E}(\dots)$	Expectation value
f	Distribution function
f_i	Discrete-velocity distribution function
$\tilde{f}_i$	Modified discrete-velocity distribution function
$F^{(0)}$	Rest state distribution function
$\boldsymbol{F}$	Body force
G	Green's function
h	Enthalpy
H	Excitation fraction of an inner degree of freedom
$\mathcal{H}$	Boltzmann entropy function
j	Particle source term
j_i	Discrete-velocity particle source term
$\boldsymbol{J}$	Moment of particle source term
k_B	Boltzmann constant
Kn	Knudsen number
m	Molecular mass
$\boldsymbol{m}$	Moment vector
$\boldsymbol{M}$	Moment transformation matrix
Ma	Mach number
p	Pressure
Pr	Prandtl number
q	Heat flux
Q	Mass source term
R	Specific gas constant k_B/m
s	Entropy
S	Heaviside step function
$\boldsymbol{S}$	Strain rate tensor
t	Coordinate in time
t_mfp	Mean free time between collisions
t_r	Retarded time $t - x/c_0$
t_shock	Lossless plane-wave shock formation time
T	Temperature
$\boldsymbol{T}$	MRT relaxation matrix
$\mathcal{T}$	Acoustic multipole tensor
$\boldsymbol{u}$	Fluid velocity
$\boldsymbol{v}$	Peculiar velocity $\boldsymbol{\xi} - \boldsymbol{u}$
V	Volume

w_i	Weighting coefficient
w	Complex error function, aka. Faddeeva function
W	Window function
$\boldsymbol{x}$	Coordinate in physical space
x_{mfp}	Mean free path between collisions
x_{shock}	Lossless plane-wave shock formation distance
X	Acoustic viscosity number $\omega_0\tau_\nu$
X_{m}	Acoustic relaxation number $\omega_0\tau_{\mathrm{m}}$
α_x	Spatial absorption coefficient
α_t	Temporal absorption coefficient
β	Coefficient of nonlinearity
γ	Heat capacity ratio c_p/c_V, aka. adiabatic index
Γ	Bulk viscosity correction tensor
$\delta_{\alpha\beta}$	Kronecker delta
$\delta(\boldsymbol{x})$	Dirac delta function
Δx	Spatial resolution
Δt	Temporal resolution
ϵ	Chapman-Enskog smallness parameter
ε	Macroscopic smallness parameter
κ	Thermal conductivity
λ	Acoustic wavelength
μ	Dynamic shear viscosity
μ_{B}	Dynamic bulk viscosity
ν	Kinematic shear viscosity
ν_{B}	Kinematic bulk viscosity
$\boldsymbol{\xi}$	Particle velocity or coordinate in velocity space
$\boldsymbol{\xi}_i$	Discrete particle velocity
$\boldsymbol{\Pi}$	Moment of f
$\breve{\boldsymbol{\Pi}}$	Moment of f_i, if inequal to the corresponding $\boldsymbol{\Pi}$
ρ	Mass density
σ	Stress tensor
σ'	Deviatoric stress tensor
τ	Kinetic relaxation time
τ_ν	Viscous relaxation time
τ_κ	Thermal relaxation time
τ_{m}	Molecular relaxation time
Ω	Collision operator
$\boldsymbol{\Omega}$	Collision matrix

2 Fundamental theory

To ensure that this thesis is approachable for people from various scientific backgrounds, we will first go through some of the fundamental theory of fluid mechanics and acoustics before delving into the specifics of kinetic theory and the lattice Boltzmann method. Some of the topics in this chapter will be covered in more detail in later chapters.

2.1 Index notation

Index notation, like vector notation, is a notation style for sets of quantities associated with different spatial directions. It is commonly used in fluid mechanics and less commonly in acoustics, and will be used throughout this thesis.

Throughout physics, many equations deal with behaviour which is similar in multiple spatial directions. As a simple example, Newton's second law can be written as three equations,

$$F_x = ma_x, \qquad F_y = ma_y, \qquad F_z = ma_z, \tag{2.1a}$$

with one equation for each spatial direction. In fact, many classic works on fluid mechanics and acoustics, written before other kinds of notation became common, used this expansive type of notation [16, 17]. Three individual but very similar equations would be given together; one for each spatial direction.

Tensor
For our purposes we can see tensors as mathematical objects generalising vectors and matrices. Scalars are tensors of zeroth order, vectors are of first order, matrices are of second order, and higher orders are also possible. The order corresponds to the number of indices required to point to a component of the tensor.

Using vector notation, which can more generally be called *tensor* notation, these three equations can be written as one single equation,

$$\boldsymbol{F} = m\boldsymbol{a}. \tag{2.1b}$$

Here, the x, y, and z components of $\boldsymbol{F}$ and $\boldsymbol{a}$ are implicitly related.

Another alternative style of notation is index notation,

$$F_\alpha = ma_\alpha. \tag{2.1c}$$

The equation is written as in (2.1a), except that a generic index α is used. This allows expressing the system of equations as explicitly as in (2.1a), but with a single equation instead of three.

The single index used in (2.1c) indicates that F_α and a_α are vector components. Index notation can also be used to point to generic components of higher order tensors. A generic component of the second-order tensor (or matrix) $\boldsymbol{A}$ would be $A_{\alpha\beta}$, and similarly a component of the third-order tensor $\boldsymbol{R}$ is $R_{\alpha\beta\gamma}$. This illuminates a strength of index notation: The order of the tensor is immediately clear from the number of unique indices.

Another important strength comes from the summation convention introduced by Einstein [18]: Repeating an index twice in a single term implies summation over all possible values of that index. Thus,

$$a_\alpha b_\alpha = \sum_\alpha a_\alpha b_\alpha = a_x b_x + a_y b_y + a_z b_z = \boldsymbol{a} \cdot \boldsymbol{b}. \tag{2.2}$$

The dot product has about the same economy of notation in tensor and index notation.

In this thesis, Greek indices and the summation convention are used for spatial components. For components of general, non-spatial tensors, indices i, j, k, ... are used, and the summation convention is not used. This practice is common in the field of lattice Boltzmann research.

Other vector operations can also be easily expressed using index notation. The outer product in tensor and index notation is

$$\boldsymbol{A} = \boldsymbol{a} \otimes \boldsymbol{b} \quad \Longleftrightarrow \quad A_{\alpha\beta} = a_\alpha b_\beta.$$

Yet another strength of index notation becomes apparent; in vector/tensor notation, we must introduce a new symbol $\otimes$ for this particular operation. In index notation, however, the meaning is immediately clear: The α, β component of the matrix $\boldsymbol{A}$ is given by the product of the α component of $\boldsymbol{a}$ and the β component of $\boldsymbol{b}$. The corresponding downside is that a large number of indices can result in a notation that looks somewhat messy.

Using index notation, we can also generalise coordinate notation, writing a general component of the spatial coordinate vector $\boldsymbol{x} = (x, y, z) = (x_1, x_2, x_3)$ as x_α. In this way, we can express e.g. gradients in index notation,

$$\nabla \lambda(\boldsymbol{x}) \quad \Longleftrightarrow \quad \frac{\partial \lambda(\boldsymbol{x})}{\partial x_\alpha}.$$

Most common vector and tensor operations can be conveniently expressed in index notation, as shown in Table 2.1. The cross product requires use of the *Levi-Civita symbol*, which is the third order tensor

$$\varepsilon_{\alpha\beta\gamma} = \begin{cases} +1 & \text{if } (\alpha,\beta,\gamma) \text{ is } (1,2,3), (3,1,2) \text{ or } (2,3,1), \\ -1 & \text{if } (\alpha,\beta,\gamma) \text{ is } (3,2,1), (1,3,2) \text{ or } (2,1,3), \\ 0 & \text{if } \alpha = \beta, \beta = \gamma, \text{ or } \gamma = \alpha. \end{cases} \tag{2.3}$$

The cross product will not be used at any point later in this thesis, however.

Table 2.1: Examples of common operations in tensor and index notation

Operation	Tensor notation	Index notation
Vector dot product	$\lambda = \boldsymbol{a} \cdot \boldsymbol{b}$	$\lambda = a_\alpha b_\alpha$
Vector cross product	$\boldsymbol{c} = \boldsymbol{a} \times \boldsymbol{b}$	$c_\alpha = \varepsilon_{\alpha\beta\gamma} a_\beta b_\gamma$
Vector outer product	$\boldsymbol{A} = \boldsymbol{a} \otimes \boldsymbol{b}$	$A_{\alpha\beta} = a_\alpha b_\beta$
Tensor contraction	$\lambda = \boldsymbol{A} : \boldsymbol{B}$	$\lambda = A_{\alpha\beta} B_{\alpha\beta}$
Gradient	$\boldsymbol{a} = \nabla\lambda$	$a_\alpha = \partial\lambda / \partial x_\alpha$
Laplacian	$\Lambda = \nabla^2\lambda$	$\Lambda = \partial^2\lambda / \partial x_\alpha \partial x_\alpha$
1st order tensor divergence	$\lambda = \nabla \cdot \boldsymbol{a}$	$\lambda = \partial a_\alpha / \partial x_\alpha$
2nd order tensor divergence	$\boldsymbol{a} = \nabla \cdot \boldsymbol{A}$	$a_\alpha = \partial A_{\alpha\beta} / \partial x_\beta$
3rd order tensor divergence	$\boldsymbol{A} = \nabla \cdot \boldsymbol{R}$	$A_{\alpha\beta} = \partial R_{\alpha\beta\gamma} / \partial x_\gamma$

Another, more widely useful, symbol is the *Kronecker delta symbol*, which is the second order tensor

$$\delta_{\alpha\beta} = \begin{cases} 1 & \text{if } \alpha = \beta, \\ 0 & \text{if } \alpha \neq \beta. \end{cases} \tag{2.4}$$

We can see by inspection that $\delta_{\alpha\beta}$ is a generic element of the identity matrix

$$\boldsymbol{I} = \begin{bmatrix} 1 & 0 & 0 \\ 0 & 1 & 0 \\ 0 & 0 & 1 \end{bmatrix}.$$

This thesis will alternate between tensor notation and index notation to some degree, generally using the former for simpler equations and the latter for more complicated equations that benefit from the explicitness of index notation.

2.1.1 Examples

Some properties and methods of index notation are best shown by example. These will be implicitly used throughout the rest of the thesis.

Arbitrariness of summation indices. When the summation convention is used, the summation index is arbitrary. Thus,

$$a_\alpha b_\alpha = a_\gamma b_\gamma, \qquad \frac{\partial A_{\alpha\beta}}{\partial x_\beta} = \frac{\partial A_{\alpha\delta}}{\partial x_\delta}. \tag{2.5}$$

The Kronecker delta and the summation convention. The Kronecker delta can change the index of other quantities,

$$\delta_{\alpha\beta} a_\beta = \delta_{\alpha x} a_x + \delta_{\alpha y} a_y + \delta_{\alpha z} a_z = a_\alpha. \tag{2.6}$$

The Kronecker delta and trace. The trace of a second order tensor can be taken by multiplying with the Kronecker delta,

$$\delta_{\alpha\beta}A_{\alpha\beta} = A_{xx} + A_{yy} + A_{zz} = A_{\gamma\gamma} = \mathrm{Tr}(\boldsymbol{A}). \tag{2.7}$$

Trace of the Kronecker delta. From Table 2.1, this is equivalent to contracting the identity matrix with itself. With three spatial dimensions, this becomes

$$\delta_{\alpha\beta}\delta_{\alpha\beta} = \boldsymbol{I} : \boldsymbol{I} = \begin{bmatrix} 1 & 0 & 0 \\ 0 & 1 & 0 \\ 0 & 0 & 1 \end{bmatrix} : \begin{bmatrix} 1 & 0 & 0 \\ 0 & 1 & 0 \\ 0 & 0 & 1 \end{bmatrix} = 3. \tag{2.8}$$

Euclidean distance. The square of the Euclidean distance is

$$\begin{aligned} |\boldsymbol{a} - \boldsymbol{b}|^2 = (a_\alpha - b_\alpha)(a_\alpha - b_\alpha) &= a_\alpha a_\alpha - 2a_\alpha b_\alpha + b_\alpha b_\alpha \\ &= \boldsymbol{a}\cdot\boldsymbol{a} - 2\boldsymbol{a}\cdot\boldsymbol{b} + \boldsymbol{b}\cdot\boldsymbol{b}. \end{aligned} \tag{2.9}$$

Weighted integral of a spherically symmetric integrand. If a function $f(\boldsymbol{x})$ is spherically symmetric around $\boldsymbol{x} = \boldsymbol{0}$, then the integral over the entire volume, weighted with $x_\alpha x_\beta$, is

$$\int x_\alpha x_\beta f(\boldsymbol{x})\,\mathrm{d}\boldsymbol{x} = \delta_{\alpha\beta}\int \frac{x_\gamma x_\gamma}{3} f(\boldsymbol{x})\,\mathrm{d}\boldsymbol{x}. \tag{2.10}$$

This follows from the integrand having odd symmetry, so that the integral becomes zero unless α and β are equal. Also, due to the spherical symmetry of $f(\boldsymbol{x})$, weighting the integral by x^2, y^2, or z^2 is equal to weighting it by $(x^2 + y^2 + z^2)/3 = x_\gamma x_\gamma/3$.

Multidimensional integration by parts. If there is a volume Ω bounded by a surface Γ, and two functions u and v that are smooth inside Ω and on Γ, then

$$\int_\Omega \frac{\partial u}{\partial x_\alpha} v\,\mathrm{d}\Omega = \int_\Gamma uv\,\mathrm{d}\Gamma_\alpha - \int_\Omega u\frac{\partial v}{\partial x_\alpha}\,\mathrm{d}\Omega, \tag{2.11a}$$

where Γ_α is the surface normal of Γ. In one dimension this reduces to normal integration by parts. The multidimensional integration by parts also holds if one or both of the functions are tensor components, e.g.

$$\int_\Omega \frac{\partial u_\alpha}{\partial x_\alpha} v\,\mathrm{d}\Omega = \int_\Gamma u_\alpha v\,\mathrm{d}\Gamma_\alpha - \int_\Omega u_\alpha\frac{\partial v}{\partial x_\alpha}\,\mathrm{d}\Omega. \tag{2.11b}$$

2.2 Fluid mechanics

The fundamental equations of fluid mechanics are conservation equations. Basic physics tells us that mass,* momentum, and total energy are always conserved in a closed system. These fluid mechanics equations express these conservation laws in the case of a macroscopic *continuum*.

Continuum
Modelling a physical body as a continuum, we disregard that the fact it is made out of atoms and empty space and assume that the body is continuous, preserving its macroscopic quantities even on the microscopic scale.

*Barring nuclear reactions and relativistic effects, of course.

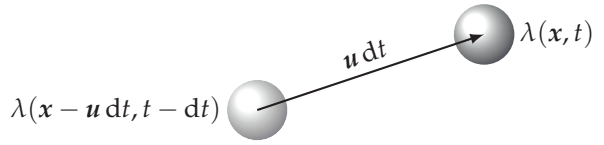

Figure 2.1: As a fluid particle moves through the fluid, its properties may change.

There are two widely used models of such conservation equations: the Euler model and the Navier-Stokes-Fourier model. The former model is older, while the latter model is more detailed. While these equations are usually derived from a continuum mechanics perspective, we will derive them from more physically fundamental kinetic theory in Chapter 3. They will only be introduced briefly in this section.

Common to both sets is the equation for conservation of mass, also known as the continuity equation,

$$\frac{\partial \rho}{\partial t} + \nabla \cdot (\rho \boldsymbol{u}) = 0. \tag{2.12}$$

Mass density, ρ
Mass per physical volume in $\mathrm{kg/m^3}$

Fluid velocity, $\boldsymbol{u}$
The local velocity of the fluid in $\mathrm{m/s}$

Material derivative, $\mathrm{D}/\mathrm{D}t$
The time derivative for a moving fluid particle

Here, $\rho = \rho(\boldsymbol{x}, t)$ is the *mass density* (or just *density*) and $\boldsymbol{u} = \boldsymbol{u}(\boldsymbol{x}, t)$ is the *fluid velocity*. This equation connects the rate of change of density at a point and the outward or inward mass flux at that point.

One notational convenience which is common throughout fluid mechanics is the use of the *material derivative*. Let's say we have a generic quantity $\lambda(\boldsymbol{x}, t)$. From the total differential of this, we have

$$\frac{\mathrm{d}\lambda}{\mathrm{d}t} = \left(\frac{\partial \lambda}{\partial t}\right)\frac{\mathrm{d}t}{\mathrm{d}t} + \left(\frac{\partial \lambda}{\partial x_\alpha}\right)\frac{\mathrm{d}x_\alpha}{\mathrm{d}t}.$$

Here, $\mathrm{d}x_\alpha/\mathrm{d}t$ is the fluid velocity $\boldsymbol{u}$. This gives us the material derivative, usually written with a capital D,

$$\frac{\mathrm{D}\lambda}{\mathrm{D}t} = \frac{\partial \lambda}{\partial t} + \boldsymbol{u} \cdot \nabla \lambda. \tag{2.13}$$

The material derivative can be interpreted as a time derivative for a fluid particle moving throughout the fluid with a velocity $\boldsymbol{u}(\boldsymbol{x}, t)$, as shown in Figure 2.1. This fluid particle represents a tiny piece of the fluid continuum, small enough that all relevant quantities are nearly constant inside of it. The first term on the right-hand side of (2.13) is the rate of change that would occur if the particle were stationary. The second term is the rate of change caused by the particle moving into a different part of the fluid where the conditions may be different.

The conservation equations can either be written in material derivative form, emphasising changes to a fluid particle, or in conservation form,

emphasising changes in a static control volume. For the generic quantity $\lambda(\boldsymbol{x}, t)$, the two are related as

$$\frac{\partial \rho\lambda}{\partial t} + \frac{\partial \rho u_\alpha \lambda}{\partial x_\alpha} = \lambda\left(\frac{\partial \rho}{\partial t} + \frac{\partial \rho u_\alpha}{\partial x_\alpha}\right) + \rho\frac{\partial \lambda}{\partial t} + \rho u_\alpha \frac{\partial \lambda}{\partial x_\alpha} = \rho\frac{\mathrm{D}\lambda}{\mathrm{D}t}, \tag{2.14}$$

with conservation form on the left and material derivative form on the right. The parenthesis in the middle is zero due to (2.12).

The *state principle* of equilibrium thermodynamics is important for fluid mechanics. It states that any *state variable*, such as the density ρ, the pressure p, the temperature T, the internal energy e, or the entropy s can be found from any other two state variables through an *equation of state* [19, Ch. 2].* The most classic example of this is the classic ideal gas law,

$$p = p(\rho, T) = \rho R T, \tag{2.15}$$

where R is the *specific gas constant*. Alternatively, the pressure could be expressed as a function of density ρ and entropy s. For ideal gases, this equation of state is [19, Ch. 2]

$$\frac{p}{p_0} = \left(\frac{\rho}{\rho_0}\right)^\gamma \mathrm{e}^{(s-s_0)/c_V}. \tag{2.16}$$

The quantities with subscripted zeroes are reference state values. $\gamma = c_p/c_V$ is the *heat capacity ratio* or *adiabatic index*, which relate the heat capacities at constant pressure c_p and at constant volume c_V.

State variable
Quantities that describe the local thermodynamic state of the system. From the state principle, knowing two state variables is sufficient to find the rest.

Pressure, p
Force per area exerted by the fluid on a real or imaginary surface in $\mathrm{N/m^2}$

Equation of state
An equation relating any three state variables

Specific gas constant, R
The proportionality constant in the ideal gas law, in $\mathrm{J/kg\,K}$. It is dependent on the mass of the gas molecules.

2.2.1 The Euler model

The Euler model is named after Leonhard Euler, who first derived the mass and momentum conservation equations [20]. The mass, momentum, and energy conservation equations are

$$\frac{\partial \rho}{\partial t} + \nabla\cdot(\rho\boldsymbol{u}) = 0, \tag{2.17a}$$

$$\rho\frac{\mathrm{D}\boldsymbol{u}}{\mathrm{D}t} = -\nabla p + \boldsymbol{F}, \tag{2.17b}$$

$$\rho\frac{\mathrm{D}e}{\mathrm{D}t} = -p\nabla\cdot\boldsymbol{u}. \tag{2.17c}$$

$\boldsymbol{F}$ is the external *body force density*, which is typically gravitational.

Body force density, $\boldsymbol{F}$
Force density of long-range forces, e.g. gravity, in $\mathrm{N/m^3}$

The momentum equation (2.17b) describes how the velocity of a particle is changed by external body forces and pressure differences; higher pressures push the particle towards lower pressures.

*We will not go into detail with these state variables at this point. They will be described in more detail in Chapter 3.

The energy equation (2.17c) describes how the internal energy is either decreased by expansion (the particle pushing on its surroundings), or increased by compression (the surroundings pushing on the particle).

The Euler model is less accurate than the Navier-Stokes-Fourier model which will be described next, as it lacks the effects of internal friction and heat conduction in the fluid. Even so, it is sufficient for use in many different cases in acoustics and aerodynamics.

2.2.2 The Navier-Stokes-Fourier model

The equations of the Navier-Stokes-Fourier model are very similar to the corresponding equations of the Euler model. The difference is additional terms that take into account the effect of internal friction and heat conduction in the fluid.

Cauchy momentum equation
A general equation for the evolution of momentum, valid for both solids and fluids

The momentum equation in this model is of the form of the *Cauchy momentum equation*,

$$\rho \frac{\mathrm{D}u_\alpha}{\mathrm{D}t} = \frac{\partial \sigma_{\alpha\beta}}{\partial x_\beta} + F_\alpha, \tag{2.18}$$

a general equation which can describe momentum conservation in any continuum, even a solid. The *Cauchy stress tensor* $\boldsymbol{\sigma}$ describes the stresses due to internal forces.

Cauchy stress tensor, σ
A second-order tensor which at any point in the fluid specifies the normal and shear stresses in the x, y, and z directions

The three equations of the Navier-Stokes-Fourier model are

$$\frac{\partial \rho}{\partial t} + \nabla \cdot (\rho \boldsymbol{u}) = 0, \tag{2.19a}$$

$$\rho \frac{\mathrm{D}u_\alpha}{\mathrm{D}t} = -\frac{\partial p}{\partial x_\alpha} + \frac{\partial \sigma'_{\alpha\beta}}{\partial x_\beta} + F_\alpha, \tag{2.19b}$$

$$\rho \frac{\mathrm{D}e}{\mathrm{D}t} = \left(-\delta_{\alpha\beta} p + \sigma'_{\alpha\beta}\right) \frac{\partial u_\beta}{\partial x_\alpha} - \frac{\partial q_\alpha}{\partial x_\alpha}. \tag{2.19c}$$

These equations include the *heat flux* $\boldsymbol{q}$ and split the Cauchy stress tensor into two terms as $\boldsymbol{\sigma} = -p\boldsymbol{I} + \boldsymbol{\sigma}'$. The pressure term was already present in the Euler momentum equation (2.17b), but the *deviatoric stress* $\boldsymbol{\sigma}'$ is new.

The deviatoric stress tensor for a simple fluid, which was first determined by Stokes [21], is

$$\sigma'_{\alpha\beta} = \mu \left(\frac{\partial u_\beta}{\partial x_\alpha} + \frac{\partial u_\alpha}{\partial x_\beta} - \frac{2}{3} \delta_{\alpha\beta} \frac{\partial u_\gamma}{\partial x_\gamma} \right) + \mu_\mathrm{B} \delta_{\alpha\beta} \frac{\partial u_\gamma}{\partial x_\gamma}, \tag{2.19d}$$

and the heat flux is assumed to be given by Fourier's law,

$$q_\alpha = -\kappa \frac{\partial T}{\partial x_\alpha}. \tag{2.19e}$$

These equations include the material coefficients of dynamic shear viscosity μ, dynamic bulk viscosity μ_B,* and thermal conductivity κ. Often the kinematic shear viscosity $\nu = \mu/\rho$ and the kinematic bulk viscosity $\nu_B = \mu_B/\rho$ are used instead of their dynamic counterparts. With this form of the deviatoric stress tensor, the momentum equation (2.19b) is also known as the Navier-Stokes equation.

In the momentum equation (2.19b), the additional $\boldsymbol{\sigma}'$ term represents the friction between adjacent parts of the fluid moving at different speeds. $\boldsymbol{\sigma}'$ also occurs in the energy equation (2.19c), representing the energy increase due to frictional heating. The final $\boldsymbol{q}$ term represents the heat conduction between adjacent parts of the fluid with different temperatures.

In many subfields of fluid mechanics, the fluid is often considered to be *incompressible*, meaning that the density ρ is constant. This assumption simplifies the mass conservation equation to $\nabla \cdot \boldsymbol{u} = 0$. Consequently, the bulk viscosity in (2.19d) becomes irrelevant, as its term is zero. For this reason, bulk viscosity is often neglected in fluid mechanics. Still, it is relevant in acoustics and high-velocity compressible flow.

Many, if not most, problems in mathematical fluid mechanics reduce to solving these equations with appropriate boundary conditions, equations of state, and approximations. The most common boundary condition is the no-slip condition, where the fluid at a wall is restricted to have the same velocity as the wall due to friction. The physical origins of this no-slip condition are not fully clear even today [23, Ch. 4].

2.3 Acoustics

The wave equation is the mathematical basis for most of acoustics. This equation can be derived directly from the conservation equations of mass and momentum. Typically the linearised Euler equations with a simplified equation of state are used, but more detailed equations can also be employed to derive a more detailed wave equation.

In this section, we will first show how the simple ideal wave equation is derived and then find a more complex wave equation that takes into account the effects of viscosity and heat conduction. In both cases, we assume that the sound wave is weak enough that the equations can be *linearised*. Later we look at the effect of molecular rotation and vibration on sound propagation, and the mathematical modeling of multipole sound sources. Towards the end of this section we will consider what happens when the sound wave is strong and nonlinear effects occur. All

Linearisation
An approximation technique where terms of higher than first order in small quantities are neglected, resulting in linear equations

*Stokes originally assumed the bulk viscosity to be zero. This assumption was later found to be valid only for dilute monatomic gases, as will be shown in Chapter 3. However, the origins of bulk viscosity are somewhat controversial even today [22].

of these topics are relevant to the research work presented in Part II of this thesis.

The field quantities of acoustics can be divided into two parts,

$$\rho(\boldsymbol{x}, t) = \rho_0 + \rho'(\boldsymbol{x}, t), \tag{2.20a}$$
$$p(\boldsymbol{x}, t) = p_0 + p'(\boldsymbol{x}, t), \tag{2.20b}$$
$$\boldsymbol{u}(\boldsymbol{x}, t) = 0 + \boldsymbol{u}'(\boldsymbol{x}, t). \tag{2.20c}$$

The subscripted zeroes denote a constant rest state, and the primed quantities are small fluctuations. Linearisation entails neglecting any term where more than one primed term occurs simulaneously, due to that term's smallness.

Linearisation is widely employed in acoustics due to its wide range of applicability. The human ear's threshold of pain is at about 140 dB, which corresponds to a relative RMS pressure $p'_{\text{rms}}/p_0 \simeq 2 \times 10^{-3}$ in air, with p_0 being the standard atmospheric pressure [24, Chs. 5 & 11]. Thus, linearisation is a highly valid approximation for the sound waves we encounter in daily life.*

2.3.1 Ideal wave equation

The *ideal* wave equation neglects as many *nonideal* effects, such as viscosity and heat conduction, as possible. Even so, it is sufficient to describe most cases in acoustics with very good accuracy.

The wave equation is derived from the linearised form of the Euler mass and momentum equations, (2.17a) and (2.17b). Except for extremely low frequencies [24, Ch. 5] or long-range atmospheric or underwater propagation [25, Ch. 2], the effects of gravitational force are also negligible. The linearised and forceless Euler mass and momentum equations are

$$\frac{\partial \rho}{\partial t} + \rho_0 \frac{\partial u_\alpha}{\partial x_\alpha} = 0, \tag{2.21a}$$
$$\rho_0 \frac{\partial u_\alpha}{\partial t} + \frac{\partial p}{\partial x_\alpha} = 0. \tag{2.21b}$$

The sum $\partial(2.21\text{a})/\partial t - \partial(2.21\text{b})/\partial x_\alpha$ gives

$$\frac{\partial^2 \rho}{\partial t^2} - \nabla^2 p = 0. \tag{2.22}$$

This is one step away from the wave equation. Note that the derivatives of ρ and p are equal to the derivatives of ρ' and p', since the rest state values ρ_0 and p_0 are constant.

*This does not necessarily mean that nonlinear effects can always be completely neglected if the amplitude is not extremely high. Nonlinear effects accumulate as a sound wave propagates; they can still be relevant if a sound wave propagates far enough [24, Ch. 16].

To take the final step to the wave equation, we need to relate p' and ρ' through an equation of state. Typically, the isentropic relation

$$\frac{p}{p_0} = \left(\frac{\rho}{\rho_0}\right)^\gamma \tag{2.23}$$

is used [19, 24, 25]. This relation follows from (2.16) and the assumption of near-constant entropy, $s \simeq s_0$. From this equation, p' and ρ' can be related as

$$\frac{p'}{\rho'} \simeq \left(\frac{\partial p}{\partial \rho}\right)_{s,0} = \frac{\gamma p_0}{\rho_0} = c_0^2, \tag{2.24}$$

where the derivative has been evaluated at the rest state. We will soon see that c_0 is the ideal speed of sound.

Using this, we can re-express the time derivative term in (2.22) as $\partial^2\rho/\partial t^2 = \partial^2\rho'/\partial t^2 = (1/c_0^2)\partial^2 p'/\partial t^2$, and at last we find the *ideal wave equation*,

$$\boxed{\frac{1}{c_0^2}\frac{\partial^2 p}{\partial t^2} - \nabla^2 p = 0.} \tag{2.25}$$

This wave equation is linear. For solutions of a single frequency ω (which is the angular frequency, linked to the natural frequency f as $\omega = 2\pi f$) we can therefore use complex *phasor notation*, which is mathematically simpler to deal with. The simplest solution of the wave equation is a one-dimensional plane wave, which in phasor notation is

Phasor notation
A method of notation for variables in linear equations. It uses complex exponentials for mathematical simplicity. The real, physical solution is found as the real part of the phasor solution.

$$\hat{p}'(x,t) = \hat{p}^\star \, \mathrm{e}^{\mathrm{i}(\omega t \mp kx)}. \tag{2.26}$$

Here, $k = \omega/c_0 = 2\pi/\lambda$ is the wavenumber, λ is the wavelength, hats indicate complex quantities, and $\hat{p}^\star$ is the complex amplitude, which has both a magnitude $|\hat{p}^\star|$ and a phase $\varphi_p = \arg(\hat{p}^\star)$,

$$\hat{p}^\star = |\hat{p}^\star| \, \mathrm{e}^{\mathrm{i}\varphi_p}.$$

This amplitude is determined by boundary or initial conditions.

The real, physical solution is found by taking the real part of the complex phasor solution,

$$p'(x,t) = \mathrm{Re}\left[\hat{p}'(x,t)\right] = |\hat{p}^\star| \cos(\omega t \mp kx + \varphi_p). \tag{2.27}$$

Thus, the magnitude $|\hat{p}^\star|$ determines the physical wave amplitude and the phase φ_p determines the phase shift. It is generally mathematically easier to deal with expressions on the phasor form of (2.26) rather than those on the physical form of (2.27).

From any of these solutions we find that the solution value is constant if the argument $\omega t \mp kx$ is constant. Equating the argument at two different times and positions, as shown in Figure 2.2, we find that

$$x_2 - x_1 = \pm c_0(t_2 - t_1).$$

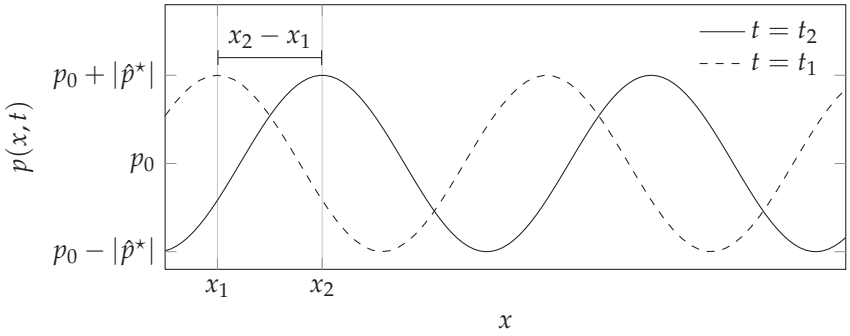

Figure 2.2: Part of a plane pressure wave described by (2.27). From time t_1 to t_2, the leftmost peak moves from position x_1 to x_2.

This proves that c_0 is the speed of sound, and that the choice of $\mp$ in the solution corresponds to propagation in the $\pm x$ direction.

Retarded time, t_r
A transformed coordinate which, when held constant, follows a wave in time and space.

If the argument $\omega t \mp kx$ is constant, then the *retarded time*

$$t_\mathrm{r} = t \mp x/c_0 \tag{2.28}$$

must also be constant. This quantity can be seen as a transformed coordinate that follows the wave as it propagates.

If the solution is assumed to be single-frequency and complex, all fluctuating field quantities vary as $\mathrm{e}^{\mathrm{i}\omega t}$. With this assumption, the wave equation (2.25) becomes the *Helmholtz equation*,

$$\nabla^2 \hat{p}' + k^2 \hat{p}' = 0. \tag{2.29}$$

Thus, the time-dependent, hyperbolic wave equation is transformed into a time-independent elliptic equation. The solution $\hat{p}'$ can still be a function of time, however; the harmonic solution $\hat{p}'(x,t)$ in (2.26) is also a valid solution of (2.29).

2.3.2 Viscous and thermoviscous wave equation

In any fluid, viscosity and heat conduction cause some absorption of sound waves. These effects become relevant at high frequencies and long propagation distances. The effect of viscosity on sound wave propagation was first examined by Stokes [21], in the same article where he derived the stress tensor for a fluid.

In this thesis, the case of purely viscous absorption will be the most relevant. We will look at this in detail, and then take a quick look at the case where both viscous and thermal effects are present.

Purely viscous case

In the previous derivation of the ideal wave equation (2.25), the isentropic equation of state (2.23) was used. Viscous effects cause entropy to increase, but this variation is of second order in the small, primed terms [25, Ch. 9]. Therefore, this entropy increase is neglected by linearisation, and (2.23) can still be assumed to hold. This is not the case if thermal absorption is present, however, and that case requires use of another equation of state.

Instead of the Euler momentum equation, the Navier-Stokes momentum equation is used to derive the wave equation. The extra stress tensor term must now be considered in the derivation. When the spatial derivative of the momentum equation is taken, this term becomes

$$\frac{\partial^2 \sigma'_{\alpha\beta}}{\partial x_\alpha \partial x_\beta} = \left(\tfrac{4}{3}\mu + \mu_\mathrm{B}\right) \nabla^2 \frac{\partial u_\gamma}{\partial x_\gamma} = -\tau_\nu \nabla^2 \frac{\partial p}{\partial t}. \tag{2.30}$$

In the last equality, the mass conservation equation (2.19a) and the speed of sound (2.24) have been used, and the *viscous relaxation time*

$$\tau_\nu = \frac{1}{c_0^2}\left(\frac{4}{3}\nu + \nu_\mathrm{B}\right) \tag{2.31}$$

has been introduced. For most physical fluids, τ_ν is $\sim 10^{-10}$ s for gases and $\sim 10^{-12}$ s for liquids [24, Ch. 8].

Otherwise the derivation proceeds as in the ideal case, and we find the *viscous wave equation*,

$$\boxed{\frac{1}{c_0^2}\frac{\partial^2 p}{\partial t^2} - \left(1 + \tau_\nu \frac{\partial}{\partial t}\right)\nabla^2 p = 0.} \tag{2.32}$$

The only difference from the ideal wave equation is the term where τ_ν appears in front of a time derivative. We will now see how this causes an absorbed solution.

Returning to complex phasor notation, we can in this case get complex wavenumbers $\hat{k}$ and frequencies $\hat{\omega}$. We denote the corresponding wavenumbers and frequencies from the ideal case as k_0 and ω_0.

Looking at a wave radiated from a source oscillating at a single frequency ω_0 and a constant amplitude, we can assume that the solution varies in time as $\mathrm{e}^{\mathrm{i}\omega_0 t}$, resulting in a Helmholtz equation

$$\nabla^2 \hat{p}' + \hat{k}^2 \hat{p}' = 0 \tag{2.33}$$

with a complex wavenumber $\hat{k}$. Assuming a solution propagating in $+x$-direction and normalising by $k_0 = \omega_0/c_0$, we find

$$\frac{\hat{k}}{k_0} = \frac{1}{\sqrt{1 + \mathrm{i}\omega_0\tau_\nu}} \simeq 1 - \mathrm{i}\tfrac{1}{2}(\omega_0\tau_\nu) - \tfrac{3}{8}(\omega_0\tau_\nu)^2 + \mathcal{O}([\omega_0\tau_\nu]^3). \tag{2.34}$$

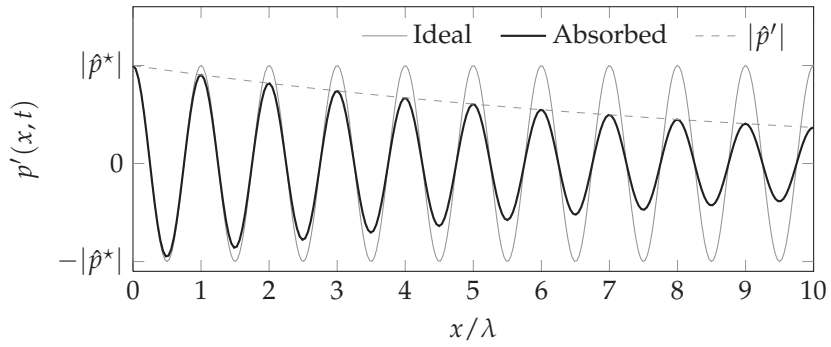

Figure 2.3: Comparison of plane wave solutions of two wave equations: the ideal (2.25) and the viscous (2.32), the latter with an exaggerated absorption coefficient α_x.

Acoustic viscosity number, $\omega_0\tau_\nu = X$
A dimensionless number indicating the effect of viscosity on sound propagation

$\omega_0\tau_\nu$ can be seen as a dimensionless parameter determining the effect of viscosity on sound wave propagation. Its name and exact form varies throughout the literature [26, 27]; we will here call it the *acoustic viscosity number*. It will be heavily used later in the thesis, where it will be denoted as X for brevity.

Following the series expansion around $\omega_0\tau_\nu = 0$ even further, we find a pattern of every even term in $\omega_0\tau_\nu$ being real and every odd term being imaginary. It is convenient to split the complex wavenumber into a real part and an imaginary part,

$$\hat{k} = k - \mathrm{i}\alpha_x. \tag{2.35}$$

α_x is known as the *spatial absorption coefficient*, for reasons that will become clear presently.

As the basic Helmholtz equation (2.29) is on the same mathematical form as its complex counterpart (2.33), their solutions are nearly identical, with the difference that the wavenumber is complex in the latter case. Thus, for a plane wave propagating in the x-direction, the solution is

$$\hat{p}'(x,t) = \hat{p}^\star\, \mathrm{e}^{-\alpha_x x}\, \mathrm{e}^{\mathrm{i}(\omega_0 t - kx)}, \tag{2.36}$$

where the complex wavenumber $\hat{k}$ has been separated into its real part k and its imaginary part α_x. The former causes the speed of sound $c = \omega_0/k$ to be different from its ideal value $c_0 = \omega_0/k_0$. The latter causes the wave to be absorbed exponentially with distance as its energy is converted into heat. The solutions to the ideal and viscous wave equations are compared in Figure 2.3.

Assuming small values of $\omega_0\tau_\nu$, which is valid in most gases for

frequencies up to $\sim 10^8$ Hz, (2.34) gives an absorption coefficient

$$\alpha_x \simeq \frac{k_0}{2}(\omega_0\tau_\nu) = \frac{\omega_0^2}{2c_0^3}\left(\frac{4}{3}\nu + \nu_\mathrm{B}\right), \tag{2.37a}$$

and a real part of the wavenumber

$$k \simeq k_0. \tag{2.37b}$$

Thus, for small $\omega_0\tau_\nu$, the absorption coefficient α_x scales with the viscosity and the square of the frequency, and there is negligible change in the speed of sound. We will see in Chapter 5 that the predictions made by the Navier-Stokes-Fourier model are incorrect at higher than first order in $\omega_0\tau_\nu$. As such, (2.37) is the best we can get from this model.

We assumed above that the wave was radiated outwards from a source. This is sometimes called a *forced wave*, since the wave is generated, or *forced*, by a source, and is absorbed with the distance to that source. Another case seen throughout the literature is based on the assumption that the wave at $t = 0$ has infinite extent and the same amplitude everywhere,

$$\hat{p}'(x, 0) = \hat{p}^\star \, \mathrm{e}^{-\mathrm{i}k_0 x}.$$

This initial-value problem causes the angular frequency to be complex instead of the wavenumber,

$$\hat{\omega} = \omega + \mathrm{i}\alpha_t, \tag{2.38}$$

giving the solution

$$\hat{p}'(x, t) = \hat{p}^\star \, \mathrm{e}^{-\alpha_t t} \, \mathrm{e}^{\mathrm{i}(\omega t - k_0 x)}. \tag{2.39}$$

Thus, the wave is absorbed exponentially in time instead of in space. Such waves are sometimes called *free waves*.

While free waves are not really physically realisable, unlike forced waves, free waves can be used to benchmark numerical methods by performing simulations with periodic boundary conditions that simulate a wave of infinite extent. We will look at this case in more detail in Chapter 5.

Thermoviscous case

In physical gases, the effect of thermal conduction on sound wave absorption is of comparable relevancy to the effect of viscosity. However, in isothermal lattice Boltzmann simulations, which will be the focus later in this thesis, there is no heat conduction and thermal absorption is therefore irrelevant. We will therefore treat this case more cursorily than the previous case of pure viscous absorption.

If thermal conduction is relevant, the nearly isentropic equation of state (2.23) no longer approximately holds, and another equation of state must be used when deriving the wave equation. From the energy equation (2.19c), an alternative equation of state can be derived under the assumptions of linearity and the gas being ideal. Adapting the method of [25, Ch. 9] to multiple spatial dimensions, we find

$$\frac{\partial(p' - c_0^2\rho')}{\partial t} = \frac{\kappa}{\rho_0 c_V}\nabla^2\left(p' - \frac{c_0^2}{\gamma}\rho'\right). \tag{2.40}$$

Using this equation of state when deriving the nonideal wave equation, the approximate *thermoviscous wave equation* can be found to be

$$\boxed{\frac{1}{c_0^2}\frac{\partial^2 p}{\partial t^2} - \left(1 + [\tau_\nu + \tau_\kappa]\frac{\partial}{\partial t}\right)\nabla^2 p = 0,} \tag{2.41}$$

where the thermal relaxation time

$$\tau_\kappa = \frac{1}{c_0^2}\frac{\kappa(\gamma - 1)}{\rho_0 c_p} \tag{2.42}$$

has been introduced. For air, $\tau_\kappa = 7.4 \times 10^{-11}$ s, of the same order as τ_ν, and for freshwater, $\tau_\kappa = 2.6 \times 10^{-16}$ s, which is negligible compared to τ_ν [24, App. 10]. Note that (2.41) is not the exact thermoviscous wave equation [25, Ch. 9], but an approximation where very small terms of order $\mathcal{O}(\tau_\nu\tau_\kappa)$ have been neglected.

Comparing the thermoviscous wave equation (2.41) with the purely viscous wave equation (2.32), it is clear that their solutions are very similar. The only difference lies in an additional term in the spatial absorption coefficient,

$$\alpha_x \simeq \frac{\omega_0^2}{2c_0^3}\left(\frac{4}{3}\nu + \nu_\mathrm{B} + \frac{\gamma - 1}{\rho_0 c_p}\kappa\right). \tag{2.43}$$

With simulation methods, such as the isothermal lattice Boltzmann method, that simulate the effect of viscosity on sound waves but not the effect of thermal conduction, the latter effect can be emulated by artificially increasing the bulk viscosity by $\kappa(\gamma - 1)/\rho_0 c_p$.

2.3.3 Molecular relaxation processes

In most polyatomic gases, the dominant mechanism of absorption at low frequencies is molecular relaxation due to relatively slow transfer of energy between the molecules' translational degrees of freedom (i.e. the energy due to the molecules' velocity) and their inner degrees of freedom (i.e. the energy due to rotation and vibration of the molecules).

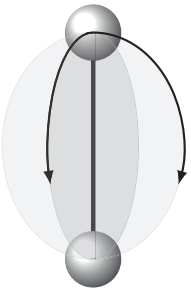

Figure 2.4: A linear molecule has two possible orthogonal rotations, and therefore classically has two rotational degrees of freedom. Nonlinear molecules have three.

In liquids, a different type of relaxation may be present, related to changes in chemical equilibria between different solutes.

While the relaxation mechanisms of polyatomic gases and liquids are very different, they can be modelled similarly. We will however focus on ideal polyatomic gases here, as they are most relevant to this thesis. We will not delve very deeply into this topic, as a full treatment requires some amount of quantum and statistical mechanics and quickly becomes very complicated. More in-depth treatment can be found elsewhere [28, 29]. The following treatment is based on simpler descriptions [24, Ch. 8][25, Ch. 9].

In a gas at rest, the energies stored in the translational and inner degrees of freedom are at equilibrium. If the gas is not at rest, external disturbances such as a passing sound wave may cause the translational energy to change.* This will push the different degrees of freedom out of equilibrium, and a gradual readjustment to equilibrium will occur.

This readjustment happens through molecular collisions. Classically, collisions will tend to slowly equilibrate the different degrees of freedom. Quantum mechanically, each collision between molecules may knock them into a higher or lower rotational or vibrational energy state with a certain probability. Classically or quantum mechanically, the overall result is the same: An equilibrium is eventually reached between the energies stored in the different degrees of freedom.

From the classical equipartition theorem [19, Ch. 2], energy is distributed evenly among all degrees of freedom when the system is at equilibrium. However, from quantum statistical mechanics, inner degrees of freedom are not fully excited and cannot store their full amount of energy unless the temperature T is high enough. From the equipartition

*We will see in section 3.2 that pressure and translational energy are proportional. Thus, a pressure change directly corresponds to a change of the translational energy.

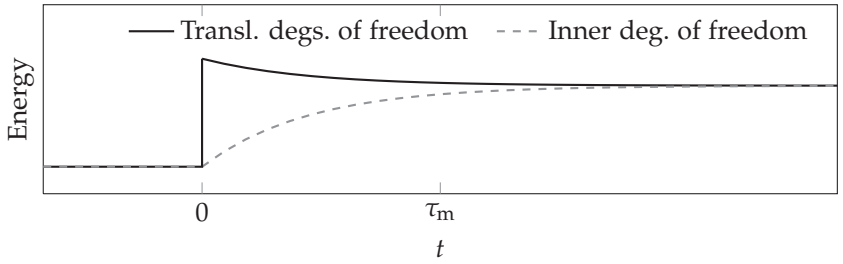

Figure 2.5: Sketch of the re-equilibration of energy after the translational energy is suddenly increased at $t = 0$.

theorem, the total heat capacity at constant volume is

$$c_V = \left(\frac{\partial e}{\partial T}\right)_V = \frac{d_{\text{tot}}}{2} R, \tag{2.44}$$

where

$$d_{\text{tot}} = d_{\text{tot}}(T) = 3 + d_{\text{i}} = 3 + \sum_i H_i(T). \tag{2.45}$$

is the total number of degrees of freedom at temperature T. This contains three translational degrees of freedom and d_{i} inner degrees of freedom. $H_i(T)$ is the excitation fraction for the inner degree of freedom i, which asymptotically varies from 0 at low temperatures, where the degree of freedom is not active, to 1 at high temperatures, where the degree of freedom is fully active.

Different inner degrees of freedom will be active in different amounts at a certain temperature T. At room temperatures, H_i is nearly 1 for rotational states in most molecules, significantly less than 1 for lower vibrational states, and nearly 0 for higher vibrational states [24, Ch. 8].

For ideal gases at equilibrium, the heat capacity at constant pressure c_p and the heat capacity ratio γ are

$$c_p = c_V + R = \frac{2 + d_{\text{tot}}}{2} R, \tag{2.46}$$

$$\gamma = \frac{c_p}{c_V} = 1 + \frac{2}{d_{\text{tot}}}. \tag{2.47}$$

Monatomic gases, which have no inner degrees of freedom, have $\gamma = 1 + 2/3 = 5/3$. For other gases, γ will tend to increase with temperature, as the excitation fractions $H_i(T)$ increase. High-temperature gases consisting of very complicated molecules with many possible vibrational states would have a very large number of degrees of freedom, so that $\gamma \to 1$.

Let us now look at the simplified case of a gas of molecules with only one relevant inner degree of freedom. If the translational energy of the

gas is suddenly increased, for instance due to a sudden compression, the translational and inner energies will re-equilibrate exponentially [24, Ch. 8], as sketched in Figure 2.5. The characteristic time for this process is the *molecular relaxation time* τ_m.

Molecular relaxation time, τ_m
The characteristic time for re-equilibration of translational energy and an inner energy mode

If the translational energy is changed periodically by a sound wave with frequency ω_0, the dimensionless product $\omega_0\tau_\mathrm{m}$ determines the character of the relaxation process:

If $\omega_0\tau_\mathrm{m} \ll 1$, the equilibration occurs quickly compared to the disturbance. The translational and inner energies are always nearly in equilibrium.

If $\omega_0\tau_\mathrm{m} \gg 1$, the equilibration occurs relatively slowly. The inner energy cannot keep up with the translational energy, and remains nearly constant, or *frozen*. In this case, the inner energy's degree of freedom does not play a part in determining heat capacity. Thus, the adiabatic index γ will go asymptotically with frequency towards a value γ_∞ where the inner degree of freedom is not included in d_tot. With only a single inner degree of freedom, the adiabatic index is the same as for a monatomic gas, $\gamma_\infty = 5/3$.

With the speed of sound determined as in (2.24), we find an asymptotic high-frequency speed of sound c_∞ determined from

$$c_\infty^2 = \frac{\gamma_\infty p_0}{\rho_0}. \tag{2.48}$$

With $\gamma_\infty = 5/3$ and γ_0 given by (2.47), the ratio between the asymptotic high-frequency and low-frequency speeds of sound is determined solely from the excitation fraction of the inner degree of freedom,

$$\frac{c_\infty^2}{c_0^2} = \frac{1 + d_\mathrm{i}/3}{1 + d_\mathrm{i}/5} \qquad \Leftrightarrow \qquad d_\mathrm{i} = \frac{5(c_\infty^2/c_0^2 - 1)}{5/3 - c_\infty^2/c_0^2}, \tag{2.49}$$

where we have from (2.45) that $d_\mathrm{i} = H(T)$, the excitation fraction of the inner degree of freedom.

The effect of molecular relaxation on acoustic propagation can be modelled using a relaxation equation of state [25, Ch. 9][22, 30],

$$\boxed{\tau_\mathrm{m}\frac{\partial}{\partial t}\left(p' - c_\infty^2\rho'\right) + \left(p' - c_0^2\rho'\right) = 0.} \tag{2.50}$$

This reduces to $p' = c_0^2\rho'$ at frequencies where $\omega_0\tau_\mathrm{m} \ll 1$, and at frequencies where $\omega_0\tau_\mathrm{m} \gg 1$ it reduces to $p' = c_\infty^2\rho'$.

Differentiating this equation of state twice with respect to time and using (2.22) to eliminate ρ' (thus neglecting thermoviscous effects), we

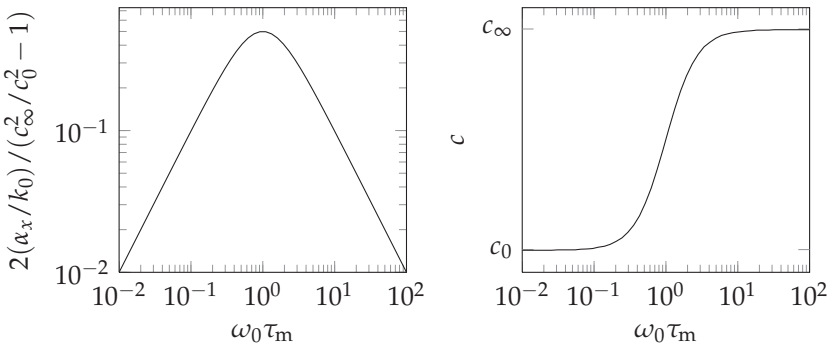

Figure 2.6: Normalised absorption coefficient and speed of sound as functions of $\omega_0\tau_\mathrm{m}$.

find the *wave equation for a single relaxation process*,

$$\boxed{\tau_\mathrm{m}\frac{\partial}{\partial t}\left(\frac{\partial^2 p'}{\partial t^2}-c_\infty^2\nabla^2 p'\right)+\left(\frac{\partial^2 p'}{\partial t^2}-c_0^2\nabla^2 p'\right)=0.} \tag{2.51}$$

This wave equation can also be found by a more fundamental approach that takes quantum statistical mechanical effects fully into account [22].

The effect of relaxation on sound wave propagation can now be found by inserting a plane forced wave trial solution $\hat{p}' = \hat{p}^\star\,\mathrm{e}^{\mathrm{i}(\omega_0 t-\hat{k}x)}$ into (2.51). The complex wavenumber is then found to be

$$\frac{\hat{k}}{k_0}=\sqrt{\frac{1+\mathrm{i}\omega_0\tau_\mathrm{m}}{1+\mathrm{i}\omega_0\tau_\mathrm{m}(c_\infty/c_0)^2}}. \tag{2.52}$$

The exact expressions for the real and imaginary parts of the wavenumber, which respectively lead to the true speed of sound c and spatial absorption coefficient α_x, are quite complicated. However, in most real fluids, c_0 and c_∞ are very close [25, Ch. 9]. Assuming the quantity c_∞^2/c_0^2-1 to be very small, the complicated expressions can be simplified [25, Ch. 9], giving

$$\boxed{\begin{aligned}\frac{\alpha_x}{k_0}&=\frac{1}{2}\left(\frac{c_\infty^2}{c_0^2}-1\right)\frac{\omega_0\tau_\mathrm{m}}{1+(\omega_0\tau_\mathrm{m})^2}, &\text{(2.53a)}\\ \frac{c^2}{c_0^2}&=\frac{1+(\omega_0\tau_\mathrm{m})^2(c_\infty^2/c_0^2)^4}{1+(\omega_0\tau_\mathrm{m})^2(c_\infty^2/c_0^2)^2}. &\text{(2.53b)}\end{aligned}}$$

These expressions are plotted in Figure 2.6. The absorption over a wavelength is maximal at $\omega_0\tau_\mathrm{m}=1$, and the speed of sound c changes smoothly from c_0 to c_∞.

When several relaxation processes and thermoviscous absorption occur simultaneously, it is often assumed that the absorption coefficients of the individual processes can be summed to find a total absorption coefficient [25, 31, 32].

In air, the relevant relaxation processes are rotational and vibrational relaxation in nitrogen and oxygen. The rotational relaxation time is typically of the order of 10^{-9} s, comparable to the viscous relaxation time τ_ν,* and the vibrational relaxation times for nitrogen and oxygen are typically of the order of 10^{-3} s and 10^{-5} s, respectively, although the latter two are strongly dependent on humidity [31].

Humidity is relevant because water molecules act as catalysts for the relaxation process: Collisions between water molecules and nitrogen or oxygen molecules has a higher probability of knocking the latter molecules into higher or lower vibrational energy states [29], so that the re-equilibration process occurs more quickly. Therefore, the relaxation times τ_m decrease with humidity.

Due to the very short rotational relaxation time, the approximation $\omega_0\tau_\mathrm{m} \ll 1$ is fully valid for all but extremely high frequencies. Using this approximation in (2.53), we find $c \simeq c_0$ and $\alpha_x \propto \omega_0^2$. A comparison of the latter with the $\omega_0\tau_\nu \ll 1$ approximation of the viscous absorption coefficient (2.37a) shows that they have the same form. In fact, several sources [28, 33, 34] suggest that bulk viscosity in dilute polyatomic gases is merely the low-frequency behaviour of rotational relaxation. A closer analysis of measurements of rotational relaxation from this perspective gives a bulk viscosity in air of $\nu_\mathrm{B} = 0.60\nu$ [33, 34].

It is important to emphasise that the modelling of rotational relaxation as a bulk viscosity is only valid at low frequencies where $\omega_0\tau_\mathrm{m} \ll 1$. At higher frequencies, this will mispredict the sound wave dispersion from rotational relaxation [22]. However, at the extremely high frequencies where this is a problem, the entire Navier-Stokes-Fourier model itself is cast into doubt, as we will see in Chapters 3 and 5.

We end this section on relaxation with Figure 2.7, which shows the composition of the absorption coefficient for air at representative conditions. The calculation was performed using formulas from the relevant ISO standard [32], which can also be found elsewhere [25, App. B]. From the figure we see that the effects of the vibrational relaxations clearly dominate at audible frequencies.

2.3.4 Acoustic multipoles and aeroacoustics

Acoustic multipoles are oscillating sound sources that generate acoustic fields of various directional radiation patterns. These sources can be either

Multipole
Any of several possible forms of oscillating sources, for example monopoles, dipoles, and quadrupoles

*Note however that viscous absorption is *not* a relaxation process like the ones described here [26].

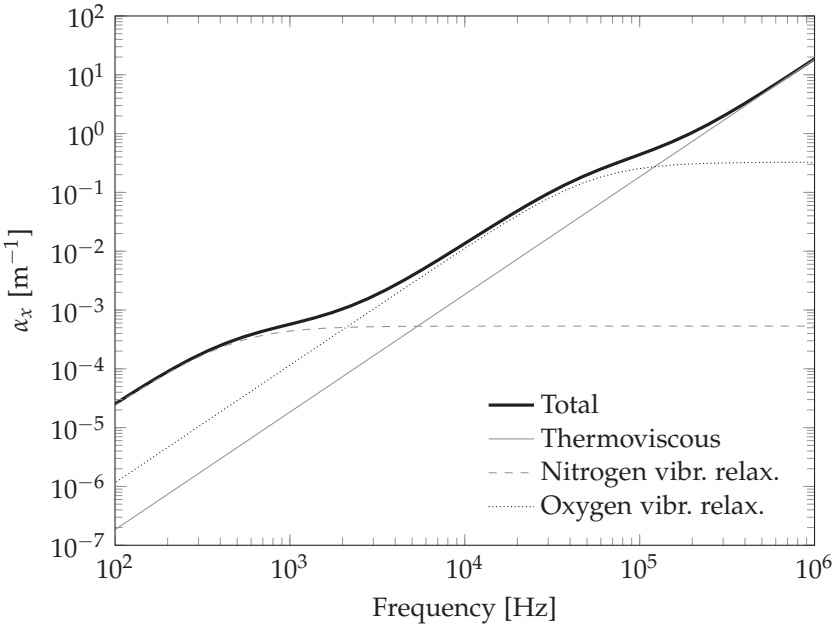

Figure 2.7: Absorption coefficient and its composition for air at 293.15 K, atmospheric pressure and 70 % relative humidity. Rotational relaxation for nitrogen and oxygen is represented as bulk viscosity.

point sources, localised at single points in space, or they can be source densities distributed throughout the medium. The the first three orders of multipoles are the most well-known: *Monopoles*, *dipoles*, and *quadrupoles* at zeroth, first, and second order, respectively.

Before going into the causes of multipole sources, we will look at how they are presented and dealt with mathematically. In general, multipole sources can be expressed by source terms in the wave equation. For the ideal wave equation, we have

$$\left(\frac{1}{c_0^2}\frac{\partial^2}{\partial t^2} - \nabla^2\right) p'(\boldsymbol{x},t) = \mathcal{T}_0(\boldsymbol{x},t) + \frac{\partial \mathcal{T}_\alpha(\boldsymbol{x},t)}{\partial x_\alpha} + \frac{\partial^2 \mathcal{T}_{\alpha\beta}(\boldsymbol{x},t)}{\partial x_\alpha \partial x_\beta} + \dots \,. \tag{2.54}$$

We shall see that $\mathcal{T}_0$, $\mathcal{T}_\alpha$, and $\mathcal{T}_{\alpha\beta}$ represents the local source strength of monopoles, dipoles, and quadrupoles, respectively.

Green's function
The solution of a differential equation with a delta function inhomogenenity

The solution of this equation is based on *Green's functions*. In this derivation we will consider time-harmonic Green's functions, with a time dependence of $\mathrm{e}^{\mathrm{i}\omega t}$. This Green's function $\hat{G}$ is defined by

$$\left(\frac{1}{c_0^2}\frac{\partial^2}{\partial t^2} - \nabla^2\right) \hat{G}(\boldsymbol{x},t) = \delta(\boldsymbol{x})\,\mathrm{e}^{\mathrm{i}\omega t}, \tag{2.55}$$

where $\delta(\boldsymbol{x})$ is the Dirac delta function. Thus, the Green's function is the pressure response to a time-harmonic point inhomogenity at $\boldsymbol{x} = 0$.

Alternatively, the impulsive Green's function could be used [35]. This is defined similarly to (2.55), but with a different source term, $\delta(\boldsymbol{x})\delta(t)$, on the right-hand side. Thus, the impulsive Green's function is the response to an inhomogenity representing a single Dirac pulse at $\boldsymbol{x} = 0$ and $t = 0$. However, since it is impossible to find analytical solutions on this form for two dimensional cylindrical waves except as far-field approximations or Fourier integrals [25, Ch. 1], we wil not consider the impulsive Green's function further. It is possible to use the Fourier transform to transform time-harmonic solutions to more general solutions.

In one, two and three dimensions, the time-harmonic Green's functions are [36]

$$\text{1D:} \qquad \hat{G}(x,t) = \frac{1}{2\mathrm{i}k}\,\mathrm{e}^{\mathrm{i}(\omega t - k|x|)}, \tag{2.56a}$$

$$\text{2D:} \qquad \hat{G}(\boldsymbol{x},t) = \frac{1}{4\mathrm{i}}\hat{H}_0^{(2)}(k|\boldsymbol{x}|)\,\mathrm{e}^{\mathrm{i}\omega t}, \tag{2.56b}$$

$$\text{3D:} \qquad \hat{G}(\boldsymbol{x},t) = \frac{1}{4\pi|\boldsymbol{x}|}\,\mathrm{e}^{\mathrm{i}(\omega t - k|\boldsymbol{x}|)}, \tag{2.56c}$$

where $\hat{H}_n^{(2)}$ is the nth order Hankel function of the second kind. The Hankel function is found from the corresponding Bessel functions of the first kind J_n and second kind Y_n, as [24]

$$\hat{H}_n^{(2)}(x) = J_n(x) - \mathrm{i}Y_n(x). \tag{2.57}$$

$|\boldsymbol{x}| = \sqrt{x^2 + y^2 + z^2}$ is the distance from the origin, often denoted as r.

Now, let us consider a simplified, time-harmonic version of (2.54),

$$\left(\frac{1}{c_0^2}\frac{\partial^2}{\partial t^2} - \nabla^2\right) p(\boldsymbol{x},t) = \hat{\mathcal{T}}_0(\boldsymbol{x})\,\mathrm{e}^{\mathrm{i}\omega t}.$$

The source term can be seen as a distribution of infinitely many individual weak point source terms $\hat{\mathcal{T}}_0(\boldsymbol{y})\delta(\boldsymbol{x}-\boldsymbol{y})\,\mathrm{d}\boldsymbol{y}$, since

$$\hat{\mathcal{T}}_0(\boldsymbol{x}) = \int \hat{\mathcal{T}}_0(\boldsymbol{y})\delta(\boldsymbol{x}-\boldsymbol{y})\,\mathrm{d}\boldsymbol{y}.$$

From the definition of the Green's function, each component source radiates a pressure field $\hat{\mathcal{T}}_0(\boldsymbol{y})\hat{G}(\boldsymbol{x}-\boldsymbol{y},t)\,\mathrm{d}\boldsymbol{y}$. Thus, we can find a general solution by adding the contributions of all these individual sources,

$$p'(\boldsymbol{x},t) = \int \hat{\mathcal{T}}_0(\boldsymbol{y})\hat{G}(\boldsymbol{x}-\boldsymbol{y},t)\,\mathrm{d}\boldsymbol{y}.$$

The pressure at the listener point $\boldsymbol{x}$ is thus found by integrating over the contributions of all source points $\boldsymbol{y}$.

To find the solution of the source term with a single spatial derivative, we can simply let $\hat{\mathcal{T}}_0(\boldsymbol{x}) \to \partial\hat{\mathcal{T}}_\alpha(\boldsymbol{x})/\partial x_\alpha$ in the solution,

$$p'(\boldsymbol{x},t) = \int \frac{\partial\hat{\mathcal{T}}_\alpha(\boldsymbol{y})}{\partial y_\alpha}\hat{G}(\boldsymbol{x}-\boldsymbol{y},t)\,\mathrm{d}\boldsymbol{y}.$$

Using multidimensional integration by parts (2.11) and assuming that $\hat{\mathcal{T}} = 0$ infinitely far away, this becomes

$$p'(\boldsymbol{x},t) = -\int \hat{\mathcal{T}}_\alpha(\boldsymbol{y})\frac{\partial\hat{G}(\boldsymbol{x}-\boldsymbol{y},t)}{\partial y_\alpha}\,\mathrm{d}\boldsymbol{y} = \int \hat{\mathcal{T}}_\alpha(\boldsymbol{y})\frac{\partial\hat{G}(\boldsymbol{x}-\boldsymbol{y},t)}{\partial x_\alpha}\,\mathrm{d}\boldsymbol{y}.$$

A similar solution can be found found for the source term with a double spatial derivative. Thus, the time-harmonic analogue of (2.54),

$$\left(\frac{1}{c_0^2}\frac{\partial^2}{\partial t^2} - \nabla^2\right)p'(\boldsymbol{x},t) = \mathrm{e}^{\mathrm{i}\omega t}\left[\hat{\mathcal{T}}_0(\boldsymbol{x}) + \frac{\partial\hat{\mathcal{T}}_\alpha(\boldsymbol{x})}{\partial x_\alpha} + \frac{\partial^2\hat{\mathcal{T}}_{\alpha\beta}(\boldsymbol{x})}{\partial x_\alpha\partial x_\beta} + \dots\right], \tag{2.58}$$

is solved by

$$\boxed{\begin{aligned} p'(\boldsymbol{x},t) = \int\Bigg[&\hat{\mathcal{T}}_0(\boldsymbol{y})\hat{G}(\boldsymbol{x}-\boldsymbol{y},t) + \hat{\mathcal{T}}_\alpha(\boldsymbol{y})\frac{\partial\hat{G}(\boldsymbol{x}-\boldsymbol{y},t)}{\partial x_\alpha} \\ &+ \hat{\mathcal{T}}_{\alpha\beta}(\boldsymbol{y})\frac{\partial^2\hat{G}(\boldsymbol{x}-\boldsymbol{y},t)}{\partial x_\alpha\partial x_\beta} + \dots\Bigg]\,\mathrm{d}\boldsymbol{y}. \end{aligned}} \tag{2.59}$$

Each term inside the integral represents one type of multipole source, and the different $\hat{\mathcal{T}}$s indicate the local source strengths of these.

The different derivatives of $\hat{G}$ have their own angular dependence. The far-field angular dependence patterns for some representative derivatives are given in Figure 2.8. $\hat{G}$ itself is omnidirectional, radiating equally in all directions; a *monopole* source. Applying a spatial derivative in x_α direction to $\hat{G}$ results in a radiation pattern known as an x_α*-dipole*, with a lobe in the x_α direction and a lobe of opposite polarity in the $-x_\alpha$ direction. Applying two spatial derivatives in x_α and x_β directions, we get $x_\alpha x_\beta$*-quadrupoles*. If the two derivatives are the same, we have a *longitudinal quadrupole* with two lobes of the same polarity in opposing directions. If the derivatives are different, we have a *lateral quadrupole* with four lobes of varying polarities in the $x_\alpha x_\beta$ plane.

Now that we know how to deal with source terms in the wave equation, we will now look at where these source terms may originate from in the first place. We will later return to this topic in Chapter 6, where the multipole source origin will be different.

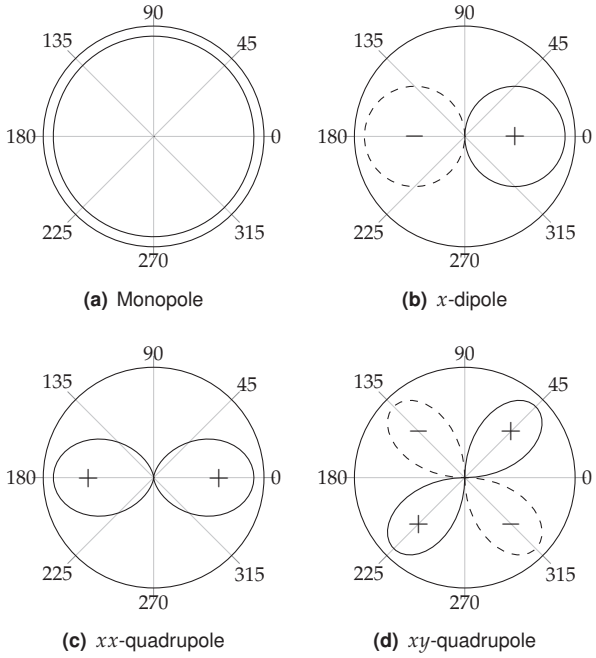

(a) Monopole **(b)** x-dipole

(c) xx-quadrupole **(d)** xy-quadrupole

Figure 2.8: Far-field (i.e. $|\boldsymbol{x}| \to \infty$) dependence on the angle to the x axis for **(a)** $\hat{G}$, **(b)** $\partial\hat{G}/\partial x$, **(c)** $\partial^2\hat{G}/\partial x^2$, **(d)** $\partial^2\hat{G}/\partial x\partial y$. Lobes with negative polarity are drawn with dashed lines. These angular dependence patterns hold for both the two- and three-dimensional Green's functions $\hat{G}$, and their common names are given in the subcaptions.

We begin with the mass and momentum conservation equations (2.17) of the Euler model. On conservation form, these are

$$\frac{\partial \rho}{\partial t} + \frac{\partial \rho u_\alpha}{\partial x_\alpha} = Q, \tag{2.60a}$$

$$\frac{\partial \rho u_\alpha}{\partial t} + \frac{\partial \rho u_\alpha u_\beta}{\partial x_\beta} = -\nabla p + \boldsymbol{F}. \tag{2.60b}$$

A mass source term Q with units $\mathrm{kg/s\,m^3}$ has been added to the mass equation. This can model the pulsations of small bodies throughout the fluid [24, Ch. 5][35, Ch. 1].

Deriving the wave equation from these equations as before, we get

$$\left(\frac{1}{c_0^2}\frac{\partial^2}{\partial t^2} - \nabla^2\right) p = \frac{\partial Q}{\partial t} - \frac{\partial F_\alpha}{\partial x_\alpha} + \frac{\partial^2 \rho u_\alpha u_\beta}{\partial x_\alpha \partial x_\beta}. \tag{2.61}$$

By comparison with equation (2.54), we explicitly find the multipole

source strengths

$$\mathcal{T}_0 = \frac{\partial Q}{\partial t}, \qquad \mathcal{T}_\alpha = -F_\alpha, \qquad \mathcal{T}_{\alpha\beta} = \rho u_\alpha u_\beta. \tag{2.62}$$

We could also perform a more general derivation by using the Navier-Stokes-Fourier model and not using the linear approximation $p' = c_0^2 \rho'$. This would result in an *exact* quadrupole strength of [35, 37]

$$\mathcal{T}_{\alpha\beta} = \rho u_\alpha u_\beta + (p - c_0^2 \rho')\delta_{\alpha\beta} - \sigma'_{\alpha\beta}.$$

In most cases, however, the two last terms are negligible, and the first term can even be approximated well as $\rho_0 u_\alpha u_\beta$ [35, 37].

Thus, monopoles are typically caused either by injection of mass, or by pulsations of small bodies which push on the fluid; identical waves are radiated in the two cases if the same amount of mass is injected and pushed [24, Chs. 5 & 7]. Dipoles are typically caused by body forces acting on the fluid. Quadrupoles are typically caused by areas with rapid spatial variations in $\rho u_\alpha u_\beta$, such as an area of turbulent flow. The fact that such flow generates sound is familiar from daily life; consider for instance the noise from the turbulent flow of air blown out of a mouth.

The study of aerodynamic sound generation is called aeroacoustics. Aeroacoustic studies are especially important to finding out how to reduce the noise generated by vehicles, in particular aircraft.

The study of aeroacoustic computer simulations is called *computational aeroacoustics*. Such studies started in the 1980s, and the two main types of methods used are:

Hybrid methods, where the flow and acoustic fields are found separately. The incompressible flow field is analysed to find the acoustic source strength of the flow, which is then used to compute the acoustic field in the surrounding domain.

Direct methods, where the acoustic field comes out as a natural part of a numerical solution to the compressible Navier–Stokes or Euler equations.

While hybrid methods are usually far more efficient than direct methods, they cannot simulate the feedback of the acoustic field on the flow field. Therefore, hybrid methods cannot be used in cases where this feedback is critical to the process of sound generation, such as the singing risers problem currently studied in the natural gas industry [38–42]. It is also difficult to capture complex geometries with such methods.

Direct methods have no such problems, but performing traditional numerical simulations of the compressible Navier–Stokes equation is far more complex and computationally demanding than using hybrid methods. We can therefore hope that the lattice Boltzmann method will

prove to be an useful direct method for computational aeroacoustics. In fact, several publications have been made on this topic recently [42–50].

2.3.5 Nonlinear acoustics

At high sound wave amplitudes, the assumptions behind the linearisation performed previously break down, and the equations of sound propagation become nonlinear.* The primary consequence of this nonlinearity is that the sound wave propagation speed can no longer be assumed to be constant; peaks propagate more quickly and troughs more slowly. There are two separate mechanisms behind this effect.

The first mechanism is the dependence of the sound speed c on local state variables. Simply put, a sound wave peak is compressed and therefore has a slightly higher temperature, which leads to a slightly higher local sound speed. Conversely, a trough is rarefied and has a lower temperature and a lower sound speed.

Evaluating the speed of sound from the isentropic relation (2.23) without assuming that the state variables are close to the rest state variables p_0 and ρ_0, we find

$$c^2 = \left(\frac{\partial p}{\partial \rho}\right) = \frac{\gamma p}{\rho} = c_0^2 \left(\frac{\rho}{\rho_0}\right)^{\gamma-1} = c_0^2 \left(\frac{p}{p_0}\right)^{(\gamma-1)/\gamma}. \tag{2.63}$$

With some effort, the speed of sound can also be expressed exactly through the acoustic fluid velocity [51][25, Ch. 2]. For a plane wave,

$$c = c_0 + \frac{\gamma - 1}{2} u, \tag{2.64}$$

the scalar u being the fluid velocity in the propagation direction of the sound wave.

The second mechanism is self-advection. The particle velocity u of a sound wave, which points towards and against the direction of sound propagation in peaks and troughs respectively, also contributes to transport of the sound wave.

Consequently, the total local wave propagation speed is $c + u$, or

$$c + u = c_0 + \beta u, \tag{2.65}$$

where β is the coefficient of nonlinearity,

$$\beta = \frac{\gamma + 1}{2}.$$

In other words, peaks propagate more quickly and troughs propagate more slowly than the small-signal sound speed c_0. As a consequence, the

*This nonlinearity also means that complex phasor notation can no longer be used; it only works for linear equations.

peaks may eventually catch up to the troughs, steepening the sound wave and distorting it into a shock wave as shown in Figure 2.9. This distortion also results in the introduction of *harmonics*.

Harmonics
Wave components with frequencies that are integer multiples of a fundamental frequency

These harmonic components have higher frequencies than the fundamental and are consequently absorbed to a larger degree. In a way, the propagation of high-amplitude sound waves may be seen as a competition between the effects of nonlinearity, which cause distortion and harmonics, and the effects of absorption, which absorb the harmonics and thus dampen the distortion.

Nonlinear acoustics can be modeled by a number of different equations [51]. To derive these, some approximations must be made. Most importantly, the effects of nonlinearity must be assumed to be *sufficiently small*.

Let us introduce a smallness order parameter ε, so that the fluctuating field quantities of pressure p', density ρ', velocity u', and so forth are all $\mathcal{O}(\varepsilon)$. Another parameter which is small up to very high ultrasonic frequencies is the acoustic viscosity number $X = \omega_0 \tau_\nu$. To derive reasonably simple model equations, an approximation scheme that neglects all terms of higher order of smallness than $\mathcal{O}(\varepsilon^2)$ and $\mathcal{O}(\varepsilon X)$ must be used [51]. By comparison, in the linearisation process used in the previous sections we neglected all terms above the orders $\mathcal{O}(\varepsilon)$ and $\mathcal{O}(\varepsilon X)$.

Perhaps the simplest model equation is the Burgers equation, which describes the nonlinear steepening of a plane wave [51].* In dimensionless form, the Burgers equation for the propagation of a forced wave with frequency ω_0 and initial amplitude $p^\star$ is [52]

$$\frac{\partial \tilde{p}}{\partial \tilde{x}} = \tilde{p} \frac{\partial \tilde{p}}{\partial \tilde{t}_\mathrm{r}} + \tilde{\alpha}_x \frac{\partial^2 \tilde{p}}{\partial \tilde{t}_\mathrm{r}^{\,2}}. \tag{2.66a}$$

The tilde indicates parameters which have been reduced to nondimensional form as

$$\tilde{p} = p'/p^\star, \quad \tilde{x} = x/x_\mathrm{shock}, \quad \tilde{t}_\mathrm{r} = \omega_0 t_\mathrm{r}, \quad \tilde{\alpha}_x = \alpha_x x_\mathrm{shock}, \tag{2.66b}$$

where x_shock is the shock formation distance, i.e. the distance it takes for the peak to catch up to the trough for a plane wave in a lossless medium, given by

$$x_\mathrm{shock} = \frac{\rho_0 c_0^3}{p^\star \beta \omega_0}. \tag{2.66c}$$

By rewriting the equation into this dimensionless form, we see that it relies only on the initial condition $\tilde{p}(0, \tilde{t}_\mathrm{r})$ and the nondimensionalised absorption coefficient $\tilde{\alpha}_x$.

*The Burgers equation is not limited to acoustics; it is used as a model equation for shock waves in other fields as well.

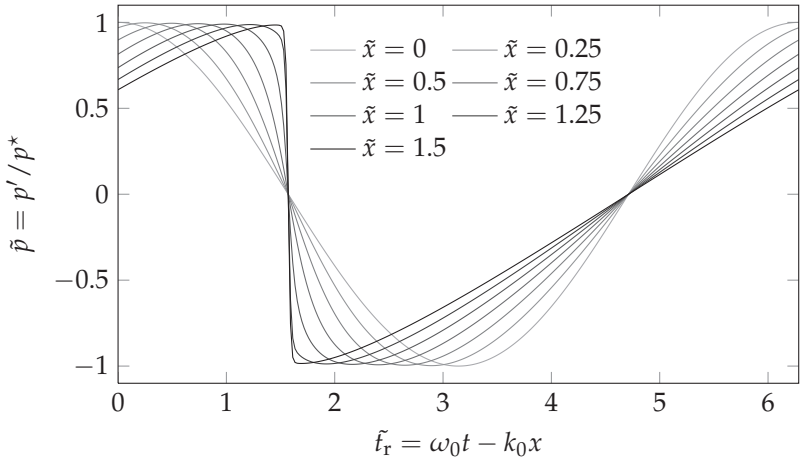

Figure 2.9: Nonlinear distortion of a sound wave; the solution to the dimensionless Burgers equation (2.66a) for $\tilde{\alpha}_x = 0.01$ and $M = 300$.

One method to solve the Burgers equation involves a transformation to the frequency domain. The solution variable $\tilde{p}$ can be written as a superposition of frequency components,

$$\tilde{p}(\tilde{x}, \tilde{t}_\mathrm{r}) = \sum_{n=1}^{\infty} \mathrm{Re}\left[\tilde{p}_n(\tilde{x})\, \mathrm{e}^{\mathrm{i}n\tilde{t}_\mathrm{r}}\right], \tag{2.67}$$

$\tilde{p}_n(\tilde{x})$ being the complex amplitudes of these frequency components. Truncating the number of components to M, the Burgers equation can be transformed into a set of coupled ordinary differential equations for the components $\tilde{p}_n$ [52],

$$\frac{\mathrm{d}\tilde{p}_n}{\mathrm{d}\tilde{x}} = -n^2\tilde{\alpha}_x\tilde{p}_n + \frac{\mathrm{i}n}{4}\left(\sum_{m=1}^{n-1}\tilde{p}_m\tilde{p}_{n-m} + 2\sum_{m=n+1}^{M}\tilde{p}_m\tilde{p}^*_{m-n}\right). \tag{2.68}$$

This set of ODEs can be solved using a number of standard methods. Here, Matlab's fourth-order Runge-Kutta method with adaptive time steps (the `ode45` function) was used. The results for $\tilde{\alpha}_x = 0.01$ and an initial condition $\tilde{p}_1(0) = 1$, $\tilde{p}_{n\neq 1}(0) = 0$ are shown in Figure 2.9.

3 The kinetic theory of gases

A gas at rest is not merely a static continuum. Instead, it is teeming with activity at the molecular level: Most of the molecules fly around at speeds higher than the speed of sound, and a single molecule typically collides with billions of other molecules within the space of a single second.

In principle, this behaviour can be described by tracking every single molecule in the gas and calculating how they collide with each other. This is naturally impossible in practice for many reasons, e.g. the enormous number of particles and the lack of knowledge of their initial states.

Knowing the position $(x, y, z) = \boldsymbol{x}$ and velocity $(\xi_x, \xi_y, \xi_z) = \boldsymbol{\xi} = \mathrm{d}\boldsymbol{x}/\mathrm{d}t$ of a single molecule means knowing 6 different variables. Consequently, knowing the position and velocity of N molecules means knowing $6N$ variables. In addition, if the molecules have internal structure as described in section 2.3.3, variables describing their rotational and vibrational state are also necessary. Considering that a single gram of oxygen consists of over 10^{22} molecules, it becomes clear that it is impossible to describe a tangible amount of gas at the microscopic level of detail.

Instead of attempting a full description of the gas, we can attempt a statistical one, where we consider *distributions* of particles; essentially expectation values of the density of particles that have a particular position and velocity.* We go from a *microscopic* description to a *mesoscopic* description of the gas, as described in Chapter 1.

In this chapter, a short introduction will be given to this field, which is known as the kinetic theory of gases. We will start by looking at the statistical description of the gas and how any distribution of particles may be connected to the macroscopic variables familiar from fluid mechanics. Then the Boltzmann equation, which describes the evolution of these particle distributions, will be derived. Finally, we will see how the conservation equations of fluid mechanics may be derived from this equation.

It is necessary to make certain assumptions about the gas to keep the following discussion at a sufficiently simple and instructive level. First, we will assume that the molecules are all identical and consist of only one atom. If the molecules have no detailed internal structure,

*For a clear yet brief explanation of the path from the full description to the statistical description, see e.g. [53].

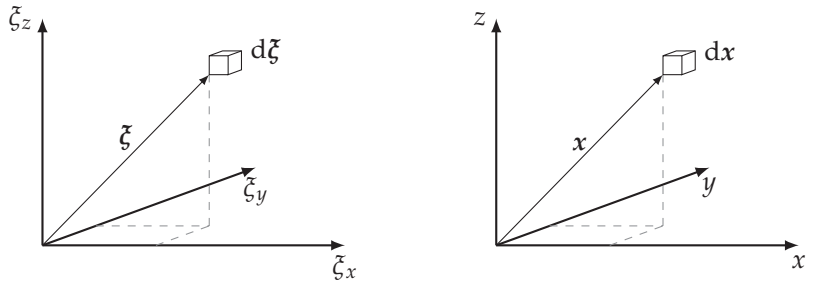

Figure 3.1: Vectors and infinitesimal volumes in velocity space (left) and physical space (right).

all their kinetic energy is *translational*, or coupled to their velocity; they cannot rotate or vibrate as described in section 2.3.3. The kinetic theory of polyatomic gases is significantly more complicated, and may be found elsewhere [54–58].

Second, Bohr's correspondence principle states that the quantum behaviour of a system reduces to classical behaviour when the system becomes large enough. We can therefore largely disregard quantum mechanical effects and assume classical behaviour at the statistical level of description.

The primary goal of this chapter is to give an introduction to the aspects of kinetic theory that are the most relevant for the lattice Boltzmann method. We will cover the basic principles, the simplest model for collisions between particles, and the link to fluid mechanics. Discussion of less relevant aspects will be kept to a minimum.

3.1 The distribution function and its moments

The *distribution function* $f(\boldsymbol{x}, \boldsymbol{\xi}, t)$ can be seen as a generalisation of density; it represents the density of particles in both physical space and velocity space simultaneously. In other words, $f(\boldsymbol{x}, \boldsymbol{\xi}, t)$ indicates the density of particles with position $\boldsymbol{x}$ and velocity $\boldsymbol{\xi}$ at time t.

Distribution function, f
Indicates the density of particles with position $\boldsymbol{x}$ and velocity $\boldsymbol{\xi}$ at time t

The distribution function lets us find other, more familiar quantities. $f(\boldsymbol{x}, \boldsymbol{\xi}, t)\, \mathrm{d}\boldsymbol{\xi}$ is the *spatial density* of particles which have velocities which lie inside an infinitesimal velocity space volume $\mathrm{d}\boldsymbol{\xi}$ at $\boldsymbol{\xi}$. Furthermore, $f(\boldsymbol{x}, \boldsymbol{\xi}, t)\, \mathrm{d}\boldsymbol{x}\, \mathrm{d}\boldsymbol{\xi}$ is the *mass* of particles with such velocities and positions which lie inside an infinitesimal physical space volume $\mathrm{d}\boldsymbol{x}$ at $\boldsymbol{x}$.

This distribution function is sufficient to find macroscopic properties such as fluid density, fluid velocity, and internal energy in the fluid. These properties can be found as *moments*, where the distribution function $f(\boldsymbol{x}, \boldsymbol{\xi}, t)$ is weighted with some function of $\boldsymbol{\xi}$ and integrated over the

Moment
An integral over all velocities with f weighted with a function of velocity as the integrand

entire velocity space. These moments, which link the mesoscopic and macroscopic scales, are somewhat similar to the equations (1.1) which link the microscopic and macroscopic scales.

For the simplest moment we do not weight with anything. As mentioned previously, $f(\boldsymbol{x}, \boldsymbol{\xi}, t)\,\mathrm{d}\boldsymbol{\xi}$ is the spatial density of particles that have velocities within a certain infinitesimal velocity range. Thus, if we integrate over all the velocities, i.e. the entire velocity space, we get the physical *mass density*, most commonly simply called *density*,

Mass density, ρ
Mass per physical volume in $\mathrm{kg/m^3}$

$$\boxed{\rho(\boldsymbol{x}, t) = \int f(\boldsymbol{x}, \boldsymbol{\xi}, t)\,\mathrm{d}\boldsymbol{\xi}.} \tag{3.1}$$

Now, if we weight with $\boldsymbol{\xi}$, we get $\boldsymbol{\xi} f(\boldsymbol{x}, \boldsymbol{\xi}, t)\,\mathrm{d}\boldsymbol{\xi}$, which is the *momentum density* of the particles in the given velocity range. Integrating over all the velocities gives us the total *momentum density*,

Momentum density, $\rho\boldsymbol{u}$
Momentum per physical volume in $\mathrm{kg/s\,m^2}$

$$\boxed{\rho\boldsymbol{u}(\boldsymbol{x}, t) = \int \boldsymbol{\xi} f(\boldsymbol{x}, \boldsymbol{\xi}, t)\,\mathrm{d}\boldsymbol{\xi}.} \tag{3.2}$$

Here, $\boldsymbol{u}$ is the average velocity of the particles, which corresponds to the *fluid velocity* in fluid mechanics.

Fluid velocity, $\boldsymbol{u}$
The average velocity of the particles in $\mathrm{m/s}$

Similarly, weighting with $\frac{1}{2}|\boldsymbol{\xi}|^2$ and integrating gives the *energy density*,

Energy density, ρE
Kinetic energy per physical volume in $\mathrm{J/m^3}$

$$\boxed{\rho E(\boldsymbol{x}, t) = \tfrac{1}{2} \int |\boldsymbol{\xi}|^2 f(\boldsymbol{x}, \boldsymbol{\xi}, t)\,\mathrm{d}\boldsymbol{\xi}.} \tag{3.3}$$

Specific energy, E
Kinetic energy per mass in $\mathrm{J/kg}$

Here, E is the *specific energy*. We have assumed here that the kinetic energy is given only by the translational movement of the particles; this is only correct if the gas is monatomic, as we earlier assumed. For a polyatomic gas, there would also be contributions from rotational and vibrational energy, which cannot be as easily represented through $f(\boldsymbol{x}, \boldsymbol{\xi}, t)$.

This total kinetic energy may be split up into two parts: The kinetic energy density due to the bulk movement of the fluid, $\frac{1}{2}\rho|\boldsymbol{u}|^2$, and the *internal energy density* ρe, which is due to random thermal movement of particles, and is independent of the fluid velocity $\boldsymbol{u}$. Thus, we can write

Internal energy density, ρe
The energy density component due to random thermal movement of particles in the gas

$$\rho E = \rho\left(e + \tfrac{1}{2}|\boldsymbol{u}|^2\right). \tag{3.4}$$

Here, e is the specific internal energy.

As an example of internal energy, let us look at a somewhat unrealistic case where all particles move in the same direction, so that the distribution function is a Dirac delta function, $f(\boldsymbol{x}, \boldsymbol{\xi}, t) = \rho\delta(\boldsymbol{\xi} - \boldsymbol{u})$. Using this to find the energy density, we find $\rho E = \frac{1}{2}\rho|\boldsymbol{u}|^2$. Comparing with (3.4), we see

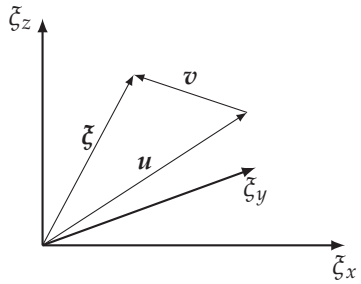

Figure 3.2: The velocity $\boldsymbol{\xi}$ is split into the fluid velocity $\boldsymbol{u}$ and the peculiar velocity $\boldsymbol{v}$.

that $\rho e = 0$ in this case where all particles have the same velocity. Thus, we see that the internal energy comes from the particle velocities' deviation from the mean. We will see later in section 3.3 that this deviation and the internal energy grows larger with temperature.

It is useful to split the particle velocity $\boldsymbol{\xi}$ into two components, as shown in Figure 3.2: The fluid velocity $\boldsymbol{u}$ and the *peculiar velocity* $\boldsymbol{v}$,

Peculiar velocity, v
The deviation of the particle velocity $\boldsymbol{\xi}$ from the fluid velocity $\boldsymbol{u}$

$$\boldsymbol{\xi} = \boldsymbol{v} + \boldsymbol{u}. \tag{3.5}$$

Because it describes the deviation from the mean velocity, the peculiar velocity cannot contribute to the momentum. This may also be shown mathematically,

$$\int \boldsymbol{v} f \,\mathrm{d}\boldsymbol{\xi} = \int \boldsymbol{\xi} f \,\mathrm{d}\boldsymbol{\xi} - \boldsymbol{u} \int f \,\mathrm{d}\boldsymbol{\xi} = \rho \boldsymbol{u} - \rho \boldsymbol{u} = 0. \tag{3.6}$$

Here the fluid velocity has been moved outside the integral, as $\boldsymbol{u}(\boldsymbol{x}, t)$ does not depend on $\boldsymbol{\xi}$.

In (3.3), we can substitute with (3.5). Using (3.6) and (3.1), we find

$$\begin{aligned}
\rho E &= \tfrac{1}{2} \int (\boldsymbol{v} + \boldsymbol{u}) \cdot (\boldsymbol{v} + \boldsymbol{u}) f(\boldsymbol{x}, \boldsymbol{\xi}, t) \,\mathrm{d}\boldsymbol{\xi} \\
&= \tfrac{1}{2} \int |\boldsymbol{v}|^2 f \,\mathrm{d}\boldsymbol{\xi} + \boldsymbol{u} \cdot \int \boldsymbol{v} f \,\mathrm{d}\boldsymbol{\xi} + \tfrac{1}{2} |\boldsymbol{u}|^2 \int f \,\mathrm{d}\boldsymbol{\xi} \\
&= \tfrac{1}{2} \int |\boldsymbol{v}|^2 f \,\mathrm{d}\boldsymbol{\xi} + \tfrac{1}{2} \rho |\boldsymbol{u}|^2.
\end{aligned}$$

By comparison with (3.4) we find the moment equation for the internal energy density,

$$\boxed{\rho e(\boldsymbol{x}, t) = \tfrac{1}{2} \int |\boldsymbol{v}|^2 f(\boldsymbol{x}, \boldsymbol{\xi}, t) \,\mathrm{d}\boldsymbol{\xi}.} \tag{3.7}$$

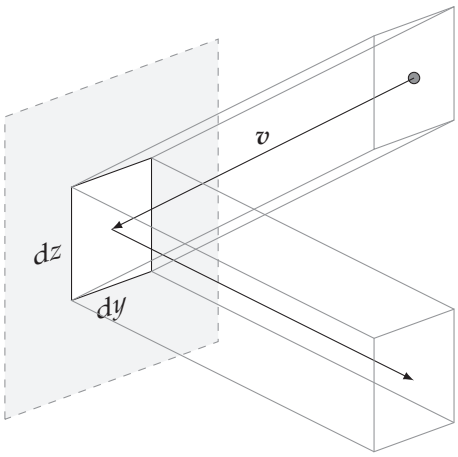

Figure 3.3: A single particle bounces elastically off a surface $\mathrm{d}A = \mathrm{d}y\,\mathrm{d}z$. In the time it takes for the particle to reach the surface, all the particles with the same velocity inside the upper collision prism around the particle's path will also have hit the surface, and will have bounced into the lower collision prism.

3.2 Pressure and heat

Pressure, p
Force per area exerted by the fluid on a real or imaginary surface in $\mathrm{N/m^2}$

Fluids exert a force on adjacent surfaces. The area density of this force is given by the *pressure* $p(\boldsymbol{x}, t)$ at the surface. In general, the pressure is an internal thermodynamic quantity of the fluid. It indicates the force density which would be exerted on a surface placed at that point, if that surface is at rest relative to the fluid.

The actual, microscopic reason why fluids exert a pressure on surfaces is that the particles in the fluid keep bouncing off the surface. Since momentum is always conserved, the momentum change imparted to the surface is equal and opposite to the momentum change of a particle bouncing off it.

In the following, we will make the assumption that the distribution function is approximately spherically symmetric around $\boldsymbol{v} = 0$, so that all velocity directions are equally probable, and the peculiar velocity does not tend to any particular directions. This assumption will be discussed further in section 3.3.

Let's say that we have placed a surface in the y–z-plane at rest relative to the fluid, and that a particle bounces elastically off it, as shown in Figure 3.3. Before and after the collision, the particle's momentum relative to the wall in the x-direction is $-mv_x$ and mv_x respectively, having changed by $2mv_x$ in the collision. The same momentum change is imparted to the wall.

We can use the distribution function to find the total momentum

change imparted to the wall over an infinitesimal time period $\mathrm{d}t$. If the aforementioned particle has a velocity $\boldsymbol{\xi}$, the total mass of the particles with similar velocities hitting the surface $\mathrm{d}A = \mathrm{d}y\,\mathrm{d}z$ in the period $\mathrm{d}t$ is $f(\boldsymbol{x}, \boldsymbol{\xi}, t)\,\mathrm{d}\boldsymbol{\xi}\,\mathrm{d}\boldsymbol{x}$. Here, $\mathrm{d}\boldsymbol{x} = \mathrm{d}x\,\mathrm{d}y\,\mathrm{d}z = v_x\,\mathrm{d}t\,\mathrm{d}y\,\mathrm{d}z$ is the volume of the collision prism shown in Figure 3.3. Thus, the total mass of particles hitting the wall with such velocities is

$$v_x f(\boldsymbol{x}, \boldsymbol{\xi}, t)\,\mathrm{d}\boldsymbol{\xi}\,\mathrm{d}t\,\mathrm{d}y\,\mathrm{d}z.$$

To find the total momentum imparted to the surface by these particles, we multiply their mass by their velocity change $2v_x$. Thus, their total imparted momentum change to the surface is

$$2v_x^2 f(\boldsymbol{x}, \boldsymbol{\xi}, t)\,\mathrm{d}\boldsymbol{\xi}\,\mathrm{d}t\,\mathrm{d}y\,\mathrm{d}z. \tag{3.8}$$

Of course, this is only an infinitesimal part of all possible velocities. This surface may be hit by particles with any velocity $\boldsymbol{\xi}$ where $v_x < 0$, i.e. the velocities that point toward the surface. To find the momentum change imparted by all particle collisions, we must integrate (3.8) over the velocity half-space where $v_x < 0$. Alternatively, since we have assumed that f is spherically symmetric around $\boldsymbol{v} = 0$, we can simply integrate over the entire velocity space and divide by 2. Thus, the momentum change imparted to the wall by all particle collisions during the period $\mathrm{d}t$ is

$$\mathrm{d}t\,\mathrm{d}y\,\mathrm{d}z \int v_x^2 f(\boldsymbol{x}, \boldsymbol{\xi}, t)\,\mathrm{d}\boldsymbol{\xi}.$$

To get the force from the momentum change, we simply need to divide by $\mathrm{d}t$, as per Newton's second law. To get the pressure from the force, we divide by the area $\mathrm{d}y\,\mathrm{d}z$. Thus, the pressure felt by the surface in Figure 3.3 is

$$p = \int v_x^2 f(\boldsymbol{x}, \boldsymbol{\xi}, t)\,\mathrm{d}\boldsymbol{\xi}.$$

Since we have assumed that the particles are distributed symmetrically about $\boldsymbol{v} = 0$, we could instead have placed the wall in Figure 3.3 in the x–z-plane or the x–y-plane and found equivalent definitions for the pressure with v_y^2 and v_z^2 inside the integral, respectively, instead of v_x^2. In fact, we can take the average of these three equivalent definitions, replacing v_x^2 with $\frac{1}{3}(v_x^2 + v_y^2 + v_z^2) = \frac{1}{3}|\boldsymbol{v}|^2$.

Having done this, the pressure integral is on a familiar form,

$$\boxed{p = \tfrac{1}{3} \int |\boldsymbol{v}|^2 f(\boldsymbol{x}, \boldsymbol{\xi}, t)\,\mathrm{d}\boldsymbol{\xi} = \tfrac{2}{3}\rho e.} \tag{3.9}$$

The last equality follows from comparison with (3.7). We have thus found that the pressure of a gas is proportional to its internal energy density!

This might also have been expected beforehand; with a higher internal energy density, particles tend to move faster. Faster-moving particles bounce off a surface harder and more often.

Equation (3.9) is an equation of state for the gas, relating the pressure p, the density ρ and the specific internal energy e. We may compare this to the ideal gas law [19, Ch. 2.5],

$$p = \rho RT = \rho \frac{k_\mathrm{B} T}{m}, \tag{3.10}$$

Specific gas constant, R
The proportionality constant in the ideal gas law, in $\mathrm{J/kg\,K}$

Temperature, T
A thermodynamic quantity related to e, in K

Boltzmann's constant, k_B
A physical constant relating e and T, approx. $1.38 \times 10^{-23}\,\mathrm{J/K}$

where $R = k_\mathrm{B}/m$ is the *specific gas constant*, T is the *temperature*, and k_B is *Boltzmann's constant*.

Combining equations (3.9) and (3.10), we find

$$e = \frac{3}{2}\frac{p}{\rho} = \frac{3}{2}RT = \frac{3}{2}\frac{k_\mathrm{B} T}{m}, \tag{3.11}$$

which relates the specific energy with the other thermodynamic quantities. This equality could also be predicted by the equipartition theorem of statistical mechanics previously described in section 2.3.3, which predicts an average molecular energy me of $\frac{1}{2}k_\mathrm{B}T$ for each degree of freedom [19, Ch. 2]. Our monatomic gas has three degrees of freedom, one for each coordinate in three-dimensional space. More complicated molecules have additional degrees of freedom, as they may also rotate and vibrate.

We may use (3.11) to calculate the heat capacities for this gas [19, Ch. 2]. The *specific heat capacity at constant volume* is

Specific heat capacity at constant volume, c_V
The rate of increase of e against T if the volume (or ρ) is kept constant, in $\mathrm{J/kg\,K}$

$$c_V = \left(\frac{\partial e}{\partial T}\right)_V = \frac{3}{2}R = \frac{3}{2}\frac{k_\mathrm{B}}{m}. \tag{3.12}$$

The *specific heat capacity at constant pressure* can be found through a property of ideal gases [19, Ch. 2],

Specific heat capacity at constant pressure, c_p
The rate of increase of the enthalpy $h = e + p/\rho$ against T if the pressure is kept constant, in $\mathrm{J/kg\,K}$

$$c_p - c_V = R = \frac{k_\mathrm{B}}{m} \quad \Rightarrow \quad c_p = \left(\frac{\partial (e + p/\rho)}{\partial T}\right)_p = \frac{5}{2}R = \frac{5}{2}\frac{k_\mathrm{B}}{m}. \tag{3.13}$$

Heat capacity ratio, γ
The dimensionless ratio c_p/c_V

The ratio between the two heat capacities is often more useful than the heat capacities themselves. For our monatomic ideal gas, it is found from (3.12) and (3.13) to be

$$\gamma = \frac{c_p}{c_V} = \frac{5}{3}, \tag{3.14}$$

which fits well with tabulated values for noble gases (see e.g. [19, App. F]). As we saw in section 2.3.1, the speed of sound in a gas depends on this heat capacity ratio.

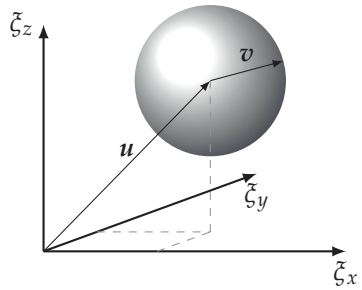

Figure 3.4: A spherical isosurface of a distribution function which is spherically symmetric around $\boldsymbol{\xi} = \boldsymbol{u}$. At any point on this isosurface, f has the same value.

3.3 Equilibrium

When two particles collide, their velocities are changed. Their new velocities depend on their pre-collision positions and velocities and the intermolecular forces during the collision. However, we can assume that collisions tend to distribute the particles' velocities evenly in all directions around their mean velocity $\boldsymbol{u}$. This means that if we take a gas of particles with any initial distribution and leave it for long enough, it will eventually reach an equilibrium state where all directions of the peculiar velocity $\boldsymbol{v}$ are equally probable.*

3.3.1 The Maxwell-Boltzmann distribution

This even distribution of velocities means that the distribution function is only dependent on the peculiar velocity. The distribution function has the same value for peculiar velocities where $|\boldsymbol{v}|^2 = v_x^2 + v_y^2 + v_z^2$ is the same, as shown in Figure 3.4. We can therefore simplify the notation for the distribution function at equilibrium to $f^{(0)}(|\boldsymbol{v}|)$.

Equilibrium distribution function, $f^{(0)}$
The distribution function of a gas that has been left undisturbed for long enough

We also assume that the distribution function is separable in the different $\boldsymbol{v}$ coordinates, so that

$$f^{(0)}(|\boldsymbol{v}|) = f_x^{(0)}(v_x) f_y^{(0)}(v_y) f_z^{(0)}(v_z).$$

For a constant $|\boldsymbol{v}|^2$, $f^{(0)}(|\boldsymbol{v}|)$ is constant, and

$$\ln f_x^{(0)}(v_x) + \ln f_y^{(0)}(v_y) + \ln f_z^{(0)}(v_z) = \text{const.}.$$

*There is an interesting paradox hidden here. At the microscale, where we look at the interaction of individual particles, the Newtonian dynamics of the particles are time reversible: Flipping all the particle velocities would cause the system to retrace its steps back in time. Why, then, does f always go to equilibrium? The short answer is that f is part of a statistical description; the microscopic system tends towards disorder, and the equilibrium state is the most disordered state. A fuller explanation is found in [58, § III.9].

This is solved only if the equilibrium distributions for the different directions are of the form

$$\ln f_x^{(0)}(v_x) = a - bv_x^2 \quad \Rightarrow \quad f_x^{(0)}(v_x) = \mathrm{e}^a \, \mathrm{e}^{-bv_x^2},$$

where a and b are two constants that are independent of $\boldsymbol{v}$. Thus, the equilibrium distribution is fn the form

$$f^{(0)}(|\boldsymbol{v}|) = \mathrm{e}^{3a} \, \mathrm{e}^{-b(v_x^2+v_y^2+v_z^2)} = \mathrm{e}^{3a} \, \mathrm{e}^{-b|\boldsymbol{v}|^2}. \tag{3.15}$$

The constants a and b can be determined from the moments of $f^{(0)}$. First, we find the moment of density,

$$\begin{aligned}\rho = \int f^{(0)}(|\boldsymbol{v}|) \, \mathrm{d}\boldsymbol{\xi} &= \mathrm{e}^{3a} \int_{-\infty}^{\infty} \mathrm{e}^{-bv_x^2} \, \mathrm{d}v_x \int_{-\infty}^{\infty} \mathrm{e}^{-bv_y^2} \, \mathrm{d}v_y \int_{-\infty}^{\infty} \mathrm{e}^{-bv_z^2} \, \mathrm{d}v_z \\ &= \mathrm{e}^{3a} \left(\frac{\pi}{b}\right)^{\frac{3}{2}}.\end{aligned}$$

We see that $\mathrm{e}^{3a} = \rho(b/\pi)^{3/2}$, and the equilibrium distribution becomes

$$f^{(0)}(|\boldsymbol{v}|) = \rho \left(\frac{b}{\pi}\right)^{\frac{3}{2}} \mathrm{e}^{-b|\boldsymbol{v}|^2}. \tag{3.16}$$

Finally we can determine b using the moment of energy. Since $f^{(0)}(|v|)$ is spherically symmetric around $\boldsymbol{v} = 0$, we can perform the substitution $\mathrm{d}\boldsymbol{\xi} = 4\pi|\boldsymbol{v}|^2 \, \mathrm{d}|\boldsymbol{v}|$. The integral is

$$\rho e = \tfrac{1}{2} \int_0^{\infty} |\boldsymbol{v}|^2 f^{(0)}(|\boldsymbol{v}|) 4\pi|\boldsymbol{v}|^2 \, \mathrm{d}|\boldsymbol{v}| = 2\rho\pi \left(\frac{b}{\pi}\right)^{\frac{3}{2}} \int_0^{\infty} |\boldsymbol{v}|^4 \, \mathrm{e}^{-b|\boldsymbol{v}|^2} \, \mathrm{d}|\boldsymbol{v}| = \frac{3\rho}{4b},$$

which lets us identify b using several different thermodynamic quantities,

$$b = \frac{3}{4e} = \frac{\rho}{2p} = \frac{m}{2k_{\mathrm{B}}T}. \tag{3.17}$$

The two last equalities follow from (3.11).

Thus, the equilibrium distribution has the possible forms

$$\boxed{\begin{aligned} f^{(0)}(|\boldsymbol{v}|) &= \rho \left(\frac{3}{4\pi e}\right)^{\frac{3}{2}} \mathrm{e}^{-3|\boldsymbol{v}|^2/4e} = \rho \left(\frac{\rho}{2\pi p}\right)^{\frac{3}{2}} \mathrm{e}^{-\rho|\boldsymbol{v}|^2/2p} \\ &= \rho \left(\frac{m}{2\pi k_{\mathrm{B}}T}\right)^{\frac{3}{2}} \mathrm{e}^{-m|\boldsymbol{v}|^2/2k_{\mathrm{B}}T}, \end{aligned}} \tag{3.18}$$

depending on which thermodynamic variables we use to describe it.

This equilibrium distribution is called the Maxwell-Boltzmann distribution. It was first found by James Clerk Maxwell using a derivation similar to the one we have used here, and was later found by Ludwig Boltzmann using more rigorous statistical mechanics.

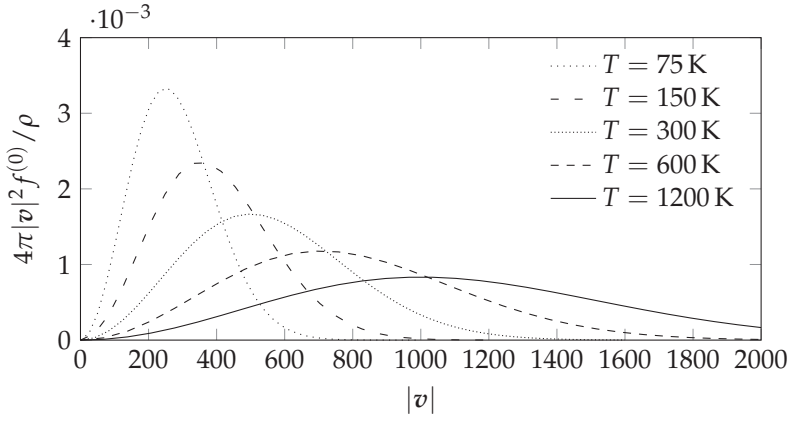

Figure 3.5: The normalised distribution of radial velocities in a neon gas at equilibrium.

3.3.2 Peculiar velocity moments at equilibrium

It will later be necessary to know several different $\boldsymbol{v}$-weighted moments of the equilibrium distribution. We will now find the first seven general moments of this kind, with $f^{(0)}$ on the general form given by (3.16). The parameter b can be related to the macroscopic state variables through (3.17).

The different moments of $f^{(0)}$ are tensors of different orders. These are most convently described using index notation, which has been previously introduced in section 2.1.

The zeroth-order moment tensor is already familiar. It is simply the density,

$$\int f^{(0)} \,\mathrm{d}\boldsymbol{\xi} = \rho. \tag{3.19a}$$

The first-order moment has already found for a general distribution function in (3.6). For the equilibrium special case $f = f^{(0)}$ it is still the same,

$$\int v_\alpha f^{(0)} \,\mathrm{d}\boldsymbol{\xi} = 0. \tag{3.19b}$$

This could also have been seen from symmetry considerations: Since $f^{(0)}$ is symmetric around $\boldsymbol{v} = 0$ and v_α is antisymmetric around $v_\alpha = 0$, the integrand is antisymmetric, and the integral is zero. This is the case for all of the odd moments, as the product of an odd number of antisymmetric functions is always also antisymmetric.

Since $f^{(0)}$ is rotationally invariant around $\boldsymbol{v} = 0$, the moment integrals are independent of the coordinate axes in velocity space, and the resulting tensors must be *isotropic*, which means that it is independent of the choice of coordinate system. For example, the tensor $\delta_{\alpha\beta}$ is one if both indices are the same, which is true for any coordinate system.

Isotropic tensor
A tensor which has identical components for any choice of orthogonal coordinate system

The general second-order isotropic tensor is $C_1\delta_{\alpha\beta}$ [59], where C_1 is a constant. The constant can be found by calculating the integral $\int v_x v_x f^{(0)}\,\mathrm{d}\boldsymbol{\xi}$, and we find that the second-order moment tensor is

$$\int v_\alpha v_\beta f^{(0)}\,\mathrm{d}\boldsymbol{\xi} = \frac{\rho}{2b}\delta_{\alpha\beta}. \tag{3.19c}$$

The third-order moment tensor is

$$\int v_\alpha v_\beta v_\gamma f^{(0)}\,\mathrm{d}\boldsymbol{\xi} = 0, \tag{3.19d}$$

due to antisymmetry.

The general form of the fourth-order isotropic tensor is $C_1\delta_{\alpha\beta}\delta_{\gamma\delta} + C_2\delta_{\alpha\gamma}\delta_{\beta\delta} + C_3\delta_{\alpha\delta}\delta_{\beta\gamma}$ [59]. Since the moment tensors are invariant with respect to index order (e.g. changing β and γ makes no difference, as $\int v_x v_x v_y v_y f^{(0)}\,\mathrm{d}\boldsymbol{\xi} = \int v_x v_y v_x v_y f^{(0)}\,\mathrm{d}\boldsymbol{\xi}$), these constants must be equal, and can be found by taking the integral $\int v_x v_x v_y v_y f^{(0)}\,\mathrm{d}\boldsymbol{\xi}$. The fourth-order moment tensor is therefore

$$\int v_\alpha v_\beta v_\gamma v_\delta f^{(0)}\,\mathrm{d}\boldsymbol{\xi} = \frac{\rho}{(2b)^2}(\delta_{\alpha\beta}\delta_{\gamma\delta} + \delta_{\alpha\gamma}\delta_{\beta\delta} + \delta_{\alpha\delta}\delta_{\beta\gamma}). \tag{3.19e}$$

The fifth-order moment tensor is also antisymmetric, which means that

$$\int v_\alpha v_\beta v_\gamma v_\delta v_\epsilon f^{(0)}\,\mathrm{d}\boldsymbol{\xi} = 0. \tag{3.19f}$$

Similar to the approach taken to find the second and fourth moment tensors, the somewhat unwieldy sixth-order moment tensor can be found to be

$$\begin{aligned}
&\int v_\alpha v_\beta v_\gamma v_\delta v_\epsilon v_\zeta f^{(0)}\,\mathrm{d}\boldsymbol{\xi} \qquad (3.19g)\\
&= \frac{\rho}{(2b)^3}\Big[\delta_{\alpha\beta}\delta_{\gamma\delta}\delta_{\epsilon\zeta} + \delta_{\alpha\beta}\delta_{\gamma\epsilon}\delta_{\delta\zeta} + \delta_{\alpha\beta}\delta_{\gamma\zeta}\delta_{\delta\epsilon} + \delta_{\alpha\gamma}\delta_{\beta\delta}\delta_{\epsilon\zeta} + \delta_{\alpha\gamma}\delta_{\beta\epsilon}\delta_{\delta\zeta}\\
&\qquad + \delta_{\alpha\gamma}\delta_{\beta\zeta}\delta_{\delta\epsilon} + \delta_{\alpha\delta}\delta_{\beta\gamma}\delta_{\epsilon\zeta} + \delta_{\alpha\delta}\delta_{\beta\epsilon}\delta_{\gamma\zeta} + \delta_{\alpha\delta}\delta_{\beta\zeta}\delta_{\gamma\epsilon} + \delta_{\alpha\epsilon}\delta_{\beta\gamma}\delta_{\delta\zeta}\\
&\qquad + \delta_{\alpha\epsilon}\delta_{\beta\delta}\delta_{\gamma\zeta} + \delta_{\alpha\epsilon}\delta_{\beta\zeta}\delta_{\gamma\delta} + \delta_{\alpha\zeta}\delta_{\beta\gamma}\delta_{\delta\epsilon} + \delta_{\alpha\zeta}\delta_{\beta\delta}\delta_{\gamma\epsilon} + \delta_{\alpha\zeta}\delta_{\beta\epsilon}\delta_{\gamma\delta}\Big].
\end{aligned}$$

The seven moment tensors which we have seen show a clear pattern: The odd-order moment tensors are zero, while the moment tensors with even order $2n$ are $\rho/(2b)^n$ multiplied with the sum of all Kronecker delta product permutations of the $2n$ different indices.

3.4 The Boltzmann equation

So far we have talked about the distribution function, its moments, and its value at equilibrium, but we still know nothing about how it actually evolves with time. We will therefore now derive the equation that describes the evolution of the distribution function.

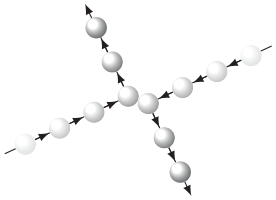

Figure 3.6: Collision between two molecules modeled as hard spheres.

The distribution function is a function of $\boldsymbol{x}$, $\boldsymbol{\xi}$, and t. Therefore, its total differential with respect to t is

$$\frac{\mathrm{d}f}{\mathrm{d}t} = \left(\frac{\partial f}{\partial x_\alpha}\right)\frac{\mathrm{d}x_\alpha}{\mathrm{d}t} + \left(\frac{\partial f}{\partial \xi_\alpha}\right)\frac{\mathrm{d}\xi_\alpha}{\mathrm{d}t} + \left(\frac{\partial f}{\partial t}\right)\frac{\mathrm{d}t}{\mathrm{d}t}.$$

$\mathrm{d}x_\alpha/\mathrm{d}t$ is the particles' velocity ξ_α. $\mathrm{d}\xi_\alpha/\mathrm{d}t$ is their acceleration, which by Newton's second law is given by the *body force density* as $\mathrm{d}\xi_\alpha/\mathrm{d}t = F_\alpha/\rho$. Thus, the equation can be rewritten as

Body force density, $\boldsymbol{F}$
Force density of long-range forces, e.g. gravity, in $\mathrm{N/m^3}$

$$\frac{\partial f}{\partial t} + \xi_\alpha\left(\frac{\partial f}{\partial x_\alpha}\right) + \frac{F_\alpha}{\rho}\left(\frac{\partial f}{\partial \xi_\alpha}\right) = \frac{\mathrm{d}f}{\mathrm{d}t}.$$

If the right hand side of this equation is zero, the equation becomes a sort of advection equation, describing collisionless propagation of the particle distribution f. This propagates with the velocity of its particles, $\boldsymbol{\xi}$, which is itself affected by the force $\boldsymbol{F}$. In general, the right hand side $\mathrm{d}f/\mathrm{d}t$ is a source term that indicates the rate of change of f, due to collisions causing particles to change their directions.

Since collisions can only happen between particles which are at the same place at the same time, $\mathrm{d}f(\boldsymbol{x}, \boldsymbol{\xi}, t)/\mathrm{d}t$ for a particular choice of $\boldsymbol{x}$, $\boldsymbol{\xi}$, and t depends on the distribution function f for all $\boldsymbol{\xi}$ at the same $\boldsymbol{x}$ and t.

Writing this equation on vector form with $\mathrm{d}f/\mathrm{d}t$ rewritten as the *collision operator* $\Omega(f)$, we find

Collision operator, Ω
An operator which can be applied to f to give its rate of change

$$\boxed{\frac{\partial f}{\partial t} + \boldsymbol{\xi}\cdot\nabla f + \frac{\boldsymbol{F}}{\rho}\cdot\nabla_\xi f = \Omega(f).} \tag{3.20}$$

Here, $\nabla_\xi f$ is the gradient of f in velocity space. This equation is called the *Boltzmann equation* after Ludwig Boltzmann, who devised it in the late 19th century.

3.5 The collision operator

The collision operator may have many different forms, as long as it fulfils certain conditions. Three quantities are always conserved in a collision:

Mass, momentum, and, if the collisions are elastic,* translational energy. These conservation conditions are expressed mathematically as

$$\text{Mass conservation:} \quad \int \Omega(f)\,\mathrm{d}\boldsymbol{\xi} = 0, \tag{3.21a}$$

$$\text{Momentum conservation:} \quad \int \boldsymbol{\xi}\,\Omega(f)\,\mathrm{d}\boldsymbol{\xi} = 0, \tag{3.21b}$$

$$\text{Energy conservation:} \quad \begin{cases} \int |\boldsymbol{\xi}|^2\,\Omega(f)\,\mathrm{d}\boldsymbol{\xi} = 0, \\ \int |\boldsymbol{v}|^2\,\Omega(f)\,\mathrm{d}\boldsymbol{\xi} = 0. \end{cases} \tag{3.21c}$$

The two energy conservation conditions are equivalent, which can be shown using the identity (2.9),

$$|\boldsymbol{v}|^2 = |\boldsymbol{\xi} - \boldsymbol{u}|^2 = |\boldsymbol{\xi}|^2 - 2\boldsymbol{\xi}\cdot\boldsymbol{u} + |\boldsymbol{u}|^2,$$

and the mass and momentum conservation conditions.

Another criterion for collision operators is that they must ensure that the distribution function *always* evolves *towards* equilibrium. We will not discuss this further before section 3.9, except stating that this criterion is fulfilled by all collision operators discussed in this section.

Boltzmann's original collision operator is of the form of a complicated double integral over velocity space. It essentially considers the outcome of all possible two-particle collisions, for any choice of intermolecular forces between the particles.

This collision operator fulfils conditions (3.21), but is very cumbersome. Alternative collision models were later proposed. The goal was to find a collision model that was simpler than Boltzmann's original one, but which still gave a largely correct macroscopic behaviour. In the scientific field of lattice Boltzmann methods, variants of the BGK collision operator,

$$\Omega(f) = -\frac{1}{\tau}\left(f - f^{(0)}\right), \tag{3.22}$$

Relaxation time, τ
A time constant indicating how quickly a gas relaxes towards an equilibrium

are generally used. Here, τ is called the *relaxation time*. This collision operator proposed by Bhatnagar, Gross, and Krook in 1954 as a very simple model for particle collisions [60]. As discussed in section 3.3, the particle distribution will tend to relax to an equilibrium. The BGK operator captures this behaviour by directly modeling the relaxation process instead of attempting to follow the details of the collisions.

*For the monatomic gas we are considering, collisions are elastic. However, for polyatomic gases as considered in section 2.3.3, collisions may be inelastic or superelastic due to energy being transferred between translational and inner (i.e. rotational or vibrational) degrees of freedom. In that case, the conservation condition must apply to the *total* energy, i.e. the sum of translational and inner energy, as in e.g. [55].

The BGK operator can easily be shown to satisfy conservation of mass, momentum, and energy. As the equilibrium distribution $f^{(0)}$ has the same moments of density, momentum, and energy as the distribution function f, the BGK operator (3.22) satisfies (3.21).

As an example, say that we have a distribution function which is spatially homogeneous ($\nabla f(\boldsymbol{\xi}, t) = 0$), but in a non-equilibrium state at $t = 0$. Neglecting external forces, the Boltzmann equation for this case is

$$\frac{\partial f(\boldsymbol{\xi}, t)}{\partial t} = -\frac{1}{\tau}\left(f(\boldsymbol{\xi}, t) - f^{(0)}(\boldsymbol{\xi})\right),$$

which is solved by

$$f(\boldsymbol{\xi}, t) = f^{(0)}(\boldsymbol{\xi}) + \left(f(\boldsymbol{\xi}, 0) - f^{(0)}(\boldsymbol{\xi})\right) \mathrm{e}^{-t/\tau}.$$

This solution describes a distribution function that relaxes exponentially to the equilibrium distribution with a time constant τ. From the results that will be found in section 3.8.3, it can be shown that $\tau \sim 10^{-10}$ for ordinary gases like air at room temperature.

However, being only a simplified model of the result of particle collisions in a gas, the BGK collision operator is not as exact as Boltzmann's original collision operator. For instance, the Boltzmann equation with the BGK operator predicts a *Prandtl number* $Pr = 1$, whereas with Boltzmann's collision operator we get a value $Pr \simeq 2/3$, which agrees with experiments with monatomic gases [58, Ch.II]. This will be discussed further in section 3.8.3.

Prandtl number, Pr
A dimensionless number relating the strengths of viscosity and thermal conductivity

3.6 Macroscopic conservation equations

By taking the appropriate moments of the Boltzmann equation (3.20) we can find general conservation equations for the three collision invariants of mass, momentum, and energy.

It will be useful to define a common notation for all the moments of f;

$$\begin{aligned} \Pi_0 &= \int f \,\mathrm{d}\boldsymbol{\xi} = \rho, & \Pi_\alpha &= \int \xi_\alpha f \,\mathrm{d}\boldsymbol{\xi} = \rho u_\alpha, \\ \Pi_{\alpha\beta} &= \int \xi_\alpha \xi_\beta f \,\mathrm{d}\boldsymbol{\xi}, & \Pi_{\alpha\beta\gamma} &= \int \xi_\alpha \xi_\beta \xi_\gamma f \,\mathrm{d}\boldsymbol{\xi}, \end{aligned} \tag{3.23}$$

and so forth. From their definitions, the moment tensors are clearly invariant with a switch of their indices, e.g. $\Pi_{xy} = \Pi_{yx}$.

For the force term it will be useful to know some moments of $\partial f / \partial \xi_\alpha$. Using multidimensional integration by parts (2.11), these can be found to

be

$$\int \frac{\partial f}{\partial \xi_\alpha} \, \mathrm{d}\boldsymbol{\xi} = 0, \tag{3.24a}$$

$$\int \xi_\alpha \frac{\partial f}{\partial \xi_\beta} \, \mathrm{d}\boldsymbol{\xi} = -\int \frac{\partial \xi_\alpha}{\partial \xi_\beta} f \, \mathrm{d}\boldsymbol{\xi} = -\rho \delta_{\alpha\beta}, \tag{3.24b}$$

$$\int \xi_\alpha \xi_\alpha \frac{\partial f}{\partial \xi_\beta} \, \mathrm{d}\boldsymbol{\xi} = -\int \frac{\partial \xi_\alpha \xi_\alpha}{\partial \xi_\beta} f \, \mathrm{d}\boldsymbol{\xi} = -2\rho u_\beta. \tag{3.24c}$$

The surface integrals vanish using the assumptions that f, $\xi_\alpha f$, and $\xi_\alpha \xi_\alpha f$ vanishes as $\boldsymbol{\xi} \to \infty$. These assumptions are quite safe, as they are necessary for the conserved quantities to be finite. Also, it is reasonable to assume that f will not be very far off in any case from the equilibrium $f^{(0)}$, which goes exponentially to zero.

3.6.1 Mass conservation

We first take the zeroth moment of all terms in the Boltzmann equation (3.20),

$$\frac{\partial}{\partial t} \int f \, \mathrm{d}\boldsymbol{\xi} + \frac{\partial}{\partial x_\alpha} \int \xi_\alpha f \, \mathrm{d}\boldsymbol{\xi} + \frac{F_\alpha}{\rho} \int \frac{\partial f}{\partial \xi_\alpha} \, \mathrm{d}\boldsymbol{\xi} = \int \Omega(f) \, \mathrm{d}\boldsymbol{\xi}.$$

Since t and $\boldsymbol{x}$ are not functions of $\boldsymbol{\xi}$, their derivatives have been moved outside the integrals. Also, $\boldsymbol{\xi}$ does not depend on $\boldsymbol{x}$ as it is merely a coordinate in velocity space, and we have used that $\xi_\alpha \partial f / \partial x_\alpha = \partial(\xi_\alpha f)/\partial x_\alpha$.

The integrals on the left hand side are the density moment (3.1), the momentum moment (3.2), and zero (by 3.24a), respectively. The right side is also zero, by conservation of mass (3.21a). Thus, the zeroth moment of the Boltzmann equation becomes

$$\boxed{\frac{\partial \rho}{\partial t} + \frac{\partial \rho u_\alpha}{\partial x_\alpha} = 0,} \tag{3.25}$$

which is exactly the continuity equation. This equation does not depend on the specific form of the distribution function f, only its conserved moments.

3.6.2 Momentum conservation

Taking the first moment of the Boltzmann equation and using the same assumptions as for the zeroth moment, we get

$$\frac{\partial}{\partial t} \int \xi_\alpha f \, \mathrm{d}\boldsymbol{\xi} + \frac{\partial}{\partial x_\beta} \int \xi_\alpha \xi_\beta f \, \mathrm{d}\boldsymbol{\xi} + \frac{F_\beta}{\rho} \int \xi_\alpha \frac{\partial f}{\partial \xi_\beta} \, \mathrm{d}\boldsymbol{\xi} = \int \xi_\alpha \, \Omega(f) \, \mathrm{d}\boldsymbol{\xi}.$$

By equations (3.2), (3.23), (3.24b), and (3.21b), this reduces to

$$\frac{\partial \rho u_\alpha}{\partial t} + \frac{\partial \Pi_{\alpha\beta}}{\partial x_\beta} = F_\alpha. \tag{3.26}$$

The moment $\Pi_{\alpha\beta} = \int \xi_\alpha \xi_\beta f \, \mathrm{d}\boldsymbol{\xi}$ can be interpreted as the flow in the α direction of the momentum component in the β direction, which is $\xi_\beta f \, \mathrm{d}\boldsymbol{\xi}$. The directions can also be vice versa, as $\Pi_{\alpha\beta}$ is symmetric.

It can be resolved into two parts by using $\xi_\alpha \xi_\beta = (u_\alpha + v_\alpha)(u_\beta + v_\beta)$ and the fact that moments of only the peculiar velocity are zero:

$$\Pi_{\alpha\beta} = \int (u_\alpha u_\beta + u_\alpha v_\beta + v_\alpha u_\beta + v_\alpha v_\beta) f \, \mathrm{d}\boldsymbol{\xi} = \rho u_\alpha u_\beta - \sigma_{\alpha\beta}. \tag{3.27}$$

Here, the first term, $\rho u_\alpha u_\beta$, represents the macroscopic flow of momentum, and the second term,

$$\sigma_{\alpha\beta} = -\int v_\alpha v_\beta f \, \mathrm{d}\boldsymbol{\xi}, \tag{3.28}$$

represents a diffusion of momentum.

Thus, the first moment of the Boltzmann equation results in the conservation form of the Cauchy momentum equation (2.18),

$$\boxed{\frac{\partial \rho u_\alpha}{\partial t} + \frac{\partial \rho u_\alpha u_\beta}{\partial x_\beta} = \frac{\partial \sigma_{\alpha\beta}}{\partial x_\beta} + F_\alpha.} \tag{3.29}$$

Cauchy stress tensor, σ
A second-order tensor which at any point in the fluid specifies the normal and shear stresses in the x, y, and z directions

$\sigma_{\alpha\beta}$ can be identified as the *Cauchy stress tensor*, which completely defines the state of stress at any point in the fluid. We see from its definition (3.28) that it is symmetric, i.e. $\sigma_{\alpha\beta} = \sigma_{\beta\alpha}$.

The Cauchy stress tensor (3.28) is determined by the form of f, and we can therefore not find a fully macroscopic momentum conservation equation before we know more about f.

3.6.3 Energy conservation

To find an energy conservation equation, we take the $\xi_\beta \xi_\beta$ moment of the Boltzmann equation,

$$\frac{\partial}{\partial t} \int \xi_\beta \xi_\beta f \, \mathrm{d}\boldsymbol{\xi} + \frac{\partial}{\partial x_\alpha} \int \xi_\alpha \xi_\beta \xi_\beta f \, \mathrm{d}\boldsymbol{\xi} + \frac{F_\alpha}{\rho} \int \xi_\beta \xi_\beta \frac{\partial f}{\partial \xi_\alpha} \, \mathrm{d}\boldsymbol{\xi} = \int \xi_\beta \xi_\beta \, \Omega(f) \, \mathrm{d}\boldsymbol{\xi}.$$

By dividing by 2 and using equations (3.3), (3.23), (3.24b), this reduces to

$$\frac{\partial \rho E}{\partial t} + \frac{1}{2} \frac{\partial \Pi_{\alpha\beta\beta}}{\partial x_\alpha} = F_\alpha u_\alpha. \tag{3.30}$$

As $\frac{1}{2} \xi_\beta \xi_\beta f \, \mathrm{d}\boldsymbol{\xi} = \frac{1}{2} |\boldsymbol{\xi}|^2 f \, \mathrm{d}\boldsymbol{\xi}$ is related to the translational energy of particles, the moment $\Pi_{\alpha\beta\beta}$ represents the flow of energy in the α direction.

It may be resolved to another form,

$$\begin{aligned}\tfrac{1}{2}\Pi_{\alpha\beta\beta} &= \tfrac{1}{2}\int (u_\alpha u_\beta u_\beta + u_\alpha v_\beta v_\beta + 2v_\alpha v_\beta u_\beta + v_\alpha v_\beta v_\beta) f \,\mathrm{d}\boldsymbol{\xi} \\ &= \tfrac{1}{2}\rho u_\alpha |\boldsymbol{u}|^2 + \rho u_\alpha e - u_\beta \sigma_{\alpha\beta} + q_\alpha = \rho u_\alpha E - u_\beta \sigma_{\alpha\beta} + q_\alpha,\end{aligned}$$

where the first term represents macroscopic advection of energy, the second term can be identified as related to the work done by the Cauchy stresses, and the last term,

$$\boldsymbol{q} = \tfrac{1}{2}\int \boldsymbol{v}|\boldsymbol{v}|^2 f \,\mathrm{d}\boldsymbol{\xi}, \tag{3.31}$$

represents the diffusion of energy.

Thus, this moment of the Boltzmann equation results in a conservation equation for the energy,

$$\frac{\partial \rho E}{\partial t} + \frac{\partial \rho u_\alpha E}{\partial x_\alpha} = \frac{\partial \sigma_{\alpha\beta} u_\beta}{\partial x_\alpha} + F_\alpha u_\alpha - \frac{\partial q_\alpha}{\partial x_\alpha}. \tag{3.32}$$

By subtracting $u_\alpha \times$ (3.29) from this (carefully switching some of the repeated indices), we can find a simpler conservation equation for the internal energy,

$$\boxed{\frac{\partial \rho e}{\partial t} + \frac{\partial \rho u_\alpha e}{\partial x_\alpha} = \sigma_{\alpha\beta}\frac{\partial u_\beta}{\partial x_\alpha} - \frac{\partial q_\alpha}{\partial x_\alpha}.} \tag{3.33}$$

This is a general form of the energy equations given in section 2.2. The first term on the right hand side describes the increase in energy due to work done by the stresses, whereas the last term, which describes diffusion of energy, can be identified with the *heat flux* vector from the macroscopic energy equation.

Heat flux, q
Macroscopically; the flow rate of heat. Microscopically; the rate of diffusion of energy. In $\mathrm{J/s\,m^2}$.

In this equation, both the Cauchy stress $\boldsymbol{\sigma}$ and the heat flux $\boldsymbol{q}$ depend of the form of the distribution function. Like the momentum conservation equation, the energy equation is not fully determined until we know more about the form of f.

3.7 Equilibrium: The Euler model

The simplest assumption we can make about the form of the distribution function is that it is always at equilibrium, i.e. $f \simeq f^{(0)}$. (In the next section we will see that this corresponds to assuming that the distance between gas particles is very small compared to any relevant macroscopic length.) It is then simple to find an equilibrium expression for the stress tensor, $\boldsymbol{\sigma}^{(0)}$, and for the heat flux, $\boldsymbol{q}^{(0)}$.

Referring to the moments of the equilibrium distribution found in section 3.3.2, we find that the stress tensor and heat flux at equilibrium are

$$\sigma_{\alpha\beta}^{(0)} = -\int v_\alpha v_\beta f^{(0)}\,\mathrm{d}\boldsymbol{\xi} = -p\delta_{\alpha\beta} \tag{3.34}$$

and

$$q_\alpha^{(0)} = \tfrac{1}{2}\int v_\alpha v_\beta v_\beta f^{(0)}\,\mathrm{d}\boldsymbol{\xi} = 0, \tag{3.35}$$

respectively.

With the assumptions that $\boldsymbol{\sigma} \simeq \boldsymbol{\sigma}^{(0)}$ and $\boldsymbol{q} \simeq \boldsymbol{q}^{(0)}$, the momentum and energy conservation equations become

$$\frac{\partial \rho u_\alpha}{\partial t} + \frac{\partial \rho u_\alpha u_\beta}{\partial x_\beta} = -\frac{\partial p}{\partial x_\alpha} + F_\alpha, \tag{3.36a}$$

$$\frac{\partial \rho e}{\partial t} + \frac{\partial \rho u_\alpha e}{\partial x_\alpha} = -p\frac{\partial u_\alpha}{\partial x_\alpha}. \tag{3.36b}$$

These and the equation of continuity correspond to Euler's equations of fluid dynamics, previously given in material derivative form in (2.17).

However, these equations lack the viscous stresses and heat conduction of the Navier-Stokes-Fourier model. The assumption that the distribution function is at an equilibrium is clearly not sufficient to reproduce all the phenomena of continuum fluid mechanics. This shows that viscosity and heat conduction are connected with the relaxation of the distribution function to equilibrium.

3.8 The Chapman-Enskog expansion

In the previous section we saw that the Euler equations can be derived from the Boltzmann equation under the assumption that the gas is always at equilibrium. This implies that more detailed fluid models, such as the Navier-Stokes-Fourier model, are connected with the deviation from equilibrium.

We can see this more clearly if we nondimensionalise the Boltzmann equation, by replacing each variable with the product of a dimensionless counterpart (denoted with a tilde) and an appropriate characteristic number. Using the characteristic length x_0, characteristic velocity ξ_0, characteristic time $t_0 = x_0/\xi_0$, *mean free path* x_{mfp}, and *mean free time* $t_{\mathrm{mfp}} = x_{\mathrm{mfp}}/\xi_0$, we get

$$\begin{aligned} t &= \tilde{t}\; x_0/\xi_0, \qquad & \boldsymbol{x} &= \tilde{\boldsymbol{x}}\; x_0, \qquad & \boldsymbol{\xi} &= \tilde{\boldsymbol{\xi}}\; \xi_0, \\ \tau &= \tilde{\tau}\; x_{\mathrm{mfp}}/\xi_0, & \boldsymbol{F} &= \tilde{\boldsymbol{F}}\; \rho\xi_0^2/x_0, & f &= \tilde{f}\; \rho/c_0^3. \end{aligned} \tag{3.37}$$

Mean free path, x_{mfp}
The average distance travelled between collisions by a particle

Mean free time, t_{mfp}
The average time between collisions for a particle

Here we have assumed that the relaxation time in the BGK collision operator is related to the time between particle collisions.

Replacing all the variables and derivatives in the Boltzmann equation (3.20) with their dimensionless counterparts, we get

$$\frac{x_{\text{mfp}}}{x_0}\left(\frac{\partial \tilde{f}}{\partial \tilde{t}} + \tilde{\xi}_\alpha \frac{\partial \tilde{f}}{\partial \tilde{x}_\alpha} + \tilde{F}_\alpha \frac{\partial \tilde{f}}{\partial \tilde{\xi}_\alpha}\right) = -\frac{1}{\tilde{\tau}}\left(\tilde{f} - \tilde{f}^{(0)}\right). \tag{3.38}$$

Knudsen number, Kn
The ratio between the mean free path and a characteristic length. If $Kn \ll 1$, the gas can be seen as a continuum.

On the left hand side we have the *Knudsen number*,

$$Kn = \frac{x_{\text{mfp}}}{x_0} = \frac{t_{\text{mfp}}}{t_0}. \tag{3.39}$$

If $Kn \to 0$, then both sides of (3.38) must also go to zero. The right side going to zero implies that $\tilde{f} \simeq \tilde{f}^{(0)}$, i.e. that the distribution function is very close to equilibrium, which again implies that the Euler equations is an approximate macroscopic description of the fluid flow for this case. As we increase Kn, the distribution function's deviation from equilibrium becomes more significant, and we need a better macroscopic model, such as the Navier-Stokes-Fourier model, to properly describe the fluid flow.

As the distribution function's deviation from equilibrium becomes more important with larger Kn, it would be natural to approximate $\tilde{f}$ by $\tilde{f}^{(0)}$ with a small perturbation which increases with Kn. We introduce a smallness parameter ϵ which serves to label a term's order in the Knudsen number, i.e. we let

$$Kn \to \epsilon Kn.$$

Going back to dimensional quantities again, we expand the distribution function around equilibrium with terms in increasing order of Kn,

$$f = f^{(0)} + \epsilon f^{(1)} + \epsilon^2 f^{(2)} + \dots, \tag{3.40}$$

where the ϵs indicate that $f^{(1)}/f^{(0)} = \mathcal{O}(Kn)$, $f^{(2)}/f^{(0)} = \mathcal{O}(Kn^2)$, and so forth.

Since the ratio between the left and right hand sides of (3.38) is $\mathcal{O}(Kn)$, the Boltzmann equation with f expanded now becomes

$$\begin{aligned}\left[\frac{\partial}{\partial t} + \xi_\alpha \frac{\partial}{\partial x_\alpha} + F_\alpha \frac{\partial f}{\partial \xi_\alpha}\right]\left(f^{(0)} + \epsilon f^{(1)} + \epsilon^2 f^{(2)} + \dots\right) \\ = -\frac{1}{\epsilon\tau}\left(\epsilon f^{(1)} + \epsilon^2 f^{(2)} + \dots\right).\end{aligned} \tag{3.41}$$

The reason for introducing ϵ is to order the terms according to their Knudsen number order. We assume that terms of different order in Kn are semi-independent. Thus, (3.41) may be seen as a hierarchy of equations; one equation at $\mathcal{O}(Kn^0)$, one at $\mathcal{O}(Kn^1)$, and so forth.* This

*The different equations are generally connected through the time derivative, which is expanded into components at each order in Kn. In the following we will not need to consider this, as we will only need the $\mathcal{O}(Kn)$ equation. However, we will need to consider this in the later Chapman-Enskog derivation in section 4.1.2.

expansion technique for attacking the Boltzmann equation is named after Sydney Chapman and David Enskog, who discovered it independently of each other in the 1910s.

At the $\mathcal{O}(Kn^0)$ level in (3.41), we have $f^{(0)}$ on the left hand side and $f^{(1)}$ on the right. Thus, we can will be able to find $f^{(1)}$ as a function of $f^{(0)}$. Similarly, we can in principle find $f^{(2)}$ from $f^{(1)}$, $f^{(3)}$ from $f^{(2)}$, and so forth.

We have seen previously that f and $f^{(0)}$ have the same moments of density, momentum, and energy. Therefore, we can assume that the contributions of the higher order terms $f^{(1)}$, $f^{(2)}$, ... to these moments are zero,

$$\int f^{(n)} \,\mathrm{d}\boldsymbol{\xi} = \int \boldsymbol{\xi} f^{(n)} \,\mathrm{d}\boldsymbol{\xi} = \int |\boldsymbol{\xi}|^2 f^{(n)} \,\mathrm{d}\boldsymbol{\xi} = \int |\boldsymbol{v}|^2 f^{(n)} \,\mathrm{d}\boldsymbol{\xi} = 0 \quad \text{for } n \geq 1. \tag{3.42}$$

Finding the stress tensor (3.28) and heat flux vector (3.31) from the expanded distribution function (3.40), we find that the stress tensor and heat flux vector are necessarily also expanded in Kn,

$$\boldsymbol{\sigma} = \boldsymbol{\sigma}^{(0)} + \epsilon \boldsymbol{\sigma}^{(1)} + \epsilon^2 \boldsymbol{\sigma}^{(2)} + \dots \,, \tag{3.43a}$$

$$\boldsymbol{q} = \boldsymbol{q}^{(0)} + \epsilon \boldsymbol{q}^{(1)} + \epsilon^2 \boldsymbol{q}^{(2)} + \dots \,, \tag{3.43b}$$

where

$$\sigma_{\alpha\beta}^{(n)} = -\int v_\alpha v_\beta f^{(n)} \,\mathrm{d}\boldsymbol{\xi}, \qquad q_\alpha^{(n)} = \tfrac{1}{2} \int v_\alpha |\boldsymbol{v}|^2 f^{(n)} \,\mathrm{d}\boldsymbol{\xi}. \tag{3.43c}$$

As our goal is to find macroscopic conservation equations beyond the Euler equations from the Boltzmann equation, we ultimately want to find at least the first-order moment perturbations $\boldsymbol{\sigma}^{(1)}$ and $\boldsymbol{q}^{(1)}$. There are several paths to these moments. One is to find an expression for $f^{(1)}$, and calculate the moments from that. Another is to take several different moments at different Kn orders in the expanded Boltzmann equation and find the stress tensor and heat flux moments through other unknown moments, which must be traced back to the known, conserved moments. In the following, we will take the former approach, using a derivation similar to [61, Ch. 7]. The latter approach will be taken later in section 4.1.2.

3.8.1 Finding the distribution function perturbation

At $\mathcal{O}(Kn^0)$, the expanded Boltzmann equation (3.41) is

$$\frac{\partial f^{(0)}}{\partial t} + \boldsymbol{\xi} \cdot \nabla f^{(0)} + \frac{\boldsymbol{F}}{\rho} \cdot \nabla_{\boldsymbol{\xi}} f^{(0)} = -\frac{f^{(1)}}{\tau}. \tag{3.44}$$

Taking the moments of mass, momentum or energy of this will give the Euler equations as described in section 3.7; the right side disappears by (3.42).

Instead, we divide both sides by $f^{(0)}$, rearrange, and use the chain rule in reverse,

$$\begin{aligned}\frac{f^{(1)}}{f^{(0)}} &= -\frac{\tau}{f^{(0)}}\left[\frac{\partial f^{(0)}}{\partial t} + \xi_\alpha \frac{\partial f^{(0)}}{\partial x_\alpha} + \frac{F_\alpha}{\rho}\frac{\partial f^{(0)}}{\partial \xi_\alpha}\right] \\ &= -\tau\left[\frac{\partial \ln f^{(0)}}{\partial t} + (u_\alpha + v_\alpha)\frac{\partial \ln f^{(0)}}{\partial x_\alpha} + \frac{F_\alpha}{\rho}\frac{\partial \ln f^{(0)}}{\partial \xi_\alpha}\right].\end{aligned} \tag{3.45}$$

The rest of this section will consist of resolving the derivatives of $\ln f^{(0)}$ into derivatives of the macroscopic variables, in order to find an entirely macroscopic relationship (3.52) between $f^{(1)}$ and $f^{(0)}$.

The logarithm of the equilibrium distribution function (3.18) has a reasonably simple form,

$$\ln f^{(0)} = \tfrac{3}{2}\ln\left(\frac{3}{4\pi}\right) + \ln\rho - \tfrac{3}{2}\ln e - \left(\frac{3}{4e}\right)|\boldsymbol{\xi} - \boldsymbol{u}|^2, \tag{3.46}$$

but the derivatives in (3.45) are not straightforward, with the exception of

$$\frac{\partial \ln f^{(0)}}{\partial \xi_\alpha} = -\frac{3}{4e}\frac{\partial}{\partial \xi_\alpha}\left(\xi_\beta\xi_\beta - 2\xi_\beta u_\beta + u_\beta u_\beta\right) = -\frac{3v_\alpha}{2e}. \tag{3.47a}$$

The equilibrium distribution function $f^{(0)}$ is uniquely determined by the conserved quantities of density, momentum, and energy, i.e.

$$f^{(0)} = f^{(0)}(\rho(\boldsymbol{x},t), \boldsymbol{u}(\boldsymbol{x},t), e(\boldsymbol{x},t), \boldsymbol{\xi}).$$

The dependence in time and space is only through the conserved quantities, and we may therefore use the chain rule for the time and space derivatives,

$$\frac{\partial \ln f^{(0)}}{\partial t} = \frac{\partial \ln f^{(0)}}{\partial \rho}\frac{\partial \rho}{\partial t} + \frac{\partial \ln f^{(0)}}{\partial u_\beta}\frac{\partial u_\beta}{\partial t} + \frac{\partial \ln f^{(0)}}{\partial e}\frac{\partial e}{\partial t}, \tag{3.47b}$$

$$\frac{\partial \ln f^{(0)}}{\partial x_\alpha} = \frac{\partial \ln f^{(0)}}{\partial \rho}\frac{\partial \rho}{\partial x_\alpha} + \frac{\partial \ln f^{(0)}}{\partial u_\beta}\frac{\partial u_\beta}{\partial x_\alpha} + \frac{\partial \ln f^{(0)}}{\partial e}\frac{\partial e}{\partial x_\alpha}. \tag{3.47c}$$

These derivatives of $\ln f^{(0)}$ can be easily resolved,

$$\frac{\partial \ln f^{(0)}}{\partial \rho} = \frac{\partial}{\partial \rho}\ln\rho = \frac{1}{\rho}, \tag{3.47d}$$

$$\frac{\partial \ln f^{(0)}}{\partial u_\beta} = -\frac{3}{4e}\frac{\partial}{\partial u_\beta}\left(\xi_\alpha\xi_\alpha - 2\xi_\alpha u_\alpha + u_\alpha u_\alpha\right) = \frac{3v_\beta}{2e}, \tag{3.47e}$$

$$\frac{\partial \ln f^{(0)}}{\partial e} = -\frac{\partial}{\partial e}\left(\frac{3|\boldsymbol{v}|^2}{4e} + \frac{3}{2}\ln e\right) = \frac{1}{e}\left(\frac{3|\boldsymbol{v}|^2}{4e} - \frac{3}{2}\right). \tag{3.47f}$$

Inserting all of (3.47) into (3.45), we find

$$\frac{f^{(1)}}{f^{(0)}} = -\tau\left[\frac{1}{\rho}\left(\frac{\partial\rho}{\partial t} + (u_\alpha + v_\alpha)\frac{\partial\rho}{\partial x_\alpha}\right) + \frac{3v_\beta}{2e}\left(\frac{\partial u_\beta}{\partial t} + (u_\alpha + v_\alpha)\frac{\partial u_\beta}{\partial x_\alpha}\right) + \frac{1}{e}\left(\frac{3|\boldsymbol{v}|^2}{4e} - \frac{3}{2}\right)\left(\frac{\partial e}{\partial t} + (u_\alpha + v_\alpha)\frac{\partial e}{\partial x_\alpha}\right) - \frac{3}{2\rho e}F_\alpha v_\alpha\right]. \quad (3.48)$$

The time derivatives may be replaced using the conservation equations. As we are working at the $\mathcal{O}(Kn^0)$ level in the Boltzmann equation, we must use the conservation equations that apply at this level, i.e. the Euler equations found in section 3.7. On material derivative form, the full set of Euler equations are

$$\left(\frac{\partial}{\partial t} + u_\alpha\frac{\partial}{\partial x_\alpha}\right)\rho = -\rho\frac{\partial u_\alpha}{\partial x_\alpha},$$
$$\left(\frac{\partial}{\partial t} + u_\alpha\frac{\partial}{\partial x_\alpha}\right)u_\beta = \frac{1}{\rho}\left(-\frac{\partial p}{\partial x_\beta} + F_\beta\right) = \frac{1}{\rho}\left(-\frac{2\rho}{3}\frac{\partial e}{\partial x_\beta} - \frac{2e}{3}\frac{\partial\rho}{\partial x_\beta} + F_\beta\right),$$
$$\left(\frac{\partial}{\partial t} + u_\alpha\frac{\partial}{\partial x_\alpha}\right)e = -\frac{p}{\rho}\frac{\partial u_\alpha}{\partial x_\alpha} = -\frac{2e}{3}\frac{\partial u_\alpha}{\partial x_\alpha}.$$

Inserting this into (3.48), we get

$$\frac{f^{(1)}}{f^{(0)}} = -\tau\left[-\frac{\partial u_\alpha}{\partial x_\alpha} + \frac{v_\alpha}{\rho}\frac{\partial\rho}{\partial x_\alpha} + \frac{3v_\beta}{2e}\left(-\frac{2}{3}\frac{\partial e}{\partial x_\beta} - \frac{2e}{3\rho}\frac{\partial\rho}{\partial x_\beta} + \frac{F_\beta}{\rho} + v_\alpha\frac{\partial u_\beta}{\partial x_\alpha}\right) + \left(\frac{3|\boldsymbol{v}|^2}{4e} - \frac{3}{2}\right)\left(-\frac{2}{3}\frac{\partial u_\alpha}{\partial x_\alpha} + \frac{v_\alpha}{e}\frac{\partial e}{\partial x_\alpha}\right) - \frac{3}{2\rho e}F_\alpha v_\alpha\right].$$

Some of the terms in this equation cancel, and we are left with

$$\frac{f^{(1)}}{f^{(0)}} = -\tau\left[\left(\frac{3|\boldsymbol{v}|^2}{4e} - \frac{5}{2}\right)\frac{v_\alpha}{e}\frac{\partial e}{\partial x_\alpha} + \frac{3}{2e}\left(v_\alpha v_\beta\frac{\partial u_\beta}{\partial x_\alpha} - \frac{|\boldsymbol{v}|^2}{3}\frac{\partial u_\alpha}{\partial x_\alpha}\right)\right]. \quad (3.50)$$

The last parenthesis is a familiar tensor in a different form. Switching the indices in one half of the first term and expanding the second, we get

$$\left(v_\alpha v_\beta\frac{\partial u_\beta}{\partial x_\alpha} - \frac{|\boldsymbol{v}|^2}{3}\frac{\partial u_\alpha}{\partial x_\alpha}\right) = v_\alpha v_\beta\left[\frac{1}{2}\left(\frac{\partial u_\beta}{\partial x_\alpha} + \frac{\partial u_\alpha}{\partial x_\beta}\right) - \frac{1}{3}\delta_{\alpha\beta}\frac{\partial u_\gamma}{\partial x_\gamma}\right] = v_\alpha v_\beta S_{\alpha\beta},$$

where

$$S_{\alpha\beta} = \frac{1}{2}\left(\frac{\partial u_\beta}{\partial x_\alpha} + \frac{\partial u_\alpha}{\partial x_\beta}\right) - \frac{1}{3}\delta_{\alpha\beta}\frac{\partial u_\gamma}{\partial x_\gamma} \quad (3.51)$$

is the symmetric *strain rate tensor*. The trace of this tensor, which may be found by multiplying with $\delta_{\alpha\beta}$, is zero.

Finally, we have the first-order perturbation of the distribution function in a reasonably simple form,

$$\boxed{f^{(1)} = -\tau f^{(0)} \left[\frac{1}{e} \frac{\partial e}{\partial x_\alpha} \left(\frac{3|\boldsymbol{v}|^2}{4e} - \frac{5}{2} \right) v_\alpha + \frac{3S_{\alpha\beta}}{2e} v_\alpha v_\beta \right].} \tag{3.52}$$

As predicted, $f^{(1)}/f^{(0)}$ is $\mathcal{O}(Kn)$. This can be shown by performing a nondimensionalisation such as the one at the start of section 3.8.

3.8.2 Finding the moment perturbations

Now that we know $f^{(1)}$, we can find the first-order moment perturbations $\boldsymbol{\sigma}^{(1)}$ and $\boldsymbol{q}^{(1)}$ directly using (3.43c).

First we find the first-order perturbation of the stress tensor,

$$\begin{aligned} \sigma_{\alpha\beta}^{(1)} &= -\int v_\alpha v_\beta f^{(1)} \, \mathrm{d}\boldsymbol{\xi} \\ &= \tau \left[\frac{1}{e} \frac{\partial e}{\partial x_\alpha} \int \left(\frac{3|\boldsymbol{v}|^2}{4e} - \frac{5}{2} \right) v_\alpha v_\beta v_\gamma f^{(0)} \, \mathrm{d}\boldsymbol{\xi} + \frac{3S_{\gamma\delta}}{2e} \int v_\alpha v_\beta v_\gamma v_\delta f^{(0)} \, \mathrm{d}\boldsymbol{\xi} \right]. \end{aligned}$$

By (3.19d) and (3.19f), the first integral disappears. By (3.19e), the second integral is

$$\int v_\alpha v_\beta v_\gamma v_\delta f^{(0)} \, \mathrm{d}\boldsymbol{\xi} = \tfrac{4}{9} \rho e^2 \left(\delta_{\alpha\beta}\delta_{\gamma\delta} + \delta_{\alpha\gamma}\delta_{\beta\delta} + \delta_{\alpha\delta}\delta_{\beta\gamma} \right).$$

Since the strain rate tensor $S_{\gamma\delta}$ is traceless, the first term in the parenthesis becomes zero. The two others, applied to $S_{\gamma\delta}$, together give $2S_{\alpha\beta}$. Thus, the first-order perturbation to the stress tensor is

$$\sigma_{\alpha\beta}^{(1)} = \tfrac{4}{3} \rho e \tau S_{\alpha\beta} = p\tau \left(\frac{\partial u_\beta}{\partial x_\alpha} + \frac{\partial u_\alpha}{\partial x_\beta} - \frac{2}{3} \delta_{\alpha\beta} \frac{\partial u_\gamma}{\partial x_\gamma} \right). \tag{3.53}$$

This corresponds exactly to the deviatoric stress tensor $\sigma'_{\alpha\beta}$ in (2.19d) with a shear viscosity

$$\mu = \tfrac{2}{3} \rho e \tau = p\tau = \rho R T \tau \tag{3.54}$$

and a bulk viscosity $\mu_\mathrm{B} = 0$.

Next, we find the the first-order heat flux perturbation,

$$\begin{aligned} q_\alpha^{(1)} = \tfrac{1}{2} \int v_\alpha |\boldsymbol{v}|^2 f^{(1)} \, \mathrm{d}\boldsymbol{\xi} = -\frac{\tau}{2} \Bigg[\frac{1}{e} \frac{\partial e}{\partial x_\beta} \int \left(\frac{3|\boldsymbol{v}|^2}{4e} - \frac{5}{2} \right) |\boldsymbol{v}|^2 v_\alpha v_\beta f^{(0)} \, \mathrm{d}\boldsymbol{\xi} \\ + \frac{3S_{\beta\gamma}}{2e} \int |\boldsymbol{v}|^2 v_\alpha v_\beta v_\gamma f^{(0)} \, \mathrm{d}\boldsymbol{\xi} \Bigg]. \end{aligned}$$

By (3.19f), the second integral is zero. The first part of the first integral is

$$\frac{3}{4e} \int |\boldsymbol{v}|^4 v_\alpha v_\beta f^{(0)} \, \mathrm{d}\boldsymbol{\xi} = \frac{3}{4e} \tfrac{1}{3} \delta_{\alpha\beta} \int |\boldsymbol{v}|^6 f^{(0)} \, \mathrm{d}\boldsymbol{\xi} = \tfrac{70}{9} \delta_{\alpha\beta} \rho e^2$$

The last equality can most easily be shown by inserting for $f^{(0)}$ and performing the integral using the spherical symmetry of the integrand. Finally we have the second part of the first integral, which can similarly be shown to be

$$-\tfrac{5}{2}\int |\boldsymbol{v}|^2 v_\alpha v_\beta f^{(0)}\,\mathrm{d}\boldsymbol{\xi} = -\tfrac{5}{6}\delta_{\alpha\beta}\int |\boldsymbol{v}|^4 f^{(0)}\,\mathrm{d}\boldsymbol{\xi} = -\tfrac{50}{9}\delta_{\alpha\beta}\rho e^2.$$

Thus, the first-order heat flux perturbation is

$$q_\alpha^{(1)} = -\tfrac{10}{9}\rho e\tau\frac{\partial e}{\partial x_\alpha}. \tag{3.55}$$

3.8.3 The Navier-Stokes-Fourier model

Now that we know the first-order perturbations $\sigma^{(1)}$ and $q^{(1)}$, we have the fluid model one order higher in Kn than the Euler model. We reabsorb the smallness parameter ϵ, letting $\epsilon Kn \to Kn$. Then we approximate $\boldsymbol{\sigma} \simeq \boldsymbol{\sigma}^{(0)} + \boldsymbol{\sigma}^{(1)}$ and $\boldsymbol{q} \simeq \boldsymbol{q}^{(0)} + \boldsymbol{q}^{(1)}$.

Inserting this approximate stress tensor into the Cauchy momentum equation (3.29), we find exactly the Navier-Stokes mass conservation equation

$$\boxed{\frac{\partial \rho u_\alpha}{\partial t} + \frac{\partial \rho u_\alpha u_\beta}{\partial x_\beta} = \frac{\partial}{\partial x_\beta}\left(-\delta_{\alpha\beta}p + \sigma'_{\alpha\beta}\right) + F_\alpha,} \tag{3.56}$$

with $\sigma'_{\alpha\beta}$ given by (3.53). This corresponds exactly to (2.19b) in conservation form, but with known values of the shear viscosity $\mu = p\tau$ and bulk viscosity $\mu_\mathrm{B} = 0$. This confirms that there is zero bulk viscosity for a monatomic dilute gas.

Inserting the stress tensor and heat flux vector into the general energy conservation equation (3.33), using (3.11) to get a temperature derivative in the heat flux, we find the energy equation

$$\boxed{\frac{\partial \rho e}{\partial t} + \frac{\partial \rho u_\alpha e}{\partial x_\alpha} = \left(-\delta_{\alpha\beta}p + \sigma'_{\alpha\beta}\right)\frac{\partial u_\beta}{\partial x_\alpha} + \frac{\partial}{\partial x_\alpha}\kappa\frac{\partial T}{\partial x_\alpha}} \tag{3.57}$$

with a thermal conductivity

$$\kappa = \tfrac{5}{3}\rho e R\tau = \tfrac{5}{2}pR\tau = \tfrac{5}{2}\rho R^2 T\tau. \tag{3.58}$$

These two equations, together with the continuity equation (3.25), form the Navier-Stokes-Fourier model previously in (2.19). This model may be derived either using kinetic theory as done here, or from continuum mechanics. In the continuum derivation, the transport coefficients μ and

κ are empirical material parameters, whereas with the kinetic derivation the transport coefficients are given only through the relaxation time τ.

The highly simplified BGK model of collisions gives the same form of the macroscopic equations as the full Boltzmann collision operator; in fact, this can be seen as a requirement for any collision model. However, from any derivation based in kinetic theory, the transport coefficients are determined by the choice of collision operator. In our case the relaxation time τ comes from the BGK operator; Boltzmann's original collision operator results in different transport coefficients, given by other parameters. In fact, assuming different intermolecular forces in Boltzmann's operator would change the resulting transport coefficients slightly [62].

Also, an underlying assumption of this entire chapter is that the gas is monatomic. It is also possible to describe polyatomic gases in kinetic theory [54–58]. This requires a different collision model and results in different transport coefficients. However, the kinetic theory of polyatomic gases is significantly more complicated.

From the viscosity (3.54), the thermal conductivity (3.58), and the heat capacity at constant pressure (3.13), we can find the *Prandtl number*

$$Pr = \frac{c_p \mu}{\kappa} = 1. \tag{3.59}$$

This is a weakness of the BGK collision operator; as mentioned previously, Boltzmann's original collision operator results in transport coefficients that give a Prandtl number of $Pr \simeq 2/3$, a value which corresponds well with measurements on monatomic gases [58]. However, this is not a problem for isothermal lattice Boltzmann models, where the thermal conductivity is irrelevant.

3.8.4 Higher-order Boltzmann equation approximations

In the previous sections, we found the first-order perturbation $f^{(1)}$ to the distribution function, and its corresponding first-order moment perturbations $\boldsymbol{\sigma}^{(1)}$ and $\boldsymbol{q}^{(1)}$.

Of course, it is possible to go further, finding $f^{(2)}$, $\boldsymbol{\sigma}^{(2)}$, and $\boldsymbol{q}^{(2)}$. While we get the Euler model by assuming $f \simeq f^{(0)}$ and the Navier-Stokes-Fourier model by assuming $f \simeq f^{(0)} + f^{(1)}$, the assumption of $f \simeq f^{(0)} + f^{(1)} + f^{(2)}$ gives us an even more detailed picture, called the *Burnett model*. A far tougher derivation leads to moment perturbations $\boldsymbol{\sigma}^{(2)}$ and $\boldsymbol{q}^{(2)}$ which contain several new terms and several new transport coefficients that cannot be predicted by continuum theory [57, Ch. 15].

Burnett model
The fluid model found by taking Chapman-Enskog one step further than the Navier-Stokes-Fourier model

Since $f^{(2)}/f^{(0)}$ is $\mathcal{O}(Kn^2)$, the extra terms of the Burnett model are usually negligible, as $Kn \ll 1$ in most flows of interest. However, the differences between the Navier-Stokes-Fourier model and the Burnett model are significant for the propagation of sound waves at very high fre-

quencies, where the acoustic Knudsen number given from the wavelength λ as $Kn = x_{\text{mfp}}/\lambda$ goes towards one.

In fact, measurements on plane sound wave propagation in rarefied noble gases have indicated that the Burnett model gives a better description than the Navier-Stokes-Fourier at such high frequencies [27, 63]. The two models depart significantly in their predictions of sound speed and sound wave absorption at $Kn \sim 0.1$, and the Burnett model agrees very well with measurements of sound propagation in noble gases up to $Kn \sim 1$.

As it is mathematically very tough to get to even the Burnett level, approximations of even higher order can instead be found through particular assumptions on the form of f. Pioneering work for plane sound waves, where f was assumed to be of the form of an infinitesimal forced plane wave around an equilibrium state, was done by Wang Chang and Uhlenbeck [64] (later collected in [65]). It was later found that even higher-order approximations to the Boltzmann equation paradoxically gives a *poorer* agreement with experiments than the Burnett model [27].

A very high-order approximation to the Boltzmann equation was later found for the propagation of plane sound waves, of the form of a power series in Kn up to $\mathcal{O}(Kn^{32})$ [66]. However, the series coefficients increase so rapidly that the series diverges unless Kn is small. This is an example of an asymptotic series, which is non-convergent unless a parameter tends to a certain limit (in this case $Kn \to 0$), and which usually is most useful and accurate when truncated to a small number of terms. Still, such series can often be approximated beyond their range of convergence, and in this case the Shanks transformation gave promising results [66].

Similarly, it has been suggested that the Chapman-Enskog expansion $f = f^{(0)} + f^{(1)} + f^{(2)} + \ldots$ itself may be asymptotic [57, Ch. 15]. If so, truncating the expansion earlier could give a better solution than truncating it later. For sound wave propagation, it seems that the Burnett model gives the best agreement, although it is only significantly better than the Navier-Stokes-Fourier model for about an order of magnitude in Kn. The agreement between the Burnett model and measurements in this single case might also be only a fortunate coincidence and cannot be taken as absolute proof that the Burnett model is generally superior.

Since the Navier-Stokes-Fourier model may be derived independently either from continuum theory, the results of the Chapman-Enskog expansion to first order can be trusted. However, the Burnett model, or any higher-order models for that matter, cannot be found from any other derivation, and have therefore historically been viewed with some suspicion [67]. Since the Burnett model differs very little from the Navier-Stokes-Fourier model at low Kn, the difference is negligible in most practical cases.

Other approaches than the Chapman-Enskog expansion can also be

used to find macroscopic equations from the Boltzmann equation. Some of the resulting models have been seen to at least agree well with measurements of the speed of sound over the entire range of Kn [68].

3.9 Boltzmann's $\mathcal{H}$-theorem

One thermodynamic quantity which has not been discussed yet in this chapter is entropy. It was shown by Boltzmann himself that a quantity $\mathcal{H}$ can be found from the distribution function f which has many of the same properties as thermodynamic entropy. $\mathcal{H}$ can only evolve in one direction, and it reaches an extremum when the system is at an equilibrium. It was later shown for ideal gases that $\mathcal{H}$ is proportional to the entropy.

The first step in finding $\mathcal{H}$ is to see from the chain rule that

$$\frac{\partial}{\partial t} f \ln f = (1 + \ln f) \frac{\partial f}{\partial t}.$$

This is valid for any derivative in the Boltzmann equation, not just $\partial/\partial t$. Thus, multiplying the Boltzmann equation with $(1 + \ln f)$, it thus becomes

$$\left(\frac{\partial}{\partial t} + \xi_\alpha \frac{\partial}{\partial x_\alpha} + \frac{F_\alpha}{\rho} \frac{\partial}{\partial \xi_\alpha} \right) f \ln f = (1 + \ln f)\, \Omega(f).$$

Integrating this over velocity space, we find

$$\frac{\partial}{\partial t} \int f \ln f \, \mathrm{d}\boldsymbol{\xi} + \frac{\partial}{\partial x_\alpha} \int \xi_\alpha f \ln f \, \mathrm{d}\boldsymbol{\xi} = \int \ln f \, \Omega(f) \, \mathrm{d}\boldsymbol{\xi}. \tag{3.60}$$

The force term disappears similarly to (3.24), as $f \ln f \to -f$ when $f \to 0$ as $\boldsymbol{\xi} \to \infty$. Also, one term on the right side disappears by mass conservation, (3.21a).

Equation (3.60) is like a conservation equation for the quantity $f \ln f$, but with a source term on the right side. Using the BGK collision operator, the right side can be shown to be

$$\begin{aligned} \int \ln f \, \Omega(f) \, \mathrm{d}\boldsymbol{\xi} &= \int \ln \left(\frac{f}{f^{(0)}} \right) \Omega(f) \, \mathrm{d}\boldsymbol{\xi} + \int \ln f^{(0)} \, \Omega(f) \, \mathrm{d}\boldsymbol{\xi} \\ &= \frac{1}{\tau} \int \ln \left(\frac{f}{f^{(0)}} \right) \left(f^{(0)} - f \right) \mathrm{d}\boldsymbol{\xi} \\ &= \frac{1}{\tau} \int f^{(0)} \ln \left(\frac{f}{f^{(0)}} \right) \left(1 - \frac{f}{f^{(0)}} \right) \mathrm{d}\boldsymbol{\xi} \leq 0. \end{aligned} \tag{3.61}$$

Here, the integral $\int \ln f^{(0)} \, \Omega(f) \, \mathrm{d}\boldsymbol{\xi}$ can be shown to disappear by inserting for $f^{(0)}$ and using the mass and energy conservation properties of $\Omega(f)$. The last inequality follows from the identity $(1 - x) \ln x \leq 0$ for $x > 0$. For $x = 1$ (i.e. $f = f^{(0)}$), it is zero.

Thus, (3.60) is equivalent to

$$\frac{\partial \mathcal{H}}{\partial t} + \frac{\partial \mathcal{H}_\alpha}{\partial x_\alpha} \leq 0, \tag{3.62}$$

where

$$\mathcal{H} = \int f \ln f \, \mathrm{d}\boldsymbol{\xi}, \qquad \mathcal{H}_\alpha = \int \xi_\alpha f \ln f \, \mathrm{d}\boldsymbol{\xi}. \tag{3.63}$$

Here, $\mathcal{H}_\alpha$ is the flux of $\mathcal{H}$, similarly to how $\rho \boldsymbol{u}$ is the flux of ρ. From the inequality, we see that $\mathcal{H}$ is not necessarily conserved like mass in the continuity equation, but will decrease if the system is not at equilibrium. However, as mentioned previously, the inequality in (3.62) becomes an equality at equilibrium. This means that $\mathcal{H}$ will decrease until the system reaches an equilibrium, where $\mathcal{H}$ reaches its lowest value. This is very similar to how thermodynamic entropy increases until the system reaches an equilibrium state.

In fact, for an ideal gas $\mathcal{H}$ is proportional to the *entropy density* ρs [58, 69],

Entropy density, ρs
Entropy ("mixedupness") per physical volume in $\mathrm{J/K\,m^3}$

$$\rho s = -\frac{k_\mathrm{B}}{m} \mathcal{H}. \tag{3.64}$$

However, for a non-ideal gas, where the equation of state is affected by intermolecular forces, this equality does not hold [69].

The inequality (3.62) can also be shown from Boltzmann's original collision operator. In fact, it is an important criterion for any collision operator, in addition to the conservation criteria discussed in section 3.5, as it states that molecular collisions will invariably drive the distribution of particles towards an equilibrium.

4 The lattice Boltzmann method

In the last chapter we derived the Boltzmann equation and saw that the familiar equations of fluid mechanics follow. In practice, is is extremely hard to find analytical solutions for the Boltzmann equation, except in trivial cases like the spatially homogeneous example in section 3.5 and other simplified cases [70].

In fact, it is also extremely hard to find solutions for the general equations of fluid mechanics, so they are simplified in almost every case. In engineering fluid mechanics, the fluid is often considered incompressible (i.e. the density ρ is considered constant). In acoustics, viscosity is usually neglected and the equations are linearised so that the flow field is considered as a small perturbation around a rest state.

However, if we somehow could find a solution for the Boltzmann equation, we would simultaneously be finding a solution to the less general but more familiar equations that follow from it. Since it is usually too difficult to attack the Boltzmann equation analytically, we must try to solve it numerically instead.

When discretising most transport equations, it is sufficient to discretise in only physical space and time. With the Boltzmann equation, however, the main variable f is a function of coordinates in physical space, velocity space, and time. We must therefore discretise it in two separate steps. First, we restrict the continuous space of velocities $\boldsymbol{\xi}$ to a finite discrete set $\boldsymbol{\xi}_i$, a set which should ideally be as small as possible. Then, we simultaneously discretise in space and time. The result of this discretisation process can be quite conveniently implemented on a computer as the lattice Boltzmann method.

There are many approaches to this discretisation, but in this chapter we will emphasise clarity and brevity over generality. Throughout, as necessary, we will refer to articles with other, more general derivations.

Isothermal fluid
A fluid with constant temperature

In this chapter, we will derive the simplest and most common variety of the LB method: The isothermal, ideal gas, forceless variety. As the fluid is isothermal with a constant temperature T_0, the ideal gas equation of state is $p = \rho R T_0$. From this follows a constant speed of sound and a simplified equation of state which does not involve the temperature,

$$c_0^2 = \left(\frac{\partial p}{\partial \rho}\right) = \frac{k_\mathrm{B} T_0}{m} \quad \Rightarrow \quad p = c_0^2 \rho. \tag{4.1}$$

Comparing this with the physical isentropic equation of state (2.23) and speed of sound (2.24), we find that this isothermal equation of state corresponds to the physical assumption of $\gamma = 1$. From (2.47), this itself implies an infinite number of inner degrees of freedom in the molecules that make up the gas.

4.1 The discrete-velocity Boltzmann equation

The first step in discretising the Boltzmann equation is to discretise velocity space. One very general method for this is based on approximating $f^{(0)}$ using a truncated basis of Hermite polynomials and a Gauss-Hermite quadrature [72, 73]. The order of the quadrature determines the number of velocities $\boldsymbol{\xi}_i$ required. With sufficiently high orders, this method can preserve the behaviour of the Boltzmann equation to arbitrary level in the Chapman-Enskog expansion [72]. However, higher levels require larger numbers of velocities, which makes the lattice Boltzmann method more difficult to implement and more resource demanding.

Hermite polynomials
An orthogonal polynomial sequence useful in kinetic theory [53, 71, 72]

Gauss-Hermite quadrature
An approximation method for certain integrals: $\int e^{-x^2} f(x)\,\mathrm{d}x \approx \sum_i w_i f(x_i)$

Instead of this general method, we will use a mathematically simpler method in this derivation. The first step is to approximate the Maxwell-Boltzmann distribution (3.18) by expanding it up to $\mathcal{O}(\boldsymbol{u}^2)$,

$$\begin{aligned} f^{(0)}(\boldsymbol{x},\boldsymbol{\xi},t) &= \frac{\rho}{(2\pi c_0^2)^{3/2}}\,\mathrm{e}^{-(\xi_\alpha\xi_\alpha - 2\xi_\alpha u_\alpha + u_\alpha u_\alpha)/2c_0^2} \\ &\approx \frac{\rho}{(2\pi c_0^2)^{3/2}}\,\mathrm{e}^{-\xi_\alpha\xi_\alpha/2c_0^2}\left(1 + \frac{\xi_\alpha u_\alpha}{c_0^2} + \frac{(\xi_\alpha u_\alpha)^2}{2c_0^4} - \frac{u_\alpha u_\alpha}{2c_0^2}\right). \end{aligned}$$

Here, (4.1) has been used, and terms of $\mathcal{O}(\boldsymbol{u}^3)$ have been neglected. While stopping at $\mathcal{O}(\boldsymbol{u}^2)$ may seem somewhat arbitrary, the following subsections will motivate this choice.

Next, we discretise velocity space, restricting $\boldsymbol{\xi}$ to a finite set of velocities $\boldsymbol{\xi}_i$. Thus, the distribution function $f(\boldsymbol{x},\boldsymbol{\xi},t)$ becomes $f_i(\boldsymbol{x},t)$, representing the density at $(\boldsymbol{x},t)$ of particles with velocity $\boldsymbol{\xi}_i$. We also replace the coefficient $\mathrm{e}^{-\xi_\alpha\xi_\alpha/2c_0^2}/(2\pi c_0^2)^{3/2}$ in front of the expansion above with a single weighting coefficient w_i, ending up with the classic [74] *discrete equilibrium distribution*

$$\boxed{f_i^{(0)} = \rho w_i\left(1 + \frac{\xi_{i\alpha}u_\alpha}{c_0^2} + \frac{\xi_{i\alpha}u_\alpha\xi_{i\beta}u_\beta}{2c_0^4} - \frac{u_\alpha u_\alpha}{2c_0^2}\right).} \tag{4.2}$$

This is arguably the optimally stable isothermal polynomial discrete equilibrium distribution [75].

Velocity set
A discrete set of velocity vectors $\boldsymbol{\xi}_i$ and accompanying weighting coefficients w_i

We will see in the following subsection how the *velocity sets* defined

by $\boldsymbol{\xi}_i$ and w_i must be constrained in order to reproduce hydrodynamics correctly.

Having discretised velocity space and using the the discrete analogue of the BGK operator (3.22), the Boltzmann equation becomes the *discrete-velocity Boltzmann equation* (DVBE),

$$\boxed{\frac{\partial f_i}{\partial t} + \xi_{i\alpha}\frac{\partial f_i}{\partial x_\alpha} = -\frac{1}{\tau}\left(f_i - f_i^{(0)}\right).} \tag{4.3}$$

4.1.1 Moments and constraints

Of course, the velocity set cannot be chosen randomly. For the DVBE to give the same mass and momentum conservation equations as found from the continuous Boltzmann equation in section 3.8, we will show in the next subsection that the zeroth to third moments of $f_i^{(0)}$ must be equal to those of $f^{(0)}$, i.e.

$$\sum_i f_i^{(0)}(\boldsymbol{x},t) = \rho(\boldsymbol{x},t), \tag{4.4a}$$

$$\sum_i \xi_{i\alpha} f_i^{(0)}(\boldsymbol{x},t) = \rho \boldsymbol{u}(\boldsymbol{x},t), \tag{4.4b}$$

$$\sum_i \xi_{i\alpha}\xi_{i\beta} f_i^{(0)}(\boldsymbol{x},t) = \Pi^{(0)}_{\alpha\beta}(\boldsymbol{x},t), \tag{4.4c}$$

$$\sum_i \xi_{i\alpha}\xi_{i\beta}\xi_{i\gamma} f_i^{(0)}(\boldsymbol{x},t) = \Pi^{(0)}_{\alpha\beta\gamma}(\boldsymbol{x},t). \tag{4.4d}$$

We will now show that these equalities give us a set of constraints (4.11) on the velocity set. As we soon shall see, the last of these equalities can only be approximately fulfilled with $f_i^{(0)}$ given as in (4.2). The result of this discrepancy will be a largely insignificant error term in the momentum equation.

For (4.4a) to hold,

$$\begin{aligned}\rho &= \sum_i f_i^{(0)} \\ &= \rho\left[\sum_i w_i + \tfrac{u_\alpha}{c_0^2}\sum_i w_i\xi_{i\alpha} + \tfrac{u_\alpha u_\beta}{2c_0^2}\left(\tfrac{1}{c_0^2}\sum_i w_i\xi_{i\alpha}\xi_{i\beta} - \delta_{\alpha\beta}\sum_i w_i\right)\right],\end{aligned}$$

i.e. the contents of the square brackets must equal 1. Given that w_i are

constants, this holds only if

$$\sum_i w_i = 1, \tag{4.5}$$

$$\sum_i w_i \xi_{i\alpha} = 0, \tag{4.6}$$

$$\sum_i w_i \xi_{i\alpha}\xi_{i\beta} = c_0^2 \delta_{\alpha\beta}. \tag{4.7}$$

These are three of the constraints on the velocity vectors $\boldsymbol{\xi_i}$ and the weighting coefficients w_i. The other moments in (4.4) will supply us with additional such constraints.

Similarly, for (4.4b) to hold,

$$\begin{aligned}\rho u_\alpha &= \sum_i \xi_{i\alpha} f_i^{(0)} \\ &= \rho \Bigg[\underbrace{\frac{u_\beta}{c_0^2} \sum_i w_i \xi_{i\alpha}\xi_{i\beta}}_{=u_\beta \delta_{\alpha\beta} = u_\alpha} + \left(1 - \frac{u_\beta u_\beta}{2c_0^2}\right) \underbrace{\sum_i w_i \xi_{i\alpha}}_{=0} + \frac{u_\beta u_\gamma}{2c_0^4} \sum_i w_i \xi_{i\alpha}\xi_{i\beta}\xi_{i\gamma} \Bigg],\end{aligned}$$

which only holds if

$$\sum_i w_i \xi_{i\alpha}\xi_{i\beta}\xi_{i\gamma} = 0. \tag{4.8}$$

From (3.27), (3.34), and (4.1) we find

$$\Pi_{\alpha\beta}^{(0)} = \int \xi_\alpha \xi_\beta f^{(0)} \, \mathrm{d}\boldsymbol{\xi} = \rho u_\alpha u_\beta + \rho c_0^2 \delta_{\alpha\beta},$$

and thus we require

$$\begin{aligned}&\rho u_\alpha u_\beta + \rho c_0^2 \delta_{\alpha\beta} = \sum_i \xi_{i\alpha}\xi_{i\beta} f_i^{(0)} \\ &= \rho \left[\left(1 - \frac{u_\gamma u_\gamma}{2c_0^2}\right) \underbrace{\sum_i w_i \xi_{i\alpha}\xi_{i\beta}}_{=c_0^2\delta_{\alpha\beta}} + \frac{u_\gamma}{c_0^2} \underbrace{\sum_i w_i \xi_{i\alpha}\xi_{i\beta}\xi_{i\gamma}}_{=0} + \frac{u_\gamma u_\delta}{2c_0^4} \sum_i w_i \xi_{i\alpha}\xi_{i\beta}\xi_{i\gamma}\xi_{i\delta} \right].\end{aligned}$$

For this to hold,

$$\frac{u_\gamma u_\delta}{2c_0^4} \sum_i w_i \xi_{i\alpha}\xi_{i\beta}\xi_{i\gamma}\xi_{i\delta} - \frac{u_\gamma u_\gamma}{2} \delta_{\alpha\beta} = \rho u_\alpha u_\beta,$$

which gives us our fifth constraint,

$$\sum_i w_i \xi_{i\alpha}\xi_{i\beta}\xi_{i\gamma}\xi_{i\delta} = c_0^4 \left(\delta_{\alpha\beta}\delta_{\gamma\delta} + \delta_{\alpha\gamma}\delta_{\beta\delta} + \delta_{\alpha\delta}\delta_{\beta\gamma} \right). \tag{4.9}$$

Using (3.19c), the third moment of $f^{(0)}$ is

$$\begin{aligned}\Pi^{(0)}_{\alpha\beta\gamma} &= \int \xi_\alpha\xi_\beta\xi_\gamma f^{(0)}\,\mathrm{d}\boldsymbol{\xi} \\ &= \int \left(u_\alpha u_\beta u_\gamma + u_\alpha v_\beta v_\gamma + u_\beta v_\alpha v_\gamma + u_\gamma v_\alpha v_\beta\right) f^{(0)}\,\mathrm{d}\boldsymbol{\xi} \\ &= \rho u_\alpha u_\beta u_\gamma + \rho c_0^2\left(u_\alpha\delta_{\beta\gamma} + u_\beta\delta_{\alpha\gamma} + u_\gamma\delta_{\alpha\beta}\right).\end{aligned}$$

However, as the polynomial (4.2) for $f^{(0)}$ lacks any $\mathcal{O}(\boldsymbol{u}^3)$ term, it is impossible to exactly reproduce this moment in the discrete case. The corresponding discrete moment* $\breve{\Pi}^{(0)}_{\alpha\beta\gamma}$ must therefore lack the $\rho u_\alpha u_\beta u_\gamma$ term, so that

$$\begin{aligned}\breve{\Pi}^{(0)}_{\alpha\beta\gamma} &= \sum_i \xi_{i\alpha}\xi_{i\beta}\xi_{i\gamma} f^{(0)}\,\mathrm{d}\boldsymbol{\xi} = \rho c_0^2\left(u_\alpha\delta_{\beta\gamma} + u_\beta\delta_{\alpha\gamma} + u_\gamma\delta_{\alpha\beta}\right) \\ &= \rho\sum_i w_i\xi_{i\alpha}\xi_{i\beta}\xi_{i\gamma}\left(1 - \tfrac{u_\delta u_\delta}{2c_0^2} + \tfrac{u_\delta}{c_0^2}\xi_{i\delta} + \tfrac{u_\delta u_\epsilon}{2c_0^4}\xi_{i\delta}\xi_{i\epsilon}\right).\end{aligned}$$

This gives us our sixth and final constraint,

$$\sum_i w_i\xi_{i\alpha}\xi_{i\beta}\xi_{i\gamma}\xi_{i\delta}\xi_{i\epsilon} = 0. \tag{4.10}$$

In summary, the constraints on the velocity set are

$$\sum_i w_i = 1, \tag{4.11a}$$

$$\sum_i w_i\xi_{i\alpha} = 0, \tag{4.11b}$$

$$\sum_i w_i\xi_{i\alpha}\xi_{i\beta} = c_0^2\delta_{\alpha\beta}, \tag{4.11c}$$

$$\sum_i w_i\xi_{i\alpha}\xi_{i\beta}\xi_{i\gamma} = 0, \tag{4.11d}$$

$$\sum_i w_i\xi_{i\alpha}\xi_{i\beta}\xi_{i\gamma}\xi_{i\delta} = c_0^4\left(\delta_{\alpha\beta}\delta_{\gamma\delta} + \delta_{\alpha\gamma}\delta_{\beta\delta} + \delta_{\alpha\delta}\delta_{\beta\gamma}\right), \tag{4.11e}$$

$$\sum_i w_i\xi_{i\alpha}\xi_{i\beta}\xi_{i\gamma}\xi_{i\delta}\xi_{i\epsilon} = 0. \tag{4.11f}$$

These conditions can be seen as symmetry properties of $\boldsymbol{\xi}_i$ and w_i, similar to the symmetry properties of $f^{(0)}$ in section 3.3.2. The odd moments

*We separate the notation for the moments of f_i from the notation of the moments of f by a breve accent. While the first three equilibrium moments agree in both cases (i.e. $\Pi^{(0)}_0 = \breve{\Pi}^{(0)}_0$, $\Pi^{(0)}_\alpha = \breve{\Pi}^{(0)}_\alpha$, $\Pi^{(0)}_{\alpha\beta} = \breve{\Pi}^{(0)}_{\alpha\beta}$) so that no difference in notation is required, the higher moments do not agree exactly due to the truncation of $f_i^{(0)}$ in (4.2) (i.e. $\Pi^{(0)}_{\alpha\beta\gamma} \neq \breve{\Pi}^{(0)}_{\alpha\beta\gamma}$, etc.). We will only use the accent to denote discrete moments if there is such a discrepancy.

disappear due to even symmetry, and the even moments are isotropic tensors.

These symmetry properties must be fulfilled for any DVBE to solve the conservation equations for mass and momentum. The number of conditions motivates truncating the polynomial in $f_i^{(0)}$ to $\mathcal{O}(\boldsymbol{u}^2)$: If we include higher-order terms, like some extended (e.g. thermal) LB methods require, we get more of these constraints (including one analogous to the somewhat bulky (3.19g)), which in turn requires a larger set of velocities [76, Ch. 2].

4.1.2 Moment-based Chapman-Enskog expansion

In the last subsection we saw that the zeroth to third moments of $f_i^{(0)}$ and $f^{(0)}$ are equal (to $\mathcal{O}(\boldsymbol{u}^2)$) if the symmetry conditions (4.11) on $\boldsymbol{\xi}_i$ and w_i are upheld. We will now prove that this is sufficient for the DVBE (4.3) to behave essentially identically to the Boltzmann equation (3.20) to the Navier-Stokes level.

The Chapman-Enskog expansion, previously seen in section 3.8, is used for this proof. However, we will use a different method here than previously. In section 3.8, the first perturbation of the distribution function, $f^{(1)}$, was found from $f^{(0)}$, and subsequently used to find the stress tensor and heat flux vector perturbations $\boldsymbol{\sigma}^{(1)}$ and $\boldsymbol{q}^{(1)}$. In the method to be used here, we find relations for the unknown moments of $f_i^{(1)}$ through the known moments of $f_i^{(0)}$, using a derivation similar to [77].

In this moment-based expansion, a new mathematical trick must be used in addition to the perturbation expansion $f_i = f_i^{(0)} + \epsilon f_i^{(1)} + \epsilon^2 f_i^{(2)} + \ldots$. In order to usefully close the system of equations for the moments, we need to perform a multiple-scale expansion of time in orders of Kn, letting $t \to t_1 + \epsilon^{-1} t_2 + \ldots$ [78, Ch. 1]. This technique is used in general perturbation theory to deal with expansions that result in unbounded terms at each order [79, Ch. 11]. A common explanation is that t_1 as a time scale dealing with fast phenomena like advection and t_2 as a time scale dealing with slower phenomena like diffusion.

Instead of expanding as $\tau \to \epsilon\tau$ as in section 3.8, we expand the derivatives as

$$\frac{\partial}{\partial t} \to \epsilon \frac{\partial}{\partial t_1} + \epsilon^2 \frac{\partial}{\partial t_2} + \ldots , \qquad \frac{\partial}{\partial x_\alpha} \to \epsilon \frac{\partial}{\partial x_\alpha}, \tag{4.12}$$

which is comparable to multiplying with ϵ in (3.41). This will not make a significant difference here, but will be convenient later when expanding the fully discrete lattice Boltzmann equation.

While the time derivative expansion is necessary for the Chapman-Enskog expansion to work, the multiple-scale expansion of time makes

little physical sense. Another, more physical, motivation for the derivative expansion is that different phenomena affect the time derivative at different orders in the Knudsen number. The time derivative must therefore be split into components for each order in ϵ. When the expansion is separated into multiple equations according to the order of ϵ, all of these phenomena will then be able to affect the time derivative.

With these expansions, the DVBE becomes

$$\left(\epsilon\frac{\partial}{\partial t_1}+\epsilon^2\frac{\partial}{\partial t_2}+\ldots\right)\left(f_i^{(0)}+\epsilon f_i^{(1)}+\ldots\right) \tag{4.13}$$
$$+\xi_{i\alpha}\epsilon\frac{\partial}{\partial x_\alpha}\left(f_i^{(0)}+\epsilon f_i^{(1)}+\ldots\right)=-\frac{1}{\tau}\left(\epsilon f_i^{(1)}+\epsilon^2 f_i^{(2)}+\ldots\right).$$

Separating terms into first and second order in ϵ, we find

$$\mathcal{O}(\epsilon)\text{:}\qquad \left(\frac{\partial}{\partial t_1}+\xi_{i\alpha}\frac{\partial}{\partial x_\alpha}\right)f_i^{(0)}=-\frac{1}{\tau}f_i^{(1)}, \tag{4.14a}$$

$$\mathcal{O}(\epsilon^2)\text{:}\qquad \frac{\partial f_i^{(0)}}{\partial t_2}+\left(\frac{\partial}{\partial t_1}+\xi_{i\alpha}\frac{\partial}{\partial x_\alpha}\right)f_i^{(1)}=-\frac{1}{\tau}f_i^{(2)}. \tag{4.14b}$$

As in the fully continuous Boltzmann equation case (3.42), the conservation of mass and momentum imply that

$$\int f_i^{(n)}\,\mathrm{d}\boldsymbol{\xi}=\int \boldsymbol{\xi}_i f_i^{(n)}\,\mathrm{d}\boldsymbol{\xi}=0\qquad\text{for } n\geq 1. \tag{4.15}$$

Thus, the zeroth to second moments of (4.14a) are

$$\frac{\partial\rho}{\partial t_1}+\frac{\partial\rho u_\alpha}{\partial x_\alpha}=0, \tag{4.16a}$$

$$\frac{\partial\rho u_\alpha}{\partial t_1}+\frac{\partial \Pi_{\alpha\beta}^{(0)}}{\partial x_\beta}=0, \tag{4.16b}$$

$$\frac{\partial \Pi_{\alpha\beta}^{(0)}}{\partial t_1}+\frac{\partial \breve{\Pi}_{\alpha\beta\gamma}^{(0)}}{\partial x_\gamma}=-\frac{1}{\tau}\breve{\Pi}_{\alpha\beta}^{(1)}, \tag{4.16c}$$

where $\breve{\Pi}_{\alpha\beta}^{(1)}=\sum_i \xi_\alpha\xi_\beta f_i^{(1)}$. Similarly, the zeroth and first moments of (4.14b) are

$$\frac{\partial\rho}{\partial t_2}=0, \tag{4.17a}$$

$$\frac{\partial\rho u_\alpha}{\partial t_2}+\frac{\partial\breve{\Pi}_{\alpha\beta}^{(1)}}{\partial x_\beta}=0. \tag{4.17b}$$

We now proceed by recombining the moment equations at different orders in ϵ to produce conservation equations. For the mass conservation

equation, we simply reverse the expansion (4.12) in the sum ϵ(4.16a) + ϵ^2(4.17a), which results in the normal continuity equation

$$\frac{\partial \rho}{\partial t} + \frac{\partial \rho u_\alpha}{\partial x_\alpha} = 0. \tag{4.18}$$

Similarly recombining (4.16b) and (4.17b), we find a momentum conservation equation

$$\frac{\partial \rho u_\alpha}{\partial t} + \frac{\partial}{\partial x_\beta}\left(\rho u_\alpha u_\beta + \rho c_0^2 \delta_{\alpha\beta} + \epsilon \breve{\Pi}^{(1)}_{\alpha\beta}\right) = 0. \tag{4.19}$$

However, this equation involves the as of yet unknown moment $\breve{\Pi}^{(1)}_{\alpha\beta}$. From a closer look at the equation, we can already now expect this moment to play the role of the stress tensor.

The necessity of expanding the time derivative into several components can now be seen. If it had not been expanded, (4.17b) would be stating that $\partial \breve{\Pi}^{(1)}_{\alpha\beta}/\partial x_\beta = 0$, since no component of the time derivative would exist at $\mathcal{O}(\epsilon^2)$. Consequently, the stress tensor would not have appeared in the momentum conservation equation. While the Chapman-Enskog analysis in section 3.8 was performed without introducing any time derivative expansion, the unused and unnecessary terms in that derivation at higher orders in ϵ similarly do not stand up to close scrutiny without this expansion.

Using (4.16c), we may find $\breve{\Pi}^{(1)}_{\alpha\beta}$ by resolving the derivatives $\partial \Pi^{(0)}_{\alpha\beta}/\partial t_1$ and $\partial \breve{\Pi}^{(0)}_{\alpha\beta\gamma}/\partial x_\gamma$. Using the product rule corollaries

$$\begin{aligned}
\frac{\partial \rho u_\alpha u_\beta}{\partial t_1} &= u_\alpha \frac{\partial \rho u_\beta}{\partial t_1} + u_\beta \frac{\partial \rho u_\alpha}{\partial t_1} - u_\alpha u_\beta \frac{\partial \rho}{\partial t_1}, \\
\frac{\partial \rho u_\alpha u_\beta u_\gamma}{\partial x_\gamma} &= u_\alpha \frac{\partial \rho u_\beta u_\gamma}{\partial x_\gamma} + u_\beta \frac{\partial \rho u_\alpha u_\gamma}{\partial x_\gamma} - u_\alpha u_\beta \frac{\partial \rho u_\gamma}{\partial x_\gamma},
\end{aligned}$$

in addition to (4.16a) and (4.16b), we can resolve the former derivative,

$$\begin{aligned}
\frac{\partial \Pi^{(0)}_{\alpha\beta}}{\partial t_1} &= \frac{\partial \rho u_\alpha u_\beta}{\partial t_1} + \frac{\partial \rho c_0^2 \delta_{\alpha\beta}}{\partial t_1} \\
&= u_\alpha \frac{\partial \rho u_\beta}{\partial t_1} + u_\beta \frac{\partial \rho u_\alpha}{\partial t_1} - u_\alpha u_\beta \frac{\partial \rho}{\partial t_1} + c_0^2 \delta_{\alpha\beta} \frac{\partial \rho}{\partial t_1} \\
&= -u_\alpha \frac{\partial}{\partial x_\gamma}\left(\rho u_\beta u_\gamma + \rho c_0^2 \delta_{\beta\gamma}\right) - u_\beta \frac{\partial}{\partial x_\gamma}\left(\rho u_\alpha u_\gamma + \rho c_0^2 \delta_{\alpha\gamma}\right) \\
&\quad + u_\alpha u_\beta \frac{\partial \rho u_\gamma}{\partial x_\gamma} - c_0^2 \delta_{\alpha\beta} \frac{\partial \rho u_\gamma}{\partial x_\gamma} \\
&= -\frac{\partial \rho u_\alpha u_\beta u_\gamma}{\partial x_\gamma} - c_0^2 \left(u_\alpha \frac{\partial \rho}{\partial x_\beta} + u_\beta \frac{\partial \rho}{\partial x_\alpha}\right) - c_0^2 \delta_{\alpha\beta} \frac{\partial \rho u_\gamma}{\partial x_\gamma}.
\end{aligned} \tag{4.20}$$

The latter derivative is more easily resolved,

$$\begin{aligned}\frac{\partial \breve{\Pi}^{(0)}_{\alpha\beta\gamma}}{\partial x_\gamma} &= \frac{\partial}{\partial x_\gamma}\rho c_0^2\left(u_\alpha\delta_{\beta\gamma}+u_\beta\delta_{\alpha\gamma}+u_\gamma\delta_{\alpha\beta}\right)\\ &= c_0^2\left(\frac{\partial \rho u_\alpha}{\partial x_\beta}+\frac{\partial \rho u_\beta}{\partial x_\alpha}\right)+c_0^2\delta_{\alpha\beta}\frac{\partial \rho u_\gamma}{\partial x_\gamma}.\end{aligned} \tag{4.21}$$

With these two derivatives resolved, (4.16c) becomes

$$\breve{\Pi}^{(1)}_{\alpha\beta} = -\rho c_0^2\tau\left(\frac{\partial u_\alpha}{\partial x_\beta}+\frac{\partial u_\beta}{\partial x_\alpha}\right)+\tau\frac{\partial \rho u_\alpha u_\beta u_\gamma}{\partial x_\gamma}. \tag{4.22}$$

The last term is an error term due to the $\rho u_\alpha u_\beta u_\gamma$ term which is missing in $\breve{\Pi}^{(0)}_{\alpha\beta\gamma}$ due to the truncation to $\mathcal{O}(\boldsymbol{u}^2)$ in the equation (4.2) for $f_i^{(0)}$. In a corresponding derivation for an isothermal, fully continuous Boltzmann equation, we would have found

$$\Pi^{(1)}_{\alpha\beta} = -\rho c_0^2\tau\left(\frac{\partial u_\alpha}{\partial x_\beta}+\frac{\partial u_\beta}{\partial x_\alpha}\right).$$

A closer look at the terms in (4.22) reveals that the error term is negligible if $u^2 \ll c_0^2$, i.e. if $Ma^2 \ll 1$. While this condition excludes using this basic LB method for simulations of transsonic and supersonic flow, the condition is otherwise not very strict. We will see in section 7.2 that the error term is negligible even for simulations of nonlinear acoustics.

Neglecting the error term, we can insert (4.22) into (4.19) to find the momentum conservation equation

$$\boxed{\frac{\partial \rho u_\alpha}{\partial t}+\frac{\partial \rho u_\alpha u_\beta}{\partial x_\beta} = -\frac{\partial p}{\partial x_\alpha}+\frac{\partial \sigma'_{\alpha\beta}}{\partial x_\beta}.} \tag{4.23}$$

This is the forceless Navier-Stokes momentum equation (2.19b) with pressure $p = \rho c_0^2$, shear viscosity $\nu = \rho c_0^2\tau = p\tau$, and bulk viscosity $\nu_B = (2/3)\nu$. This bulk viscosity appears solely due to the isothermal equation of state [77].

Thus, we have shown that the discrete-velocity Boltzmann equation (4.3), given the velocity set conditions (4.11), correctly reproduces the mass and momentum conservation equations of fluid mechanics, with the exception of a $\mathcal{O}(\boldsymbol{u}^3)$ error term which is negligible if $Ma^2 \ll 1$.

4.1.3 Velocity sets

So far, we have found the conditions (4.11) on the velocity set given by $\boldsymbol{\xi}_i$ and w_i and proven that these are sufficient for the discrete-velocity

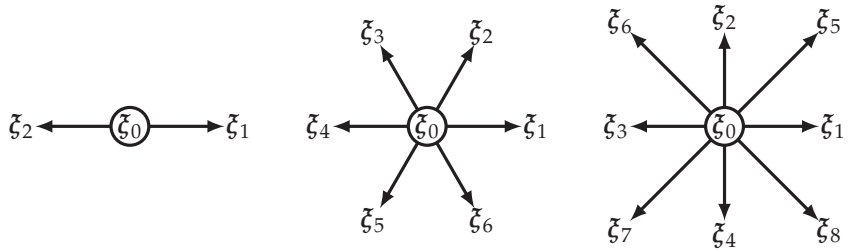

(a) D1Q3 **(b)** D2Q7 **(c)** D2Q9

Figure 4.1: Velocity vectors of simple one- and two-dimensional velocity sets

Boltzmann equation (4.3) to reproduce the mass and momentum equations of the Navier-Stokes-Fourier model. It is now time to look at specific velocity sets that fulfil these conditions.

In the early years of lattice Boltzmann, velocity sets were developed by finding weighting coefficients w_i that fulfil conditions such as (4.11), given a certain choice of velocity vectors [74]. These velocity vectors were chosen for their ability to tile physical space; each velocity brings particles from one point on a regular periodic grid (or *lattice*) to another neighbouring point (unless the velocity is zero, in which case the particles are immobile). Later it was discovered how to develop both velocity vectors and weighting coefficients simultaneously through the Gauss-Hermite quadrature method mentioned previously [72, 73]. In the following, we will consider the former method, which is mathematically simpler, although more ad-hoc and less general.

Lattice
A regular periodic grid of nodes in physical space. In LB, lattices are defined by the velocity vectors $\boldsymbol{\xi}_i$.

In LB terminology, it is common to denote different velocity sets and the lattices that they form as DdQq, d being the number of spatial dimensions, and q the number of velocities. The velocity vectors of the most simple velocity sets in one and and two dimensions, namely D1Q3, D2Q7, and D2Q9, are shown in Figure 4.1. Each of these velocity sets has a zero velocity vector $\boldsymbol{\xi}_0 = \mathbf{0}$, which corresponds to particles being at rest.

The one-dimensional D1Q3 lattice is a line of regularly spaced points. The two-dimensional D2Q7 and D2Q9 lattices are hexagonal and square, respectively. While D2Q7 has the advantage of having fewer velocities than D2Q9 and thus being less computationally expensive, the square D2Q9 lattice is much easier to deal with in computer implementations. Thus, the latter lattice is more commonly chosen for two-dimensional simulations.

In the D1Q3 and D2Q7 velocity sets, the nonzero velocity vectors $\boldsymbol{\xi}_{i\neq 0}$ all have the same magnitude, which we define as $\Delta x/\Delta t$.* In the D2Q9

*The notational choice of Δx and Δt foreshadows the discretisation of space and time.

velocity set, not all nonzero velocity vectors have the same magnitude; the diagonal velocity vectors $\boldsymbol{\xi}_5$–$\boldsymbol{\xi}_8$ have the higher magnitude of $\sqrt{2}\Delta x/\Delta t$.

With the D1Q3 velocity vectors defined, we can derive the weighting coefficients w_i that satisfy the symmetry conditions (4.11). First, for (4.11b) to hold, $w_1 = w_2 = w_s$ (the letter s being an abbreviation of *short*). Then, the other nonzero symmetry conditions form the system of equations

$$\begin{aligned} \sum_i w_i &= \quad w_0 + 2w_s = 1, \\ \sum_i w_i \xi_{ix}^2 &= (\tfrac{\Delta x}{\Delta t})^2 (2w_s) = c_0^2, \\ \sum_i w_i \xi_{ix}^4 &= (\tfrac{\Delta x}{\Delta t})^4 (2w_s) = 3c_0^4, \end{aligned} \tag{4.24a}$$

the solution of which is

$$c_0 = (\tfrac{\Delta x}{\Delta t})/\sqrt{3}, \quad w_0 = 2/3, \quad w_s = 1/6. \tag{4.24b}$$

For the D2Q9 velocity vectors, we set $w_1 = w_2 = w_3 = w_4 = w_s$ and $w_5 = w_6 = w_7 = w_8 = w_l$ for similar reasons (the letter l being an abbreviation of *long*). Again, we get a system of equations from the nonzero symmetry conditions,

$$\begin{aligned} \sum_i w_i &= \quad w_0 + 4w_s + 4w_l = 1, \\ \sum_i w_i \xi_{ix}^2 = \sum_i w_i \xi_{iy}^2 &= (\tfrac{\Delta x}{\Delta t})^2 (2w_s + 4w_l) = c_0^2, \\ \sum_i w_i \xi_{ix}^2 \xi_{iy}^2 &= (\tfrac{\Delta x}{\Delta t})^4 (4w_l) = c_0^4, \\ \sum_i w_i \xi_{ix}^4 = \sum_i w_i \xi_{iy}^4 &= (\tfrac{\Delta x}{\Delta t})^4 (2w_s + 4w_l) = 3c_0^4. \end{aligned} \tag{4.25a}$$

This is solved by

$$c_0 = (\tfrac{\Delta x}{\Delta t})/\sqrt{3}, \quad w_0 = 4/9, \quad w_s = 1/9, \quad w_l = 1/36. \tag{4.25b}$$

A similar derivation can be performed for the D2Q7 lattice. In summary, the velocity vectors and weighting coefficients for the simple one- and two-dimensional lattices are given in Table 4.1.

In three dimensions, the simplest velocity sets are D3Q15, D3Q19, and D3Q27 [74]. These three velocity sets are shown graphically in Figure 4.2, and are fully described in Table 4.2.

Note that D1Q3 is a one-dimensional projection of D2Q9, which itself is a two-dimensional projection of D3Q15, D3Q19, and D3Q27. This means, for example, that a D3Q27 simulation of a case where all variables are invariant in the y and z direction could be performed using D1Q3 with the same results.

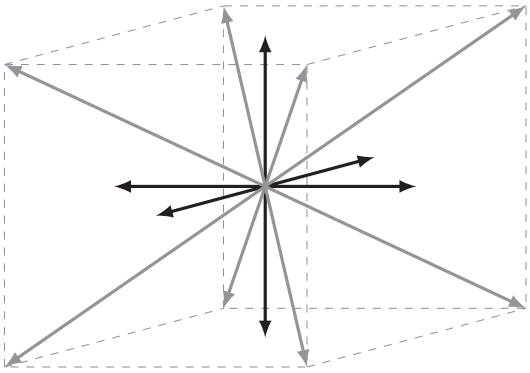

(a) D3Q15

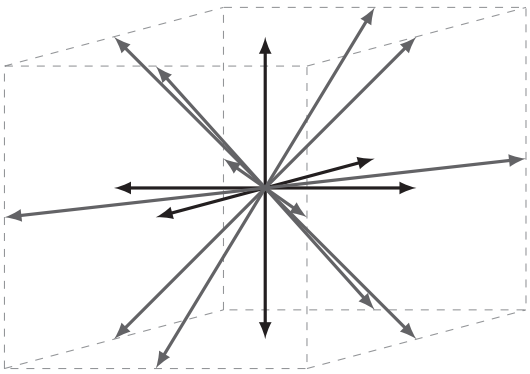

(b) D3Q19

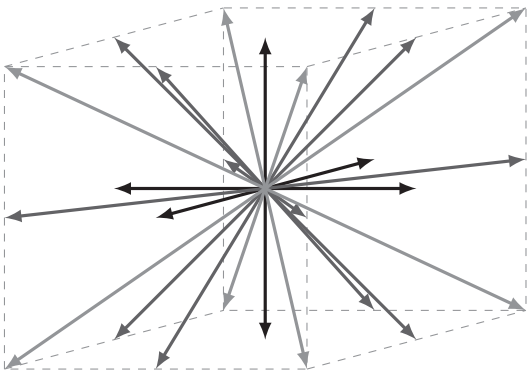

(c) D3Q27

Figure 4.2: Velocity vectors of the simple three-dimensional velocity sets. Velocity vectors to the six nearest neighbours are in black, those to the twelve second nearest neighbours are in dark grey, and those to the eight third nearest neighbours are in grey.

Table 4.1: Simple one- and two-dimensional velocity sets

(a) D1Q3, $c_0 = (\frac{\Delta x}{\Delta t})/\sqrt{3}$

i	$\boldsymbol{\xi}_i/(\frac{\Delta x}{\Delta t})$	w_i
0	(0)	$\frac{2}{3}$
1	(1)	$\frac{1}{6}$
2	(-1)	$\frac{1}{6}$

(b) D2Q7, $c_0 = (\frac{\Delta x}{\Delta t})/2$

i	$\boldsymbol{\xi}_i/(\frac{\Delta x}{\Delta t})$	w_i
0	$(0,0)$	$\frac{1}{2}$
1	$(1,0)$	$\frac{1}{12}$
2	$(\frac{1}{2}, \frac{\sqrt{3}}{2})$	$\frac{1}{12}$
3	$(-\frac{1}{2}, \frac{\sqrt{3}}{2})$	$\frac{1}{12}$
4	$(-1,0)$	$\frac{1}{12}$
5	$(-\frac{1}{2}, -\frac{\sqrt{3}}{2})$	$\frac{1}{12}$
6	$(\frac{1}{2}, -\frac{\sqrt{3}}{2})$	$\frac{1}{12}$

(c) D2Q9, $c_0 = (\frac{\Delta x}{\Delta t})/\sqrt{3}$

i	$\boldsymbol{\xi}_i/(\frac{\Delta x}{\Delta t})$	w_i
0	$(0,0)$	$\frac{4}{9}$
1	$(1,0)$	$\frac{1}{9}$
2	$(0,1)$	$\frac{1}{9}$
3	$(-1,0)$	$\frac{1}{9}$
4	$(0,-1)$	$\frac{1}{9}$
5	$(1,1)$	$\frac{1}{36}$
6	$(-1,1)$	$\frac{1}{36}$
7	$(-1,-1)$	$\frac{1}{36}$
8	$(1,-1)$	$\frac{1}{36}$

Table 4.2: Simple three-dimensional velocity sets. $(\dots)_{\text{cycle}}$ indicates all possible spatial and sign permutations of the given vector coordinates.

(a) D3Q15, $c_0 = (\frac{\Delta x}{\Delta t})/\sqrt{3}$

i	$\boldsymbol{\xi}_i/(\frac{\Delta x}{\Delta t})$	w_i
0	$(0,0,0)$	$\frac{2}{9}$
1–6	$(\pm 1,0,0)_{\text{cycle}}$	$\frac{1}{9}$
7–14	$(\pm 1,\pm 1,\pm 1)_{\text{cycle}}$	$\frac{1}{72}$

(b) D3Q19, $c_0 = (\frac{\Delta x}{\Delta t})/\sqrt{3}$

i	$\boldsymbol{\xi}_i/(\frac{\Delta x}{\Delta t})$	w_i
0	$(0,0,0)$	$\frac{1}{3}$
1–6	$(\pm 1,0,0)_{\text{cycle}}$	$\frac{1}{18}$
7–18	$(\pm 1,\pm 1,0)_{\text{cycle}}$	$\frac{1}{36}$

(c) D3Q27, $c_0 = (\frac{\Delta x}{\Delta t})/\sqrt{3}$

i	$\boldsymbol{\xi}_i/(\frac{\Delta x}{\Delta t})$	w_i
0	$(0,0,0)$	$\frac{8}{27}$
1–6	$(\pm 1,0,0)_{\text{cycle}}$	$\frac{2}{27}$
7–18	$(\pm 1,\pm 1,0)_{\text{cycle}}$	$\frac{1}{54}$
19–26	$(\pm 1,\pm 1,\pm 1)_{\text{cycle}}$	$\frac{1}{216}$

All of the LB velocity sets described in this section contain a zero velocity vector $\boldsymbol{\xi}_0$ with a corresponding weighting coefficient w_0. This is in contrast to the simple lattice gas described in section 1.1.2, in which no zero velocity particles exist. However, these rest velocities are necessary for the lattice Boltzmann method to behave correctly; otherwise, the velocity set conditions (4.11) cannot all be simultaneously fulfilled. This can be demonstrated by trying to remove the rest particles from the D1Q3 and D2Q9 velocity sets by setting $w_0 = 0$: The systems of equations (4.24a) and (4.25a) would both then become underdetermined and unsolvable.

4.1.4 Digression: Linearised DVBE

Instead of keeping terms to $\mathcal{O}(\boldsymbol{u}^2)$ in the Taylor expansion of $f^{(0)}$, we could linearise the expansion. Consequently, the DVBE will be fully linear, which means that the resulting macroscopic equations will also necessarily be linear. This linearised DVBE will not be used until later chapters, but showing it here serves to emphasise how important the equilibrium distribution is to the resulting physics of the model.

As in section 2.3, we assume that there is only a very small perturbation in density and velocity from the rest state. Thus, we can linearise the equilibrium distribution (4.2),

$$f_i^{(0)} = w_i \left(\rho + \frac{\rho_0 u_\alpha \xi_{i\alpha}}{c_0^2} \right). \tag{4.26}$$

This is, in fact, the only alteration we make in this section to the previously described DVBE.

Using the symmetry properties in (4.11), we find without approximation the discrete equilibrium moments

$$\begin{gathered} \check{I\!I}_0^{(0)} = \rho, \qquad \check{I\!I}_\alpha^{(0)} = \rho_0 u_\alpha, \qquad \check{I\!I}_{\alpha\beta}^{(0)} = \rho c_0^2 \delta_{\alpha\beta}, \\ \check{I\!I}_{\alpha\beta\gamma}^{(0)} = \rho_0 c_0^2 \left(u_\alpha \delta_{\beta\gamma} + u_\beta \delta_{\alpha\gamma} + u_\gamma \delta_{\alpha\beta} \right). \end{gathered} \tag{4.27}$$

Following the Chapman-Enskog derivation in section 4.1.2 with these moments, we exactly find

$$\check{I\!I}_{\alpha\beta}^{(1)} = -\tau \left(\frac{\partial \check{I\!I}_{\alpha\beta}^{(0)}}{\partial t_1} + \frac{\partial \check{I\!I}_{\alpha\beta\gamma}^{(0)}}{\partial x_\gamma} \right) = -p_0 \tau \left(\frac{\partial u_\alpha}{\partial x_\beta} + \frac{\partial u_\beta}{\partial x_\alpha} \right), \tag{4.28}$$

and the macroscopic mass and momentum conservation equations

$$\frac{\partial \rho}{\partial t} + \rho_0 \frac{\partial u_\alpha}{\partial x_\alpha} = 0, \tag{4.29a}$$

$$\rho_0 \frac{\partial u_\alpha}{\partial t} = -\frac{\partial p}{\partial x_\alpha} + p_0 \tau \left(\frac{\partial u_\alpha}{\partial x_\beta} + \frac{\partial u_\beta}{\partial x_\alpha} \right). \tag{4.29b}$$

These equations are linearised versions of the corresponding equations of the Navier-Stokes-Fourier model (2.19), with viscosities $\mu = p_0 \tau$ and $\mu_\mathrm{B} = 2\mu/3$. No error terms had to be neglected in this derivation, unlike the previous derivation of the DVBE where the momentum equation gained a $\mathcal{O}(u^3)$ error term.

4.2 The lattice Boltzmann equation

While the discrete-velocity Boltzmann equation (4.3) is discrete in velocity space, it is still continuous in physical space and time. To find

the fully discrete lattice Boltzmann equation, we must perform further discretisation.

Characteristics
Curves in the function variables (e.g. space and time) along which a hyperbolic partial differential equation becomes an ordinary differential equation

The Boltzmann equation and the DVBE are both hyperbolic equations, and a possible way of discretising these is to integrate along *characteristics*. We assume that we can write the distribution function as $f_i = f_i(\boldsymbol{x}(a), t(a))$, where a denotes the position along the characteristic. The total differential of f_i in a, assuming no external forces, is

$$\frac{\mathrm{d}f_i}{\mathrm{d}a} = \left(\frac{\partial f_i}{\partial t}\right)\frac{\mathrm{d}t}{\mathrm{d}a} + \left(\frac{\partial f_i}{\partial x_\alpha}\right)\frac{\mathrm{d}x_\alpha}{\mathrm{d}a} = -\frac{1}{\tau}(f_i - f_i^{(0)}). \tag{4.30}$$

The right equality holds if the total differential is the left-hand side of the DVBE (4.3), which is true if

$$\frac{\mathrm{d}t}{\mathrm{d}a} = 1, \qquad \frac{\mathrm{d}x_\alpha}{\mathrm{d}a} = \xi_{i\alpha}.$$

Thus, allowing a minor abuse of notation, f_i can be written as $f_i(\boldsymbol{x} + \boldsymbol{\xi}_i a, t + a)$.*

Integrating (4.30) from $a = 0$ to $a = \Delta t$ (i.e. from one time step to the next) and using the fundamental theorem of calculus on the left side, we find

$$\begin{aligned} &f_i(\boldsymbol{x} + \boldsymbol{\xi}_i \Delta t, t + \Delta t) - f_i(\boldsymbol{x}, t) \\ &\quad = -\frac{1}{\tau}\int_0^{\Delta t} \left[f_i(\boldsymbol{x} + \boldsymbol{\xi}_i a, t + a) - f_i^{(0)}(\boldsymbol{x} + \boldsymbol{\xi}_i a, t + a)\right] \mathrm{d}a. \end{aligned} \tag{4.31}$$

While the left side is exact, the integral on the right-hand side must be approximated. There are two main ways to do this, which we shall describe in the following subsections.

When implementing the lattice Boltzmann equation on a computer, it is convenient to scale time and space so that the lattice resolution Δx and time resolution Δt both equal one. This choice of units is called *lattice units*. We will use this choice henceforth, and go into how to convert between lattice and physical units in section 4.2.4.

Lattice units
A simplified nonphysical choice of units for simulations, where $\Delta x = \Delta t = 1$

4.2.1 First order discretisation

With the most common "first order"† discretisation, the integral in (4.31) is approximated with the rectangle method, giving the first order *lattice Boltzmann equation*,

$$\boxed{f_i(\boldsymbol{x} + \boldsymbol{\xi}_i, t + 1) - f_i(\boldsymbol{x}, t) = -\frac{1}{\tau}\left[f_i(\boldsymbol{x}, t) - f_i^{(0)}(\boldsymbol{x}, t)\right].} \tag{4.32}$$

*Strictly speaking, this should be $f_i(\boldsymbol{x}_0 + \boldsymbol{\xi}_i a, t_0 + a)$, where $\boldsymbol{x}_0$ and t_0 are constants defining the starting point, $a = 0$, of the characteristic. Thence, the abuse of notation.

†It is correct but slightly misleading to call this discretisation *first order*, as the resulting scheme will turn out to have second order accuracy in space and time.

The resulting numerical scheme is fully explicit, as all populations f_i of the next time step is determined by the populations f_i of the current time step. However, the rectangle method is generally only a first order accurate approximation. Therefore, we should determine its actual numerical accuracy using the Chapman-Enskog expansion as in section 4.1.2.

However, the left-hand side of (4.32) must first be de-discretised. Truncating its Taylor expansion to second order, we find

$$\begin{aligned} &f_i(\boldsymbol{x}+\boldsymbol{\xi}_i, t+1) - f_i(\boldsymbol{x}, t) \\ &\quad\approx \left(\frac{\partial}{\partial t} + \xi_{i\alpha}\frac{\partial}{\partial x_\alpha}\right) f_i + \frac{1}{2}\left(\frac{\partial^2}{\partial t^2} + 2\xi_{i\alpha}\frac{\partial}{\partial t}\frac{\partial}{\partial x_\alpha} + \xi_{i\alpha}\xi_{i\beta}\frac{\partial}{\partial x_\alpha}\frac{\partial}{\partial x_\beta}\right) f_i. \end{aligned}$$

Due to the perturbation of the derivatives in (4.12), third order derivative terms in this expansion will be $\mathcal{O}(\epsilon^3)$ and therefore not contribute at the Navier-Stokes level.

Using this expression for the left-hand side, and performing the Chapman-Enskog expansion as in section 4.1.2, we get

$$\mathcal{O}(\epsilon): \qquad \left(\frac{\partial}{\partial t_1} + \xi_{i\alpha}\frac{\partial}{\partial x_\alpha}\right) f_i^{(0)} = -\frac{1}{\tau} f_i^{(1)} \tag{4.33a}$$

to first order in ϵ, which is identically to the corresponding DVBE equation (4.14a). To second order, we find an initially bulky expression which can be simplified by subtracting $\frac{1}{2}(\partial/\partial t_1 - \xi_{i\beta}\partial/\partial x_\beta)$(4.33a), giving

$$\mathcal{O}(\epsilon^2): \qquad \frac{\partial f_i^{(0)}}{\partial t_2} + \left(\frac{\partial}{\partial t_1} + \xi_{i\alpha}\frac{\partial}{\partial x_\alpha}\right)\left(1 - \frac{1}{2\tau}\right) f_i^{(1)} = -\frac{1}{\tau} f_i^{(2)}. \tag{4.33b}$$

There is one difference here from (4.14b): the parenthesis $(1 - 1/2\tau)$.

By comparison with the corresponding DVBE expressions, we can see that the following derivation would result in the same equation for $\breve{\Pi}^{(1)}_{\alpha\beta}$, but that the $(1 - 1/2\tau)$ factor changes the shear viscosity to

$$\nu = c_0^2\left(\tau - \tfrac{1}{2}\right). \tag{4.34}$$

Thus, while the rectangle method is only first order accurate, the effect of the second order error terms is only to alter the viscosity by $c_0^2/2$.

4.2.2 Second order discretisation

With the less common, "second order" discretisation, the integral in (4.31) is approximated with the trapezium rule, giving

$$\begin{aligned} f_i(\boldsymbol{x}+\boldsymbol{\xi}_i, t+1) - f_i(\boldsymbol{x}, t) = -\frac{1}{2\tau}\Big[& f_i(\boldsymbol{x}+\boldsymbol{\xi}_i, t+1) \\ & - f_i^{(0)}(\boldsymbol{x}+\boldsymbol{\xi}_i, t+1) \\ & + f_i(\boldsymbol{x}, t) - f_i^{(0)}(\boldsymbol{x}, t)\Big], \end{aligned} \tag{4.35}$$

which can be rewritten into the cleaner form

$$f_i(\boldsymbol{x}+\boldsymbol{\xi}_i,t+1)-f_i(\boldsymbol{x},t)=-\frac{1}{2\tau}\left[f_i^{\mathrm{neq}}(\boldsymbol{x}+\boldsymbol{\xi}_i,t+1)+f_i^{\mathrm{neq}}(\boldsymbol{x},t)\right] \quad (4.36)$$

using $f_i^{\mathrm{neq}}=f_i-f_i^{(0)}$ for the nonequilibrium part of f.

This is not a fully explicit system of equations, as there is a co-dependence between $f_i(\boldsymbol{x}+\boldsymbol{\xi}_i,t+1)$ and $f_i^{(0)}(\boldsymbol{x}+\boldsymbol{\xi}_i,t+1)$. We shall later see that a substitution can be done to make it explicit, but we will first examine at the macroscopic behaviour of this discretisation.

Using the same methods as in the previous section, we find the Taylor expansion of (4.36) to second order,

$$\begin{aligned}&\left(\frac{\partial}{\partial t}+\xi_{i\alpha}\frac{\partial}{\partial x_\alpha}\right)f_i+\frac{1}{2}\left(\frac{\partial^2}{\partial t^2}+2\xi_{i\alpha}\frac{\partial}{\partial t}\frac{\partial}{\partial x_\alpha}+\xi_{i\alpha}\xi_{i\beta}\frac{\partial}{\partial x_\alpha}\frac{\partial}{\partial x_\beta}\right)f_i\\&=-\frac{1}{2\tau}\left[2f_i^{\mathrm{neq}}+\left(\frac{\partial}{\partial t}+\xi_{i\alpha}\frac{\partial}{\partial x_\alpha}\right)f_i\right],\end{aligned} \quad (4.37)$$

and subsequently find the first and second order terms in ϵ,

$$\mathcal{O}(\epsilon): \qquad \left(\frac{\partial}{\partial t_1}+\xi_{i\alpha}\frac{\partial}{\partial x_\alpha}\right)f_i^{(0)}=-\frac{1}{\tau}f_i^{(1)}, \quad (4.38a)$$

$$\mathcal{O}(\epsilon^2): \qquad \frac{\partial}{\partial t_2}f_i^{(0)}+\left(\frac{\partial}{\partial t_1}+\xi_{i\alpha}\frac{\partial}{\partial x_\alpha}\right)f_i^{(1)}=-\frac{1}{\tau}f_i^{(2)}. \quad (4.38b)$$

These equations correspond exactly to those of the DVBE, (4.14). Thus we know that this discretisation is a fully consistent approximation to the DVBE, with viscosity

$$\nu=c_0^2\tau.$$

The implicit discretisation (4.36) can be made fully explicit through the substitution

$$\bar{f}_i(\boldsymbol{x},t)=f_i(\boldsymbol{x},t)+\frac{1}{2\tau}f_i^{\mathrm{neq}}(\boldsymbol{x},t), \quad (4.39)$$

after which (4.36) becomes the fully explicit second order *lattice Boltzmann equation*,

$$\boxed{\bar{f}_i(\boldsymbol{x}+\boldsymbol{\xi}_i,t+1)-\bar{f}_i(\boldsymbol{x},t)=-\frac{1}{\tau+1/2}\left[\bar{f}_i(\boldsymbol{x},t)-f_i^{(0)}(\boldsymbol{x},t)\right].} \quad (4.40)$$

By (4.39) and (4.15), the two first moments of $\bar{f}_i$ are equal to the corresponding moments of f_i,

$$\sum_i\bar{f}_i=\rho=\sum_i f_i, \quad (4.41a)$$

$$\sum_i\boldsymbol{\xi}_i\bar{f}_i=\rho\boldsymbol{u}=\sum_i\boldsymbol{\xi}_i f_i. \quad (4.41b)$$

Therefore, $f_i^{(0)}$ can be constructed from $\bar{f}_i$ as if it were f_i. However, the second moment of $\bar{f}_i$ differs,

$$\sum_i \xi_{i\alpha}\xi_{i\beta}\bar{f}_i = \left(1+\frac{1}{2\tau}\right)\Pi_{\alpha\beta} - \frac{1}{2\tau}\Pi^{(0)}_{\alpha\beta}. \tag{4.41c}$$

Comparing the lattice Boltzmann equations of first and second order, (4.32) and (4.40) respectively, we find that they are nearly identical except for the the second moment and the denominator of the collision operator. The latter may be seen as a redefinition of τ that compensates for the viscosity difference. Thus, for simple LB models, the difference between the two discretisations is not relevant and we will henceforth use the simpler first order version.

However, more complex extended LB models (e.g. [80]) may require using the second order discretisation. Also, if an alternate DVBE model is devised, performing a second-order discretisation will always result in a numerical scheme which is consistent with the DVBE model to the Navier-Stokes-Fourier level, unlike the first-order discretisation which may only be consistent to the Euler level. As we have seen for this basic model, this inconsistency in the first-order discretisation was manifested as a change in the numerical viscosity.

4.2.3 Summary: The lattice Boltzmann method

The preceding sections have been quite mathematical, focusing on the derivation of the lattice Boltzmann equation. Therefore, it is prudent to now give a short, more practical summary of the lattice Boltzmann method.

In a regular spatial grid of nodes (a *lattice*), each node contains a number of distribution functions $f_i(\boldsymbol{x}, t)$. These represent the density of particles with velocity $\boldsymbol{\xi}_i$ in the node at $\boldsymbol{x}$, at time t. These velocity vectors are chosen so that particles are brought from one node to its neighbours (or remain stationary in the case $\boldsymbol{\xi}_0 = \boldsymbol{0}$) during one time step. Some simple velocity sets in one, two, and three dimensions are shown in Figures 4.1 and 4.2, and are specified in Tables 4.1 and 4.2.

The distribution functions f_i can be used to find the more familiar macroscopic quantites of mass density and momentum density,

$$\rho(\boldsymbol{x}, t) = \sum_i f_i(\boldsymbol{x}, t),$$
$$\rho\boldsymbol{u}(\boldsymbol{x}, t) = \sum_i \boldsymbol{\xi}_i f_i(\boldsymbol{x}, t).$$

The fluid velocity is found as $\boldsymbol{u}(\boldsymbol{x}, t) = (\sum_i \boldsymbol{\xi}_i f_i)/(\sum_i f_i)$. The pressure is determined through the isothermal relation $p = c_0^2\rho$, where the ideal

speed of sound c_0 is determined by the choice of velocity set (though in most cases, $c_0 = 1/\sqrt{3}$).

Once in each time step, the particles in each node collide, which is modelled as a relaxation of the distribution function f_i towards the equilibrium distribution

$$f_i^{(0)} = \rho w_i \left[1 + \frac{\boldsymbol{\xi}_i \cdot \boldsymbol{u}}{c_0^2} + \frac{(\boldsymbol{\xi}_i \cdot \boldsymbol{u})^2}{2c_0^4} - \frac{\boldsymbol{u} \cdot \boldsymbol{u}}{2c_0^2} \right].$$

This is constructed from the macroscopic moments of density ρ and fluid velocity $\boldsymbol{u}$, found using the above relations. The weighting coefficients w_i are determined by the choice of velocity set.

What happens in each time step is this: In each node, collisions between incoming particles f_i are represented by a relaxation with characteristic time τ towards the equilibrium distribution $f_i^{(0)}$, resulting in a new distribution of particles which is streamed on to the neighbouring nodes. All this is represented by the lattice Boltzmann equation,

$$f_i(\boldsymbol{x} + \boldsymbol{\xi}_i, t+1) = f_i(\boldsymbol{x}, t) - \frac{1}{\tau} \left[f_i(\boldsymbol{x}, t) - f_i^{(0)}(\boldsymbol{x}, t) \right]. \tag{4.42}$$

The right-hand side represents the distribution of particles after collisions have taken place, and the left-hand side represents these particles appearing in neighbouring nodes in the next time step.

This very simple numerical scheme is sufficient to evolve the macroscopic density ρ and fluid velocity $\boldsymbol{u}$ in accordance with the mass and momentum conservation equations of fluid mechanics, often known as the continuity equation and the compressible Navier-Stokes equation. In the latter, we get a kinematic shear viscosity $\nu = c_0^2(\tau - 1/2)$ and a kinematic bulk viscosity $\nu_\mathrm{B} = (2/3)\nu$. (Note that there are some problems in the low-viscosity limit $\tau \to 1/2$, which will be discussed in section 4.3.) There is also an error term in the momentum conservation which is negligible only if $Ma^2 = (u/c_0)^2 \ll 1$.

In summary, the lattice Boltzmann algorithm consists of the following steps in each node:

- **Macroscopic quantities:** From the distribution of particles f_i, calculate the node's fluid density ρ and fluid velocity $\boldsymbol{u}$.
- **Equilibrium distribution:** From the fluid density ρ and fluid velocity $\boldsymbol{u}$, calculate the node's equilibrium distribution $f_i^{(0)}$.
- **Collision:** The post-collision distribution functions are calculated according to the right-hand side of (4.42).
- **Streaming:** The post-collision distribution functions are streamed to neighbouring nodes according to their velocities, completing (4.42).

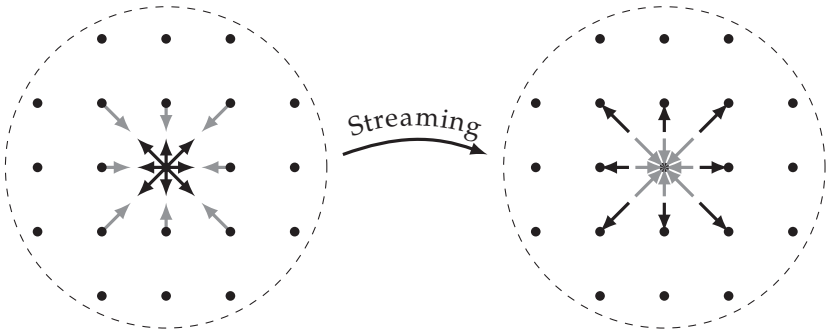

Figure 4.3: Particle distributions f_i (black) streaming from the central node to its neighbours, from which new distributions (black) are streamed back.

Apart from the streaming step, each step is completely local within each node, meaning no quantities outside that node are used. In the streaming step, particles only stream to neighbouring nodes. This locality is a very important property of the lattice Boltzmann method which allows for massive parallelisation of the algorithm.

However, the steps above require some starting condition. The most simple (but not necessarily the most accurate!) way to initialise the simulation is to calculate $f_i^{(0)}$ throughout the system based on specified values of ρ and $\boldsymbol{u}$, set $f_i = f_i^{(0)}$ everywhere, and start directly on the streaming step.

This summarises how the lattice Boltzmann method works in normal fluid nodes. So far we have said nothing about boundary conditions, which are handled differently to the steps above. We will touch on boundary conditions in section 4.4.

4.2.4 Lattice Boltzmann units

Relating lattice units to physical units is a surprisingly tricky topic, especially as it actually depends on what is being simulated.

If LB is being used to simulate incompressible flow, sound propagation in the simulation is considered physically irrelevant as sound propagation cannot occur in an incompressible fluid. Sound-like propagation might especially occur at the start of a simulation run, but is considered to be a transient error due to the initial condition of the flow field being different from the steady-state condition. Other sound-like propagation might occur due to the non-infinite information propagation speed of the numerical model.*

*Disturbing a theoretical incompressible fluid at a point, the disturbance is felt throughout the entire fluid immediately. In a compressible fluid and LB simulations (even "incom-

As the speed of sound is not a physically relevant quantity in an incompressible fluid, it does not put any constraints on the LB units in incompressible cases. This topic is well explained elsewhere [81], and we shall not go into it here as incompressibility is incompatible with acoustics. Instead, we shall look at the case of compressible flow, where the units are quite constrained.

The time and space resolutions Δx and Δt relate quantites in lattice units and physical units. For instance, the physical and lattice fluid speeds are connected as

$$u_{\mathrm{ph}} = u_{\mathrm{la}} \frac{\Delta x}{\Delta t}.$$

Since u_{la} can be freely scaled throughout the system, this does not form a constraint on the units. However, the speed of sound is a constant and *does* form a constraint,

$$c_{0,\mathrm{ph}} = c_{0,\mathrm{la}} \frac{\Delta x}{\Delta t}. \tag{4.43}$$

Similarly, the kinematic viscosity, with physical units m^2/s, forms another constraint,

$$\nu_{\mathrm{ph}} = \nu_{\mathrm{la}} \frac{\Delta x^2}{\Delta t}. \tag{4.44}$$

As $c_{0,\mathrm{ph}}$ and ν_{ph} are determined by the simulated case, we now have two equations for the two unknowns Δx and Δt. Solving them, we find

$$\Delta x = \frac{\nu_{\mathrm{ph}}}{\nu_{\mathrm{la}}} \frac{c_{0,\mathrm{la}}}{c_{0,\mathrm{ph}}}, \tag{4.45a}$$

$$\Delta t = \frac{\nu_{\mathrm{ph}}}{\nu_{\mathrm{la}}} \left(\frac{c_{0,\mathrm{la}}}{c_{0,\mathrm{ph}}} \right)^2. \tag{4.45b}$$

The only tunable parameter we are left with is the relaxation time τ, which determines the lattice viscosity ν_{la}. To avoid Δx and Δt becoming prohibitively small so that an extreme number of nodes and time steps are required to resolve the physical case to be simulated, the relaxation time τ should generally be made as small as possible. However, the BGK collision operator can be quite unstable and inaccurate for small τ. In section 4.3 we will look at some alternative collision operators which may perform better than BGK as ν_{la} becomes very small.

Density can also be represented in lattice units, for instance with the rest state density normalised to $\rho_{0,\mathrm{la}} = 1$. Δx and Δt are clearly insufficient to convert between lattice and physical density as their units are metres and seconds, respectively. Converting density to physical units requires

pressible" ones), the disturbance propagates with the speed of sound. From the definition of the speed of sound (2.24), we see that it actually goes to infinity as the fluid becomes incompressible.

units of kilograms. We therefore define the density conversion factor C_ρ so that

$$\rho_{\text{ph}} = C_\rho \rho_{\text{la}}, \tag{4.46}$$

with units kg/m^3.

Δx, Δt, and C_ρ are sufficient to convert the pressure to physical units. From the isothermal equation of state 4.1, the pressure in lattice and physical units is

$$p_{\text{ph}} = c_{0,\text{ph}}^2 \rho_{\text{ph}}, \qquad p_{\text{la}} = c_{0,\text{la}}^2 \rho_{\text{la}}. \tag{4.47}$$

From these, we find

$$p_{\text{ph}} = C_\rho \left(\frac{c_{0,\text{ph}}}{c_{0,\text{la}}} \right)^2 p_{\text{la}} = C_\rho \left(\frac{\Delta x}{\Delta t} \right)^2 p_{\text{la}}. \tag{4.48}$$

Thus, converting from lattice to physical pressure requires the use of both Δx, Δt, and C_ρ.

It may seem from this that the LB method is restricted to simulating unphysical isothermal fluids, since the equation of state (4.47) gives a fully linear relationship between pressure and density. However, as only the pressure *gradient* ∇p occurs in the momentum equation, the absolute pressure does not matter.* In cases where the state variables vary little from constant rest values, e.g.

$$p = p_0 + p' \qquad \text{where } p' \ll p_0, \tag{4.49}$$

the pressure deviation p' can be expressed as a linearised state function of density ρ and entropy s,

$$p' = \left(\frac{\partial p}{\partial \rho} \right)_s \rho' + \left(\frac{\partial p}{\partial s} \right)_\rho s'. \tag{4.50}$$

In nearly isentropic cases like acoustics, s' is negligible as discussed in section 2.3.2. Using the definition of the speed of sound (2.24), (4.49) becomes

$$p = p_0 + c_0^2 \rho' = p_0 + c_0^2 (\rho - \rho_0). \tag{4.51}$$

Therefore, in the momentum equation, $\nabla p \simeq c_0^2 \nabla \rho$. This is a valid approximation, no matter the equation of state, as long as the processes involved are nearly isentropic and $\rho' (\partial p / \partial \rho)_s \gg (\rho'^2/2)(\partial^2 p / \partial \rho^2)_s$.

Since the absolute pressure does not matter in the mass and momentum conservation equations simulated by the LB method, the rest pressure p_0 is irrelevant and we can in principle choose it arbitrarily, ignoring its "true" but irrelevant value of $p_0 = c_0^2 \rho_0$.

*The absolute pressure only plays a role in the energy equation, which is not relevant unless an extended energy-conserving LB method is used.

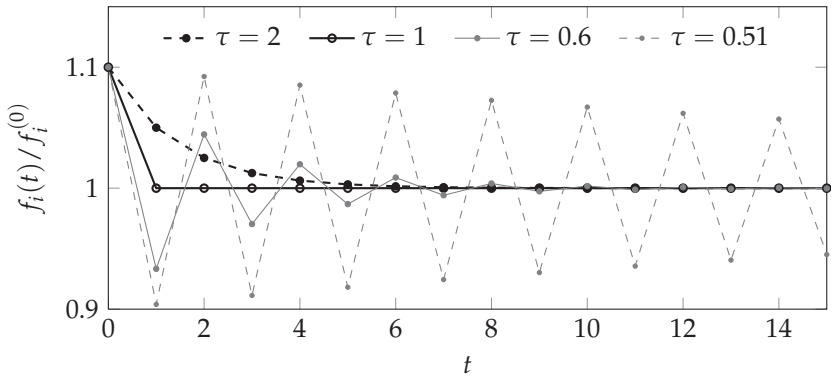

Figure 4.4: BGK relaxation with different relaxation times in the spatially homogeneous case described by (4.52) with $f_i(0)/f_i^{(0)} = 1.1$.

4.3 Alternative collision operators

The BGK operator is the simplest known collision operator for lattice Boltzmann, that is still sufficient to reproduce most hydrodynamic behaviour. However, it has its problems, most importantly that it is prone to instability and inaccuracy at low viscosities.

In a spatially homogenous case analogous to the one in section 3.5, the first order scheme (4.32) gives

$$f_i(t+1) = \left(1 - \frac{1}{\tau}\right) f_i(t) + \frac{1}{\tau} f_i^{(0)}. \tag{4.52}$$

If $\tau = 1$, f_i is fully relaxed to $f_i^{(0)}$ in one time step. If $\tau > 1$, it is underrelaxed; gradually relaxed towards $f_i^{(0)}$. If $1/2 < \tau < 1$, it is overrelaxed, oscillating around $f_i^{(0)}$ with a decaying amplitude. Having $\tau < 1/2$ would be an unstable overrelaxation with the amplitude *increasing* instead of decaying. Thus, $\tau = 1/2$ is the linear stability limit. The different cases of relaxation are illustrated in Figure 4.4.

When a very low viscosity is required and $\tau \to 1/2$, the BGK overrelaxation is close to the linear stability limit, causing f_i to tend to decay very slowly towards $f_i^{(0)}$ in an oscillatory manner. The combined effect of such oscillations and particle streaming can cause values of f_i to go far away from equilibrium and even become negative. If a number of such far-off-equilibrium distributions f_i are streamed into the same node, a very small or even negative density $\rho = \sum_i f_i$ may result and destabilising effects may occur [82]. For instance, if the density ρ goes towards zero, the fluid velocity $\boldsymbol{u} = (\sum_i \boldsymbol{\xi}_i f_i)/\rho$ may explode. If this happens, f_i will then be

overrelaxing past an entirely unrealistic distribution function $f_i^{(0)}$, likely going even further away from the correct local equilibrium distribution.

Note that overrelaxation can occur only due to the discretisation of time. With the continuous BGK operator, the distribution function f is always relaxed *towards* $f^{(0)}$, but never *past* it. Therefore, the continuous BGK operator is not potentially unstable in the same way as the discrete BGK operator.

Before the discrete BGK operator became common, the collision operator was often written in a more general way using a collision matrix Ω_{ij} [8],

$$f_i(\boldsymbol{x}+\boldsymbol{\xi}_i, t+1) - f_i(\boldsymbol{x}, t) = \sum_j \Omega_{ij} \left(f_j - f_j^{(0)} \right). \tag{4.53}$$

The collision matrix acts on the nonequilibrium distribution vector $f_j - f_j^{(0)}$, resulting in a vector of changes to the distribution function. Other linear discrete collision operators, including BGK, can be found as a special case of this general linear discrete collision operator. In the BGK case, $\Omega_{ij} = -\delta_{ij}/\tau$.

A number of alternative, more complex collision operators have been proposed to improve on the occasionally problematic BGK operator, though they generally build on the same principle of relaxing towards equilibrium. We will briefly go through the main ones as they all give a valuable additional understanding of the LB method.

4.3.1 Multiple relaxation time

Multiple relaxation time (MRT) operators evolved out of early experiments with general collision operators as described by (4.53) [8]. The distribution functions f_i can be represented as a q-dimensional vector $\boldsymbol{f}$, which can be transformed to another basis. With MRT models, this basis is q hydrodynamic and nonhydrodynamic moments of f_i.

The hydrodynamic moments are typically $\Pi_0 = \rho$, $\Pi_\alpha = \rho \boldsymbol{u}$, and $\Pi_{\alpha\beta}$, the moments which are relevant for the link to hydrodynamics. The nonhydrodynamic moments are not directly relevant for the hydrodynamics behaviour of the model, but must usually be present to fill out the moment basis.

The relaxation to equilibrium is performed in the moment basis instead of the $\boldsymbol{f}$ basis like the BGK operator. After relaxation, the moments are then transformed back to the f_i basis for streaming. The advantage of relaxing in the moment basis is that different moments can be relaxed at different rates.

The transformation to moment basis is done using the moment transformation matrix M_{ij}, where

$$\boldsymbol{M}\boldsymbol{f} = \boldsymbol{m}, \qquad \boldsymbol{M}\boldsymbol{f}^{(0)} = \boldsymbol{m}^{(0)}. \tag{4.54}$$

$\boldsymbol{m}$ and $\boldsymbol{m}^{(0)}$ are the resulting moment vectors of the transformation.

The simplest possible practical example is the D1Q3 velocity set described in section 4.1.3. Slightly abusing the notation of the indices of f_i by using $f_+ = f_1$ for the particles moving in the $+x$-direction and $f_- = f_2$ for those moving in the $-x$-direction, (4.54) becomes

$$\begin{bmatrix} 1 & 1 & 1 \\ -1 & 0 & 1 \\ 1 & 0 & 1 \end{bmatrix} \begin{bmatrix} f_- \\ f_0 \\ f_+ \end{bmatrix} = \begin{bmatrix} \rho \\ \rho u \\ \Pi_{xx} \end{bmatrix}, \tag{4.55a}$$

$$\begin{bmatrix} 1 & 1 & 1 \\ -1 & 0 & 1 \\ 1 & 0 & 1 \end{bmatrix} \begin{bmatrix} f_-^{(0)} \\ f_0^{(0)} \\ f_+^{(0)} \end{bmatrix} = \begin{bmatrix} \rho \\ \rho u \\ \Pi_{xx}^{(0)} \end{bmatrix}. \tag{4.55b}$$

D1Q3 can be handily transformed into a fully hydrodynamic basis. However, other velocity sets also need some nonhydrodynamic moments to fill out the moment basis, as the number of hydrodynamic quantities is smaller than the number of velocities.

For instance, D2Q9 has six independent hydrodynamic variables: $\breve{\Pi}_0$, $\breve{\Pi}_x$, $\breve{\Pi}_y$, $\breve{\Pi}_{xx}$, $\breve{\Pi}_{xy}$, and $\breve{\Pi}_{yy}$. The other three possible moments needed to fill out the basis cannot be entirely hydrodynamic, as they have to be linearly independent from the fully hydrodynamic moments which have been accounted for already. Choosing $\breve{\Pi}_{xxy}$, $\breve{\Pi}_{xyy}$, and $\breve{\Pi}_{xxyy}$ for the other moments as in [83, Ch. 4], we get

$$\begin{bmatrix} 1 & 1 & 1 & 1 & 1 & 1 & 1 & 1 & 1 \\ 0 & 1 & 0 & -1 & 0 & 1 & -1 & -1 & 1 \\ 0 & 0 & 1 & 0 & -1 & 1 & 1 & -1 & -1 \\ 0 & 1 & 0 & 1 & 0 & 1 & 1 & 1 & 1 \\ 0 & 0 & 0 & 0 & 0 & 1 & -1 & 1 & -1 \\ 0 & 0 & 1 & 0 & 1 & 1 & 1 & 1 & 1 \\ 0 & 0 & 0 & 0 & 0 & 1 & 1 & -1 & -1 \\ 0 & 0 & 0 & 0 & 0 & 1 & -1 & -1 & 1 \\ 0 & 0 & 0 & 0 & 0 & 1 & 1 & 1 & 1 \end{bmatrix} \begin{bmatrix} f_0 \\ f_1 \\ f_2 \\ f_3 \\ f_4 \\ f_5 \\ f_6 \\ f_7 \\ f_8 \end{bmatrix} = \begin{bmatrix} \breve{\Pi}_0 \\ \breve{\Pi}_x \\ \breve{\Pi}_y \\ \breve{\Pi}_{xx} \\ \breve{\Pi}_{xy} \\ \breve{\Pi}_{yy} \\ \breve{\Pi}_{xxy} \\ \breve{\Pi}_{xyy} \\ \breve{\Pi}_{xxyy} \end{bmatrix}. \tag{4.56}$$

Ghost modes
Nonhydrodynamic behaviour that coexists with the hydrodynamic behaviour in LB simulations

The nonhydrodynamic moments are often called *ghost modes*. These moments are not relevant to the Chapman-Enskog expansion, and therefore affect the fluid behaviour in LB simulations only indirectly. Using the discrete BGK collision operator, these moments decay to equilibrium with the relaxation time τ, like the other moments.

The $q \times q$ collision matrix $\boldsymbol{\Omega}$ is assumed to be diagonalisable, or expressable as

$$\boldsymbol{\Omega} = \boldsymbol{M}^{-1}\boldsymbol{T}\boldsymbol{M} \tag{4.57}$$

where the *relaxation matrix* $\boldsymbol{T}$ is usually diagonal.

Relaxation matrix
The matrix in the MRT collision operator containing individual relaxation times for each moment

The generalised LBE (4.53), left-multiplied with $\boldsymbol{M}$, results in a relaxation equation in moment space,

$$\boldsymbol{m}_{\text{out}} = \boldsymbol{m} + \boldsymbol{T}\left(\boldsymbol{m} - \boldsymbol{m}^{(0)}\right). \tag{4.58}$$

$\boldsymbol{m}_{\text{out}}$ can be seen as the post-collision moment vector, or the moment vector of the particles being streamed out of the node. We see that each element in the diagonal matrix $\boldsymbol{T}$ is a relaxation time for one of the moments in $\boldsymbol{m}$. In the BGK special case, all relaxation times are equal, and $\boldsymbol{T} = -\frac{1}{\tau}\boldsymbol{I}$ so that

$$\boldsymbol{\Omega} = -\frac{1}{\tau}\boldsymbol{M}^{-1}\boldsymbol{I}\boldsymbol{M} = -\frac{1}{\tau}\boldsymbol{I};$$

the case mentioned previously.

More generally, the different moments can have different relaxation times. For the conserved moments, the relaxation times do not matter, as $\rho = \rho^{(0)}$ and $\boldsymbol{u} = \boldsymbol{u}^{(0)}$. For symmetry reasons, the non-conserved hydrodynamic moments $\Pi_{\alpha\beta}$ should all have the same relaxation time;* from section 4.1.2 we have that the relaxation of this second order moment determines the viscosity of the model.

The post-collision moments $\boldsymbol{m}_{\text{out}}$ cannot be propagated directly, and must be converted back to the distribution function basis like $\boldsymbol{f} = \boldsymbol{M}^{-1}\boldsymbol{m}$ before streaming. Thus, in principle, the MRT algorithm works by streaming, conversion to moment basis, relaxation of the moments, conversion back to the distribution function basis, and streaming again. In practice, it is more efficient to compute $\boldsymbol{\Omega}$ directly and perform the relaxation as in (4.53).

The usefulness of MRT lies in setting different relaxation times for the different nonhydrodynamic moments. For a given lattice and a given moment basis, an analysis can be carried out to find the optimal nonhydrodynamic relaxation times to optimise certain aspects of the behaviour of the LB method [83–86].

A downside is that such analyses do not give universal results. The results are specific to each velocity set, each choice of moment basis, and each desired optimal behaviour. These analyses can also be difficult both to perform and to comprehend.

However, one simple general-purpose choice that can vastly improve the accuracy and stability of the LBM is to choose a relaxation time of 1

*Note however that it is possible to use some special techniques when relaxing $\Pi_{\alpha\beta}$ to allow setting the shear and bulk viscosity independently [83, Ch. 4].

for the nonhydrodynamic moments [8, 78]. Thus, the nonhydrodynamic moments are always fully relaxed in each time step instead of oscillating analogously to the underrelaxation shown in Figure 4.4. In section 6.3 we shall look at a case where this choice allows accurate simulations with $\tau = 1/2$, i.e. with no viscosity at all.

One argument leveled against MRT is that it is a numerical technique with no corresponding physical basis in kinetic theory [87]. However, that does not in itself make the method less valuable.

4.3.2 Regularised

The regularised collision operator [76, 88, 89]* is based on a different idea than the MRT operator. The idea is to fully reconstruct the distribution function in the collision step,

$$f_i(\boldsymbol{x} + \boldsymbol{\xi}_i, t+1) = \left(f_i^{(0)} + f_i^{[1]}\right) - \frac{1}{\tau} f_i^{[1]}. \tag{4.59}$$

By comparing this scheme with (4.32), we see that $f_i^{[1]}$ has been substituted for $f_i^{\text{neq}} = f_i - f_i^{(0)}$. $f_i^{[1]}$ is an approximation for $f_i^{(1)}$, constructed from the incoming distribution functions f_i.

$f_i^{(1)}$ itself can be found from the Chapman-Enskog expansion of the lattice Boltzmann equation, similarly to how $f^{(1)}$ was found in section 3.8.1. The construction is designed so that $f_i^{[1]}$ only contains the $\Pi_{\alpha\beta}$ terms from $f_i^{(1)}$ that are necessary to reproduce the correct momentum equation.

The details of how $f_i^{[1]}$ is constructed are somewhat complicated and can be found elsewhere [76], but the result is

$$f_i^{[1]} = \frac{w_i}{2c_0^4}\left(\xi_{i\alpha}\xi_{i\beta} - c_0^2\delta_{\alpha\beta}\right)\sum_j \xi_{j\alpha}\xi_{j\beta}\left(f_j - f_j^{(0)}\right), \tag{4.60}$$

resulting in a regularised lattice Boltzmann equation

$$\begin{aligned} &f_i(\boldsymbol{x} + \boldsymbol{\xi}_i, t+1) \\ &= f_i^{(0)} + \frac{(1-1/\tau)w_i}{2c_0^4}\left(\xi_{i\alpha}\xi_{i\beta} - c_0^2\delta_{\alpha\beta}\right)\sum_j \xi_{j\alpha}\xi_{j\beta}\left(f_j - f_j^{(0)}\right). \end{aligned} \tag{4.61}$$

While the principle of the regularised collision operator is different from that of the MRT operator, the regularised operator can also be expressed as a general linear LB collision operator as in (4.53) and be analysed using MRT principles. The result is that the regularised scheme

*The principles behind the regularised collision operator have also been presented in different contexts in other articles [90, 91].

is equivalent to the aforementioned general-purpose MRT scheme that relaxes the second order moments $\Pi_{\alpha\beta}$ with a relaxation time τ, and the other moments with a relaxation time of 1 [76, 89].

This tells us that $f_i^{[1]}$ can be seen as an *improved* approximation to $f_i^{(1)}$. Both have the same moment $\Pi_{\alpha\beta}$, but $f_i^{[1]}$ is constructed with the ghost modes set directly to equilibrium.

The regularised collision operator offers an interesting insight to the LB method. However, since it is in practice equivalent to the aforementioned simple general-purpose MRT method, which one to use of the two is to some degree a matter of taste and familiarity.

4.3.3 Entropic

There are several different approaches to entropic LB methods (e.g. [75, 82]). Only their common general concepts will be presented here as a brief overview. For details on the implementation of entropic methods it will be necessary to refer to the literature.

The original motivation for introducing entropic LB methods was to improve the stability of LB methods. In the process of discretising the Boltzmann equation in velocity and physical space, the $\mathcal{H}$-theorem is lost, and the direct discrete analogue of (3.62),

$$\sum_i f_i \ln f_i$$

is not a valid $\mathcal{H}$-function [82]. Instead other appropriate functions must be found that can play the role of entropy. Such functions must be convex, i.e. monotonically decreasing towards their minimum, which corresponds to the highest "entropy". The value of f_i at this minimum thus defines the equilibrium distribution function $f_i^{(0)}$.

An entropic LB method is therefore based on specifying a valid alternative $\mathcal{H}$ function, finding $f_i^{(0)}$ as its minimum (either implicitly [82] or explicitly [75]), and ensuring that $\mathcal{H}$ is never increased in the collision step. With the BGK collision operator, it is possible for the $\mathcal{H}$ function to increase in collisions when overrelaxing, especially when τ is close to the stability limit of $\tau = 1/2$.* Therefore, there can be a boundary on the lowest possible value of τ; the one where the post- and pre-collision values of $\mathcal{H}$ are the same.

*Even if $\mathcal{H}$ is monotonically decreasing towards $f_i^{(0)}$, it is not necessarily *symmetric* around $f_i^{(0)}$. Since overrelaxation moves f_i *past* $f_i^{(0)}$, strong overrelaxation could move f_i to a point where $\mathcal{H}$ is higher than before.

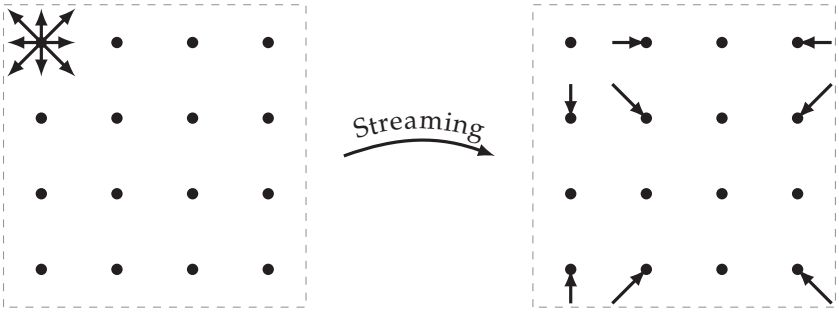

Figure 4.5: A fully periodic D2Q9 lattice of 4 × 4 nodes. The upper left node is connected to "neighbouring" nodes on the opposite edges of the lattice.

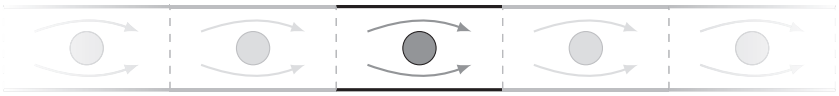

Figure 4.6: A system with periodic boundaries emulates an infinitely large periodic system.

4.4 Simple boundary conditions

Obviously, the lattice Boltzmann method cannot simulate infinitely large systems. The system size must be finite, and the edges of the system must be handled by applying some boundary condition (BC). Many of these boundary conditions may also be applied within the fluid, for instance to create walls with no-slip boundary conditions where $\boldsymbol{u} = \mathbf{0}$.

The literature on various LB boundary conditions is extensive, and we will only go into the bare minimum here, referring to other boundary conditions at the end of this section.

In every time step, unknown particles distributions f_i enter the finite system from imaginary nodes on the outside. A LB boundary condition must at least specify the value of these unknown incoming particle distributions, and the entire boundary of the system must be covered by such boundary conditions.

Periodic BC
A boundary condition where the edge of the system is connected to the opposite edge

The simplest boundary condition is the periodic one, where the edge of the system is connected to the opposite edge. Thus, a node on the edge of the system streams some of its particles to nodes at the other side of the system, as shown in Figure 4.5.

Having a periodic boundary, where information that leaves on one side re-enters on the other, is equivalent to having an identical copy of the system on both sides of itself. In the case shown in Figure 4.6,

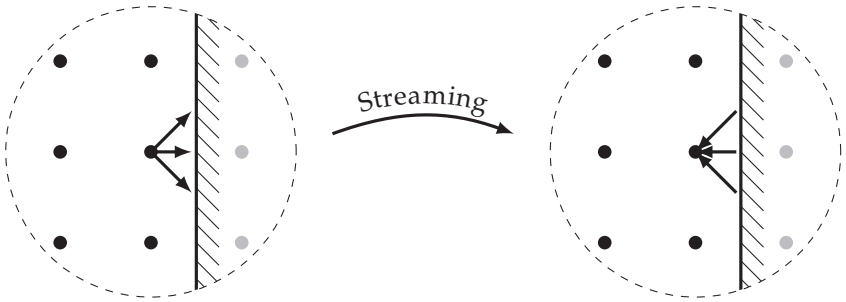

Figure 4.7: Mid-grid bounceback. The distributions streamed towards the wall rebound and reappear with opposite velocity in their node of origin after streaming.

with hard walls on two sides and periodic boundaries on the other two, the simulation emulates an infinitely long periodic duct, with the actual simulated system as a section of this.

Simple no-slip boundary conditions can be implemented in LB simulations through the principle of *bounceback*. While there are many variations on bounceback BCs with varying capabilities and accuracy [92], they all share the idea of bouncing particles back to their node of origin.

Bounceback BCs
Boundary conditions where no-slip walls are achieved by reflecting particles back the way they came

One bounceback method which is simple to implement and retains the second-order accuracy of the LB scheme is the mid-grid bounceback BC [78]. With this method, walls can be placed at the centrelines between nodes. Whenever particle distributions are streamed towards such walls, they reappear after streaming in their node of origin with their velocities reversed, as shown in Figure 4.7.

We can look at this reflection of particles from several perspectives. One is that the particles stream towards the wall, hit it at time $t + 1/2$, have their velocity reversed, and reappear at time $t + 1$ in the node where they began. Thus, the wall should be exactly in between the nodes. Another perspective is that the particles propagate through the wall, but that "ghost" nodes on the other side (marked in grey in Figure 4.7) stream identical particle distributions back. Thus, at $t + 1/2$, the particle distributions that meet at the wall cancel each other's velocity out, resulting in a net fluid velocity $\boldsymbol{u} = \mathbf{0}$ at the wall.

We can conceptually separate the particle bounceback into normal bounceback and tangential bounceback. The bounceback in the normal direction ensures that the normal component of the fluid velocity is zero. It therefore also ensures that the walls actually block the fluid, so that no net mass actually enters the wall, and that the particle distributions that enter the fluid from the wall are known. The tangential bounceback ensures that the tangential component of the fluid velocity is zero, resulting in a no-slip condition.

It is also possible to not include the tangential bounceback. Having particles bounce specularly off the wall instead results in a free-slip condition [78], where the normal velocity on the wall is still zero but there is no constraint placed on the tangential velocity. In the field of acoustics, walls are generally assumed to be free-slip for mathematical simplicity, as the acoustic effects of no-slip conditions are usually only particularly relevant for enclosed geometries such as small pipes [24, 25].

A number of other, more complex, boundary conditions may also be used to implement no-slip boundary conditions [93]. However, as their relative accuracy and stability vary between different applications, there is no single method that is superior in every case.

Some simulations require inlets and outlets, where fluid can enter or exit the system with a specified fluid velocity $\boldsymbol{u}$ or density ρ. The Zou-He boundary condition [94] is often used for this purpose. However, this boundary condition has stability problems at high Reynolds numbers [93].

In cases where there is generation of sound waves or similar unsteady flow patterns, such inlet and outlet boundary conditions can cause errors, as they reflect pressure waves back into the simulation domain [95]. To avoid such reflections, we can instead use *non-reflecting boundary conditions* (NRBCs).

Non-reflecting BCs
Boundary conditions that let waves propagate smoothly out of the system without being reflected back in

One widely used type of NRBC throughout computational physics is the *perfectly matched layer*. The concept is to put an absorbing layer around the computational domain. This layer is in principle *perfectly matched* to the medium inside the domain in such a way that an incoming wave should not be reflected due to the difference in material parameters. As the wave propagates into the absorbing layer, it is exponentially damped. Multiple articles have proposed LB implementations of this concept [96, 97]. Other articles have used similar but simpler "sponge layer" areas where the relaxation time τ increases smoothly towards the edge of the domain [98, 99]. The increased τ causes sound waves to be absorbed more quickly, and the gradual increase means that there is little reflection from the layer. However, one disadvantage common to all such methods is that they require a thick layer of many nodes around the computational domain. Since each of these nodes must also be updated in each time step, the required simulation workload and time can increase significantly.

Another type of NRBC is the *characteristic boundary condition*. These take advantage of the fact that the hyperbolic system of conservation equations can be separated into a number of characteristics.* On the boundary, one characteristic belongs to waves entering the system, and the amplitude of such waves can be set to zero. Again, multiple articles have been published on this topic [100, 101].

In addition to these methods, there also exist various other NRBC methods for lattice Boltzmann [102]. It is difficult to know what to

*Such characteristics were previously described in section 4.2.

choose among this smorgasbord of different methods, and there would certainly be room for a review article that compares these different lattice Boltzmann NRBC methods.

Part II

Research

5 Acoustic linearisation analysis

Acoustic linearisation analysis is a mathematical method for studying the absorption and dispersion of propagating sound waves. The goal of this chapter is to apply this method to both the discrete-velocity Boltzmann equation and the lattice Boltzmann equation. In the latter case, we will end up with an equation which very accurately describes how sound propagates in lattice Boltzmann simulations.

Linearisation analysis is based on inserting trial solutions with weakly fluctuating field variables into the governing equations of the medium of propagation. The first article with such an analysis for fluids was Stokes' 1845 article on the fluid stress tensor [21]. From that point on, various theories were advanced for the details of the governing equations of different media. The predictions of sound wave propagation from these governing equations could then be tested by experiments. An account of the research up to 1953, much of which is still fairly current, was given by Truesdell [26].

For gases, the picture of separate, simultaneous effects of viscosity, thermal conduction, and molecular relaxation has been found to successfully describe the absorption and dispersion of sound for frequencies sufficiently low that $Kn = x_{\mathrm{mfp}}/\lambda \ll 1$ [28, 29, 31, 32]. However, for higher frequencies with $Kn \sim 1$ and above, thermoviscous behaviour dominates but the assumptions behind the Navier-Stokes-Fourier model are no longer valid. There is even today a mismatch between current thermoviscous models and measurements at these extreme frequencies [68].

Usually, the field variables are assumed to be on steady-state plane wave form with complex angular frequency $\hat{\omega}$ and wavenumber $\hat{k}$,*

$$\begin{bmatrix} \hat{\rho}(x,t) \\ \hat{u}(x,t) \\ \hat{p}(x,t) \end{bmatrix} = \begin{bmatrix} \rho_0 \\ 0 \\ p_0 \end{bmatrix} + \begin{bmatrix} \hat{\rho}'(x,t) \\ \hat{u}'(x,t) \\ \hat{p}'(x,t) \end{bmatrix} = \begin{bmatrix} \rho_0 \\ 0 \\ p_0 \end{bmatrix} + \begin{bmatrix} \hat{\rho}^\star \\ \hat{u}^\star \\ \hat{p}^\star \end{bmatrix} \mathrm{e}^{\mathrm{i}(\hat{\omega}t - \hat{k}x)}. \tag{5.1}$$

The primed variables, such as $\hat{p}'(x,t) = \hat{p}^\star \, \mathrm{e}^{\mathrm{i}(\hat{\omega}t - \hat{k}x)}$, are assumed to be infinitesimally small, so that any term where they appear more than once can be neglected. By putting such harmonic solutions into the

*As shown in section 2.3.2 the plane wave form is not necessary for forced waves since a complex Helmholtz equation (2.33) can be found for these. Therefore, the wavenumbers found for forced waves are valid for any type of wave, and not merely plane waves.

governing equations, the equations are simplified as $\partial/\partial t \to \mathrm{i}\hat{\omega}$ and $\nabla \to -\mathrm{i}\hat{k}$. These simplified equations can then be solved for $\hat{\omega}$ or $\hat{k}$ to find all possible wavelike modes allowed by the governing equations.

As discussed in section 2.3.2, the real and imaginary parts of the complex frequency and wavenumber are responsible for different effects. Splitting them as

$$\hat{\omega} = \omega + \mathrm{i}\alpha_t, \qquad \hat{k} = k - \mathrm{i}\alpha_x, \tag{5.2}$$

we find

$$\mathrm{e}^{\mathrm{i}(\hat{\omega}t - \hat{k}x)} = \mathrm{e}^{\mathrm{i}(\omega t - kx)}\,\mathrm{e}^{-\alpha_t t}\,\mathrm{e}^{-\alpha_x x}. \tag{5.3}$$

Thus, the imaginary parts of $\hat{\omega}$ and $\hat{k}$ are clearly absorption coefficients in time and space, respectively. The real parts ω and k determine the wave's phase speed,

$$c = \omega/k. \tag{5.4}$$

In the low-frequency limit $\omega \to 0$, $k \to 0$, or in an ideal medium as described by the Euler equations (2.17) and the ideal wave equation (2.25), $\hat{\omega} = \omega_0$ and $\hat{k} = k_0$ are real, and the ideal speed of sound is

$$c_0 = \omega_0/k_0. \tag{5.5}$$

In general, $\hat{\omega}$ and $\hat{k}$ are partly determined by boundary or initial conditions. As described in section 2.3.2 there are two main cases. In the first, $\hat{\omega} = \omega_0$ is real. In the second, $\hat{k} = k_0$ is real.

Forced wave
A wave generated by a source, absorbed exponentially with the distance to this source.

The first case of *forced* or *spatially absorbed* waves is a boundary value problem. In simplified form, there may be a source at $x = 0$ which fluctuates at a single frequency ω_0. The fluid surrounding the source necessarily also fluctuates at this frequency, causing a wave proportional to

$$\mathrm{e}^{\mathrm{i}(\omega_0 t - \hat{k}x)} = \mathrm{e}^{\mathrm{i}(\omega_0 t - kx)}\,\mathrm{e}^{-\alpha_x x} \tag{5.6}$$

to be propagated away from the source.

Free wave
A spatially periodic wave with a spatially constant amplitude which decreases exponentially with time.

The second case of *free* or *temporally absorbed* waves is an initial value problem. At $t = 0$, there exists a plane wave of infinite extent and wavenumber k_0. At $t > 0$, the wave is damped as it propagates, i.e.

$$\mathrm{e}^{\mathrm{i}(\hat{\omega}t - k_0 x)} = \mathrm{e}^{\mathrm{i}(\omega t - k_0 x)}\,\mathrm{e}^{-\alpha_t t}. \tag{5.7}$$

However, it is very difficult to imagine any physical cause of this kind of sound wave.* Even a standing wave needs to be generated by a source, making it a forced wave. Still, the free wave case is useful in benchmarks of numerical methods, as the spatially periodic nature of the wave allows using a small but periodic simulation domain.

*Kelvin-Helmholtz instabilities, caused e.g. by wind blowing over a water surface, are free waves [103, Ch. 5]. However, these are not *sound* waves.

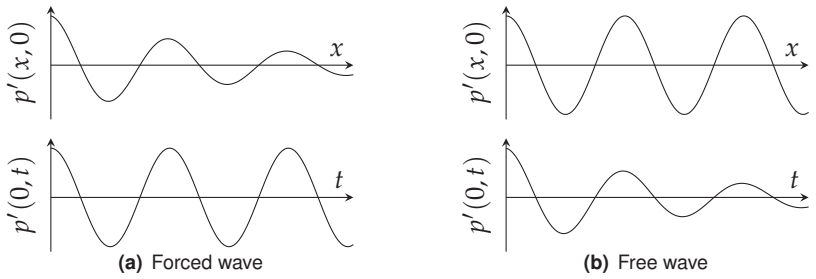

Figure 5.1: Sketch of forced and free waves. Forced waves are absorbed in space, whereas free waves are absorbed with time.

These two cases of *forced waves* and *free waves* are sketched in Figure 5.1. Note that these two types of waves are so physically different that the results for one cannot be used to derive results for the other [26].

With an isothermal equation of state as assumed in Chapter 4 there is no heat conduction. Only viscosity affects the absorption and dispersion of waves, through the *viscous relaxation time*

$$\tau_\nu = \frac{1}{c_0^2}\left(\frac{4}{3}\nu + \nu_\mathrm{B}\right) \tag{5.8a}$$

previously introduced in section 2.3.2. This usually appears together with the frequency ω_0. Together they form the dimensionless *acoustic viscosity number*. Using the notation of [26], this is

Acoustic viscosity number, X
A dimensionless number indicating the effect of viscosity on sound propagation

$$X = \omega_0 \tau_\nu. \tag{5.8b}$$

For audible sound, this number is *very* small: A 20 kHz sound wave in normal air gives $X \sim 10^{-5}$. Only for extremely high ultrasonic frequencies of $\sim 1\,\mathrm{GHz}$ do we get $X \sim 1$.

As $\hat{k}$ and $\hat{\omega}$ turn out to be functions of X only, it is useful to compare their expressions for different models of the form of series expansions around $X = 0$,

$$\begin{aligned} \frac{\hat{k}}{k_0} &= 1 + a_1 X + a_2 X^2 + a_3 X^3 + a_4 X^4 + \mathcal{O}(X^5), \\ \frac{\hat{\omega}}{\omega_0} &= 1 + b_1 X + b_2 X^2 + b_3 X^3 + b_4 X^4 + \mathcal{O}(X^5). \end{aligned} \tag{5.9}$$

The exact expressions can be both extremely cumbersome and hard to compare.

Relating the viscosity to the mean free path x_mfp [62], a closer look at X reveals that

$$\left.\begin{aligned} \omega_0 &\sim c_0/\lambda \\ \nu \sim \nu_\mathrm{B} &\sim c_0 x_\mathrm{mfp} \end{aligned}\right\} \quad \Rightarrow \quad X \sim \frac{x_\mathrm{mfp}}{\lambda} = Kn. \tag{5.10}$$

Therefore, the acoustic viscosity number X represents an acoustic Knudsen number, which relates the mean molecular collision distance x_{mfp} with the acoustic wavelength λ. For the extremely high frequencies where $X \sim 1$, the wavelength is comparable to the "fine-grainedness" of the gas in which it is propagating.

In section 3.8 on the Chapman-Enskog expansion we showed that the Euler model is only valid to $O(Kn^0) = O(X^0)$. With the ideal acoustics that follow from this model, we find $\hat{k}/k_0 = 1$ and $\hat{\omega}/\omega_0 = 1$. Above $O(X^0)$, where the model cannot be trusted, it makes an incorrect prediction. Similarly, the Navier-Stokes-Fourier model was shown valid only to $O(Kn^1) = O(X^1)$; its predictions above this order in X are not to be trusted [27].

A similar technique to this linearisation analysis, called *Von Neumann analysis*, is used in numerical analysis [104, Chs. 9 & 10]. There, a wavelike trial solution is inserted into a discrete numerical scheme to examine how the solution would evolve in time. The main purpose of this analysis is usually to determine the stability limit of the numerical scheme; beyond this limit the unstable solution may *increase* exponentially in time instead of remaining constant or decreasing as above. The analysis can also determine the artificial dispersion and absorption that may be caused by discretisation error in the numerical scheme.

Von Neumann analysis
A technique in numerical analysis to determine the numerical stability, numerical absorption, and numerical dispersion of a numerical scheme.

With the lattice Boltzmann equation, the linearisation analysis of sound propagation will let us separate the effects of the physical model from such discretisation errors stemming from the numerical scheme.

For the reader who does not wish to read through everything, the end products of the LBE analysis come from the eigenvalue problem (5.59). Two equations on the series expansion form of (5.9) are found: (5.63) for forced waves, and (5.64) for free waves. These series expansions can be used to predict the wavenumber or frequency in lattice Boltzmann simulations with good accuracy. For the forced wave case, a slightly cumbersome but exact solution (5.62) is also available.

Many of the calculations later on in this chapter are far too complicated to carry out by hand, and therefore the computer algebra system Maple was used for these. In some cases, the results were so cumbersome that they would require an unfeasible amount of space to display here. When necessary, these results will be presented here in series expansion form instead.

5.1 Isothermal Navier-Stokes-Fourier model

From the Navier-Stokes-Fourier model (2.19), a viscous (2.32) and a thermoviscous (2.41) wave equation can be found. In the isothermal case, the energy equation and its corresponding thermal effects are not relevant,

and the viscous wave equation

$$\frac{1}{c_0^2}\frac{\partial^2 p'}{\partial t^2} - \left(1 + \tau_\nu \frac{\partial}{\partial t}\right)\nabla^2 p' = 0 \tag{5.11}$$

describes sound propagation with no approximations other than linearisation. While the acoustic behaviour of this model is well-known [24–26], its analysis will be instructive.

5.1.1 Absorption and dispersion

Dispersion relation
An equation connecting the angular frequency $\hat{\omega}$ and the wavenumber $\hat{k}$

Inserting the trial solution (5.1) into the viscous wave equation, we immediately find a *dispersion relation*

$$-\frac{\hat{\omega}^2}{c_0^2} + (1 + \mathrm{i}\hat{\omega}\tau_\nu)\,\hat{k}^2 = 0. \tag{5.12}$$

This relation can be solved easily for either forced waves or free waves.

Forced waves

If the frequency is assumed real, we find the complex wavenumber

$$\boxed{\frac{\hat{k}}{k_0} = \pm\frac{1}{\sqrt{1 + \mathrm{i}X}}, \qquad \hat{\omega} = \omega_0.} \tag{5.13}$$

Here, the $\pm$ sign corresponds directly to propagation direction. This relation holds in general, not only for the plane wave trial solution: In section 2.3.2 it was derived through the complex Helmholtz equation (2.33), which is independent of the spatial form of the solution.

The positive solution above, which corresponds to a wave propagating in the $+x$-direction, predicts an absorption and dispersion of

$$\frac{\alpha_x}{k_0} = \sqrt{\frac{\sqrt{1+X^2}-1}{2+2X^2}}, \qquad \frac{c}{c_0} = \frac{k_0}{k} = \sqrt{\frac{2+2X^2}{\sqrt{1+X^2}+1}}. \tag{5.14}$$

At very high frequencies where $X \gg 1$, this predicts that the phase speed increases as $\sqrt{X}$. This implies that the phase speed grows with the frequency without bound, which is clearly unphysical. Still, incorrect predictions at very high frequencies could be expected, since we know that the Navier-Stokes-Fourier model is only valid for $X \ll 1$.

In the series expanded form of (5.9), (5.13) becomes

$$\tfrac{\hat{k}}{k_0} = 1 - \mathrm{i}\tfrac{1}{2}X - \tfrac{3}{8}X^2 + \mathrm{i}\tfrac{5}{16}X^3 + \tfrac{35}{128}X^4 + \mathcal{O}(X^5). \tag{5.15}$$

Free waves

If the wavenumber is assumed real, we find the complex frequency

$$\boxed{\frac{\hat{\omega}}{\omega_0} = \mathrm{i}\frac{X}{2} \pm \sqrt{1 - \left(\frac{X}{2}\right)^2}, \qquad \hat{k} = k_0.} \tag{5.16}$$

Again, the $\pm$ sign corresponds to propagation direction. The imaginary part is always positive, so that the wave amplitude always *decreases* with time.

One surprising feature of this solution is that it predicts that free waves cannot propagate beyond $X = 2$. At this point, the real part of $\hat{\omega}$ vanishes, resulting in a fully imaginary solution. For $0 < X < 2$, the absorption coefficient and dispersion are

$$\frac{\alpha_t}{\omega_0} = \frac{X}{2}, \qquad \frac{c}{c_0} = \frac{\omega}{\omega_0} = \sqrt{1 - \left(\frac{X}{2}\right)^2}. \tag{5.17}$$

While the phase speed was predicted to increase with X for forced waves, we see that the phase speed for free waves is predicted to *decrease* with X.

In series expanded form, (5.16) is

$$\tfrac{\hat{\omega}}{\omega_0} = 1 + \mathrm{i}\tfrac{1}{2}X - \tfrac{1}{8}X^2 - \tfrac{1}{128}X^4 + \mathcal{O}(X^6). \tag{5.18}$$

In the series expansions for both forced and free waves, there is a clear pattern of even terms in X being real and odd terms being imaginary. This pattern also applies beyond $\mathcal{O}(X^5)$, and seems to continue indefinitely. Thus, even terms affect dispersion and odd terms affect absorption. We will see that this pattern also holds for the other models considered in this chapter.

5.1.2 Magnitude ratios and phase differences

Not only does an increase in X cause absorption and dispersion, it also affects the complex amplitudes of the wave components: momentum $\rho_0\hat{u}^\star$, density $\hat{\rho}^\star$, and pressure $\hat{p}^\star$.

As explained in section 2.3.1 and shown in Figure 5.2, the magnitude of these complex amplitudes, e.g. $|\hat{\rho}^\star|$, determines the physical amplitude, while their complex phase angles or *arguments*, e.g. $\arg(\hat{\rho}^\star)$, determines the physical phase shift.

Argument
A mathematical function that returns the complex angle of a complex number, e.g. $\arg(\hat{z}) = \varphi$ for $\hat{z} = r\,\mathrm{e}^{\mathrm{i}\varphi}$

Therefore, $|\rho_0\hat{u}^\star/\hat{\rho}^\star| = |\rho_0\hat{u}^\star|/|\hat{\rho}^\star|$ represents the ratio of the physical amplitudes of the momentum and density components of the wave, and $\arg(\rho_0\hat{u}^\star/\hat{\rho}^\star) = \arg(\rho_0\hat{u}^\star) - \arg(\hat{\rho}^\star)$ represents the difference in phase of the components. If this phase difference is nonzero, the peaks of the wave components are situated at different positions.

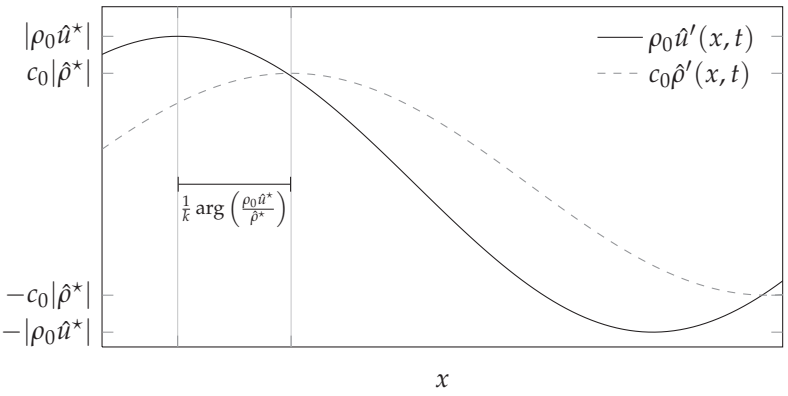

Figure 5.2: Exaggerated sketch of differences in amplitude and phase of the momentum and density components of a wave. For an acoustic viscosity number $X = 0$, corresponding to the Euler model and the ideal wave equation, these differences are zero and the two wave components would overlap.

In the Navier-Stokes-Fourier case, these relative amplitudes can be determined using the mass and momentum conservation equations, which in linearised one-dimensional form are

$$\frac{\partial \rho}{\partial t} + \rho_0 \frac{\partial u}{\partial x} = 0, \tag{5.19a}$$

$$\rho_0 \frac{\partial u}{\partial t} + \frac{\partial p}{\partial x} = \left(\frac{4}{3}\mu + \mu_\mathrm{B}\right) \frac{\partial^2 u}{\partial x^2}. \tag{5.19b}$$

Inserting the trial solutions (5.1) and rearranging, we find

$$\frac{\rho_0 \hat{u}^\star}{\hat{\rho}^\star} = \frac{\hat{\omega}}{\hat{k}}, \tag{5.20a}$$

$$\frac{\hat{p}^\star}{\rho_0 \hat{u}^\star} = \frac{\hat{\omega}}{\hat{k}} - \mathrm{i}\hat{k}\left(\frac{4}{3}\nu + \nu_\mathrm{B}\right). \tag{5.20b}$$

By inserting the forced or free wave solutions of $\hat{k}$ and $\hat{\omega}$ from the previous section, these amplitude ratios become explicit functions of X.

These equations can also be used to relate $\hat{p}^\star$ and $\hat{\rho}^\star$,

$$\frac{\hat{p}^\star}{\hat{\rho}^\star} = \frac{\rho_0 \hat{u}^\star}{\hat{\rho}^\star} \frac{\hat{p}^\star}{\rho_0 \hat{u}^\star} = \left(\frac{\hat{\omega}}{\hat{k}}\right)^2 - \mathrm{i}c_0^2 \hat{\omega} \tau_\nu. \tag{5.20c}$$

This could seem to predict a phase difference between pressure and density, contrary to the isentropic assumption of $p' = c_0^2 \rho'$ which was used to derive the viscous wave equation. However, by inserting any of the two solutions (5.13) or (5.16) and simplifying, we find

$$\frac{\hat{p}^\star}{\hat{\rho}^\star} = c_0^2. \tag{5.20d}$$

Thus, this is still consistent with the original isentropic assumption.*

In fact, the dispersion relation (5.12) can be found directly from (5.20c) and (5.20d). Such an approach will be followed in section 5.2 on the linearisation of the discrete-velocity Boltzmann equation.

Forced waves

Substituting the complex wavenumber (5.13) of the forced wave case into (5.20a), we find the magnitude ratio

$$\begin{aligned} \frac{1}{c_0}\left|\frac{\rho_0\hat{u}^\star}{\hat{\rho}^\star}\right| = \left|\frac{k_0}{\hat{k}}\right| &= \sqrt[4]{1+X^2} \\ &= 1+\tfrac{1}{4}X^2-\tfrac{3}{32}X^4+\mathcal{O}(X^6), \end{aligned} \tag{5.21a}$$

and the phase difference

$$\begin{aligned} \arg\left(\frac{\rho_0\hat{u}^\star}{\hat{\rho}^\star}\right) = \arg\left(\frac{k_0}{\hat{k}}\right) &= \tfrac{1}{2}\arctan(X) \\ &= \tfrac{1}{2}X-\tfrac{1}{6}X^3+\mathcal{O}(X^5). \end{aligned} \tag{5.21b}$$

This shows that the amplitude of the momentum component will increase relative to the amplitude of the density component as X increases. Also, the momentum component of the wave will propagate ahead of the density component for nonzero X.

Free waves

Substituting the complex frequency of the free wave case, we find the magnitude ratio and phase difference

$$\frac{1}{c_0}\left|\frac{\rho_0\hat{u}^\star}{\hat{\rho}^\star}\right| = \left|\frac{\hat{\omega}}{\omega_0}\right| = 1 \qquad \text{for } X \le 2, \tag{5.22a}$$

$$\begin{aligned} \arg\left(\frac{\rho_0\hat{u}^\star}{\hat{\rho}^\star}\right) = \arg\left(\frac{\hat{\omega}}{\omega_0}\right) &= \arctan\left(\frac{X}{\sqrt{4-X^2}}\right) \qquad \text{for } X \le 2 \\ &= \tfrac{1}{2}X+\tfrac{1}{48}X^3+\mathcal{O}(X^5). \end{aligned} \tag{5.22b}$$

As in the forced wave case, the momentum component is ahead of the density component, but the ratio between the momentum and density amplitudes are predicted to be constant.

5.2 Discrete-velocity Boltzmann equation

As seen in section 4.1, the discrete-velocity Boltzmann equation (4.3) (DVBE) is a semi-discretised form of the Boltzmann equation where the continuous velocity space of the Boltzmann equation is restricted to a

*This disproves a statement in one of this author's previous publications [11].

discrete set of velocities. In addition, the equilibrium distribution is approximated as the series (4.2), which is truncated to $\mathcal{O}(u^2)$.

The DVBE can be seen as an intermediary step in the discretisation of the Boltzmann equation. The final step is the lattice Boltzmann equation (LBE), where space and time have also been discretised. Consequently, as the numerical resolution of the LBE is improved, the numerical errors in space and time are reduced and the LBE converges towards the DVBE.

Since the DVBE and isothermal Navier-Stokes-Fourier models do not exactly agree, sound propagation with the LBE will not exactly agree with the Navier-Stokes-Fourier model either, even with an infinitely fine numerical resolution.

The fineness of the discretisation of velocity space and the approximation of the equilibrium distribution determines how well the DVBE can capture the Boltzmann equation. We saw in section 4.1 that the DVBE presented there cannot do any better than the isothermal Navier-Stokes-Fourier model with a $\mathcal{O}(u^3)$ error term. However, with a discrete velocity space containing more velocities and a less truncated equilibrium distribution, the behaviour of the Boltzmann equation could be captured correctly to the Burnett level and beyond [72].

5.2.1 Linearisation process

Analogously to the wavelike trial solution (5.1), let us assume that the solution to the DVBE is of the form

$$\hat{f}_i(x,t) = F_i^{(0)} + \hat{f}_i^{\star}\, \mathrm{e}^{\mathrm{i}(\hat{\omega}t - \hat{k}x)}. \tag{5.23}$$

Here, $\hat{f}_i^{\star}\, \mathrm{e}^{\mathrm{i}(\hat{\omega}t-\hat{k}x)}$ is an infinitesimal fluctuation around the equilibrium rest state $F_i^{(0)}$.*

For this one-dimensional problem it is sufficient to use the D1Q3 velocity set introduced in section (4.1.3), with velocities $(\xi_-, \xi_0, \xi_+) = (-1, 0, 1)$, weighting coefficients $(w_-, w_0, w_+) = (1/6, 2/3, 1/6)$, and speed of sound $c_s = 1/\sqrt{3}$. Since higher-dimensional velocity sets such as D2Q9, D3Q15, D3Q19, and D3Q27 have D1Q3 as their one-dimensional projection, using D1Q3 here is sufficient to predict the behaviour of waves propagating along a main (i.e. x, y, or z) axis in any of these other sets. In section 5.2.5 on the isotropy of the D2Q9 velocity set, this will be demonstrated.

*A note on notation: While rest states have been denoted with a subscripted zero elsewhere, we use a capital "F" here since denoting it as f_0 would lead to confusion with the zero-velocity particle distribution f_0. $F_i^{(0)}$ should not be confused with the body force density $\boldsymbol{F}$, which will not appear in this chapter.

Since the fluctuation is infinitesimal, we can linearise the equilibrium distribution function like in section 4.1.4,

$$\hat{f}_i^{(0)} = w_i \left(\hat{\rho} + \frac{\rho_0 \hat{u}'}{c_0^2} \xi_i \right). \tag{5.24a}$$

This can then be split into two parts associated with the rest state and the fluctuation,

$$F_i^{(0)} = \rho_0 w_i, \tag{5.24b}$$

$$\hat{f}_i^{\star(0)} = w_i \left(\hat{\rho}^\star + \frac{\rho_0 \hat{u}^\star}{c_0^2} \xi_i \right). \tag{5.24c}$$

The moments of this solution are entirely analogous to the previously used trial solution (5.1),

$$\begin{bmatrix} \sum_i \hat{f}_i(x,t) \\ \sum_i \xi_i \hat{f}_i(x,t) \end{bmatrix} = \begin{bmatrix} \hat{\rho}(x,t) \\ \rho_0 \hat{u}(x,t) \end{bmatrix} = \begin{bmatrix} \rho_0 \\ 0 \end{bmatrix} + \begin{bmatrix} \hat{\rho}^\star \\ \rho_0 \hat{u}^\star \end{bmatrix} \mathrm{e}^{\mathrm{i}(\hat{\omega}t - \hat{k}x)}. \tag{5.25}$$

The pressure can be found directly through the isothermal equation of state $p = c_0^2 \rho$, or the pressure fluctuation can equivalently be found from the fluctuation equilibrium distribution (5.24c) using the velocity set constraint (4.11c) as

$$\sum_i \xi_i \xi_i \hat{f}_i^{\star(0)} = \hat{\Pi}_{xx}^{\star(0)} = c_0^2 \hat{\rho}^\star = \hat{p}^\star. \tag{5.26}$$

Inserting the trial solution (5.23) into the DVBE, applying the derivatives and rearranging, we find the *harmonic linearised discrete-velocity Boltzmann equation*,

$$\boxed{\left[1 + \mathrm{i}\tau \left(\hat{\omega} - \hat{k}\xi_i \right) \right] \hat{f}_i^\star = \hat{f}_i^{\star(0)}.} \tag{5.27}$$

This relates the distribution function amplitude $\hat{f}_i^\star$ to its equilibrium counterpart $\hat{f}_i^{\star(0)}$. Due to the presence of ξ_i on the left hand side, any moment of this equation will relate that moment of $\hat{f}_i^\star$ with the moment of one order higher. Thus, it would seem that this equation leads to an infinite hierarchy of moments. However, we will soon see that this is not so, because of the finite number of velocities.

Due to the conservation of mass and momentum, the zeroth and first moments of the fluctuation distribution function and its equilibrium counterpart are identical,

$$\sum_i \hat{f}_i^\star = \sum_i \hat{f}_i^{\star(0)} = \hat{\rho}^\star, \qquad \sum_i \xi_i \hat{f}_i^\star = \sum_i \xi_i \hat{f}_i^{\star(0)} = \rho_0 \hat{u}^\star.$$

Consequently, the zeroth, first, and second moments of (5.27) give

$$\frac{\rho_0 \hat{u}^\star}{\hat{\rho}^\star} = \frac{\hat{\omega}}{\hat{k}}, \tag{5.28a}$$

$$\frac{\hat{\Pi}^\star_{xx}}{\rho_0 \hat{u}^\star} = \frac{\hat{\omega}}{\hat{k}}, \tag{5.28b}$$

$$\hat{\Pi}^\star_{xx} = \frac{c_0^2 \hat{\rho}^\star + \mathrm{i}\hat{k}\tau \hat{\Pi}^\star_{xxx}}{1 + \mathrm{i}\hat{\omega}\tau}. \tag{5.28c}$$

Due to the limited number of velocities, the number of independent moments is also limited. As a consequence, the third moment is non-unique and is given by the first moment,

$$\hat{\Pi}^\star_{xxx} = \sum_i \xi_i \xi_i \xi_i \hat{f}_i^\star = (\tfrac{\Delta x}{\Delta t})^2 \sum_i \xi_i \hat{f}_i^\star = 3c_0^2 \rho_0 \hat{u}^\star. \tag{5.29}$$

Thus, the system of moments (5.28) is closed, and we can find a dispersion relation

$$\left(\frac{\hat{\omega}}{\hat{k}}\right)^2 = \frac{\hat{\Pi}^\star_{xx}}{\hat{\rho}^\star} = \frac{1}{1 + \mathrm{i}\hat{\omega}\tau}\left(\frac{c_0^2 \hat{\rho}^\star + 3\mathrm{i}c_0^2 \hat{k}\tau \rho_0 \hat{u}^\star}{\hat{\rho}^\star}\right) = c_0^2 \frac{1 + 3\mathrm{i}\hat{\omega}\tau}{1 + \mathrm{i}\hat{\omega}\tau}.$$

We can relate the BGK relaxation time τ to the viscous relaxation time τ_ν using the DVBE values of the shear and bulk viscosities,

$$\left.\begin{aligned} \nu &= \tau c_0^2 \\ \nu_\mathrm{B} &= 2\nu/3 \end{aligned}\right\} \quad \Rightarrow \quad \tau_\nu = 2\tau. \tag{5.30}$$

Thus, the above dispersion relation is

$$\boxed{\left(\frac{\hat{\omega}}{\hat{k}}\right)^2 = c_0^2 \frac{1 + 3\mathrm{i}\hat{\omega}\tau_\nu/2}{1 + \mathrm{i}\hat{\omega}\tau_\nu/2}.} \tag{5.31}$$

This may now be used to find expressions for $\hat{k}$ or $\hat{\omega}$ for forced or free waves, respectively.

If $\hat{k}$ and $\hat{\omega}$ are known, the values of $\hat{f}_i^\star$ can also be found if necessary. Adapting (4.55a) and using (5.28),

$$\begin{bmatrix} 1 & 1 & 1 \\ -1 & 0 & 1 \\ 1 & 0 & 1 \end{bmatrix} \begin{bmatrix} \hat{f}_-^\star \\ \hat{f}_0^\star \\ \hat{f}_+^\star \end{bmatrix} = \begin{bmatrix} \hat{\rho}^\star \\ \rho_0 \hat{u}^\star \\ \hat{\Pi}^\star_{xx} \end{bmatrix} = \hat{\rho}^\star \begin{bmatrix} 1 \\ \hat{\omega}/\hat{k} \\ (\hat{\omega}/\hat{k})^2 \end{bmatrix}.$$

Inverting the matrix results in an equation for the values of $\hat{f}_i^\star$,

$$\begin{bmatrix} \hat{f}_-^\star \\ \hat{f}_0^\star \\ \hat{f}_+^\star \end{bmatrix} = \frac{\hat{\rho}^\star}{2} \begin{bmatrix} 0 & -1 & 1 \\ 2 & 0 & -2 \\ 0 & 1 & 1 \end{bmatrix} \begin{bmatrix} 1 \\ \hat{\omega}/\hat{k} \\ (\hat{\omega}/\hat{k})^2 \end{bmatrix} = \hat{\rho}^\star \begin{bmatrix} (\hat{\omega}/\hat{k})^2/2 - \hat{\omega}/2\hat{k} \\ 1 - (\hat{\omega}/\hat{k})^2 \\ (\hat{\omega}/\hat{k})^2/2 + \hat{\omega}/2\hat{k} \end{bmatrix}. \tag{5.32}$$

In the ideal fluid case $X \to 0$, these values are

$$\begin{bmatrix} \hat{f}_-^\star \\ \hat{f}_0^\star \\ \hat{f}_+^\star \end{bmatrix} = \hat{\rho}^\star \begin{bmatrix} (c_0^2 - c_0)/2 \\ 1 - c_0^2 \\ (c_0^2 + c_0)/2 \end{bmatrix}.$$

5.2.2 Properties of forced and free waves

From the dispersion relation (5.31), the absorption and dispersion properties of the DVBE model can be found. In addition, after having found $\hat{k}$ or $\hat{\omega}$, (5.28a) gives us the complex amplitude ratio of the momentum and density wave components.

Forced waves

Assuming $\hat{\omega}$ real and solving (5.31) for $\hat{k}$, we find

$$\boxed{\frac{\hat{k}}{k_0} = \pm\sqrt{\frac{1 + \mathrm{i}X/2}{1 + 3\mathrm{i}X/2}}, \qquad \hat{\omega} = \omega_0.} \tag{5.33a}$$

Again, we have two possible solutions, one for each propagation direction. This wavenumber equation is actually identical in form to the wavenumber equation (2.52) for molecular relaxation processes, with $\tau_\mathrm{m} = \tau$ and $c_\infty/c_0 = \sqrt{3}$. We will soon go into this connection.

As in the molecular relaxation case, the expressions for the real and imaginary parts of $\hat{k}/k_0$ are not simple. We will make do with the series expansion

$$\tfrac{\hat{k}}{k_0} = 1 - \mathrm{i}\tfrac{1}{2}X - \tfrac{5}{8}X^2 + \mathrm{i}\tfrac{13}{16}X^3 + \tfrac{139}{128}X^4 + \mathcal{O}(X^5). \tag{5.33b}$$

A quick comparison with the equivalent Navier-Stokes-Fourier expansion (5.15) shows an agreement at $\mathcal{O}(X)$ but not above. Thus, the same absorption is predicted to the lowest order, but the predicted dispersion is different. A more detailed comparison is deferred to section 5.2.4.

The magnitude ratios and phase differences found from the solution are

$$\tfrac{1}{c_0}\left|\tfrac{\rho_0 \hat{u}^\star}{\hat{\rho}^\star}\right| = \left|\tfrac{k_0}{\hat{k}}\right| = 1 + \tfrac{1}{2}X^2 - \tfrac{1}{2}X^4 + \mathcal{O}(X^6), \tag{5.33c}$$

$$\arg\left(\tfrac{\rho_0 \hat{u}^\star}{\hat{\rho}^\star}\right) = \arg\left(\tfrac{k_0}{\hat{k}}\right) = \tfrac{1}{2}X - \tfrac{13}{24}X^3 + \mathcal{O}(X^5). \tag{5.33d}$$

Free waves, propagating mode

In the free wave case, $\hat{k}$ is assumed real and (5.31) is solved for $\hat{\omega}$. An examination of the equation reveals that it is a cubic equation in $\hat{\omega}$, with

three solutions. These solutions become very cumbersome and are most easily found using computer assistance.

The three different solutions correspond to three modes of propagation. As in the Navier-Stokes-Fourier case, two of these modes correspond to normal plane wave propagation in the $\pm x$-direction. However, there is also a third, *non-propagating* solution where $\omega = \mathrm{Re}(\hat{\omega}) = 0$.

We first consider the solution that propagates in the x-direction. As the exact solution is too cumbersome, we go directly to the series expansion,

$$\boxed{\frac{\hat{\omega}}{\omega_0} = 1 + \mathrm{i}\tfrac{1}{2}X + \tfrac{1}{8}X^2 + \mathrm{i}\tfrac{1}{8}X^3 + \tfrac{15}{128}X^4 + \mathcal{O}(X^5), \qquad \hat{k} = k_0.} \tag{5.34a}$$

Again we can find by comparison with the Navier-Stokes-Fourier equivalent (5.16) that the expansions agree only to $\mathcal{O}(X)$.

The magnitude ratios and phase differences found from this solution are

$$\tfrac{1}{c_0}\left|\tfrac{\rho_0\hat{u}^\star}{\hat{p}^\star}\right| = \left|\tfrac{\hat{\omega}}{\omega_0}\right| = 1 + \tfrac{1}{4}X^2 + \tfrac{5}{32}X^4 + \mathcal{O}(X^6), \tag{5.34b}$$

$$\arg\left(\tfrac{\rho_0\hat{u}^\star}{\hat{p}^\star}\right) = \arg\left(\tfrac{\hat{\omega}}{\omega_0}\right) = \tfrac{1}{2}X + \tfrac{1}{48}X^3 + \mathcal{O}(X^5). \tag{5.34c}$$

Free waves, diffusive mode

The purely imaginary solution corresponds to a mode where the waves do not propagate, they are merely absorbed. This solution is therefore *diffusive*, similarly to solutions of the heat equation. Even so, this solution is not related to diffusion of heat, which cannot happen in the isothermal DVBE.

On series expansion form, the diffusive solution is

$$\boxed{\frac{\hat{\omega}}{\omega_0} = \mathrm{i}2X^{-1} - \mathrm{i}X - \mathrm{i}\tfrac{1}{4}X^3 + \mathcal{O}(X^5), \qquad \hat{k} = k_0.} \tag{5.35a}$$

Note that the absorption coefficient goes to infinity as $X \to 0$. Thus, for immediate relaxation to equilibrium, this mode is *absorbed instantly*.

The magnitude ratios and phase differences are also on a substantially different form than previously,

$$\tfrac{1}{c_0}\left|\tfrac{\rho_0\hat{u}^\star}{\hat{p}^\star}\right| = \left|\tfrac{\hat{\omega}}{\omega_0}\right| = 2X^{-1} - X - \tfrac{1}{4}X^3 + \mathcal{O}(X^5), \tag{5.35b}$$

$$\arg\left(\tfrac{\rho_0\hat{u}^\star}{\hat{p}^\star}\right) = \arg\left(\tfrac{\hat{\omega}}{\omega_0}\right) = \tfrac{\pi}{2}. \tag{5.35c}$$

For low X, the momentum component of the wave dominates over the density component. Also, the two components are out of phase by $\pi/2$, so that the peaks and troughs in one coincide with zeroes in the other.

5.2.3 Comparison with relaxation processes

Section 2.3.3 described how relaxation processes affect absorption and dispersion. In gases, the nature of such processes is usually the transfer of energy between translational and inner (i.e. vibrational and rotational) degrees of freedom of the gas molecules. For a single relaxation process with no additional thermoviscous effects, the result is the relaxation wave equation (2.51),

$$\tau_{\mathrm{m}} \frac{\partial}{\partial t} \left(\frac{\partial^2 p'}{\partial t^2} - c_\infty^2 \nabla^2 p' \right) + \left(\frac{\partial^2 p'}{\partial t^2} - c_0^2 \nabla^2 p' \right) = 0.$$

Here, τ_{m} is the relaxation time of the process, and c_∞ is the "frozen" speed of sound. The latter occurs at frequencies where $\omega_0 \tau_{\mathrm{m}} \gg 1$, frequencies so high that the relaxation process cannot keep up with the rapid changes in translational energy. Consequently, the inner energy is stationary, or "frozen".

Inserting the plane wave trial solution (5.1) into this wave equation, applying the derivatives and rearranging results in a dispersion relation for relaxation,

$$\left(\frac{\hat{\omega}}{\hat{k}} \right)^2 = c_0^2 \frac{1 + \mathrm{i}\hat{\omega}\tau_{\mathrm{m}} (c_\infty / c_0)^2}{1 + \mathrm{i}\hat{\omega}\tau_{\mathrm{m}}}. \tag{5.36}$$

A comparison with the corresponding DVBE dispersion relation (5.31) shows that the two equations are identical, with the substitutions $c_\infty / c_0 = \sqrt{3}$ and $\tau_{\mathrm{m}} = \tau_\nu / 2 = \tau$. Thus, the wave modes found for the DVBE case correspond exactly to the wave modes of for a single relaxation process without any thermoviscous influence.

While this connection would seem significant, it is not clear what it *means*. The DVBE and relaxation cases are not very similar. The major similarity is that both cases involve relaxation to a changing equilibrium state. However, the DVBE gives a macroscopic stress tensor with viscosity like the isothermal Navier-Stokes-Fourier model, while the relaxational wave equation does not. It is based on the more limited Euler model with a non-isothermal relaxational equation of state.

By some early authors, absorption and dispersion in fluids was assumed to stem completely from relaxational phenomena. Absorption was assumed to occur only "when the density gets out of phase with the pressure" [105]. Even the effect of viscosity was treated in this way, though it can be shown not to cause a phase lag between density and pressure in the limit of weak waves [25, Ch. 9]. Even though such assumptions may have been wrong in general [26], a relaxation model could successfully be made to fit either the absorption or the dispersion of a purely thermoviscous model to lowest order [22]. As we soon shall see, the DVBE fits the absorption to lowest order when the shear viscosity is matched as $\mu = p\tau$.

5.2.4 Comparison to other models

With known sound propagation behaviour for the Navier-Stokes-Fourier, DVBE, and single relaxation models, a comparison is now possible. It is not necessary to consider relaxation separately from the DVBE, as we have shown them to qualitatively predict the same type of absorption and dispersion.

Forced waves

Maxwell molecules
Molecules with a particular form of the intermolecular force field which simplifies Boltzmann's original collision operator

This section is augmented by calculations done by Greenspan [27] for forced waves with the Burnett model. He found equations for $\hat{k}/k_0$ for ideal gases of *Maxwell molecules* with otherwise arbitrary material properties. To adapt his expressions to our isothermal case, we set $\gamma = 1$ as in (4.1). From (2.46) and (2.47), this implies heat capacities which go to infinity, which determines Greenspan's *thermal Reynolds number* as $1/s \to 0$. Finally, Greenspan's assumption of zero bulk viscosity determines his *viscous Reynolds number* as $1/r = 3\gamma X/4$.

With these assumptions, Greenspan's Navier-Stokes-Fourier model is identical to the one described in section 5.1. His dispersion relation for forced waves with the Burnett model becomes the biquadratic equation

$$\tfrac{3}{4}\left(\tfrac{\hat{k}}{k_0}\right)^4 X^2 + \left(\tfrac{\hat{k}}{k_0}\right)^2 (1 + \mathrm{i}X) - 1 = 0,$$

which has the four solutions

$$\frac{\hat{k}}{k_0} = \pm\sqrt{\frac{2}{3X^2}}\sqrt{\pm\sqrt{1 + 2\mathrm{i}X + 2X^2} - (1 + \mathrm{i}X)}. \tag{5.37}$$

Two of these solutions are normal propagating waves in the $\pm x$-direction, while the other two are waves that propagate, but with an absorption coefficient where $\alpha_x \to \infty$ as $X \to 0$. We will only consider the normal x-propagating solution in the following.

Gathering the exact solutions of the isothermal Navier-Stokes-Fourier model, the isothermal Burnett model, and the DVBE model, we have

$$\text{N-S-F:} \quad \frac{\hat{k}}{k_0} = \frac{1}{\sqrt{1 + \mathrm{i}X}}, \tag{5.38a}$$

$$\text{Burnett:} \quad \frac{\hat{k}}{k_0} = \sqrt{\frac{2}{3X^2}}\sqrt{\sqrt{1 + 2\mathrm{i}X + 2X^2} - (1 + \mathrm{i}X)}, \tag{5.38b}$$

$$\text{DVBE:} \quad \frac{\hat{k}}{k_0} = \sqrt{\frac{1 + \mathrm{i}X/2}{1 + 3\mathrm{i}X/2}}. \tag{5.38c}$$

While the analytical expressions are difficult to compare by themselves, the series expansion around $X = 0$ is more instructive,

$$\text{N-S-F:} \quad \frac{\hat{k}}{k_0} = 1 - \mathrm{i}\tfrac{1}{2}X - \tfrac{3}{8}X^2 + \mathrm{i}\tfrac{5}{16}X^3 + \tfrac{35}{128}X^4 + \mathcal{O}(X^5), \tag{5.39a}$$

$$\text{Burnett:} \quad \frac{\hat{k}}{k_0} = 1 - \mathrm{i}\tfrac{1}{2}X - \tfrac{6}{8}X^2 + \mathrm{i}\tfrac{20}{16}X^3 + \tfrac{308}{128}X^4 + \mathcal{O}(X^5), \tag{5.39b}$$

$$\text{DVBE:} \quad \frac{\hat{k}}{k_0} = 1 - \mathrm{i}\tfrac{1}{2}X - \tfrac{5}{8}X^2 + \mathrm{i}\tfrac{13}{16}X^3 + \tfrac{139}{128}X^4 + \mathcal{O}(X^5). \tag{5.39c}$$

As pointed out previously, the terms always alternate between real (dispersion) and imaginary (absorption). All of the models agree up to $\mathcal{O}(X)$, meaning that they predict the same absorption to the lowest order. However, there is disagreement above this point, meaning that they predict different dispersion even to the lowest order.

It should not be a surprise that the Navier-Stokes-Fourier model does not match the rest, as its derivation was found by truncating the Chapman-Enskog expansion to $\mathcal{O}(X)$; it should not be trusted above this order. That the Burnett and DVBE models disagree requires some more explanation, however. There are at least two reasons:

Firstly, the Burnett model includes higher-order transport coefficients, which can be seen as second-order viscosities and conductivities. Their relation to the normal viscosity and conductivity is determined by the choice of collision operator and molecular model, although the results seem not to vary greatly between different molecular models [27]. Even so, Greenspan's Burnett expressions were derived via Boltzmann's original collision operator while the DVBE expressions were derived using the BGK model. As the BGK model has weaknesses such as an incorrect Prandtl number, i.e. an incorrect ratio between conductivity and viscosity (as seen in section 2.2.2), it is not unlikely that it also predicts a wrong ratio between the transport coefficients at the Navier-Stokes-Fourier level and the Burnett level.

Secondly, when deriving the DVBE, the equilibrium distribution was approximated as a truncated series in $\boldsymbol{u}$ and velocity space was discretised. The order of the series approximation determines both the required size of the discrete velocity set and to which level in the Chapman-Enskog expansion the DVBE will be accurate [72]. With the truncation to $\mathcal{O}(u^2)$, we saw that the momentum equation was not even fully accurate to the Navier-Stokes level, as it contained a $\mathcal{O}(u^3)$ error term which disappears during linearisation. To get a momentum equation which is fully accurate to the Burnett level, the equilibrium distribution would need to be approximated to a higher order.

Even so, any terms in $f_i^{(0)}$ above $\mathcal{O}(u)$ would disappear in the linearisation. In fact, all terms above first order in the isothermal Hermite expansion of $f_i^{(0)}$ are removed by linearisation [72]. The order of the

Hermite expansion determines what level of the Chapman-Enskog expansion to which a DVBE is valid. Consequently, this would suggest that the linearised isothermal equilibrium distribution (5.24) is valid at every level in the Chapman-Enskog expansion.

Binomial series
The series expansion of a function of the form $f(x) = (1+x)^a$

The Navier-Stokes-Fourier expansion in (5.39a) is a typical *binomial series*, which converges for $X \leq 1$ and diverges for higher values, even though the original function (5.38a) is valid for any physical (i.e. real and non-negative) value of X. If the coefficients in the corresponding Burnett and DVBE series expansions are always of larger magnitude, then by the comparison test the convergence range of these series cannot be larger. As explained in section 3.8.4, series like these are *asymptotic*; they do not converge unless X is sufficiently small.

Consequently, these series expansions are not very useable unless $X \ll 1$. For $X \gg 1$, the exact normalised wavenumbers (5.38) asymptotically go to

$$\text{N-S-F:} \qquad \lim_{X\gg 1} \frac{\hat{k}}{k_0} = (1-\mathrm{i})\sqrt{\frac{1}{2X}}, \tag{5.40a}$$

$$\text{Burnett:} \qquad \lim_{X\gg 1} \frac{\hat{k}}{k_0} = \sqrt{\frac{\sqrt{3}+\sqrt{2}}{3X}} - \mathrm{i}\sqrt{\frac{\sqrt{3}-\sqrt{2}}{3X}}, \tag{5.40b}$$

$$\text{DVBE:} \qquad \lim_{X\gg 1} \frac{\hat{k}}{k_0} = \frac{1}{\sqrt{3}} - \mathrm{i}\frac{\sqrt{12}}{9X}. \tag{5.40c}$$

Thus, we see that the normalised speed of sound $c/c_0 = \mathrm{Re}(k_0/\hat{k})$ unphysically goes to infinity for the Navier-Stokes-Fourier and Burnett models, while it plateaus at $\sqrt{3}$ for the DVBE model. Since $c_0 = 1/\sqrt{3}$, the maximum speed of sound is $c = 1$. This equals the speed of particles in the D1Q3 velocity set, and correspondingly the speed at which information propagates.

CFL condition
A stability condition in numerical mathematics. For hyperbolic equations it states that information must not propagate in the simulation more slowly than the characteristics of the solution (e.g. the speed of sound).

In fact, any higher speeds of sound would mean that the *Courant-Friedrichs-Lewy condition* would be violated and the DVBE model would necessarily be unstable [104, Ch. 10]. From this, we can suspect that extended velocity sets would have different behaviour for $X \gg 1$.

Interestingly, measurements in real gases at very high X indicate the same qualitative behaviour as the DVBE model [63].

We now know the sound propagation predicted from the models at $X \ll 1$ and at $X \gg 1$. To compare them for $X \sim 1$, we can plot the exact absorption and dispersion as in Figure 5.3.

From these plots, we find that the three models behave almost identically up to $X \sim 0.1$, where only the lowest-order terms in X are felt. The DVBE and Burnett models behave very similarly up until about $X \sim 1$, in particular the dispersion. As the thermal Burnett model has been seen to match measurements better than the thermal Navier-Stokes-Fourier-model [27, 63], we can assume that for moderate X, sound propagates

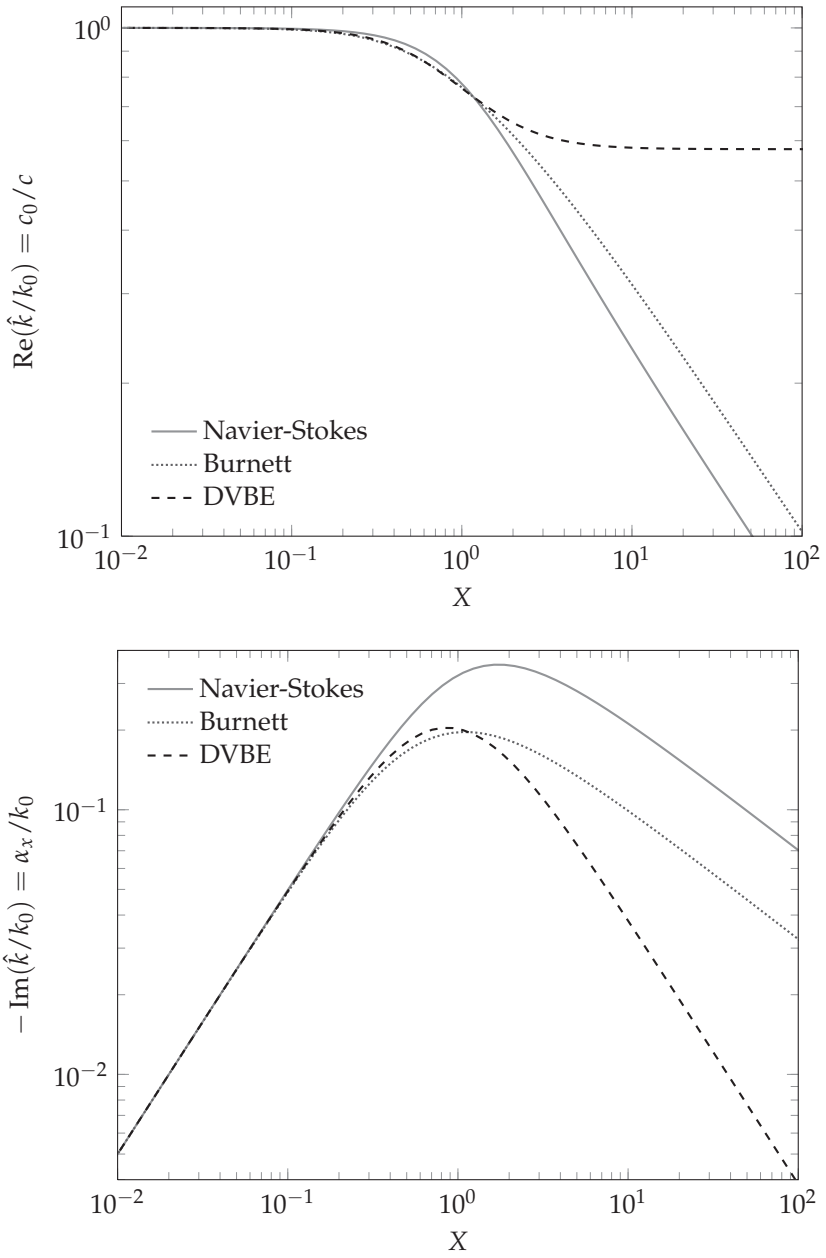

Figure 5.3: Comparison of the normalised inverse dispersion (upper) and the normalised absorption (lower) of forced waves for three different models.

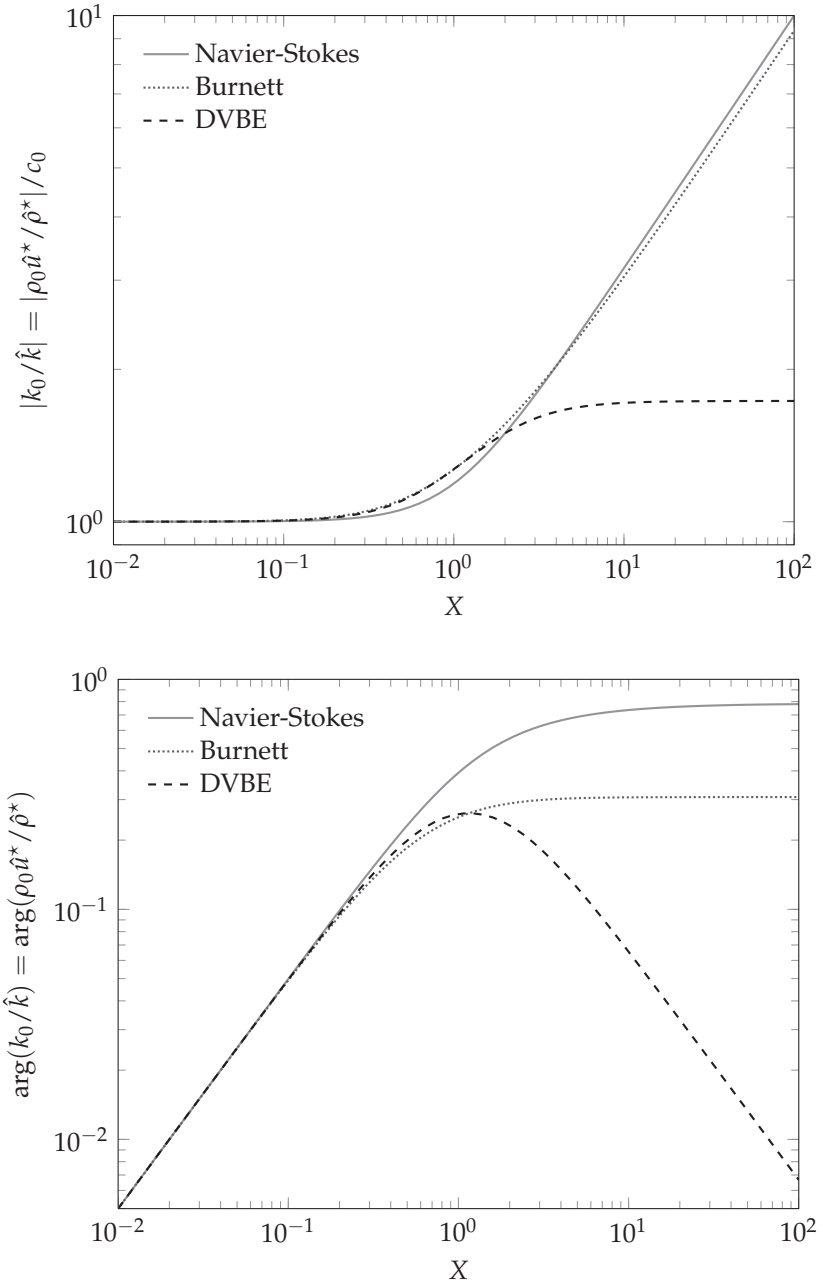

Figure 5.4: Comparison of the normalised magnitude ratios (upper) and the phase differences (lower) of the momentum and density components of forced waves for two different models.

more correctly in the isothermal DVBE model than in the isothermal Navier-Stokes-Fourier model itself.

Neither the predictions of the Navier-Stokes-Fourier model nor those of the Burnett model match well with measurements of sound propagation after $X \sim 1$ [27]. The problem of finding models that can predict sound propagation well was previously explained in section 3.8.4.

Up to this point, we have only considered absorption and dispersion. We should also take a brief look at the relative amplitudes and phase differences of the momentum and density components of the sound wave. As described previously, these quantities are found from the relation

$$\frac{\rho_0 \hat{u}^\star}{\hat{\rho}^\star} = \frac{\hat{\omega}}{\hat{k}}.$$

Since this relation is a consequence of the mass conservation equation which holds for all the models, we can also include the Burnett model in this comparison.

The magnitude ratios and amplitude differences of the three models are

$$\text{N-S-F:} \quad \begin{cases} \frac{1}{c_0}\left|\frac{\rho_0 \hat{u}^\star}{\hat{\rho}^\star}\right| = 1 + \frac{1}{4}X^2 - \frac{3}{32}X^4 + \mathcal{O}(X^6), \\ \arg\left(\frac{\rho_0 \hat{u}^\star}{\hat{\rho}^\star}\right) = \frac{1}{2}X - \frac{1}{6}X^3 + \mathcal{O}(X^5), \end{cases} \tag{5.41a}$$

$$\text{Burnett:} \quad \begin{cases} \frac{1}{c_0}\left|\frac{\rho_0 \hat{u}^\star}{\hat{\rho}^\star}\right| = 1 + \frac{5}{8}X^2 - \frac{189}{128}X^4 + \mathcal{O}(X^6), \\ \arg\left(\frac{\rho_0 \hat{u}^\star}{\hat{\rho}^\star}\right) = \frac{1}{2}X - \frac{11}{12}X^3 + \mathcal{O}(X^5), \end{cases} \tag{5.41b}$$

$$\text{DVBE:} \quad \begin{cases} \frac{1}{c_0}\left|\frac{\rho_0 \hat{u}^\star}{\hat{\rho}^\star}\right| = 1 + \frac{1}{2}X^2 - \frac{1}{2}X^4 + \mathcal{O}(X^6), \\ \arg\left(\frac{\rho_0 \hat{u}^\star}{\hat{\rho}^\star}\right) = \frac{1}{2}X - \frac{13}{24}X^3 + \mathcal{O}(X^5). \end{cases} \tag{5.41c}$$

Again, we find that the three models agree only up to $\mathcal{O}(X)$, as could be expected. There is no agreement at $\mathcal{O}(X^2)$ and above, just as for the absorption and dispersion.

The exact values are plotted in Figure 5.4. Again, we see that the Burnett and DVBE solutions are fairly close. The phase differences for the Navier-Stokes-Fourier model and the Burnett model converge to $\arctan(1) = \pi/4$ and to $\arctan\left(\sqrt{\sqrt{3}-\sqrt{2}}\Big/\sqrt{\sqrt{3}+\sqrt{2}}\right)$, respectively. Both values can be found from the asymptotics (5.39).

Free waves

For completeness, we will also take a look at the case of free waves. We will not go into the same depth as for forced waves; the remarks that can be made are mostly similar, and free waves are physically less relevant. Greenspan's Burnett solution is only given for the more physically relevant case of forced waves and cannot be used here. We will ignore

the diffusive DVBE mode, which has no analogue in the Navier-Stokes-Fourier model.

As the exact DVBE solution for propagating free waves is too cumbersome, we jump straight to the series expansions,

$$\text{N-S-F:} \qquad \frac{\hat{\omega}}{\omega_0} = 1 + \mathrm{i}\tfrac{1}{2}X - \tfrac{1}{8}X^2 - \tfrac{1}{128}X^4 + \mathcal{O}(X^6), \tag{5.42a}$$

$$\text{DVBE:} \qquad \frac{\hat{\omega}}{\omega_0} = 1 + \mathrm{i}\tfrac{1}{2}X + \tfrac{1}{8}X^2 + \mathrm{i}\tfrac{1}{8}X^3 + \tfrac{15}{128}X^4 + \mathcal{O}(X^5). \tag{5.42b}$$

The exact values are plotted in Figure 5.5.

The corresponding series expansions for magnitude ratios and phase differences are

$$\text{N-S-F:} \qquad \begin{cases} \frac{1}{c_0}\left|\frac{\rho_0\hat{u}^\star}{\hat{\rho}^\star}\right| = 1, \\ \arg\left(\frac{\rho_0\hat{u}^\star}{\hat{\rho}^\star}\right) = \frac{1}{2}X + \frac{1}{48}X^3 + \mathcal{O}(X^5), \end{cases} \tag{5.43a}$$

$$\text{DVBE:} \qquad \begin{cases} \frac{1}{c_0}\left|\frac{\rho_0\hat{u}^\star}{\hat{\rho}^\star}\right| = 1 + \frac{1}{4}X^2 + \frac{5}{32}X^4 + \mathcal{O}(X^6), \\ \arg\left(\frac{\rho_0\hat{u}^\star}{\hat{\rho}^\star}\right) = \frac{1}{2}X + \frac{1}{48}X^3 + \mathcal{O}(X^5). \end{cases} \tag{5.43b}$$

The exact values are plotted in Figure 5.6.

Three aspects are identical in the forced and free wave cases: Firstly, the two models agree up to $\mathcal{O}(X)$ but not beyond that order. Secondly, from the figures we see that the models agree well up to around $X \sim 0.1$. However, in the free wave case, the Navier-Stokes-Fourier model entirely changes character at $X = 2$, the point at which the wave stops propagating. Thirdly, the high-X limit of the DVBE phase speed is $c = 1$.

5.2.5 Anisotropy in two dimensions

Isotropy/anisotropy
Uniformity/nonuniformity with respect to direction

The previous DVBE results in this section were found using the D1Q3 velocity set, and therefore hold only for higher-dimensional velocity sets when sound propagates along any of the main (i.e. x, y, or z) axes as explained previously. Since higher-dimensional velocity sets are not themselves isotropic, and in fact *cannot be*, we might expect some amount of anisotropy: The wave propagation properties may depend on angle, at least for high X.

We now use a more general trial solution; a plane wave propagating at an angle θ to the x axis,

$$\hat{f}_i(x, y, t) = F_i^{(0)} + \hat{f}_i^\star \, \mathrm{e}^{\mathrm{i}(\hat{\omega}t - \hat{k}_x x - \hat{k}_y y)}, \tag{5.44}$$

where

$$\hat{k}_x = \hat{k}\cos(\theta), \qquad \hat{k}_y = \hat{k}\sin(\theta).$$

For $\theta = 0$, this reduces to the previously used trial solution.

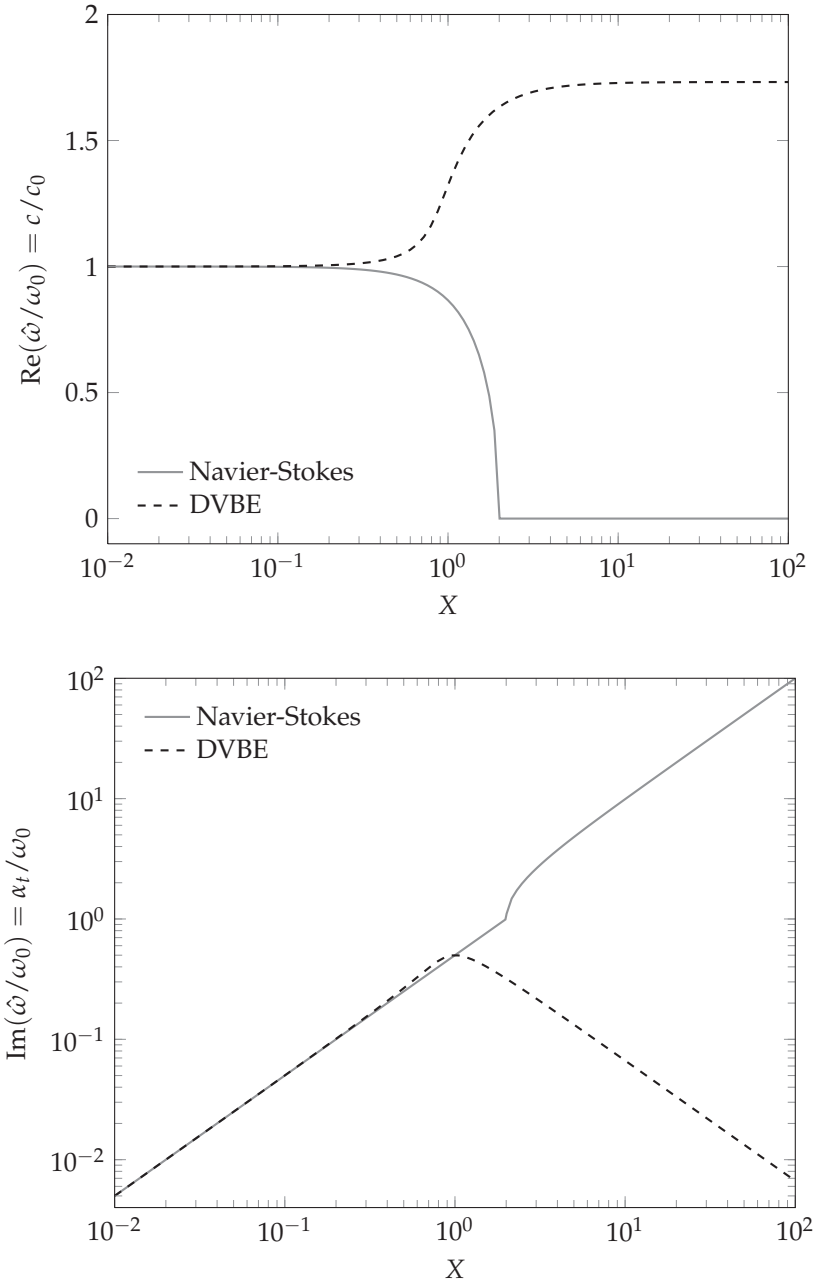

Figure 5.5: Comparison of the normalised dispersion (upper) and the normalised absorption (lower) of free waves for two different models.

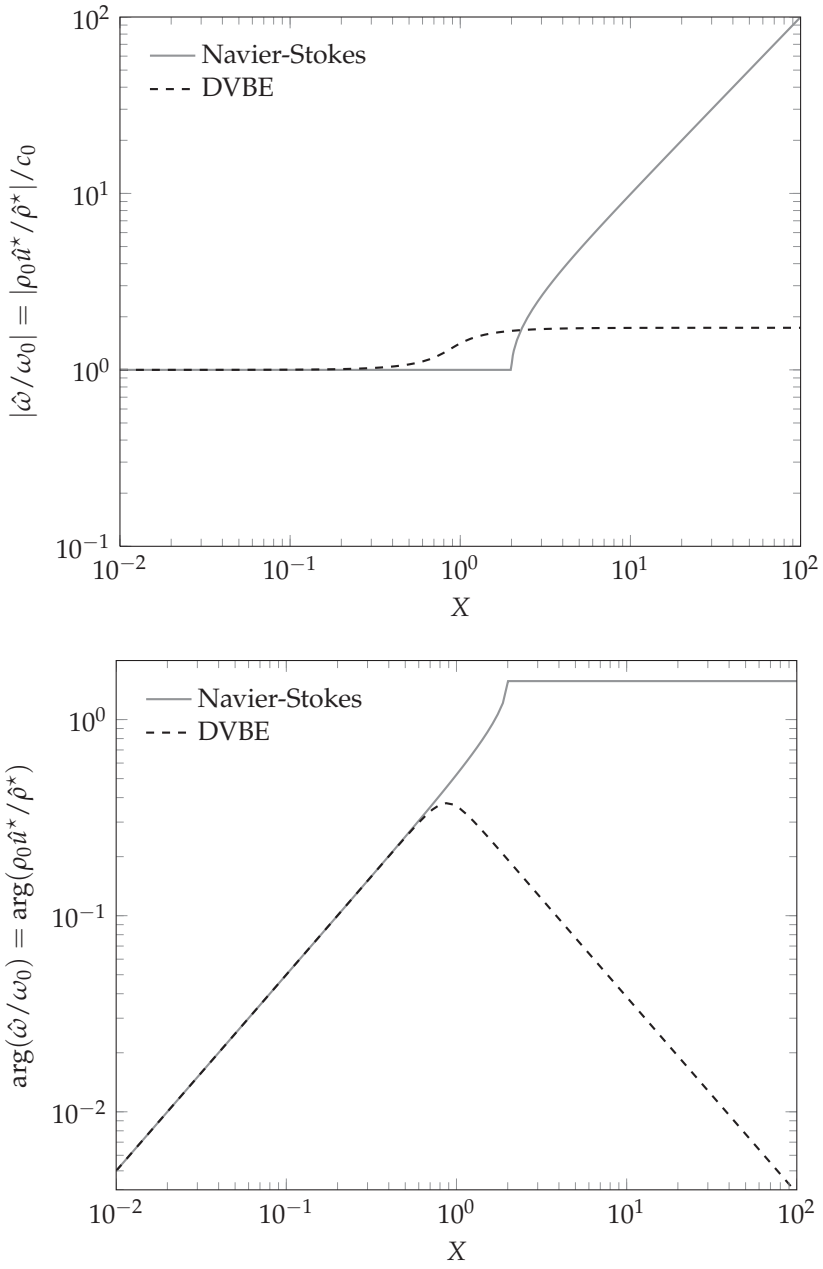

Figure 5.6: Comparison of the magnitude ratios (upper) and the phase differences (lower) of free waves for two different models.

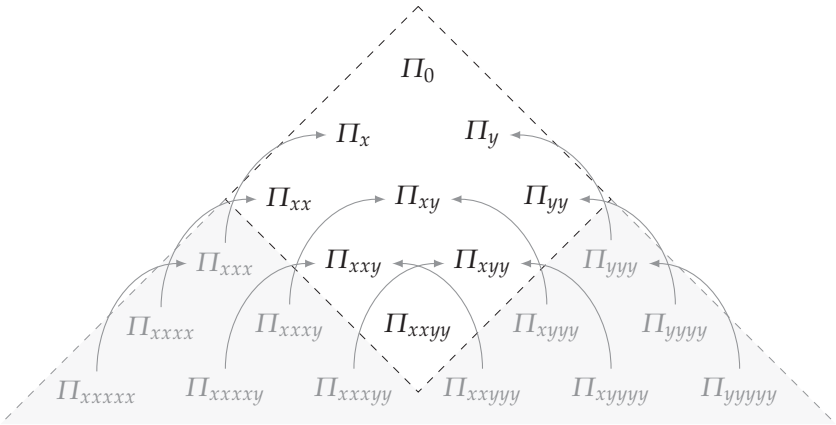

Figure 5.7: The nine independent moments of the D2Q9 velocity set and the dependence of higher-order moments on these.

It is natural to capture this behaviour with the D2Q9 velocity set introduced in section 4.1.3. This is a two-dimensional projection of the D3Q15, D3Q19, and D3Q27 velocity sets, in the same way as the D1Q3 velocity set is a one-dimensional projection of all of these. Consequently, the results found here will also be valid for these three-dimensional velocity sets for plane waves which propagate normal to at least one of the main axes.

We will simplify this section by making full use of lattice units, setting $\Delta x = \Delta t = 1$. As in the D1Q3 case, the answer will not actually depend on the value of these. Also, to avoid unnecessarily heavy notation, we suppress the breve accent in the notation for the moments $\check{\Pi}$ of the discrete distribution function f_i. There should be no chance of misunderstanding, as the moments Π of the continuous distribution function f are not relevant here.

Like in (3.23), we again introduce a consistent notation for the complex linearised moments,

$$\begin{aligned} \hat{\Pi}^\star_0 &= \sum_i \hat{f}^\star_i = \hat{\rho}^\star, & \hat{\Pi}^\star_\alpha &= \sum_i \xi_{i\alpha} \hat{f}^\star_i = \rho_0 \hat{u}^\star_\alpha, \\ \hat{\Pi}^\star_{\alpha\beta} &= \sum_i \xi_{i\alpha}\xi_{i\beta} \hat{f}^\star_i, & \hat{\Pi}^\star_{\alpha\beta\gamma} &= \sum_i \xi_{i\alpha}\xi_{i\beta}\xi_{i\gamma} \hat{f}^\star_i, \end{aligned} \tag{5.45}$$

and so forth.

In the D1Q3 case, we found that there were only three independent moments: $\hat{\Pi}^\star_0$, $\hat{\Pi}^\star_x$, and $\hat{\Pi}^\star_{xx}$; the higher-order moment $\hat{\Pi}^\star_{xxx}$ was found in (5.29) to depend on $\hat{\Pi}^\star_x$. By the same derivation there are nine independent moments in the D2Q9 velocity set [83, Ch. 4], and higher-order

moments are given from these as

$$\begin{aligned} \hat{\Pi}^{\star}_{xxx} &= \hat{\Pi}^{\star}_{x}, \qquad \hat{\Pi}^{\star}_{xxxy} = \hat{\Pi}^{\star}_{xy}, \qquad \hat{\Pi}^{\star}_{xxxyy} = \hat{\Pi}^{\star}_{xyy}, \\ \hat{\Pi}^{\star}_{yyy} &= \hat{\Pi}^{\star}_{y}, \qquad \hat{\Pi}^{\star}_{xyyy} = \hat{\Pi}^{\star}_{xy}, \qquad \hat{\Pi}^{\star}_{xxyyy} = \hat{\Pi}^{\star}_{xxy}. \end{aligned} \tag{5.46}$$

This dependence on the nine independent moments is also shown graphically in Figure 5.7.

For this two-dimensional plane wave, the fluctuating equilibrium distribution function is generalised to

$$\hat{f}^{\star(0)}_{i} = w_i \left[\hat{\Pi}^{\star}_{0} + \frac{\hat{\Pi}^{\star}_{\epsilon} \xi_{i\epsilon}}{c_0^2} \right]. \tag{5.47}$$

The equilibrium moments of this can be found using the symmetry properties (4.11) to be

$$\hat{\Pi}^{\star(0)}_{\alpha\beta} = c_0^2 \hat{\Pi}^{\star}_{0} \delta_{\alpha\beta}, \tag{5.48a}$$

$$\hat{\Pi}^{\star(0)}_{\alpha\beta\gamma} = c_0^2 \left(\hat{\Pi}^{\star}_{\alpha} \delta_{\beta\gamma} + \hat{\Pi}^{\star}_{\beta} \delta_{\alpha\gamma} + \hat{\Pi}^{\star}_{\gamma} \delta_{\alpha\beta} \right), \tag{5.48b}$$

$$\hat{\Pi}^{\star(0)}_{\alpha\beta\gamma\delta} = c_0^4 \hat{\Pi}^{\star}_{0} \left(\delta_{\alpha\beta}\delta_{\gamma\delta} + \delta_{\alpha\gamma}\delta_{\beta\delta} + \delta_{\alpha\delta}\delta_{\beta\gamma} \right). \tag{5.48c}$$

The harmonic linearised discrete-velocity Boltzmann equation (5.27) in generalised form is

$$(1 + \mathrm{i}\hat{\omega}\tau)\, \hat{f}^{\star}_{i} = \hat{f}^{\star(0)}_{i} + \mathrm{i}\tau \hat{k}_{\epsilon} \xi_{i\epsilon} \hat{f}^{\star}_{i}. \tag{5.49}$$

In the D1Q3 case, we took all the independent moments of this and related them to each other using the higher-order moments' dependence on the independent moments. In the D2Q9 case, we will do essentially the same thing. However, it is now more complicated due to the higher number of moments and the two-dimensional nature of the plane wave.

The zeroth-order moment of (5.49) is

$$\hat{\omega} \hat{\Pi}^{\star}_{0} = \left(\hat{k}_x \hat{\Pi}^{\star}_{x} + \hat{k}_y \hat{\Pi}^{\star}_{y} \right), \tag{5.50a}$$

and the two first-order moments are

$$\begin{aligned} \hat{\omega} \hat{\Pi}^{\star}_{x} &= \left(\hat{k}_x \hat{\Pi}^{\star}_{xx} + \hat{k}_y \hat{\Pi}^{\star}_{xy} \right), \\ \hat{\omega} \hat{\Pi}^{\star}_{y} &= \left(\hat{k}_x \hat{\Pi}^{\star}_{xy} + \hat{k}_y \hat{\Pi}^{\star}_{yy} \right). \end{aligned} \tag{5.50b}$$

For the second-order moments, we must start using the equilibrium moments and the moment dependence relations, resulting in

$$\begin{aligned} (1 + \mathrm{i}\hat{\omega}\tau) \hat{\Pi}^{\star}_{xx} &= c_0^2 \hat{\Pi}^{\star}_{0} + \mathrm{i}\tau \left(\hat{k}_x \hat{\Pi}^{\star}_{x} + \hat{k}_y \hat{\Pi}^{\star}_{xxy} \right), \\ (1 + \mathrm{i}\hat{\omega}\tau) \hat{\Pi}^{\star}_{xy} &= \mathrm{i}\tau \left(\hat{k}_x \hat{\Pi}^{\star}_{xxy} + \hat{k}_y \hat{\Pi}^{\star}_{xyy} \right), \\ (1 + \mathrm{i}\hat{\omega}\tau) \hat{\Pi}^{\star}_{yy} &= c_0^2 \hat{\Pi}^{\star}_{0} + \mathrm{i}\tau \left(\hat{k}_x \hat{\Pi}^{\star}_{xyy} + \hat{k}_y \hat{\Pi}^{\star}_{y} \right). \end{aligned} \tag{5.50c}$$

Similarly, the third-order moments are

$$\begin{aligned}(1+\mathrm{i}\hat{\omega}\tau)\hat{I}I^{\star}_{xxy} &= c_0^2\hat{I}I^{\star}_{y} + \mathrm{i}\tau\left(\hat{k}_x\hat{I}I^{\star}_{xy} + \hat{k}_y\hat{I}I^{\star}_{xxyy}\right),\\ (1+\mathrm{i}\hat{\omega}\tau)\hat{I}I^{\star}_{xyy} &= c_0^2\hat{I}I^{\star}_{x} + \mathrm{i}\tau\left(\hat{k}_x\hat{I}I^{\star}_{xxyy} + \hat{k}_y\hat{I}I^{\star}_{xy}\right),\end{aligned} \tag{5.50d}$$

and the fourth-order moment is

$$(1+\mathrm{i}\hat{\omega}\tau)\hat{I}I^{\star}_{xxyy} = c_0^4\hat{I}I^{\star}_{y} + \mathrm{i}\tau\left(\hat{k}_x\hat{I}I^{\star}_{xyy} + \hat{k}_y\hat{I}I^{\star}_{xxy}\right). \tag{5.50e}$$

To deal with this complicated system of equations we put it in matrix form,

$$\begin{bmatrix}
1+\mathrm{i}\hat{\omega}\tau & -\mathrm{i}\hat{k}_x\tau & -\mathrm{i}\hat{k}_y\tau & 0 & 0 & 0 & 0 & 0 & -c_0^4\\
-\mathrm{i}\hat{k}_x\tau & 1+\mathrm{i}\hat{\omega}\tau & 0 & 0 & -\mathrm{i}\hat{k}_y\tau & 0 & 0 & -c_0^2 & 0\\
-\mathrm{i}\hat{k}_y\tau & 0 & 1+\mathrm{i}\hat{\omega}\tau & 0 & -\mathrm{i}\hat{k}_x\tau & 0 & -c_0^2 & 0 & 0\\
0 & -\mathrm{i}\hat{k}_x\tau & 0 & 1+\mathrm{i}\hat{\omega}\tau & 0 & 0 & -\mathrm{i}\hat{k}_y\tau & 0 & -c_0^2\\
0 & -\mathrm{i}\hat{k}_y\tau & -\mathrm{i}\hat{k}_x\tau & 0 & 1+\mathrm{i}\hat{\omega}\tau & 0 & 0 & 0 & 0\\
0 & 0 & -\mathrm{i}\hat{k}_y\tau & 0 & 0 & 1+\mathrm{i}\hat{\omega}\tau & 0 & -\mathrm{i}\hat{k}_x\tau & -c_0^2\\
0 & 0 & 0 & -\hat{k}_y & -\hat{k}_x & 0 & \hat{\omega} & 0 & 0\\
0 & 0 & 0 & 0 & -\hat{k}_y & -\hat{k}_x & 0 & \hat{\omega} & 0\\
0 & 0 & 0 & 0 & 0 & 0 & -\hat{k}_y & -\hat{k}_x & \hat{\omega}
\end{bmatrix}
\begin{bmatrix}
\hat{I}I^{\star}_{xxyy}\\ \hat{I}I^{\star}_{xyy}\\ \hat{I}I^{\star}_{xxy}\\ \hat{I}I^{\star}_{yy}\\ \hat{I}I^{\star}_{xy}\\ \hat{I}I^{\star}_{xx}\\ \hat{I}I^{\star}_{y}\\ \hat{I}I^{\star}_{x}\\ \hat{I}I^{\star}_{0}
\end{bmatrix} = \mathbf{0}. \tag{5.51}$$

As this system becomes too difficult to handle unaided, it is necessary to use a computer algebra system to deal with it.

We must now try to coax a dispersion relation from this system. Performing Gaussian elimination on the matrix, the last row becomes an equation $g(\hat{\omega},\hat{k},\theta,X)\hat{I}I^{\star}_{0} = 0$, where the function g is too cumbersome to fit here. Since we can safely assume that $\hat{I}I^{\star}_{0} \neq 0$, this reduces to a dispersion relation $g(\hat{\omega},\hat{k},\theta,X) = 0$.

This dispersion relation can be solved for $\hat{k}$ for forced waves, or for $\hat{\omega}$ for free waves. While the exact solutions are extremely complicated and not really comprehensible to look at, it is possible to find interesting information from the series expansions. Also, the exact solutions can be plotted for different angles θ. Due to the symmetry of the D2Q9 velocity set, we only need to consider the angular interval $0 \leq \theta \leq \pi/4$; the anisotropy is determined by the angle to *any* main axis, as shown in Figure 5.8.

Forced waves

For forced waves where $\hat{\omega} = \omega_0$, the series expansion of the normalised wavenumber is

$$\begin{aligned}\frac{\hat{k}}{k_0} = 1 - \mathrm{i}\tfrac{1}{2}X - \tfrac{5}{8}X^2 + \mathrm{i}\tfrac{13}{16}\left[1+\tfrac{18}{13}\sin^2(\theta)\cos^2(\theta)\right]X^3\\ + \tfrac{139}{128}\left[1+\tfrac{576}{139}\sin^2(\theta)\cos^2(\theta)\right]X^4 + \mathcal{O}(X^5).\end{aligned} \tag{5.52}$$

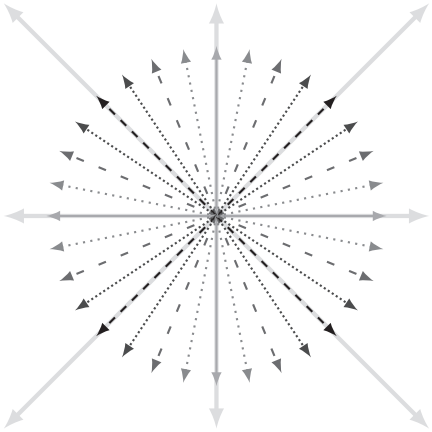

Figure 5.8: Directions of wave propagation, superimposed on the D2Q9 velocity vectors. The line styles of the different propagation directions correspond with Figures 5.9 and 5.10. The wave propagation properties have a similar angular periodicity as the velocity set.

This indicates that the angular dependence of DVBE sound propagation does not start until $\mathcal{O}(X^3)$. Consequently, both absorption and dispersion is isotropic to lowest order in X. For angles $\theta = 0, \pi/2, \pi, 3\pi/2$, where the propagation direction coincides with a main axis, this series expansion reduces to the corresponding D1Q3 series expansion (5.39c) as predicted.

The exact dispersion and absorption is plotted for five different angles in the interval $0 \leq \theta \leq \pi/4$ in Figure 5.9, and the exact magnitude ratios and phase differences are plotted similarly in Figure 5.10.

While these figures show practically isotropic behaviour up to $X \sim 0.1$, significant angular variations are found beyond that point. In particular, the dispersion and magnitude ratios have entirely different limits at $X \to \infty$ for different angles. For the dispersion, the $X \to \infty$ limit of the phase speed c is $\cos(\theta)$ for $0 \leq \theta \leq \pi/4$. This asymptotic phase speed is shown for all angles in Figure 5.11. At $\theta = \pi/4$, when sound propagates parallel to the diagonal particle velocities, the speed of sound is $c = 1/\sqrt{2}$, half the speed $|\boldsymbol{\xi}_{i\in\{5\text{–}8\}}|$ of the diagonal particles.

The absorption still behaves qualitatively the same for any angle, although the position of the absorption peak is a function of angle, and the peak itself is somewhat uneven for angles not coinciding with a main axis.

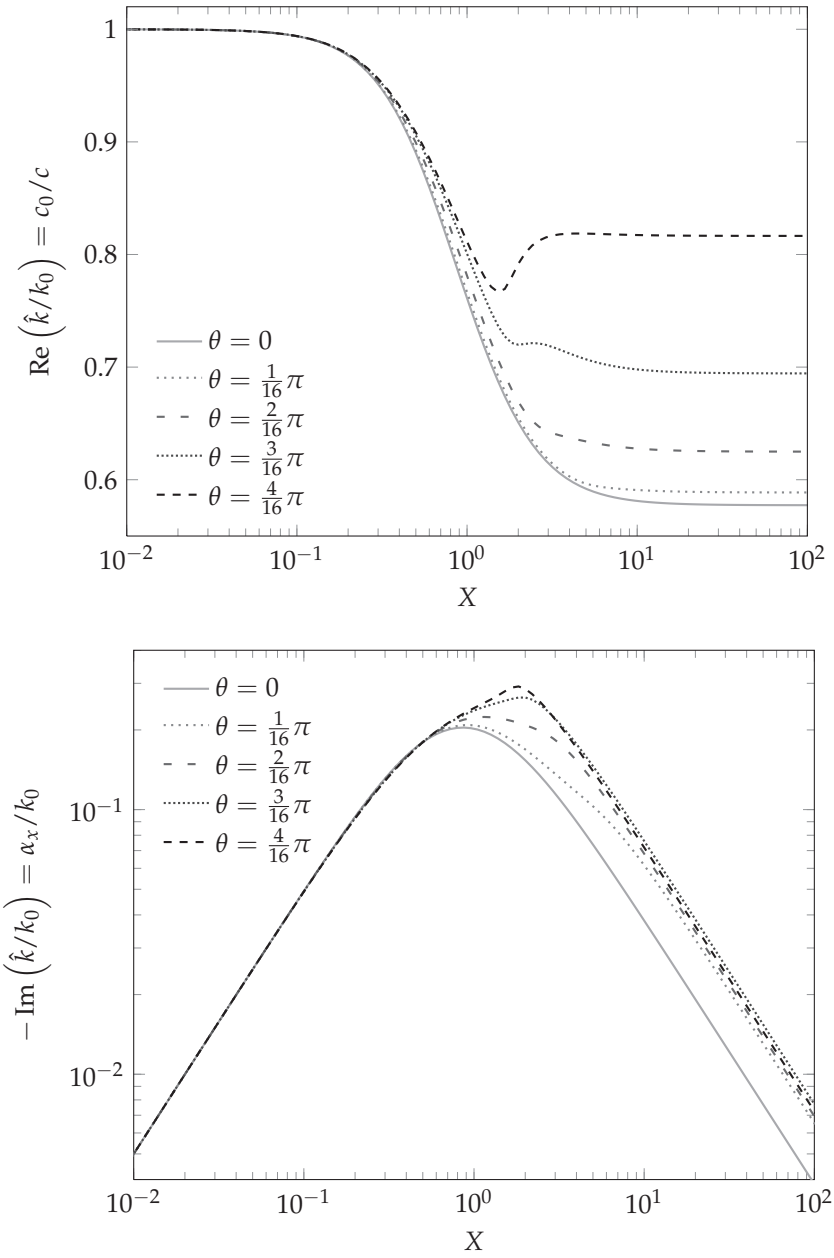

Figure 5.9: Comparison of the normalised inverse dispersion (upper) and the normalised absorption (lower) of forced waves for a D2Q9 velocity set and five different angles.

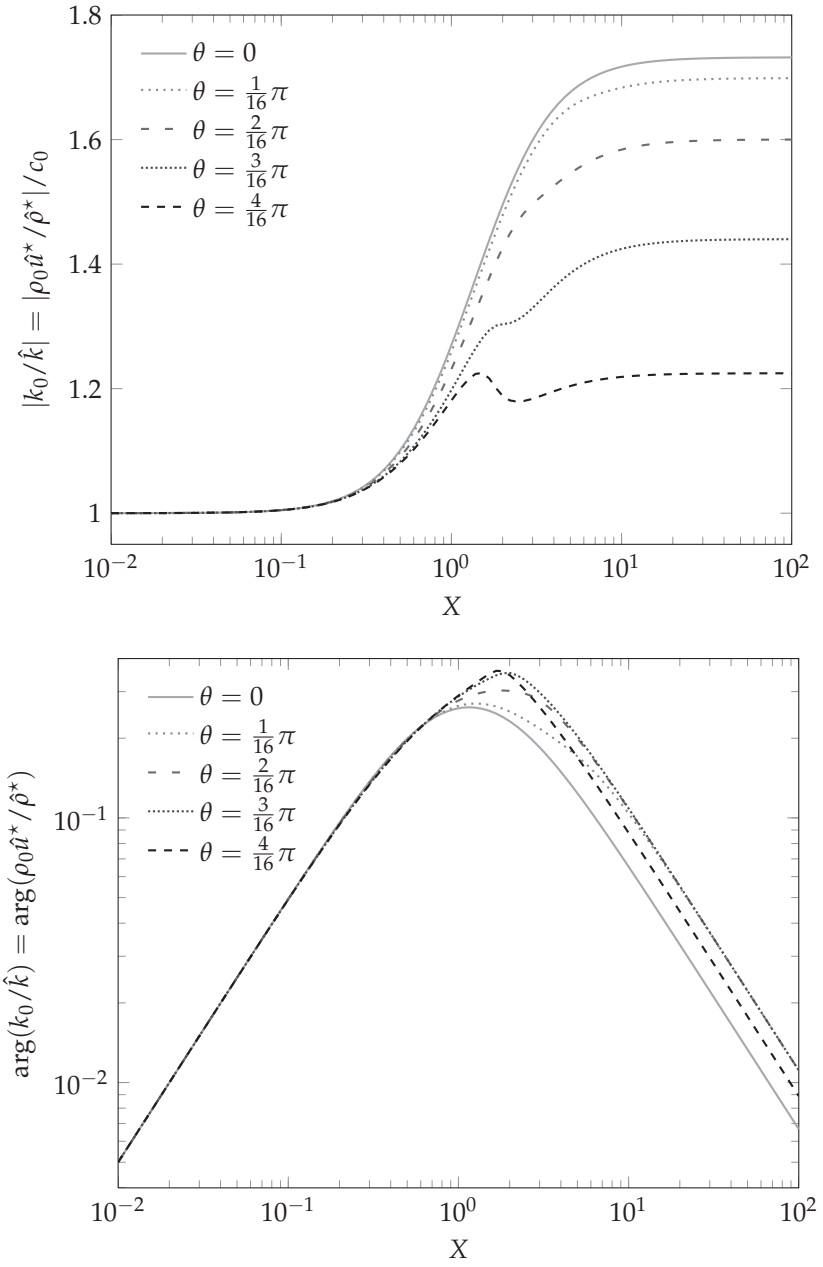

Figure 5.10: Comparison of the magnitude ratios (upper) and the phase differences (lower) of forced waves for for five different angles for a D2Q9 velocity set and five different angles.

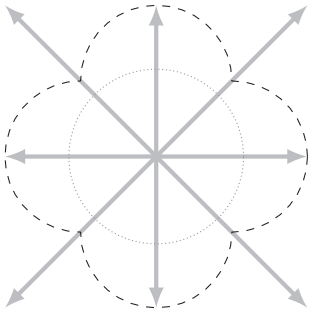

Figure 5.11: Phase speed c for $X = 0$ (·····) and $X \to \infty$ (- - -) as function of angle, superimposed on and drawn to the same scale as the D2Q9 velocity vectors. This holds both for forced and for free waves.

Free waves

In the free wave case, the corresponding series expansion is

$$\boxed{\begin{aligned}\tfrac{\hat{\omega}}{\omega_0} = 1 + \mathrm{i}\tfrac{1}{2}X + \tfrac{1}{8}X^2 + \mathrm{i}\tfrac{1}{8}\left[1 - 9\sin^2(\theta)\cos^2(\theta)\right]X^3 \\ + \tfrac{15}{128}\left[1 - \tfrac{48}{5}\sin^2(\theta)\cos^2(\theta)\right]X^4 + \mathcal{O}(X^5).\end{aligned}} \tag{5.53}$$

Again, the expansion reduces to the D1Q3-based expansion (5.42b) for the angles $\theta = 0, \pi/2, \pi, 3\pi/2$.

In the same way as for the forced wave case, the dispersion and absorption are plotted in Figure 5.12 and the magnitude ratios and phase differences in Figure 5.13.

The comments for the forced wave case hold for the free wave case as well. The asymptotic phase speed is the same as in the forced wave case; the same as shown in Figure 5.11.

5.3 Lattice Boltzmann equation

In the last section we examined in detail the sound propagation properties of the discrete-velocity Boltzmann equation. The lattice Boltzmann equation is simply this DVBE, discretised in space and time. For infinitely fine time and space resolution Δt and Δx, the sound propagation of the LBE must therefore behave like the DVBE. With a finite resolution, numerical errors will be felt for the dispersion and absorption.

The derivation is similar to the one for the DVBE, with one major difference: The DVBE has exact derivatives in space and time, whereas for the LBE we must evaluate functions at different points and times. Consequently, the LBE analysis will be similar to a von Neumann analysis.

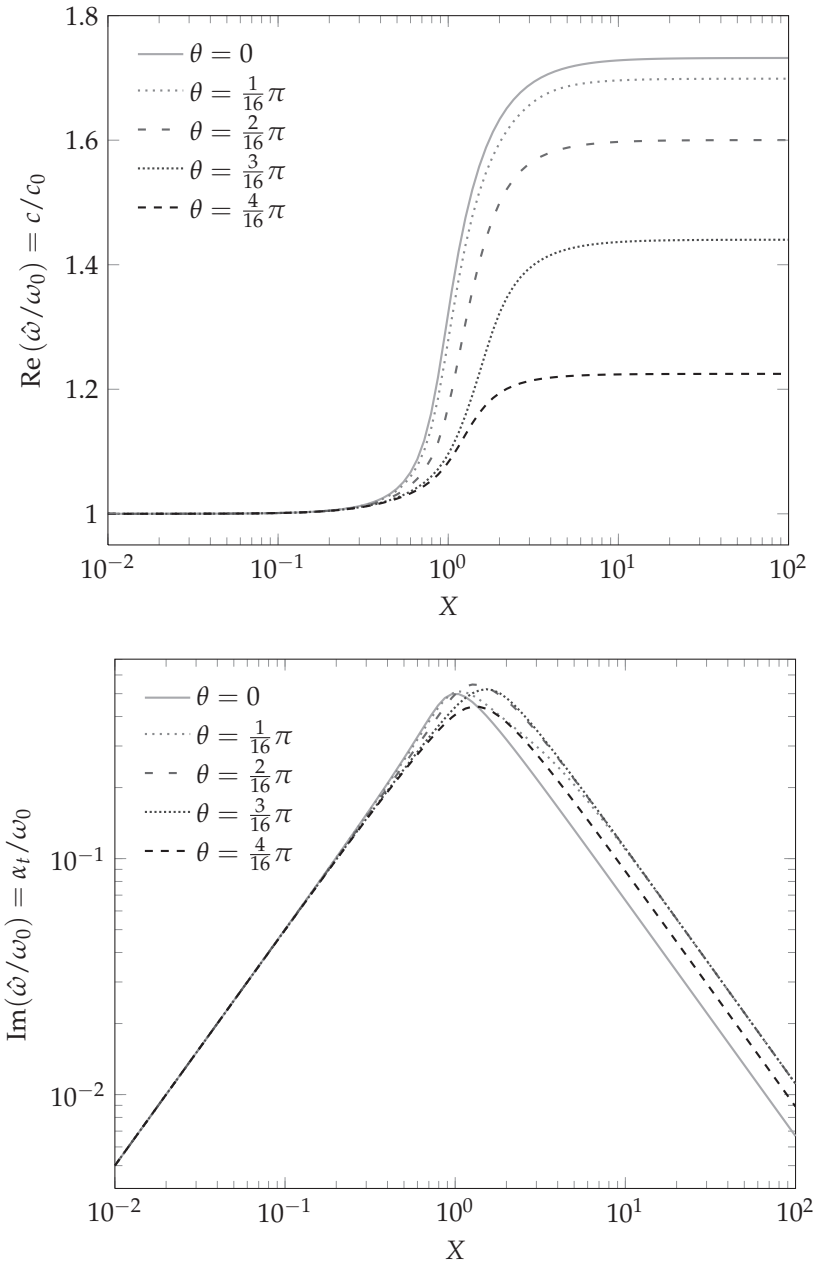

Figure 5.12: Comparison of the normalised dispersion (upper) and the normalised absorption (lower) of free waves for a D2Q9 velocity set and five different angles.

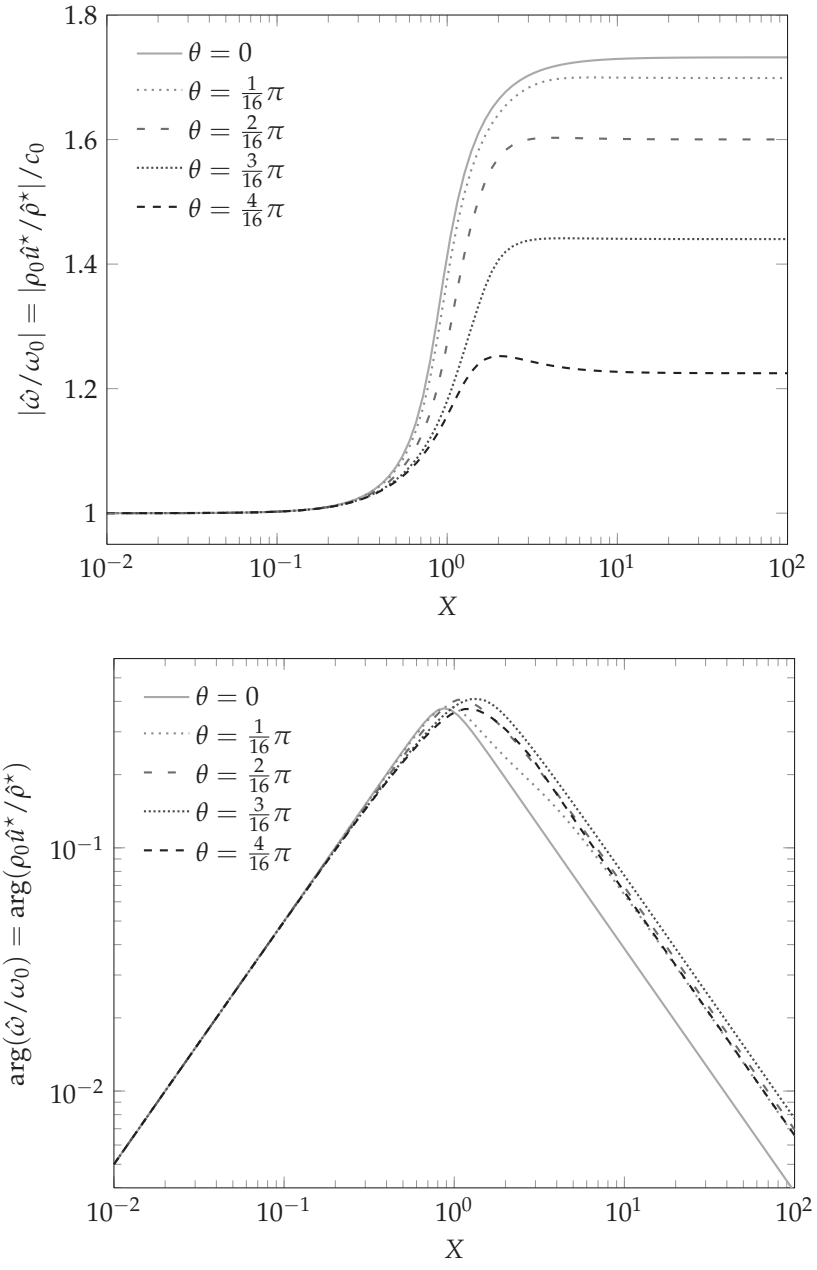

Figure 5.13: Comparison of the magnitude ratios (upper) and the phase differences (lower) of free waves for for five different angles for a D2Q9 velocity set and five different angles.

Similar work has been done before for the LBE, though only for the free wave case. Sterling and Chen performed an early linearisation stability analysis [106]. Lallemand and Luo [84], and later Reis and Phillips [107], performed an analysis for wavelike perturbations the D2Q9 velocity set and the MRT collision operator. Dellar compared the results of a BGK D1Q3 analysis with measurements of sound absorption in simulations, finding full agreement [77]. Wilde gave numerical results for the D2Q9 and D3Q19 velocity sets [44]. Marié et al. compared the sound propagation of lattice Boltzmann and high-order finite-difference-Runge-Kutta schemes for the wave equation, concluding that the LBE is the faster method for a given dispersion error [108].

However, the previous work is lacking in two areas. Firstly, it considers only free waves, where the analysis is the simplest to perform, but where the results are not particularly physically relevant and cannot be used to derive results for the more relevant forced waves [26]. Secondly, none of the previous work separates the effects of the model (DVBE) and the numerical error. This current work will both consider forced waves and the separation of model and error, though it will refrain from analysing more complex cases than the isothermal D1Q3 model and a medium at rest.

5.3.1 Linearisation process

As done when linearising the DVBE, we here use the D1Q3 velocity set with particle velocities $(\xi_-, \xi_0, \xi_+) = (-1, 0, 1)$, weighting coefficients $(w_-, w_0, w_+) = (1/6, 2/3, 1/6)$, and speed of sound $c_s = 1/\sqrt{3}$. This D1Q3 analysis will predict how waves propagate along main axes in any lattice that can be projected to D1Q3, and will therefore not include the effects of anisotropy.

The trial solution is on the same form as for the DVBE,

$$\hat{f}_i(x,t) = F_i^{(0)} + \hat{f}_i'(x,t) = F_i^{(0)} + \hat{f}_i^\star \, \mathrm{e}^{\mathrm{i}(\hat{\omega}t - \hat{k}x)}. \tag{5.54}$$

The difference is that x and t are discrete here, whereas they were continuous in the DVBE case. The equilibrium distributions are the same as in (5.24). For the fluctuating amplitude, it is

$$\hat{f}_i^{\star(0)} = w_i \left(\hat{\rho}^\star + \frac{\rho_0 \hat{u}^\star}{c_0^2} \xi_i \right) = w_i \left[\hat{f}_-^\star + \hat{f}_0^\star + \hat{f}_+^\star + 3 \left(\hat{f}_+^\star - \hat{f}_-^\star \right) \xi_i \right]. \tag{5.55}$$

Since the "first order" LBE (4.32) and the "second order" LBE (4.40) are on the same form, it does not matter which one we use for the linearisation. We will use the more common first order LBE here. Subtracting the background rest state from it, we get a linearised LBE,

$$\hat{f}_i'(x + \xi_i, t + 1) = \left(1 - \tfrac{1}{\tau} \right) \hat{f}_i' + \tfrac{1}{\tau} \hat{f}_i'^{(0)}. \tag{5.56}$$

Using the plane wave trial solution and the equilibrium distribution of the fluctuation, we find

$$\hat{f}_i^\star \, \mathrm{e}^{\mathrm{i}(\hat{\omega}-\hat{k}\xi_i)} = \left(1-\tfrac{1}{\tau}\right)\hat{f}_i^\star + \tfrac{w_i}{\tau}\left[\hat{f}_-^\star + \hat{f}_0^\star + \hat{f}_+^\star + 3\left(\hat{f}_+^\star - \hat{f}_-^\star\right)\xi_i\right]. \quad (5.57)$$

Evaluating for the three different distribution functions, we get the system of equations

$$\hat{f}_-^\star \, \mathrm{e}^{\mathrm{i}\hat{\omega}} \, \mathrm{e}^{\mathrm{i}\hat{k}} = \left(1-\tfrac{1}{3\tau}\right)\hat{f}_-^\star + \tfrac{1}{6\tau}\hat{f}_0^\star - \tfrac{1}{3\tau}\hat{f}_+^\star, \quad (5.58a)$$

$$\hat{f}_0^\star \, \mathrm{e}^{\mathrm{i}\hat{\omega}} = \tfrac{2}{3\tau}\hat{f}_-^\star + \left(1-\tfrac{1}{3\tau}\right)\hat{f}_0^\star + \tfrac{2}{3\tau}\hat{f}_+^\star, \quad (5.58b)$$

$$\hat{f}_+^\star \, \mathrm{e}^{\mathrm{i}\hat{\omega}} \, \mathrm{e}^{-\mathrm{i}\hat{k}} = -\tfrac{1}{3\tau}\hat{f}_-^\star + \tfrac{1}{6\tau}\hat{f}_0^\star + \left(1-\tfrac{1}{3\tau}\right)\hat{f}_+^\star. \quad (5.58c)$$

In matrix form, this is

$$\frac{1}{3}\begin{bmatrix} \mathrm{e}^{-\mathrm{i}\hat{k}}(3-1/\tau) & \mathrm{e}^{-\mathrm{i}\hat{k}}/2\tau & -\mathrm{e}^{-\mathrm{i}\hat{k}}/\tau \\ 2/\tau & 3-1/\tau & 2/\tau \\ -\mathrm{e}^{\mathrm{i}\hat{k}}/\tau & \mathrm{e}^{\mathrm{i}\hat{k}}/2\tau & \mathrm{e}^{\mathrm{i}\hat{k}}(3-1/\tau) \end{bmatrix} \begin{bmatrix} \hat{f}_-^\star \\ \hat{f}_0^\star \\ \hat{f}_+^\star \end{bmatrix} = \mathrm{e}^{\mathrm{i}\hat{\omega}} \begin{bmatrix} \hat{f}_-^\star \\ \hat{f}_0^\star \\ \hat{f}_+^\star \end{bmatrix}. \quad (5.59)$$

The matrix form of the system of equations is a typical eigenvalue problem $\hat{\boldsymbol{A}}\hat{\boldsymbol{f}}^\star = \mathrm{e}^{\mathrm{i}\hat{\omega}}\hat{\boldsymbol{f}}^\star$, with $\mathrm{e}^{\mathrm{i}\hat{\omega}}$ as the eigenvalue. For the free wave case, this is simple to handle: With $\hat{k} = k_0$ known, $\hat{\omega}$ can be found directly from the matrix's eigenvalues.

The forced wave case is more difficult. Here, the eigenvalue $\mathrm{e}^{\mathrm{i}\hat{\omega}} = \mathrm{e}^{\mathrm{i}\omega_0}$ is known, but the matrix contains the unknown complex wavenumber $\hat{k}$. In a previous publication, this author used a numerical search to find the value of $\hat{k}$ that gave the correct eigenvalue $\mathrm{e}^{\mathrm{i}\omega_0}$ [11]. However, this approach does not lead to analytical expressions.

An analytical technique which works both for free and for forced waves uses the characteristic polynomial of (5.59),

$$\det(\hat{\boldsymbol{A}} - \boldsymbol{I}\,\mathrm{e}^{\mathrm{i}\hat{\omega}}) = g(\hat{\omega}, \hat{k}, \tau) = 0. \quad (5.60)$$

The characteristic polynomial g, which also doubles as a dispersion relation, is unwieldy and we do not gain much by displaying it here. However, it can be solved for either $\hat{k}$ or $\hat{\omega}$, leading to useful results for forced or free waves, respectively.

The eigenvector also contains useful information. For any forced or free wave propagation mode, the complex amplitude ratio of the momentum and density wave components are

$$\frac{\rho_0 \hat{u}^\star}{\hat{\rho}^\star} = \frac{\hat{f}_+^\star - \hat{f}_-^\star}{\hat{f}_-^\star + \hat{f}_0^\star + \hat{f}_+^\star}. \quad (5.61)$$

A simulation of free waves can be initialised exactly using (5.54) if the values of $\hat{f}_i^\star$ are known. On the other hand, if the initialisation is performed using standard acoustical expressions based on the Euler model,

several wave modes will be present simultaneously. The initial state will typically contain the intended wave mode with a small contribution of the mode of wave propagation in the opposite direction, leading to a slight standing wave effect in the simulation. We will demonstrate this in section 5.3.3.

5.3.2 Results

Analytically finding the eigenvectors $\hat{f}^\star$ in (5.59) seems to be a problem too difficult to handle for the computer algebra system used here. We will therefore restrict ourselves to the absorption and dispersion properties that can be found from $\hat{k}$ and $\hat{\omega}$. However, it was found numerically that the magnitude ratios and phase differences correspond with the DVBE linearisation results for forced waves (5.41c) and free waves (5.43b) in the limit of an infinitely fine numerical resolution [11].

To determine whether solutions of the eigenvalue problem (5.59) can be used to predict LB sound propagation, the predicted LB waves should be compared with actual waves. Indeed, this has been done previously both for free waves [77] and for forced waves [11]. We will also see in the next chapters that the solutions accurately predict LB wave propagation even for two-dimensional simulations of non-plane waves.

Forced waves

In the case of forced waves, where $\hat{\omega} = \omega_0$, we can solve the characteristic polynomial for $\hat{k}$. There are two solutions, one for each direction of propagation. For propagation in the $+x$-direction, the exact analytical solution is

$$\boxed{\hat{k} = \mathrm{i} \ln \left[\frac{3\tau(\zeta^2 - \zeta + 1 - \zeta^{-1}) + \zeta - 2 + \zeta^{-1}(3 + \sqrt{3\Xi})}{4 + 6\tau(\zeta - 1) - 2\zeta} \right],} \tag{5.62}$$

where the shorthands $\zeta = \mathrm{e}^{\mathrm{i}\omega_0}$ and

$$\Xi = (\zeta + 1)(\zeta - 1)^2(\tau\zeta + 1 - \tau)(3\tau\zeta^2 - \zeta + 3 - 3\tau)$$

have been used. While this solution is complicated, it is far less so than the exact solutions that have been judged too cumbersome to display elsewhere in this chapter.

If we series expand this exact solution, we can separate between the numerical error and the physical behaviour by nesting series expansions in ω_0 into a series expansion in X. The angular frequency ω_0 in lattice units expresses the numerical resolution as it determines the number of

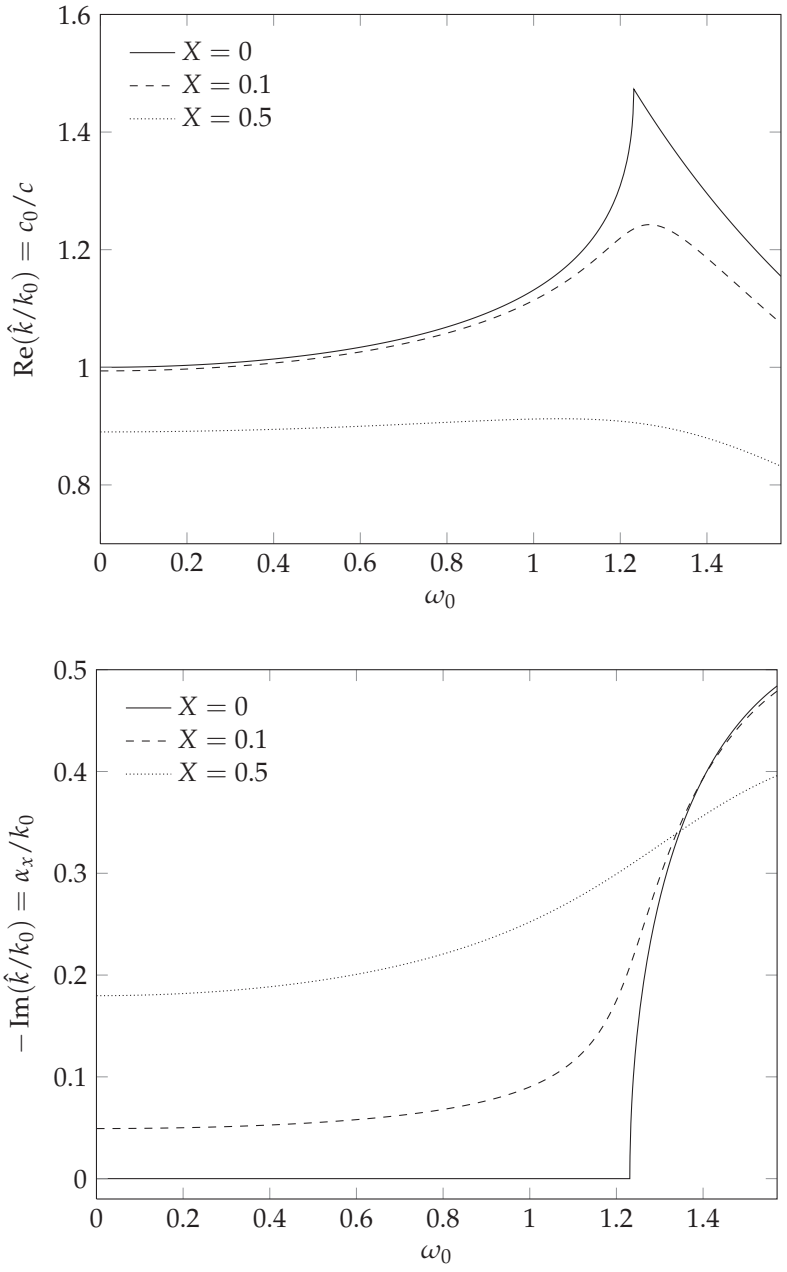

Figure 5.14: The normalised inverse dispersion (upper) and the normalised absorption (lower) of forced waves as functions of the numerical resolution ω_0 for three different values of X.

time steps that resolve a period of the wave. The series expansion is

$$\begin{aligned}\frac{\hat{k}}{k_0} = &\left[1 + \tfrac{1}{12}\omega_0^2 + \tfrac{13}{480}\omega_0^4 + \mathcal{O}(\omega_0^6)\right] \\ &- \mathrm{i}\tfrac{1}{2}X\left[1 + \tfrac{5}{12}\omega_0^2 + \mathcal{O}(\omega_0^4)\right] \\ &- \tfrac{5}{8}X^2\left[1 + \tfrac{13}{20}\omega_0^2 + \mathcal{O}(\omega_0^4)\right] + \mathcal{O}(X^3).\end{aligned} \tag{5.63}$$

This series expansion has at least two interesting consequences. Firstly, when the numerical resolution is infinitely refined as ω_0 goes to zero, this series expansion goes to the DVBE solution (5.39c), as expected. Secondly, the numerical error is second-order in ω_0. This shows analytically that LB is a second order scheme, at least in the linear limit, even with the "first order" discretisation of the DVBE.

The exact dispersion and absorption are shown in Figure 5.14.* The most striking result is how the character of the solution changes at $\omega \approx 1.23$. Beyond this point, even waves in the inviscid limit $X = 0$ are heavily absorbed. A closer look reveals that this is the point where $\lambda = 2\pi c/\omega_0 = 2$; the shortest wavelength which is possible to resolve in discretised space.

Free waves

For free waves, $\hat{k} = k_0$. The wavenumber k_0 determines the number of nodes per wavelength, and expresses the numerical resolution like ω_0 did in the forced wave case.

There are three different solutions of the characteristic polynomial, similar to the three wave modes found for the DVBE case. Two modes propagate in opposite directions. The third mode is diffusive and does not propagate. Unlike the forced wave case, the mathematical expression of all the three modes are too cumbersome to write out here.

For the DVBE model, the diffusive mode is immediately absorbed when $X = 0$, i.e. when the solution relaxed immediately to equilibrium. For the LBE, the diffusive mode is immediately absorbed when $\tau = 1$. This similarly corresponds to immediate relaxation to equilibrium, but it does *not* correspond to $X = 0$. For general values of τ, numerical experimentation indicates that the diffusive eigenvalue is $\mathrm{e}^{\mathrm{i}\hat{\omega}} = 1 - 1/\tau$ for infinitely fine numerical resolution, i.e. $k_0 \to 0$. This leads to the amplitude of the diffusive wave mode being under- or overrelaxed analogously to the BGK relaxation shown in Figure 4.4. Consequently, if

*Because of a roundoff error due to limited numerical precision, the solution originally plotted by the computer algebra system diverged for very small ω_0. The solution from the series expansion (5.63) had to be substituted in Figure 5.14 where the "exact solution" was in error. This also had to be done in the free wave case.

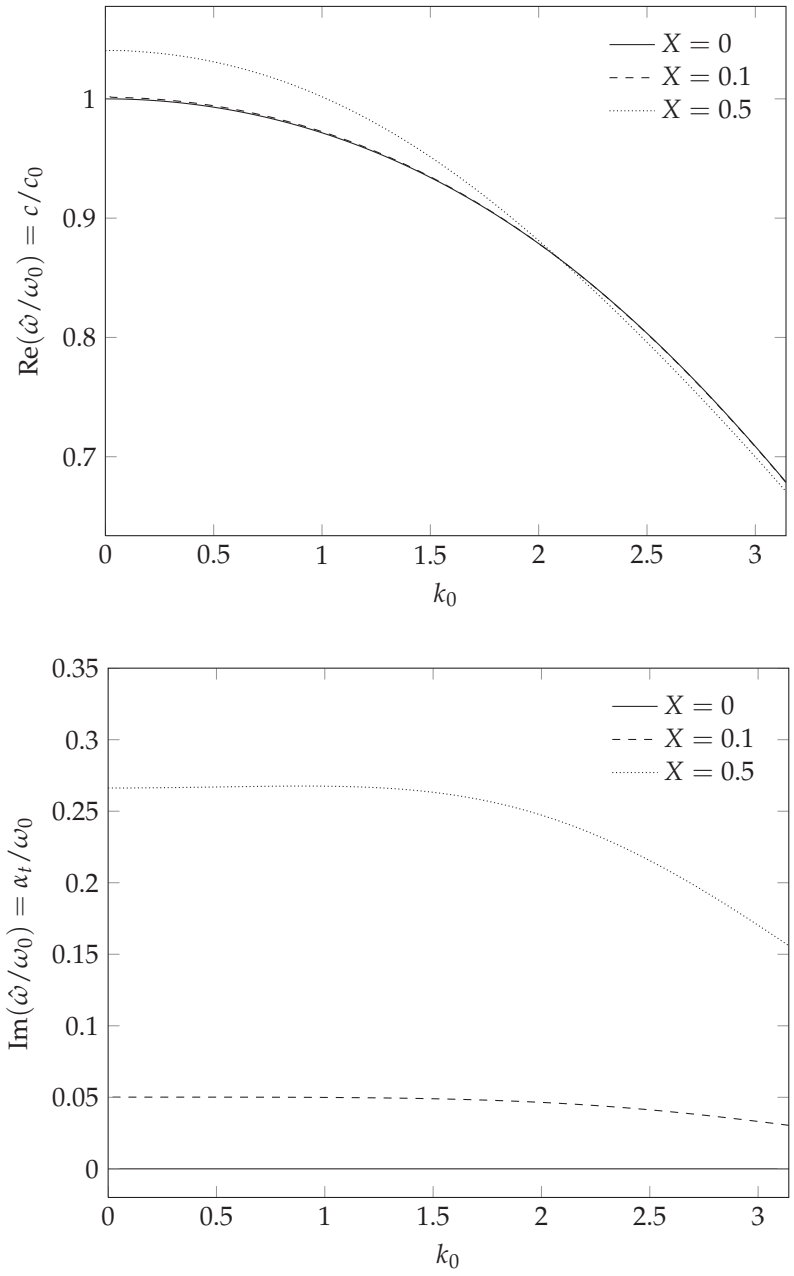

Figure 5.15: The normalised dispersion (upper) and the normalised absorption (lower) of free waves as functions of the numerical resolution k_0 for three different values of X.

this mode is present at initialisation in a simulation at low viscosity, it will be slow to disappear.

The mode propagating in the x-direction can be expressed as the series expansion

$$\boxed{\begin{aligned}\tfrac{\hat{\omega}}{\omega_0} = &\left[1 - \tfrac{1}{36}k_0^2 - \tfrac{1}{1440}k_0^4 + \mathcal{O}(k_0^6)\right] + \mathrm{i}\tfrac{1}{2}X\left[1 + \mathcal{O}(k_0^4)\right] \\ &+ \tfrac{1}{8}X^2\left[1 - \tfrac{1}{4}k_0^2 + \mathcal{O}(k_0^4)\right] + \mathcal{O}(X^3).\end{aligned}} \tag{5.64}$$

As in the forced wave case, this reduces to the DVBE solution (5.42b) as $k_0 \to 0$. The numerical accuracy is second order except the lowest order absorption, where the the lack of a k_0^2 term has been shown in an earlier numerical study [11].

Indeed, the exact dispersion and absorption, plotted in Figure 5.15, show that the absorption changes slowly with k_0. In addition, there is always zero absorption for $X = 0$, unlike the forced wave case.

Accuracy

We have seen that the lattice Boltzmann equation is second-order accurate in space and time, at least in the linear limit. As the numerical resolution is improved, the LBE solution converges to the solution of the discrete-velocity Boltzmann equation, on which the LBE is based. This DVBE predicts the same lowest-order absorption but different dispersion to the isothermal Navier-Stokes-Fourier model. The series expansions of $\hat{k}/k_0$ (5.63) and $\hat{\omega}/\omega_0$ (5.64) quantify the severity of numerical errors in absorption and dispersion.

Let us determine when the numerical dispersion is one percent, meaning that numerical errors cause sound waves to propagate one percent more slowly than they should. For forced and free waves at low X, the series expansions indicate to a good approximation that this occurs when $\omega_0^2/12 = 0.01$ and $k_0^2/36 = 0.01$, respectively. Relating these to the wavelength, both lead to $\lambda_0 = 2\pi/\sqrt{0.36} \approx 10.5$. Thus, with more than 10.5 nodes per wavelength, the numerical dispersion is less than one percent.

5.3.3 Example: Exact wave initialisation

The usefulness of the eigenvalue problem (5.59) is not limited to predicting the wavenumber $\hat{k}$ of forced waves or the frequency $\hat{\omega}$. The eigenvector $\hat{f}^\star$ can also be useful when initialising a simulation. Not so much in the forced wave case where the wave is generated by a source,* but more so

*Such acoustic sources will be described in Chapter 6.

in the free wave case where the wave must already exist fully formed when the simulation is started.

Let us look at a simple one-dimensional free wave case. With one wavelength of a wave of spatially constant amplitude initialised inside a periodic system, an infinite wave is simulated. The initial conditions thus fulfil

$$\rho'(x,0) = \rho^\star \cos(-k_0 x + \varphi_\rho), \tag{5.65a}$$
$$u'(x,0) = u^\star \cos(-k_0 x + \varphi_u), \tag{5.65b}$$

for $0 \leq x \leq \lambda - 1$, with the wavenumber being $k_0 = 2\pi/\lambda$. The periodic boundary condition connects the nodes at $x = 0$ and $x = \lambda - 1$, making them neighbours.

One oft-used initialisation method for this case is to initialise at equilibrium with the amplitudes and phases initialised using the Euler-level relationships $\rho_0 u^\star = c_0 \rho^\star$ and $\varphi_\rho = \varphi_u$ [109–111]. These can be found from (5.22) with $X = 0$. This results in an initial distribution function

$$f_i(x,0) = \rho_0 w_i + \rho^\star w_i \left(1 + \xi_i / c_0\right) \cos(-k_0 x + \varphi_\rho). \tag{5.66}$$

In another, similar initialisation method the choice $u^\star = 0$ is made instead [77, 112], so that the initial condition represents the superposition of two plane waves propagating in opposite directions.*

However, this type of initialisation is inexact for two reasons. Firstly, it neglects the small magnitude ratio difference and phase shift caused by viscosity and discretisation error, as described previously in this chapter. Secondly, the system is initialised at equilibrium with $f_i^{\text{neq}} = 0$, a state which ends immediately when the simulations start unless $\tau = 1$.

Instead, the free wave can be initialised using the eigenvalue problem (5.59). Nonlinear effects notwithstanding, this method should be exact since is based on an exact solution of the same problem. As the wavenumber k_0 is known from the system size λ, we can directly numerically find the eigenvector $\hat{\boldsymbol{f}}^\star$ from the matrix $\hat{\boldsymbol{A}}$ and use it to initialise the simulation as

$$f_i(x,0) = \rho_0 w_i + \operatorname{Re}\left(\hat{f}_i^\star \, \mathrm{e}^{-\mathrm{i}k_0 x}\right). \tag{5.67}$$

The two methods of initialisation can be compared directly to each other by simulation. We choose a system length of $\lambda = 11$ which as previously shown should give a dispersion error of less than one percent. This choice corresponds to $\omega_0 \approx 0.33$ and $k_0 \approx 0.57$. A relaxation time of $\tau = 0.52$ is chosen, resulting in an acoustic viscosity number $X \approx 0.013$. The amplitude was chosen as $\rho^\star/\rho_0 = 10^{-6}$ in order to avoid nonlinear effects.

*The Euler-level amplitude relationship is in general $\rho_0 u^\star = \pm c_0 \rho^\star$; the sign corresponds to propagation in the $\pm x$-direction.

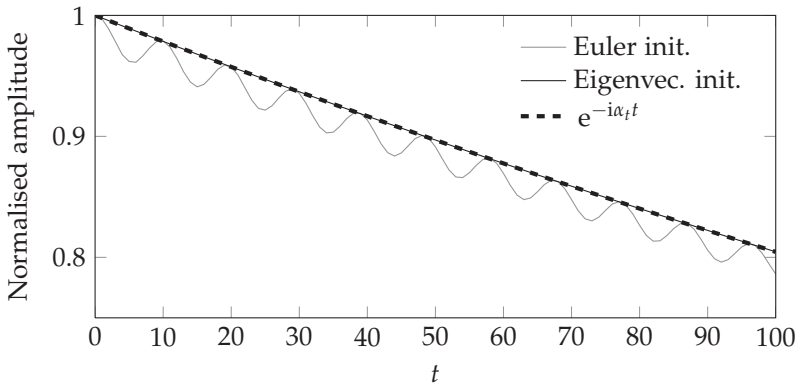

Figure 5.16: Normalised amplitude of the fundamental frequency component absorbed in time, for two different methods of free wave initialisation, along with the predicted Navier-Stokes model absorption. Simulation parameters are $\lambda = 11$, $\tau = 0.52$ (leading to $X \approx 0.013$), and $\rho^\star/\rho_0 = 10^{-6}$.

The comparison of the absorption in time for the two different initialisation methods is shown in Figure 5.16, along with the absorption (5.17) predicted from the Navier-Stokes-Fourier model. The eigenvector initialisation (5.67) and the Navier-Stokes-Fourier model agrees to plotting accuracy. However, with the Euler initialisation (5.66) the wave misbehaves, with a strong periodic ripple in the amplitude.

The errors in the Euler initialisation are caused by the wave being initialised in a way which is not fully consistent with the desired $+x$-propagating wave mode. The initialisation is based on Euler-level expressions which do not take into account the effects of viscosity and discretisation error. Consequently, the actual initialised state is a superposition of two waves: A strong one propagating in the $+x$-direction and a weak one propagating in the $-x$-direction.

The ripple in Figure 5.16 comes from constructive and destructive interference of the two waves. They are initialised at constructive interference, and interfere twice in each wave period. If this explanation of the Euler initialisation errors holds, the ripple period must be half of the wave's period, or approximately $\lambda/2c_0 \approx 9.5$, which matches the observed ripple period quite well.

Of course, this example is somewhat exaggerated, with fairly large values of k_0 and X. If these quantities are smaller, the deviations between the two initialisation methods, which should scale with k_0^2 and X^2, will also decrease. Even so, the eigenvector-based initialisation should still be chosen if possible for the highest possible accuracy.

5.4 Summary and discussion

In this chapter, a linearisation analysis was applied to three comparable, but different models of a fluid: The isothermal Navier-Stokes-Fourier (N-S-F) model, the Boltzmann equation with discretised velocity space (DVBE), and the fully discretised lattice Boltzmann equation (LBE). The analysis resulted in a prediction of how sound would propagate for each model; most importantly, how the speed of sound and the absorption of sound would be altered by governing parameters. Forced wave results for a fourth model, called the Burnett model, were taken from the literature [27].

For the N-S-F model, the single governing parameter is the dimensionless acoustic viscosity number $X = \mathcal{O}(Kn)$, which describes the effect of viscosity on sound propagation. This model and the DVBE and Burnett models do not agree beyond $\mathcal{O}(X)$. This is reasonable considering that the N-S-F model can be derived as a $\mathcal{O}(Kn)$ approximation to the Boltzmann equation. Above this order, that model's predictions cannot be trusted.

The DVBE model is an intermediary step between the Boltzmann equation and the lattice Boltzmann equation, where velocity space has been discretised but not physical space and time. The sound propagation properties of this model also depend on the velocity set used when discretising the velocity space, and the sound waves' angle of propagation. For the D2Q9 velocity set, sound propagation is anisotropic at $\mathcal{O}(X^3)$ and at higher orders.

One particularly interesting result of this anisotropy is the maximum speed of sound at different angles. When a sound wave propagates along a main axis with the D2Q9 velocity set, dispersion causes the phase speed to go asymptotically to $c = |\boldsymbol{\xi}_{i\in\{1\text{–}4\}}| = 1$ as $X \to \infty$. This limit is reasonable, as a higher c would break the CFL condition. However, as the propagation angle moves away from a main axis, the asymptotic phase speed decreases to a minimum of $1/\sqrt{2}$ for diagonal propagation, as shown in Figure 5.11. In Chapter 7, which is about changing the model's equation of state and speed of sound, we will see that increasing the D2Q9 sound speed c_0 above $1/\sqrt{2}$ leads to instability.

Finally, the linearisation analysis on the lattice Boltzmann equation itself shows that sound in LB simulations propagates as predicted by the DVBE model, with the addition of discretisation error terms which start at second order in the numerical resolution. The sound propagation properties of the LBE thus go asymptotically to those of the DVBE as the resolution is increased.

All analyses show major differences in the results for forced waves (generated by a source and absorbed with distance to the source) and free waves (plane waves of infinite extent and constant amplitude, absorbed with time). As an example taken from the isothermal N-S-F model,

the phase speed of *forced waves increases* with frequency, while for *free waves* it *decreases* with frequency. It is not possible to predict the sound propagation properties of one type of wave from those of the other [26]. While both types of wave will be used later in this thesis, only forced waves are physically realisable.

For simulations of sound in the audible range, the acoustic viscosity number X is generally so small that the $\mathcal{O}(X^2)$ deviations between the models are entirely negligible. The discretisation error may as always be decreased by increasing the numerical resolution.

The sound propagation expressions for the DVBE model and the LBE are of course not fully general. These results depend on the choice of equilibrium distribution, propagation angle, and the choice of collision operator. However, for the fully one-dimensional case of plane wave propagation along a main axis with D2Q9, D3Q15, D3Q19, or D3Q27 velocity sets, the problem can be projected down to D1Q3. Then, any original linear collision operator of the form of (4.53) reduces to BGK, as there is only one remaining nonconserved parameter and consequently only one relevant relaxation time. As for dependence on the equilibrium distribution, we will look at a linearisation analysis of a more general equilibrium distribution in Chapter 7.

Plane waves have some different properties to other simple waveforms such as cylindrical and spherical waves. For instance, for $X = 0$, spherical waves have a phase difference between the pressure and velocity component which goes asymptotically to $\pi/2$ as the distance to the origin of the wave goes to 0 [24, Ch. 5]. However, since forced waves lead to a Helmholtz equation where $\hat{k}$ is independent of the waveform, as seen in section 2.3.2, we may expect that the plane wave wavenumber prediction is accurate also for other waveforms. In fact, we will see in Chapter 6 that the predicted wavenumber (5.62) accurately describes the propagation of a simulated cylindrical wave.

The work in this section may be extended by performing thorough analyses on the sound propagation properties of forced waves in the LBE for other velocity sets than D1Q3. This is necessary to describe the anisotropy of the discretisation error for each velocity set.* In the literature, such analyses currently only exist for free waves.

*Similarly to how the D1Q3 results are valid for 1D propagation in a number of other velocity sets, such D2Q9 results would be valid for 2D propagation in the D3Q15, D3Q19, and D3Q27 velocity sets.

6 Mesoscopic acoustic sources

Lattice Boltzmann simulations may deal with sound waves, but where can these sound waves come from?

In some cases, sound is generated aerodynamically by the instability of the flow field itself [42–50, 113–117]. In other cases, sound waves are set up through initial conditions; the initial distribution of f_i is such that sound waves start propagating when the simulation starts running.* For free waves, this initial distribution is typically one wavelength of a sound wave, fit in a periodic system so that it represents a wave of infinite extent [77, 109–112], as done in section 5.3.3. For forced waves, there is typically an initial condition where the density is increased in an area, often with a Gaussian or similar distribution in space [9, 98, 101, 102, 108, 118–120]. This results in a wave propagating outwards from this area.

We will now look at yet another case, where sound is generated continuously throughout the simulation by some kind of source. One such method uses a time-varying boundary condition to generate a sound wave that propagates into the domain [121–123]. Another is based on pinning the density and optionally the velocity in one or more nodes to fixed, oscillating values, i.e.

$$\rho = \rho_0 + \rho^\star \sin(\omega_0 t). \tag{6.1}$$

The earliest published instance of such an LB source was for a heavily modified LBM for wave propagation [124], equivalent to the TLM method [125, 126]. Later versions of such sources were implemented for more standard LBMs for fluid flow [9–11, 86, 98, 99, 127–129].

The latter source method has its disadvantages. Firstly, it fully relaxes the source node(s) to equilibrium in each time step, locally removing the nonequilibrium distribution f_i^{neq} which is relevant to the physical behaviour of the model.† Secondly, it can generate errors in the source node(s) by overwriting the density and fluid velocity of the background flow. This is most easily seen in the limit $\rho^\star = 0$, where the method still

*This also happens as an undesired side effect in cases when a flow field is initialised to an incorrect state, for example when flow in a channel *with* an obstruction is initialised as a normal Poiseuille flow for a channel *without* any obstruction.

†However, alternative implementations of this method that negate this disadvantage by replacing only $f_i^{(0)}$, thus leaving f_i^{neq} intact, should be possible.

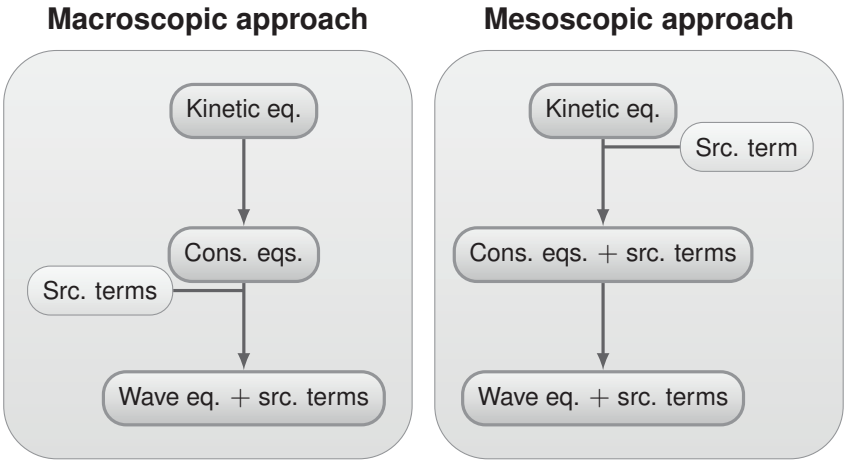

Figure 6.1: Two approaches to multipole source terms in the wave equation. With the classic approach (left), source terms are added at the conservation equation level. With the current approach (right), a single source term is added at the kinetic level.

pins the density to ρ_0. Such errors will propagate outward, polluting the rest of the flow field. Thirdly, no expressions, neither regression- nor theory-based, have been found to relate the amplitudes and phases of the source node and the radiated wave. Therefore, it is hard to predict what comes out of such a source.

In this section we describe and verify a new type of source, based on adding a source term to the kinetic equation; either the Boltzmann equation or the lattice Boltzmann equation. This approach is somewhat analogous to the approach in section 2.3.4, where terms in the conservation equations for mass and momentum lead to multipole source terms in the wave equation. For example, an artificial mass flux source term in the mass conservation equation results in a monopole source term.

With the current method, we go one level deeper: Instead of source terms in the conservation equations, we put a more general particle source term in the kinetic equation. We will see that this causes source terms to appear in the conservation equations derived from the kinetic equation. These source terms lead in turn to source terms in the wave equation. The two different approaches are illustrated in Figure 6.1.

Other extensions to the lattice Boltzmann method also work by adding source terms to the lattice Boltzmann equation. For example, body forces [130], adjustable speed of sound [111], adjustable bulk viscosity [76, Ch. 3], and axisymmetric geometries [131, 132] have all been implemented in a similar way.

6.1 Source terms for the Boltzmann equation

First, we will go through the general case of a source term in the continuous Boltzmann equation. In section 6.2 we will look at the highly related and more directly applicable case of a source term in the lattice Boltzmann equation.

In this derivation, we will make certain approximations: We neglect the effects of heat conduction and molecular relaxation, and use the isentropic equation of state (2.23), to approximate p from ρ as

$$\frac{p}{p_0} = \left(\frac{\rho}{\rho_0}\right)^\gamma. \tag{6.2}$$

This equation of state lets us include the effects of equipartition of energy between translational and inner degrees of freedom.* It also leads to the ideal speed of sound $c_0^2 = \partial p/\partial\rho = \gamma p_0/\rho_0$. Generalising the reference state, we have

$$c_0^2 = \gamma p/\rho. \tag{6.3}$$

Next, we add a source term to the forceless Boltzmann equation (3.20) with the BGK collision operator (3.22),

$$\boxed{\frac{\partial f}{\partial t} + \boldsymbol{\xi}\cdot\nabla f = j - \frac{1}{\tau}\left(f - f^{(0)}\right)} \tag{6.4}$$

Particle source term, j or j_i
An artificial source term in the (lattice) Boltzmann equation which represents the flux of particles being added with position x and velocity ξ at time t

where $j(\boldsymbol{x},\boldsymbol{\xi},t)$ is the *particle source term*, which describes the rate at which particles are added into or removed from the distribution function $f(\boldsymbol{x},\boldsymbol{\xi},t)$. Consequently, the source term lets us specify not only *how much* mass is added, but also the velocity distribution of that mass. In fact, no net mass is necessarily added; for instance $j(\boldsymbol{x},\boldsymbol{\xi},t)$ could be an odd function in velocity space.

We will find the moments of j very useful, and we define them similarly to the moments (3.23) of f,

$$J_0(\boldsymbol{x},t) = \int j(\boldsymbol{x},\boldsymbol{\xi},t)\,\mathrm{d}\boldsymbol{\xi}, \tag{6.5a}$$

$$J_\alpha(\boldsymbol{x},t) = \int \xi_\alpha j(\boldsymbol{x},\boldsymbol{\xi},t)\,\mathrm{d}\boldsymbol{\xi}, \tag{6.5b}$$

$$J_{\alpha\beta}(\boldsymbol{x},t) = \int \xi_\alpha\xi_\beta j(\boldsymbol{x},\boldsymbol{\xi},t)\,\mathrm{d}\boldsymbol{\xi}, \tag{6.5c}$$

and so forth. J_0 represents the instantaneous mass flux, J_α is associated with odd symmetries in velocity space, and $J_{\alpha\beta}$ is associated with even symmetries.

*We now assume that the equilibration process is instant, meaning that the translational and inner degrees of freedom are always in equilibrium, unlike the slower equilibration process described in section 2.3.3.

6.1.1 Macroscopic conservation equations

Our goal now is to find the wave equation that results from the Boltzmann equation with an added source term. This must be found via the conservation equations, which in turn must be found via a Chapman-Enskog expansion of (6.4). As we only need the mass and momentum equations to derive the wave equation, it is easiest to perform a moment-based expansion as in section 4.1.2.

To close the expanded system of equations usefully, we must assume that the source term is at first order of smallness, i.e. $j \to \epsilon j$. (Expanding j across several orders gives no extra benefit in this case.) Expanding (6.4) and separating the orders, we have

$$\mathcal{O}(\epsilon): \qquad \left(\frac{\partial}{\partial t_1} + \xi_\alpha \frac{\partial}{\partial x_\alpha}\right) f^{(0)} = j - \frac{1}{\tau} f^{(1)}, \tag{6.6a}$$

$$\mathcal{O}(\epsilon^2): \qquad \frac{\partial f^{(0)}}{\partial t_2} + \left(\frac{\partial}{\partial t_1} + \xi_\alpha \frac{\partial}{\partial x_\alpha}\right) f^{(1)} = -\frac{1}{\tau} f^{(2)}. \tag{6.6b}$$

The zeroth to second order moments of the terms at first order in smallness are

$$\frac{\partial \rho}{\partial t_1} + \frac{\partial \rho u_\alpha}{\partial x_\alpha} = J_0, \tag{6.7a}$$

$$\frac{\partial \rho u_\alpha}{\partial t_1} + \frac{\partial \Pi^{(0)}_{\alpha\beta}}{\partial x_\beta} = J_\alpha, \tag{6.7b}$$

$$\frac{\partial \Pi^{(0)}_{\alpha\beta}}{\partial t_1} + \frac{\partial \Pi^{(0)}_{\alpha\beta\gamma}}{\partial x_\gamma} = J_{\alpha\beta} - \frac{1}{\tau} \Pi^{(1)}_{\alpha\beta}, \tag{6.7c}$$

and the zeroth and first order moments at second order in smallness are

$$\frac{\partial \rho}{\partial t_2} = 0, \tag{6.8a}$$

$$\frac{\partial \rho u_\alpha}{\partial t_2} + \frac{\partial \Pi^{(1)}_{\alpha\beta}}{\partial x_\beta} = 0. \tag{6.8b}$$

As before, to find the momentum equation we must find $\Pi^{(1)}_{\alpha\beta}$ through

$$\begin{aligned} \frac{\partial \Pi^{(0)}_{\alpha\beta}}{\partial t_1} + \frac{\partial \Pi^{(0)}_{\alpha\beta\gamma}}{\partial x_\gamma} = p\left(\frac{\partial u_\alpha}{\partial x_\beta} + \frac{\partial u_\beta}{\partial x_\alpha}\right) + \delta_{\alpha\beta}\left(\frac{\partial p}{\partial t_1} + \frac{\partial p u_\gamma}{\partial x_\gamma}\right) \\ + \left(u_\alpha J_\beta + u_\beta J_\alpha - u_\alpha u_\beta J_0\right). \end{aligned} \tag{6.9}$$

The second parenthesis previously disappeared in the isothermal case where $\gamma = 1$. In this more general case we will see that it leads to a

γ-dependent bulk viscosity. The parenthesis can be simplified by

$$\frac{\partial p}{\partial t_1} = \frac{\partial p}{\partial \rho}\frac{\partial \rho}{\partial t_1} = c_0^2 \frac{\partial \rho}{\partial t_1}, \qquad \frac{\partial p}{\partial x_\alpha} = \frac{\partial p}{\partial \rho}\frac{\partial \rho}{\partial x_\alpha} = c_0^2 \frac{\partial \rho}{\partial x_\alpha},$$

to get

$$\frac{\partial p}{\partial t_1} + \frac{\partial p u_\gamma}{\partial x_\gamma} = c_0^2 J_0 + (p - c_0^2\rho)\frac{\partial u_\gamma}{\partial x_\gamma} = c_0^2 J_0 + p(1-\gamma)\frac{\partial u_\gamma}{\partial x_\gamma}.$$

This gives us the first order perturbation to the second order moment of f,

$$\begin{aligned} \Pi^{(1)}_{\alpha\beta} = -p\tau \left[\frac{\partial u_\alpha}{\partial x_\beta} + \frac{\partial u_\beta}{\partial x_\alpha} + \delta_{\alpha\beta}(1-\gamma)\frac{\partial u_\gamma}{\partial x_\gamma} \right] \\ + \tau \left(J_{\alpha\beta} - \delta_{\alpha\beta} c_0^2 J_0 - u_\alpha J_\beta - u_\beta J_\alpha + u_\alpha u_\beta J_0 \right). \end{aligned} \tag{6.10}$$

Now we can find the mass and momentum conservation equations,

$$\frac{\partial \rho}{\partial t} + \frac{\partial \rho u_\alpha}{\partial x_\alpha} = J_0, \tag{6.11a}$$

$$\begin{aligned} \frac{\partial \rho u_\alpha}{\partial t} + \frac{\partial \rho u_\alpha u_\beta}{\partial x_\beta} = -\frac{\partial p}{\partial x_\alpha} + \frac{\partial \sigma'_{\alpha\beta}}{\partial x_\beta} \\ + J_\alpha - \frac{\partial}{\partial x_\beta}\tau \left(J_{\alpha\beta} - \delta_{\alpha\beta} c_0^2 J_0 - u_\alpha J_\beta - u_\beta J_\alpha + u_\alpha u_\beta J_0 \right). \end{aligned} \tag{6.11b}$$

with a stress tensor

$$\sigma'_{\alpha\beta} = p\tau \left[\frac{\partial u_\alpha}{\partial x_\beta} + \frac{\partial u_\beta}{\partial x_\alpha} + \delta_{\alpha\beta}(1-\gamma)\frac{\partial u_\gamma}{\partial x_\gamma} \right]. \tag{6.11c}$$

The bulk viscosity $\nu_B = (5/3 - \gamma)\nu$ contained in this stress tensor has been found in previous literature for the same limit of instant equilibration of energy between degrees of freedom [55, 133]. This bulk viscosity also has some familiar limits: For a monatomic gas, $\gamma = 5/3$ and $\nu_B = 0$, as found in section 3.8. For an isothermal gas, $\gamma = 1$ and $\nu_B/\nu = 2/3$, as found in section 4.1.2.

Comparing with the classic source terms in (2.60), we find that the zeroth moment J_0 is equivalent to the mass flux source term Q, as could be expected, and the first moment J_α is analogous to the body force density F_α. The terms in the momentum equation which are proportional to τ have no such analogue.

6.1.2 Linear wave equation

From these conservation equations, we can derive the wave equation. We will perform this derivation under the assumption that the acoustic

fluctuation and viscosity are both small, so that we can linearise by dropping the source moment terms that include both the relaxation time τ and the fluid velocity $\boldsymbol{u}$.

Deriving the wave equation as done previously in section 2.3 but with the inhomogenous continuity equation, we find

$$\frac{\partial^2 \sigma'_{\alpha\beta}}{\partial x_\alpha \partial x_\beta} = \left(\tfrac{4}{3}\mu + \mu_\mathrm{B}\right) \nabla^2 \frac{\partial u_\gamma}{\partial x_\gamma} = -\tau_\nu \nabla^2 \frac{\partial p}{\partial t} + \tau \frac{3-\gamma}{\gamma} \frac{\partial^2 \delta_{\alpha\beta} c_0^2 J_0}{\partial x_\alpha \partial x_\beta}, \quad (6.12)$$

and consequently

$$\boxed{\left[\frac{1}{c_0^2}\frac{\partial^2}{\partial t^2} - \left(1 + \tau_\nu \frac{\partial}{\partial t}\right)\nabla^2\right] p = \frac{\partial J_0}{\partial t} - \frac{\partial J_\alpha}{\partial x_\alpha} + \tau \frac{\partial^2 \left(J_{\alpha\beta} - 3\delta_{\alpha\beta} c_0^2 J_0/\gamma\right)}{\partial x_\alpha \partial x_\beta}.} \quad (6.13)$$

Comparing with the general inhomogeneous wave equation (2.54), the multipole source strengths are

$$\mathcal{T}_0 = \frac{\partial J_0}{\partial t}, \qquad \mathcal{T}_\alpha = -J_\alpha, \qquad \mathcal{T}_{\alpha\beta} = \tau\left(J_{\alpha\beta} - 3\delta_{\alpha\beta} c_0^2 J_0/\gamma\right). \quad (6.14)$$

As the relaxation time $\tau = \mu/p$ is typically very small, the quadrupole strength resulting from j is typically negligible. This could have been expected by the fact that $J_{\alpha\beta}$ appears through $\mathit{\Pi}^{(1)}_{\alpha\beta}$, which is of one order deeper in the smallness parameter ϵ than the Euler-level terms.

Going to the Burnett level, another order deeper in ϵ, might lead to a $\partial^2 J_{\alpha\beta\gamma}/\partial x_\beta \partial x_\gamma$ term in the momentum equation, leading in turn to an octupole term in the wave equation. However, since this term would be at a further level of smallness, it should be even more negligible than the quadrupole term.

6.2 Source terms for the lattice Boltzmann equation

Now that we know and understand the effect of adding a source term to the Boltzmann equation, it is time to investigate what happens when we similarly add a source term to the *lattice* Boltzmann equation.

We start by inputting a source term into the isothermal discrete-velocity Boltzmann equation (4.3),

$$\frac{\partial f_i}{\partial t} + \xi_{i\alpha}\frac{\partial f_i}{\partial x_\alpha} = j_i - \frac{1}{\tau}\left(f_i - f_i^{(0)}\right). \quad (6.15)$$

Since we know from the derivation in 4.1.2 that the DVBE results in the same mass and momentum equations as the continuous Boltzmann

equation (with the exception of a negligible error term), we know that the effect of the source term at this stage in the discretisation process corresponds with that found in the previous section. However, we must consider what happens when we discretise time and space to get a lattice Boltzmann equation with a source term.

We'll assume in this section that we choose the first-order discretisation of the f_i-related terms as in section 4.2.1. Thus, by integrating along the characteristic as in section 4.2, the discretised LBE is

$$\begin{aligned} f_i(\boldsymbol{x}+\boldsymbol{\xi}_i, t+1) - f_i(\boldsymbol{x}, t) = &\int_0^1 j_i(\boldsymbol{x}+\boldsymbol{\xi}_i a, t+a)\,\mathrm{d}a \\ &- \frac{1}{\tau}\left[f_i(\boldsymbol{x}, t) - f_i^{(0)}(\boldsymbol{x}, t)\right]. \end{aligned} \tag{6.16}$$

We must now consider how to approximate the integral over j_i. In the following derivations, we will assume that the source moments are defined as discrete analogues to (6.5), i.e. as

$$J_0(\boldsymbol{x}, t) = \sum_i j_i(\boldsymbol{x}, \boldsymbol{\xi}, t), \tag{6.17a}$$

$$J_\alpha(\boldsymbol{x}, t) = \sum_i \xi_{i\alpha} j_i(\boldsymbol{x}, \boldsymbol{\xi}, t), \tag{6.17b}$$

$$J_{\alpha\beta}(\boldsymbol{x}, t) = \sum_i \xi_{i\alpha}\xi_{i\beta} j_i(\boldsymbol{x}, \boldsymbol{\xi}, t), \tag{6.17c}$$

and so forth.

6.2.1 First order discretisation

Approximating the integral using the rectangle method as in section 4.2.1, the LBE becomes

$$f_i(\boldsymbol{x}+\boldsymbol{\xi}_i, t+1) - f_i(\boldsymbol{x}, t) = j_i(\boldsymbol{x}, t) - \frac{1}{\tau}\left[f_i(\boldsymbol{x}, t) - f_i^{(0)}(\boldsymbol{x}, t)\right]. \tag{6.18}$$

Performing subsequent Taylor and Chapman-Enskog expansions and separating the orders, we have

$$\mathcal{O}(\epsilon): \qquad \left(\frac{\partial}{\partial t_1} + \xi_{i\alpha}\frac{\partial}{\partial x_\alpha}\right) f_i^{(0)} = j_i - \frac{1}{\tau} f_i^{(1)}, \tag{6.19a}$$

$$\begin{aligned} \mathcal{O}(\epsilon^2): \qquad &\frac{\partial f_i^{(0)}}{\partial t_2} + \left(\frac{\partial}{\partial t_1} + \xi_{i\alpha}\frac{\partial}{\partial x_\alpha}\right)\left(1 - \frac{1}{2\tau}\right) f_i^{(1)} \\ &\qquad = -\frac{1}{2}\left(\frac{\partial}{\partial t_1} + \xi_{i\alpha}\frac{\partial}{\partial x_\alpha}\right) j_i - \frac{1}{\tau} f_i^{(2)}. \end{aligned} \tag{6.19b}$$

Following the previous derivation with the additional assumption of $\partial j_i/\partial t_2 = 0$, we end up with the macroscopic conservation equations

$$\frac{\partial \rho}{\partial t} + \frac{\partial \rho u_\alpha}{\partial x_\alpha} = J_0 - \frac{1}{2}\left(\frac{\partial J_0}{\partial t} + \frac{\partial J_\alpha}{\partial x_\alpha}\right), \tag{6.20a}$$

$$\begin{aligned}\frac{\partial \rho u_\alpha}{\partial t} + \frac{\partial \rho u_\alpha u_\beta}{\partial x_\beta} = &-\frac{\partial p}{\partial x_\alpha} + \frac{\partial \sigma'_{\alpha\beta}}{\partial x_\beta} + \left(1 - \frac{1}{2}\frac{\partial}{\partial t}\right) J_\alpha - \frac{\partial \tau J_{\alpha\beta}}{\partial x_\beta} \\ &+ \frac{\partial}{\partial x_\beta}(\tau - \tfrac{1}{2})\left(\delta_{\alpha\beta} c_0^2 J_0 + u_\alpha J_\beta + u_\beta J_\alpha - u_\alpha u_\beta J_0\right),\end{aligned} \tag{6.20b}$$

with the stress tensor

$$\sigma'_{\alpha\beta} = \rho c_0^2 (\tau - \tfrac{1}{2})\left(\frac{\partial u_\alpha}{\partial x_\beta} + \frac{\partial u_\beta}{\partial x_\alpha}\right). \tag{6.20c}$$

The viscosities are the same as before for the first-order discretisation, $\nu = c_0^2(\tau - 1/2)$ and $\nu_B/\nu = 2/3$.

The linearised wave equation derived from these conservation equations is

$$\boxed{\begin{aligned}\left[\frac{1}{c_0^2}\frac{\partial^2}{\partial t^2} - \left(1 + \tau_\nu \frac{\partial}{\partial t}\right)\nabla^2\right] p = &\left(1 - \frac{1}{2}\frac{\partial}{\partial t}\right)\frac{\partial J_0}{\partial t} - \frac{\partial J_\alpha}{\partial x_\alpha} \\ &+ \tau \frac{\partial^2 J_{\alpha\beta}}{\partial x_\alpha \partial x_\beta} - (\tau - \tfrac{1}{2})\frac{\partial^2 3\delta_{\alpha\beta} c_0^2 J_0}{\partial x_\alpha \partial x_\beta}\end{aligned}} \tag{6.21}$$

with multipole strengths

$$\begin{aligned}\mathcal{T}_0 = \left(1 - \frac{1}{2}\frac{\partial}{\partial t}\right)\frac{\partial J_0}{\partial t}, \qquad \mathcal{T}_\alpha = -J_\alpha, \\ \mathcal{T}_{\alpha\beta} = \tau J_{\alpha\beta} - (\tau - \tfrac{1}{2}) 3\delta_{\alpha\beta} c_0^2 J_0.\end{aligned} \tag{6.22}$$

Comparing these with the multipole strengths (6.14) of the undiscretised Boltzmann equation, we clearly see two effects of the discretisation error. Firstly, there is an extra term in the monopole strength, which is less relevant at low frequencies. Secondly, the quadrupole strength does not disappear with viscosity as in the continuous case; in the inviscid case $\tau = 1/2$ we have $\mathcal{T}_{\alpha\beta} = J_{\alpha\beta}/2$.

In other words, the errors that occur when performing this discretisation of the source term in space and time have the beneficial effect of giving non-vanishing quadrupoles even at low viscosities.

6.2.2 Second order discretisation

For comparison, let us now look at the second order discretisation. Using the trapeze method as in section 4.2.2 to approximate the integral, the

LBE becomes

$$f_i(\boldsymbol{x}+\boldsymbol{\xi}_i,t+1)-f_i(\boldsymbol{x},t)=\frac{1}{2}\left[j_i(\boldsymbol{x}+\boldsymbol{\xi}_i,t+1)+j_i(\boldsymbol{x},t)\right] - \frac{1}{\tau}\left[f_i(\boldsymbol{x},t)-f_i^{(0)}(\boldsymbol{x},t)\right]. \tag{6.23}$$

Thus, when calculating $f_i(\boldsymbol{x}+\boldsymbol{\xi}_i,t+1)$ we add particles both for the current time step in the current node, and for the next time step in the neighbouring node.

Performing the Taylor and Chapman-Enskog expansions and separating the orders, we have

$$\mathcal{O}(\epsilon): \qquad \left(\frac{\partial}{\partial t_1}+\xi_{i\alpha}\frac{\partial}{\partial x_\alpha}\right)f_i^{(0)}=j_i-\frac{1}{\tau}f_i^{(1)}, \tag{6.24a}$$

$$\mathcal{O}(\epsilon^2): \quad \frac{\partial f_i^{(0)}}{\partial t_2}+\left(\frac{\partial}{\partial t_1}+\xi_{i\alpha}\frac{\partial}{\partial x_\alpha}\right)\left(1-\frac{1}{2\tau}\right)f_i^{(1)}=-\frac{1}{\tau}f_i^{(2)}. \tag{6.24b}$$

Except for the parenthesis $(1-1/2\tau)$, which changes the relation between τ and ν, this is equivalent to the continuous case. The conservation equations are the same as (6.11), except with $\gamma=1$, and we therefore get an equivalent wave equation,

$$\boxed{\left[\frac{1}{c_0^2}\frac{\partial^2}{\partial t^2}-\left(1+\tau_\nu\frac{\partial}{\partial t}\right)\nabla^2\right]p=\frac{\partial J_0}{\partial t}-\frac{\partial J_\alpha}{\partial x_\alpha} + (\tau-\tfrac{1}{2})\frac{\partial^2\left(J_{\alpha\beta}-3\delta_{\alpha\beta}c_0^2J_0\right)}{\partial x_\alpha\partial x_\beta},} \tag{6.25}$$

and equivalent multipole source strengths

$$\mathcal{T}_0=\frac{\partial J_0}{\partial t}, \qquad \mathcal{T}_\alpha=-J_\alpha, \qquad \mathcal{T}_{\alpha\beta}=(\tau-\tfrac{1}{2})\left(J_{\alpha\beta}-3\delta_{\alpha\beta}c_0^2J_0\right). \tag{6.26}$$

As in the continuous case, the quadrupole strength disappears with the viscosity. Consequently, while this discretisation is more true to the continuous case, the first order discretisation is paradoxically *more useful* because its discretisation errors allow the generation of quadrupoles even at $\tau=1/2$.

6.2.3 Multipole basis

Regardless of the chosen discretisation, how we add particles through j_i will determine which multipole moments $\boldsymbol{J}$ we generate. The question is now how to add particles in unique ways that generate only one multipole moment at a time.

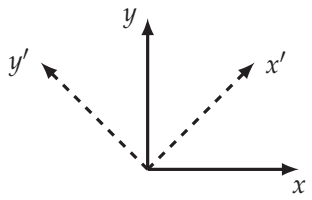

Figure 6.2: The x–y (solid) and x'–y' (dashed) coordinate systems.

For a velocity set with q velocities, j_i can be seen as a q-dimensional vector, which can be found from a q-dimensional orthogonal *particle source basis vector* B_j as $\boldsymbol{j} = \boldsymbol{AB}$. The transformation matrix A_{ij} can be chosen so that each component of B_j represents the strength of a particular multipole.

As all LB velocity sets are symmetric and have an odd number of velocities, one reasonable choice is to have one monopole in addition to $(q-1)/2$ pairs of oddly symmetric dipoles and evenly symmetric longitudinal quadrupoles; one such pair for each pair of opposing velocities $\boldsymbol{\xi}_i$. As we soon shall see, these longitudinal quadrupoles may also be used to construct lateral quadrupoles.

As a concrete example, take the D2Q9 velocity set described in section 4.1.3. Here we get one monopole, four dipoles, and four longitudinal quadrupoles, as shown in Figure 6.3. For the diagonal dipoles and quadrupoles we have introduced a new x'–y' coordinate system, rotated $\pi/4$ to the x–y system, as shown in Figure 6.2. The particle source term j_i is related to the multipole bases B_j through the transformation matrix A_{ij} as

$$\begin{bmatrix} j_0 \\ j_1 \\ j_2 \\ j_3 \\ j_4 \\ j_5 \\ j_6 \\ j_7 \\ j_8 \end{bmatrix} = \begin{bmatrix} w_0 & 0 & 0 & -1 & -1 & 0 & 0 & -1/2 & -1/2 \\ w_1 & 1/2 & 0 & 1/2 & 0 & 0 & 0 & 0 & 0 \\ w_2 & 0 & 1/2 & 0 & 1/2 & 0 & 0 & 0 & 0 \\ w_3 & -1/2 & 0 & 1/2 & 0 & 0 & 0 & 0 & 0 \\ w_4 & 0 & -1/2 & 0 & 1/2 & 0 & 0 & 0 & 0 \\ w_5 & 0 & 0 & 0 & 0 & 1/\sqrt{8} & 0 & 1/4 & 0 \\ w_6 & 0 & 0 & 0 & 0 & 0 & 1/\sqrt{8} & 0 & 1/4 \\ w_7 & 0 & 0 & 0 & 0 & -1/\sqrt{8} & 0 & 1/4 & 0 \\ w_8 & 0 & 0 & 0 & 0 & 0 & -1/\sqrt{8} & 0 & 1/4 \end{bmatrix} \begin{bmatrix} B_0 \\ B_x \\ B_y \\ B_{xx} \\ B_{yy} \\ B_{x'} \\ B_{y'} \\ B_{x'x'} \\ B_{y'y'} \end{bmatrix}. \quad (6.27)$$

The diagonal multipoles, i.e. the ones oriented in the x' and y' directions, are scaled so that they radiate with the same strength as the multipoles oriented in the x and y directions.

From the values of j_i generated by each multipole basis B_j, we can find the corresponding source moments $\boldsymbol{J}$. Table 6.1 shows how the multipole basis defined by (6.27) maps onto the source moments defined in (6.17). The monopole has a quadrupole component due to its even symmetry. The non-diagonal dipoles and quadrupoles map exactly onto the corresponding source moments; the diagonal ones would similarly

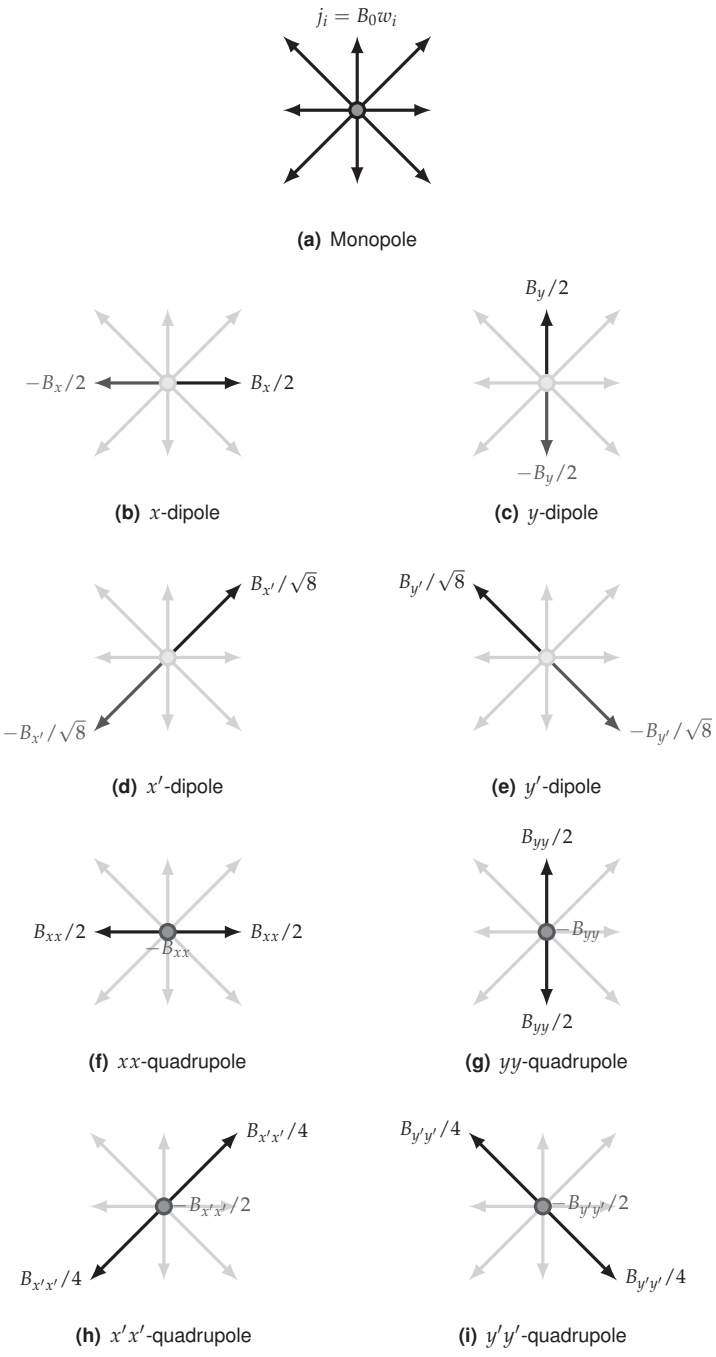

(a) Monopole

(b) x-dipole

(c) y-dipole

(d) x'-dipole

(e) y'-dipole

(f) xx-quadrupole

(g) yy-quadrupole

(h) $x'x'$-quadrupole

(i) $y'y'$-quadrupole

Figure 6.3: Graphical overview of the nine multipole bases for the D2Q9 velocity set.

Table 6.1: Nonzero moments of the D2Q9 basis multipoles B_j

	B_0	B_x	B_y	B_{xx}	B_{yy}	$B_{x'}$	$B_{y'}$	$B_{x'x'}$	$B_{y'y'}$
J_0	1								
J_x		1				$1/\sqrt{2}$	$-1/\sqrt{2}$		
J_y			1			$1/\sqrt{2}$	$1/\sqrt{2}$		
J_{xx}	c_0^2			1				$1/2$	$1/2$
J_{yy}	c_0^2				1			$1/2$	$1/2$
J_{xy}								$1/2$	$-1/2$
J_{yx}								$1/2$	$-1/2$

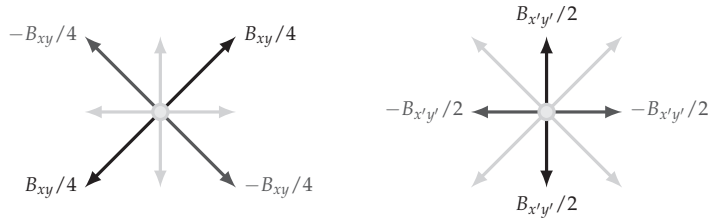

(a) xy-quadrupole **(b)** $x'y'$-quadrupole

Figure 6.4: Virtual bases for lateral quadrupoles, constructed from the longitudinal quadrupole bases.

map exactly onto hypothetical source moments in the x'–y' coordinate system.

To represent the dipole and quadrupole strengths, the dipole vector and the symmetric quadrupole tensor can be introduced [36],

$$\mathcal{D} = \begin{bmatrix} \mathcal{T}_x \\ \mathcal{T}_y \end{bmatrix}, \qquad \mathcal{Q} = \begin{bmatrix} \mathcal{T}_{xx} & \mathcal{T}_{yx} \\ \mathcal{T}_{xy} & \mathcal{T}_{yy} \end{bmatrix}. \tag{6.28}$$

With $B_0 = 0$, both possible discretisations of j result in $\mathcal{T}_{\alpha\beta} \propto J_{\alpha\beta}$. With $B_{xx} = B_{yy} = 0$, we can introduce a virtual basis $B_{xy} = B_{x'x'} = -B_{y'y'}$. Referring to Table 6.1, the quadrupole tensor becomes

$$\mathcal{Q} \propto \begin{bmatrix} 0 & B_{xy} \\ B_{xy} & 0 \end{bmatrix}.$$

Thus we can get lateral xy quadrupoles by setting $B_{x'x'} = -B_{y'y'}$. Similarly we could get lateral $x'y'$ quadrupoles by setting $B_{xx} = -B_{yy}$. These virtual bases are shown in Figure 6.4.

In a sense, the basis we have chosen in (6.27) is overdetermined. We only need to have a basis that can recreate six different source moments: J_0, J_x, J_y, J_{xx}, J_{yy}, and J_{xy}. Consequently, not all nine basis multipoles

in (6.27) are necessary; we could make do with a basis containing B_0, B_x, B_y, B_{xx}, B_{yy}, and B_{xy}. However, while this would be a complete multipole basis, it would not be a complete basis for the nine distribution functions f_i. The chosen basis has the advantage of being trivial to extend to other velocity sets, such as the three-dimensional ones described in section 4.1.3.

6.3 Numerical experiments

To ensure that the lattice Boltzmann multipole sources work as expected, we must verify their behaviour with numerical experiments. We will use only the first order discretisation of the source term performed in section 6.2.1.

This section will use the linearised LBE described in section 4.1.4. This linearity lets us use complex phasor sources, which makes analysis simpler: Anywhere in the domain, we can find the local wave amplitude as $|\hat{p}'|$ and the local wave phase as $\arg(\hat{p}')$. Only the fluctuating part $\hat{f}_i'$ of $\hat{f}_i$ will be simulated.

Explicitly, the numerical scheme used is

$$\hat{f}_i'(\boldsymbol{x}+\boldsymbol{\xi}_i, t+1) - \hat{f}_i'(\boldsymbol{x}, t) = \hat{j}_i - \frac{1}{\tau}\left[\hat{f}_i'(\boldsymbol{x}, t) - \hat{f}_i'^{(0)}(\boldsymbol{x}, t)\right], \tag{6.29a}$$

with an equilibrium distribution

$$\hat{f}_i'^{(0)}(\boldsymbol{x}, t) = w_i\left(\hat{\rho}' + \frac{\rho_0 \hat{u}_\alpha' \xi_{i\alpha}}{c_0^2}\right) \tag{6.29b}$$

and moments

$$\hat{\rho}' = \sum_i \hat{f}_i', \qquad \rho_0 \hat{u}_\alpha' = \sum_i \xi_{i\alpha} \hat{f}_i'. \tag{6.29c}$$

In the cases simulated here, the boundary condition at the edge of the simulated system will not matter; the simulation will be stopped before the first wavefront reaches the boundary.

The waves simulated here will all be forced waves, generated by a source. The exact D1Q3 forced wave numerical wavenumber (5.62) will be used in the following to match the numerical and the analytical solutions.

6.3.1 Plane waves

For the first, simplest case, we simulate forced plane waves generated at one end of the system and propagating towards the other.

Since this is an inherently one-dimensional problem, we use the one-dimensional D1Q3 velocity set with velocities $(\xi_-, \xi_0, \xi_+) = (-1, 0, 1)$, weighting coefficients $(w_-, w_0, w_+) = (1/6, 2/3, 1/6)$, and speed of sound $c_s = 1/\sqrt{3}$. The source is a monopole point source, representing an

infinite pulsating plate in the y-z plane, situated at the leftmost node at $x = 0$. The particle source term consequently becomes

$$\hat{j}_i(x,t) = -\mathrm{i}w_i\,\mathrm{e}^{\mathrm{i}\omega_0 t}S(t)\delta(x). \tag{6.30}$$

Here $\delta(x)$ is a discrete delta function which equals 1 for $x = 0$ and 0 otherwise, while $S(t)$ is the Heaviside step function,

$$S(t) = \begin{cases} 0 & \text{for } t < 0, \\ \frac{1}{2} & \text{for } t = 0, \\ 1 & \text{for } t > 0. \end{cases} \tag{6.31}$$

This function is present to account for the fact that the source does not radiate before the simulation starts at $t = 0$. Also, the complex source is phase shifted so that its real, physical part $j_i = \mathrm{Re}\left(\hat{j}_i\right)$ smoothly starts to increase from 0 at $t = 1$.

A symmetry boundary condition was chosen at $x = 0$, where the unknown distribution function $\hat{f}'_+(0,t)$, which represents particles entering the $x = 0$ node from *outside* the system, is set equal to the known distribution function $\hat{f}'_-(0,t)$, which represents particles entering that node from *inside* the system. This simulates a source which is radiating equally into the simulated domain at $x > 0$ and a symmetric domain at $x < 0$.

Simple forced wave

The first simulation is performed with relaxation time $\tau = 0.6$, and source frequency $\omega_0 = 0.1$, leading to an acoustic viscosity number $X = 0.02$. Due to linearity, the source strength $\hat{p}^\star$ is arbitrary. The simulation is stopped when the first wavefront has reached the position $\alpha_x x = 1$.

Using section 2.3.4 and approximating* the multipole strengths (6.22) of the discrete source term, we find the steady-state analytical solution of this plane wave case as

$$\hat{p}'(x,t) = -\mathrm{i}\hat{p}^\star\frac{c_0}{2}\,\mathrm{e}^{-\alpha_x x}\,\mathrm{e}^{\mathrm{i}(\omega_0 t - kx)}. \tag{6.32}$$

The simulation results are compared with this analytical solution in Figure 6.5. Both the amplitude and the real part of the wave are compared directly, without any artificial scaling or phase shifting of the solutions. There is an excellent match between the numerical and analytical solutions except near the first wavefront, where the numerical solution has simply not had the time to propagate farther before the simulation was stopped.

*The second derivative term in $\mathcal{T}_0$ and the quadrupole contributions of B_0 can be shown to approximately cancel if $\omega_0(\tau - 1/2) \ll 1$. This also holds true in the two-dimensional case, as shown later in section 6.3.2.

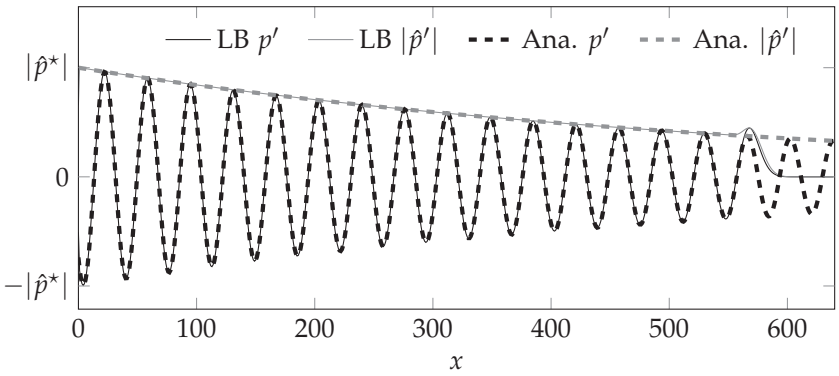

Figure 6.5: Comparison of numerical and steady-state analytical solution of a forced plane wave being radiated into a viscous fluid. Simulation parameters are $\tau = 0.6$, source frequency $\omega_0 = 0.1$, and acoustic viscosity number $X = 0.02$.

Interestingly, the numerical solution is terminated with a bump and a smooth transition to zero, which will be examined next.

Comparing the amplitudes of the numerical and the analytical solution (6.32), we find a relative error of constant amplitude,

$$\left| \frac{|\hat{p}'|_{\text{num}} - |\hat{p}'|_{\text{ana}}}{|\hat{p}'|_{\text{ana}}} \right| \simeq 0.0019$$

everywhere except near the first wavefront. The phase error is similarly constant, at

$$\arg(\hat{p}'_{\text{ana}}) - \arg(\hat{p}'_{\text{num}}) \simeq 0.03 \simeq 0.01\pi.$$

We defer a proper numerical benchmarking of the lattice Boltzmann sources to the end of this chapter.

Precursors

As noted, there is a bump near the first wavefront in Figure 6.5. Such transients, often called *precursors*, appear when a sound wave is radiated into a viscous fluid, and have previously been described in the literature [134]. Close to the source, i.e. for $\alpha_x x \ll 1$, the precursor is weak. However, it is attenuated at a slower rate than the wave itself, and will be clearly visible at $\alpha_x x \sim 1$ and increasingly significant above.

Precursors
In general, transients that occur when a wave is radiated into a dispersive medium

If the boundary condition at $x = 0$ is $u' = u^\star \sin(\omega_0 t) S(t)$, the radiated transient solution is [134]

$$u'(x,t) = u'_{\text{st}}(x,t) + u'_{\text{tr}}(x,t), \tag{6.33a}$$

where the truncated steady-state part u'_{st} and the transient part u'_{tr} are given by

$$u'_{\mathrm{st}}(x,t) = u^\star \,\mathrm{e}^{-\alpha_x x} \sin(\omega_0 t - kx) S(\omega t - kx), \tag{6.33b}$$

$$u'_{\mathrm{tr}}(x,t) = \frac{u^\star}{2} \,\mathrm{e}^{-(\omega_0 t - kx)^2/4\alpha_x x} \,\mathrm{Im}\left[w\left(\sqrt{\alpha_x x} + \mathrm{i}\frac{|\omega_0 t - kx|}{\sqrt{4\alpha_x x}} \right) \right], \tag{6.33c}$$

$w(\ldots)$ being the complex error function known as the Faddeeva function. $u'_{\mathrm{st}}(x,t)$ is a normal steady-state solution, truncated at the first wavefront by the Heaviside function. The transient solution $u'_{\mathrm{tr}}(x,t)$ represents the precursor caused by the viscosity.

While the source in the simulation is a monopole and therefore has $u = 0$ at $x = 0$, the specified velocity boundary condition still holds for the $x > 0$ domain. It is merely cancelled at $x = 0$ by the velocity component of the wave radiated into the $x < 0$ domain.

The numerical solution is compared with (6.33) in Figure 6.6. At the same resolution as in Figure 6.5, the solutions match almost to plotting accuracy. At reduced resolution with $\omega_0 = 0.5$ and $X = 0.02$ held constant, the precursor is smeared out and does not fit the analytical solution well. Even so, the analytical and numerical solution well away from the first wavefront and precursor match very well, as the exact D1Q3 numerical wavenumber (5.62) is used in the comparision.

Note also that the normalised wavelength $\alpha_x \lambda$ is longer in the low-resolution case. This is as expected from equation (5.63), which predicts

$$\alpha_x \lambda = -2\pi \frac{\mathrm{Im}(\hat{k})}{\mathrm{Re}(\hat{k})} \approx \pi X \frac{1 + 5\omega_0^2/24}{1 + \omega_0^2/12}$$

assuming $\omega_0^4 \ll \omega_0^2$, i.e. a normalised wavelength that increases with a coarser numerical resolution.

Inviscid forced wave

Previous authors have successfully simulated LB sound waves at a very low viscosity [45, 108, 115, 120]. We will now attempt to perform a simulation at $\tau = 0.5$, with no viscosity at all.

The simulation is set up like before. The numerical frequency is set to $\omega_0 = 0.1$, and since the simulation is inviscid, we have an acoustic viscosity number $X = 0$.

The simulation results are compared with the analytical truncated steady-state solution in Figure 6.7(a). The real part p' of the numerical solution is smooth and matches the analytical solution very well, apart from a small amount of smoothing near the first wavefront. The wave amplitude $|\hat{p}'|$ shows some ripple, especially around the first wavefront. Since this ripple is not present in the real part p' of the full complex solution $\hat{p}'$, it must be contained in the imaginary part $\mathrm{Im}(\hat{p}')$.

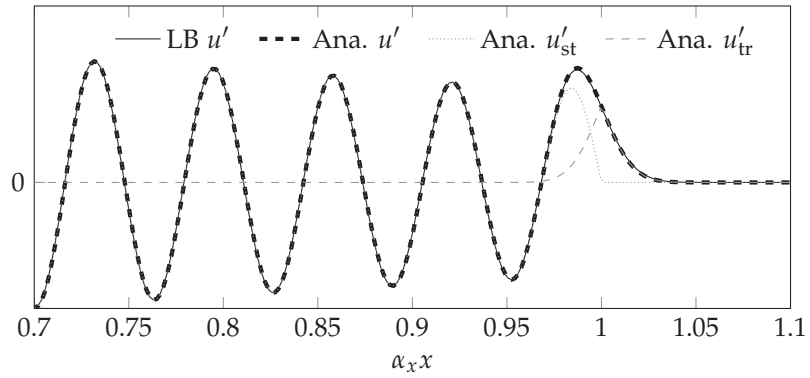

(a) The same case as in Figure 6.5: $\omega_0 = 0.1$, $\tau = 0.6$, $X = 0.02$.

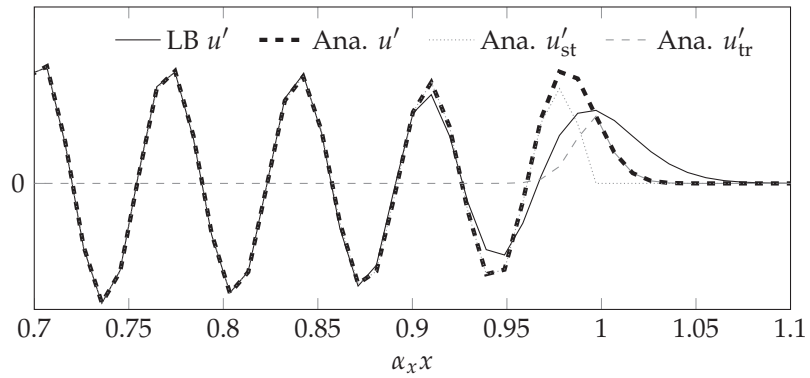

(b) Decreased numerical resolution: $\omega_0 = 0.5$, $\tau = 0.52$, $X = 0.02$.

Figure 6.6: Numerical and analytical solutions of a forced plane wave in a viscous fluid, near the first wavefront. Note how the discretisation error affects the wavelength.

As the imaginary part of the source function (6.30) starts sharply as $\cos(\omega_0 t)S(t)$ unlike the real part which starts smoothly as $\sin(\omega_0 t)S(t)$, it is clear that such ripples occur when starting the source sharply.

A likely cause for this effect is that the Heaviside function in the source function $\hat{j}_i$ represents a rectangular half-window, giving a truncated steady-state solution of

$$\hat{p}'(x,t) = \hat{p}^\star \, \mathrm{e}^{\mathrm{i}(\omega_0 t - kx)} \, S(\omega_0 t - kx). \tag{6.34}$$

From signal theory it is well-known that multiplying a single-frequency signal with a *window function* results in *spectral leakage*, meaning that unwanted frequency components appear in the resulting signal. With the rectangular window, this effect is especially prominent [135, Ch. 10].

Window function
A function of time, only non-zero inside an interval. Typically multiplied with a finite time signal to minimise spectral leakage.

Spectral leakage
A spreading of a signal's frequency components which occurs when the signal is finite in the time domain

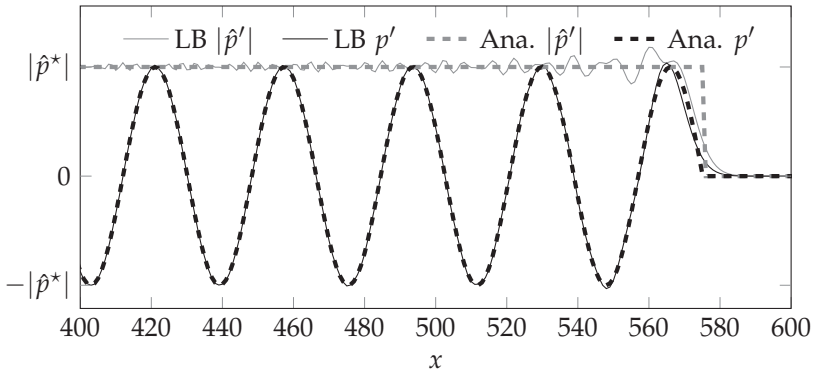

(a) Rectangular half-window

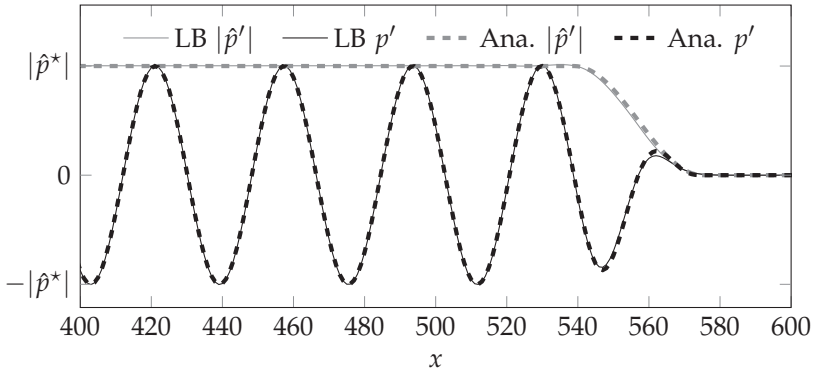

(b) Hann half-window

Figure 6.7: Comparison of two methods of starting an acoustic source in a simulation with $\omega_0 = 0.1$ and $\tau = 0.5$

Consequently, with a rectangular half-window as in the simulation, the signal contains additional frequency components different from ω_0. Since there is an element of numerical dispersion in the LBM as shown in section 5.3, these other frequency components propagate with a slightly different phase speed. Thus, numerical dispersion near the first wavefront is likely the cause of the ripple.

In signal analysis, other window functions can used that have less spectral leakage than a rectangular window. No window functions can avoid it entirely, but one simple window function with better properties is the Hann window, also known as the von Hann or Hanning window [135, Ch. 10]. Adapting it to a half-window covering one wavelength, we get

$$W(t) = \begin{cases} S(t)\left[\frac{1}{2} - \frac{1}{2}\cos(\omega_0 t/2)\right] & \text{for } t \leq 2\pi/\omega_0, \\ 1 & \text{for } 2\pi/\omega_0 \leq t. \end{cases} \tag{6.35}$$

Using this Hann half-window instead of the Heaviside function, the source function is

$$\hat{j}_i(x,t) = -\mathrm{i}\omega w_i \, \mathrm{e}^{\mathrm{i}\omega_0 t} W(t)\delta(x), \tag{6.36}$$

giving an analytical solution

$$\hat{p}'(x,t) = \hat{p}^\star \, \mathrm{e}^{\mathrm{i}(\omega_0 t - kx)} \; W(\omega_0 t - kx). \tag{6.37}$$

The result of a simulation performed like as before but with a Hann half-window is shown in Figure 6.7(b). We see that using the Hann half-window fully eliminates the ripple near the first wavefront, with only a minor deviation remaining.

6.3.2 Multipoles in two dimensions

Having verified that the source term works in one dimension, we turn our attention to multipole sources in two dimensions.

As the pressure responses of the two-dimensional multipole sources are expressed through derivatives of the two-dimensional Green's function (2.56b),

$$\hat{G}(\boldsymbol{x},t) = \frac{1}{4\mathrm{i}} \hat{H}_0^{(2)}(\hat{k}|\boldsymbol{x}|) \, \mathrm{e}^{\mathrm{i}\omega t}, \tag{6.38a}$$

we should find the resulting functions of these derivatives for later use. Using polar coordinates given through $|\boldsymbol{x}|$ and θ, the first derivatives of the Green's function result in

$$\frac{\partial}{\partial x}\hat{G}(\boldsymbol{x},t) = \frac{-\hat{k}}{4\mathrm{i}} \cos\theta \; \hat{H}_1^{(2)}(\hat{k}|\boldsymbol{x}|) \, \mathrm{e}^{\mathrm{i}\omega t}, \tag{6.38b}$$

$$\frac{\partial}{\partial y}\hat{G}(\boldsymbol{x},t) = \frac{-\hat{k}}{4\mathrm{i}} \sin\theta \; \hat{H}_1^{(2)}(\hat{k}|\boldsymbol{x}|) \, \mathrm{e}^{\mathrm{i}\omega t}. \tag{6.38c}$$

The second derivatives result in

$$\begin{aligned}\frac{\partial^2}{\partial x^2}\hat{G}(\boldsymbol{x},t) = \frac{\hat{k}^2}{4\mathrm{i}} \Bigg\{ &\frac{1}{2}\cos^2\theta \; \left[\hat{H}_2^{(2)}(\hat{k}|\boldsymbol{x}|) - \hat{H}_0^{(2)}(\hat{k}|\boldsymbol{x}|)\right] \\ &- \frac{1}{\hat{k}|\boldsymbol{x}|}\sin^2\theta \; \hat{H}_1^{(2)}(\hat{k}|\boldsymbol{x}|) \Bigg\} \mathrm{e}^{\mathrm{i}\omega t},\end{aligned} \tag{6.38d}$$

$$\begin{aligned}\frac{\partial^2}{\partial y^2}\hat{G}(\boldsymbol{x},t) = \frac{\hat{k}^2}{4\mathrm{i}} \Bigg\{ &\frac{1}{2}\sin^2\theta \; \left[\hat{H}_2^{(2)}(\hat{k}|\boldsymbol{x}|) - \hat{H}_0^{(2)}(\hat{k}|\boldsymbol{x}|)\right] \\ &- \frac{1}{\hat{k}|\boldsymbol{x}|}\cos^2\theta \; \hat{H}_1^{(2)}(\hat{k}|\boldsymbol{x}|) \Bigg\} \mathrm{e}^{\mathrm{i}\omega t},\end{aligned} \tag{6.38e}$$

$$\frac{\partial^2}{\partial x \partial y}\hat{G}(\boldsymbol{x},t) = \frac{\hat{k}^2}{4\mathrm{i}} \cos\theta \; \sin\theta \; \hat{H}_2^{(2)}(\hat{k}|\boldsymbol{x}|) \, \mathrm{e}^{\mathrm{i}\omega t}. \tag{6.38f}$$

Also useful is $\partial^2\hat{G}/\partial x_\alpha \partial x_\alpha$, which becomes remarkably simple,

$$\left(\frac{\partial^2}{\partial x^2} + \frac{\partial^2}{\partial y^2}\right)\hat{G}(\boldsymbol{x},t) = -\frac{\hat{k}^2}{4\mathrm{i}}\hat{H}_0^{(2)}(\hat{k}|\boldsymbol{x}|)\,\mathrm{e}^{\mathrm{i}\omega t} = -\hat{k}^2\hat{G}(\boldsymbol{x},t). \tag{6.38g}$$

With the exception of the longitudinal quadrupoles $\partial^2\hat{G}/\partial x^2$ and $\partial^2\hat{G}/\partial y^2$, each of these functions can be handily separated into a θ-dependent part and a $|\boldsymbol{x}|$-dependent part.

Note how the functions $\hat{G}$ and $\partial^2\hat{G}/\partial x_\alpha\partial x_\alpha$ are simply proportional. Using this, the inhomogeneous wave equation (6.21), and the map from B_0 to $J_{\alpha\alpha}$ in Table 6.1 we have that the response of a monofrequency basis source B_0 is

$$\hat{p}'(\boldsymbol{x},t) = \left(\mathrm{i}\omega_0 + \tfrac{\omega_0^2}{2} - \tau c_0^2\hat{k}^2\right)\frac{B_0}{4\mathrm{i}}\hat{H}_0^{(2)}(\hat{k}|\boldsymbol{x}|)\,\mathrm{e}^{\mathrm{i}\omega t},$$

where the three terms in the parenthesis are the contributions from the correct monopole term, the monopole discretisation error term, and the $\mathcal{T}_{\alpha\beta}$ quadrupole contribution of the monopole basis B_0, respectively. For $\tau \to 1/2$ and $\omega_0^2 \ll 1$, we have from (5.63) that $\omega_0^2/2 \simeq \tau c_0^2\hat{k}^2$, and the two latter terms in the parenthesis cancel. In other words: For low viscosity and decent numerical resolution, the unwanted contributions of the monopole source basis cancel.

The simulations in this section are set up as follows. Using the D2Q9 velocity set described in section 4.1.3, we place a point source in the centre of the two-dimensional simulation domain, with

$$\hat{j}_i(x,t) = -\mathrm{i}w_i\,\mathrm{e}^{\mathrm{i}\omega_0 t}W(t)\delta(\boldsymbol{x}). \tag{6.39}$$

Again, $\delta(\boldsymbol{x})$ is a discrete delta function which equals 1 for $\boldsymbol{x} = \boldsymbol{0}$ and 0 elsewhere, and $W(t)$ is the Hann half-window (6.35). The simulation is stopped when the first wavefront reaches the boundary. The simulation performed are inviscid with $\tau = 1/2$. We will see that the BGK collision operator works poorly in this limit. Instead we will for the most part use the general-purpose MRT operator described in section (4.3.1), where the relaxation time of the nonhydrodynamic moments is set to one.

Radial variation of pressure

First we will compare the radial pressure variation, i.e. how $\hat{p}'$ varies with $|\boldsymbol{x}|$, of the numerical multipole sources with the corresponding analytical solutions. These simulations were performed with $\omega_0 = 0.25$, $\tau = 1/2$ (resulting in $X = 0$), in a domain of 201×201 nodes. Although the boundary conditions should not matter since the wave will not reach the outer boundary, periodic boundaries were used. Each simulation was performed once with the BGK operator and once with the MRT operator.

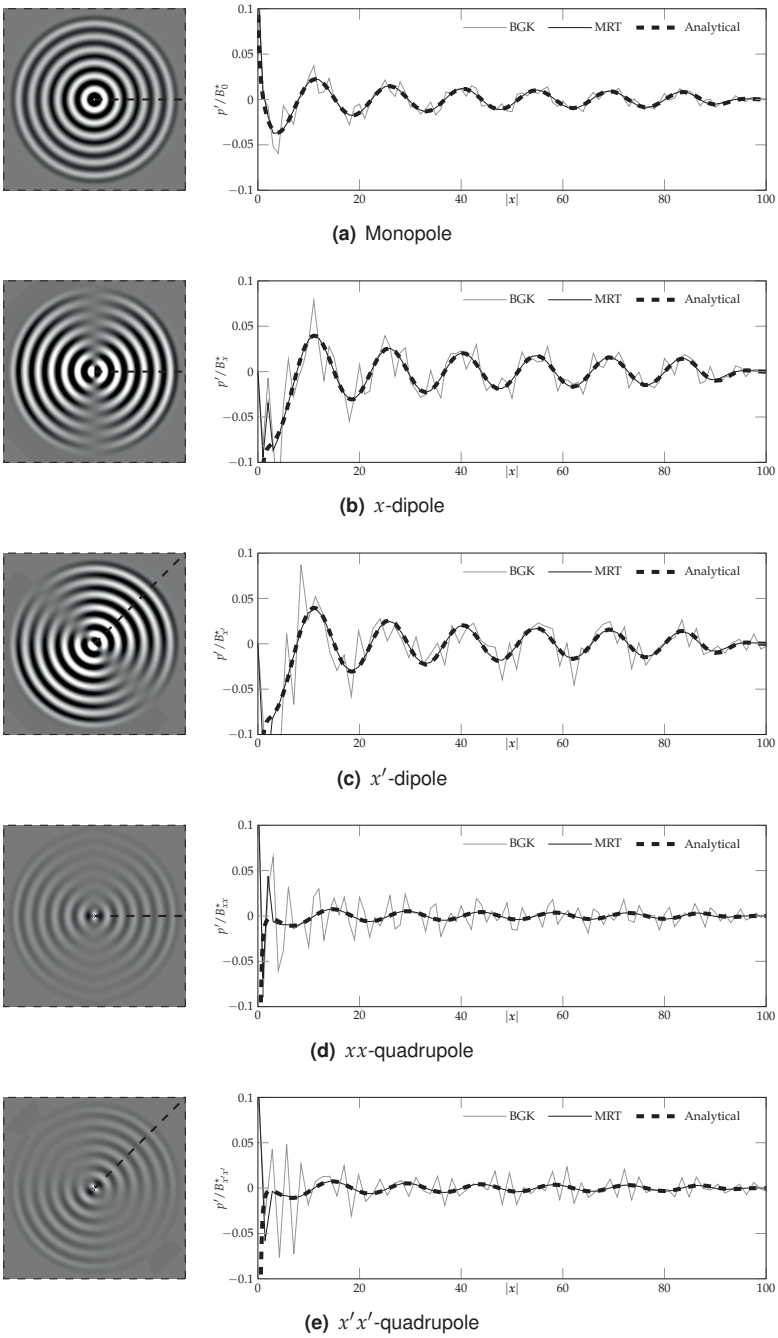

(a) Monopole

(b) x-dipole

(c) x'-dipole

(d) xx-quadrupole

(e) $x'x'$-quadrupole

Figure 6.8: Radial pressure from representative multipoles, simulated with BGK and MRT and compared to analytical solutions. The left-hand images come from the MRT simulations, and indicate the lines along which the right-hand pressures were measured.

The results of the simulations and comparisons with analytical solutions found from (2.59), (6.22), and (6.38) are shown in Figure 6.8 for five representative multipoles: A monopole, x- and x'-dipoles, and xx- and $x'x'$-quadrupoles. The remaining four multipoles are not necessary to verify because of the rotational symmetry of the D2Q9 velocity set.

Most strikingly, the BGK results display strong spurious oscillations which dominate the solution in the dipole and quadrupole case. On the other hand, the MRT results demonstrate a largely excellent agreement with the analytical solution, with two exceptions: There are minor errors near the first wavefront like in Figure 6.7(b), and there are major errors in the immediate vicinity of the source node.

The errors close to the source node are likely caused by the high spatial derivatives compared to the spatial resolution close to the source. With a point source, it is impossible to refine the resolution in such a way that the spatial derivatives near the source become managable; as the resolution is improved, the effective size of the point source node shrinks. In addition, the singularity present at the source point in the analytical solutions can never be reproduced numerically, since the particle source term must be finite. However, perhaps the problems near the source could be alleviated using a spatially smoothed source that spans several nodes [136], or by using a wider dipole and quadrupole basis which involves more particle distributions than the minimal basis used here.

The errors close to the source are present and of similar magnitude in both the BGK and the MRT solutions. The MRT operator used here differs from the BGK operator only in that it fully supresses nonhydrodynamic moments in each timestep. Consequently, these results suggest that errors in the nonhydrodynamic moments are created at the source, and the BGK operator propagates them outwards with the wave while the MRT operator suppresses them, leaving an accurate solution.

Angular variation of pressure

We have now verified that the radial variation of the pressure of the numerical solution agrees with that of the analytical solution except in the immediate vicinity of the source if the MRT collision operator is used. We should subsequently verify that the angular variation of the pressure is also correct.

In order to compare pressure at a constant distance from the source and different angles, the numerical solution must be sampled between the nodes. For this reason, some interpolation of the solution is required. In order to improve the quality of this interpolation, the numerical resolution was increased by 250 % compared to the previous simulations. The simulations were performed with parameters $\omega_0 = 0.1$, $\tau = 1/2$ (leading to $X = 0$), and a domain of 501×501 nodes.

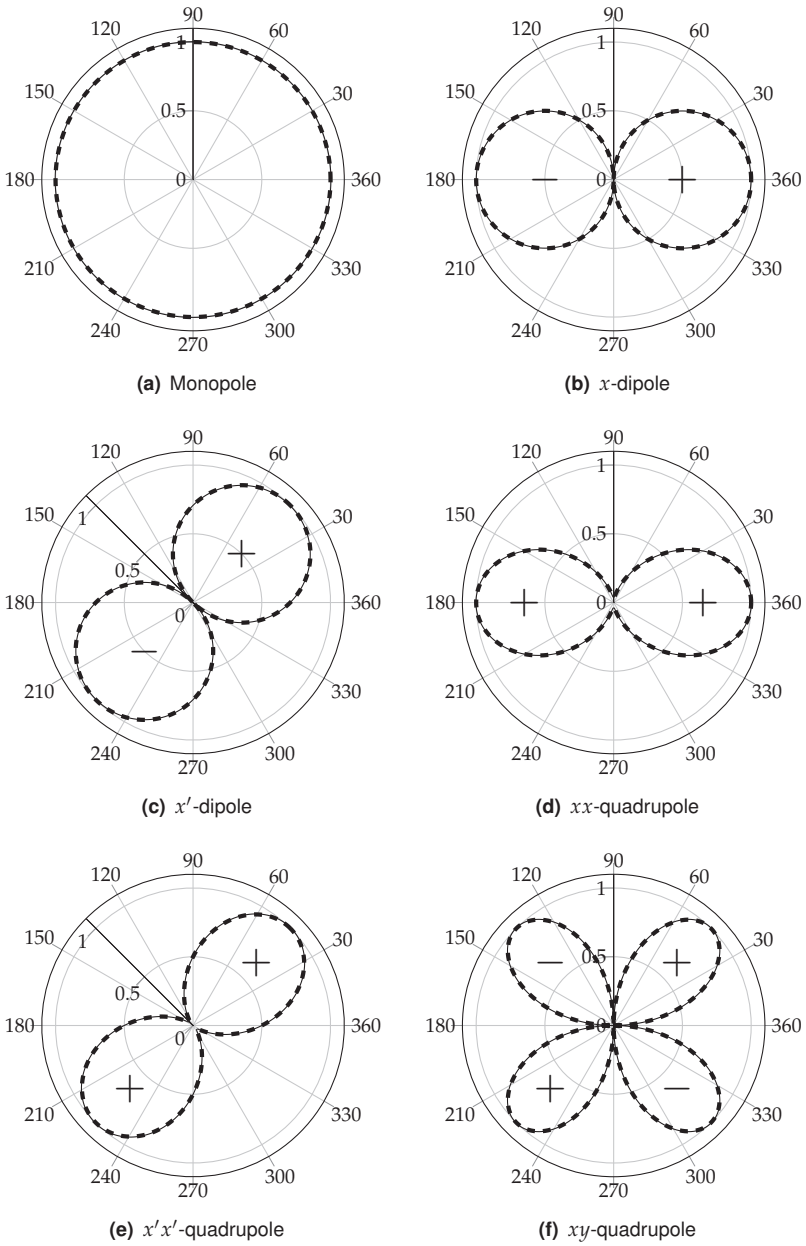

(a) Monopole **(b)** x-dipole

(c) x'-dipole **(d)** xx-quadrupole

(e) $x'x'$-quadrupole **(f)** xy-quadrupole

Figure 6.9: $|\hat{p}'|$ as function of angle θ at $k|\boldsymbol{x}| = 25$, compared between MRT-based simulations (——) and analytical solutions (**- - -**) and normalised by the maximum of the analytical solution. Relative lobe phase is indicated by plus and minus signs.

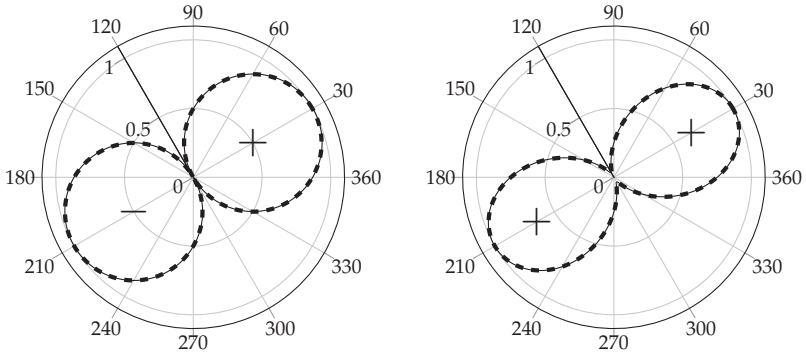

(a) Rotated x-dipole **(b)** Rotated xx-quadrupole

Figure 6.10: Angular variation of two rotated multipoles, plotted as in Figure 6.9.

In addition to the five multipoles simulated in the previous comparison, the xy-quadrupole, generated by superposition of the $x'x'$- and $y'y'$-quadrupoles as described in section 6.2.3, was simulated. The numerical solutions were measured for all angles at a distance of $k|\boldsymbol{x}| = 25$, corresponding to a distance of roughly four wavelengths. The results are compared with the corresponding analytical solutions in Figure 6.9, with both the numerical and the analytical solutions normalised by the maximum of the analytical solutions. In all cases, there is an excellent agreement between the numerical and analytical solutions.

Rotated multipoles and composite sources

The basic multipoles that have been described and verified so far may be superposed in order to generate more complex sources. As examples of this, we will look at multipole rotation and a highly directive composite source.

Dipoles and quadrupoles can be rotated with an angle θ by applying the rotation matrix

$$\boldsymbol{a} = \begin{bmatrix} \cos\theta & -\sin\theta \\ \sin\theta & \cos\theta \end{bmatrix} \tag{6.40}$$

to the dipole vector or the quadrupole tensor (6.28) as [137, App. 6]

$$\mathcal{D}_\alpha^{\text{rot}} = a_{\alpha\beta}\mathcal{D}_\beta, \qquad \mathcal{Q}_{\alpha\beta}^{\text{rot}} = a_{\alpha\gamma}a_{\beta\delta}\mathcal{Q}_{\gamma\delta}. \tag{6.41}$$

For example, taking an x-dipole and an xx-quadrupole and rotating results in

$$\mathcal{D}^{\text{rot}} \propto \begin{bmatrix} \cos\theta \\ \sin\theta \end{bmatrix}, \qquad \mathcal{Q}^{\text{rot}} \propto \begin{bmatrix} \cos^2\theta & \sin\theta\cos\theta \\ \sin\theta\cos\theta & \sin^2\theta \end{bmatrix}.$$

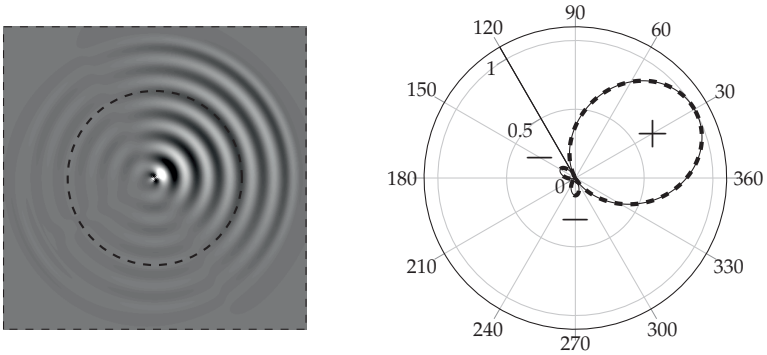

Figure 6.11: The MRT simulation result of a rotated supercardioid source (left) and its normalised angular variation at $|\boldsymbol{x}| = 25/k$, plotted as in Figure 6.9 (right).

Both longitudinal and lateral quadrupoles are present in the resulting quadrupole tensor. Results of simulations where the basis strengths were chosen to reproduce the dipole vector and quadrupole tensor for a rotation of 30° are shown in Figure 6.10.

By superposing different types of multipoles, we can generate composite sources that have other properties that might be useful, such as being focused in a particular direction. For instance, one type of source is generated by requiring that the x-dipole and the xx-quadrupole have the same amplitude at $\theta = 0$ and some particular distance $\boldsymbol{x}$ (which may be in the far-field limit). Mathematically, this leads to

$$\mathcal{T}_x \frac{\partial \hat{G}(\boldsymbol{x},t)}{\partial x} = \mathcal{T}_{xx} \frac{\partial^2 \hat{G}(\boldsymbol{x},t)}{\partial x^2} \quad \Rightarrow \quad \frac{B_x}{B_{xx}} = \frac{\hat{k}\left[\hat{H}_2^{(2)}(\boldsymbol{x},t) - \hat{H}_0^{(2)}(\boldsymbol{x},t)\right]}{4\hat{H}_1^{(2)}(\boldsymbol{x},t)}.$$

This type of source is called a supercardioid [138]. This was simulated with the dipole and quadrupole amplitudes normalised at $|\boldsymbol{x}| = 25/k$ and the resulting dipole vector and quadrupole tensor rotated 30°. The simulation results of this rotated supercardioid are shown in Figure 6.11. As could be expected by this point, the agreement is excellent.

Numerical convergence of radiated wave

It is insufficient to merely compare the numerical and analytical solutions at a particular resolution and verify that they agree well. The source must also be shown to radiate a wave which corresponds *increasingly well* to the analytical solution as the numerical resolution is increased. The LBM itself has a second order accuracy [92], meaning that the numerical error, i.e. the difference between a numerical and a corresponding analytical solution, decreases proportionally to the square of the numerical resolution. In

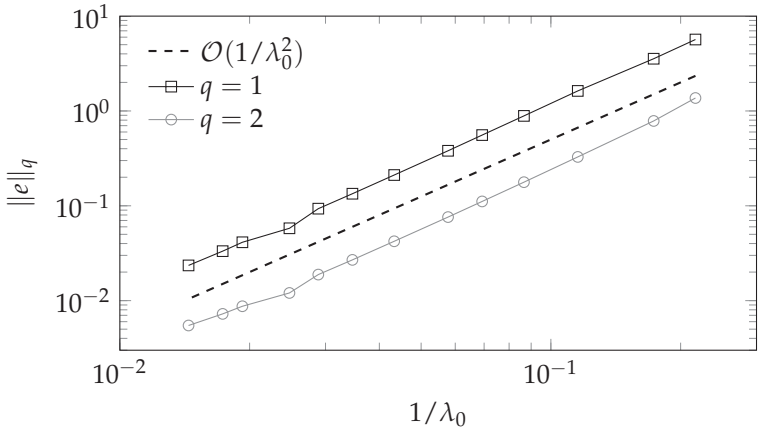

Figure 6.12: 1- and 2-norm of the relative error of the monopole pressure amplitude as found by (6.42), compared with second-order convergence.

order to not degrade the total order of accuracy of the simulation, any extension to the LBM must also have second order accuracy.

To determine the order of accuracy of the waves radiated by the source node, the numerical error must be calculated at a number of different resolutions. The order of accuracy can be extrapolated from how quickly the error decreases as the resolution is increased. In the case of our source, we must determine how quickly the radiated waves converge towards the analytical solution. For quantification, the q-norm of the relative error [104, App. A] of the monopole pressure amplitude,

$$\|e\|_q = \sqrt[q]{\frac{1}{\lambda_0^2} \sum_{|\boldsymbol{x}|=\lambda_0}^{3\lambda_0} \left| \frac{|p'|_{\text{num}} - |p'|_{\text{ana}}}{|p'|_{\text{ana}}} \right|^q}, \tag{6.42}$$

was calculated. The error computation was restricted to $\lambda_0 \leq |\boldsymbol{x}| \leq 3\lambda_0$, with $\lambda_0 = 2\pi c_0/\omega_0$, in order to restrict the comparison to the areas unaffected by the aforementioned discrepancies near the source and the first wavefront.

This analysis was performed for an article by this author [13] using the regularised collision operator described in section 4.3.2. Since this operator is equivalent to the MRT operator previously used in this chapter [76, 89], these results are also equivalent.

The results of the analysis for the 1- and 2-norms are shown in Figure 6.12 against the relative resolution $1/\lambda_0$. The norms are compared to a curve representing second-order convergence. From the comparison, it is clear that the sound wave radiated from the source converges at second order.

6.4 Summary and discussion

Macroscopically, multipole source terms in the wave equation stem from terms in the mass and momentum conservation equations. Monopoles come from mass source terms, dipoles from force terms, and quadrupoles come from the nonlinear advection term.

In this chapter we have seen a mesoscopic approach to such source terms, based on adding a particle source term to the Boltzmann equation. The resulting multipole source terms, as found through a Chapman-Enskog analysis, are given by the moments of this particle source term.

This mesoscopic approach can be motivated in a similar way to the traditional macroscopic monopole where a source term is added to the mass conservation equation to model the pulsations of small bodies. The mesoscopic approach simply lets us capture more general vibrations of such bodies.

This mesoscopic approach can be implemented in the lattice Boltzmann method simply by including the particle source term in the discretisation in velocity space, physical space, and time. Similarly to the non-discretised case, a Chapman-Enskog analysis can be used to determine how the moments of these discrete particle source terms cause acoustic multipoles.

Interestingly, the first order discretisation in space and time turn out to be more useful than the second order discretisation. While the latter is consistent with the continuous case, the former allows the simulation of quadrupoles which do not vanish in the inviscid limit.

Numerical results from the multipole sources simulated using this method largely show very good agreement with predictions based on the Chapman-Enskog analysis and the analytical wavenumber (5.62) from Chapter 5. An exception is the immediate vicinity of a point source, where the singularity in the analytical solution is impossible to capture numerically. Using a MRT scheme with instantaneous relaxation of the nonhydrodynamic moments, accurate results were achieved even for fully inviscid simulations.

We have seen that the cylindrical waves radiated by a monopole D2Q9 source are second order convergent. This indicates that the sound wave radiation of the source and the application of the D1Q3 forced plane wave propagation prediction to this cylindrical wave case are both second order accurate.

The choice of multipole basis is somewhat arbitrary, which means that the D2Q9 multipole choices shown in (6.27) and Figure 6.3 are not unique. This basis was chosen because it is simple in form, it is complete when applied to any velocity set, and it maps well onto the particle source moments as shown in Table 6.1. However, other bases are possible, and spreading the particles emitted by the source more evenly

by including more velocities in the bases may lessen the discrepancy between simulation and analytical solution near dipole and quadrupole sources. Bases containing lateral quadrupole moments such as J_{xy} would also be useful, as these must currently be constructed from multiple bases such as $B_{x'x'}$ and $B_{y'y'}$.

In this chapter we have seen that the mesoscopic multipole source works well for the D1Q3 and D2Q9 velocity sets. While there is no reason to believe that it would not also work well in all the 3D velocity sets described in section 4.1.3, this was not tested in the course of this work.

7 Variable equation of state

The basic LBM that we have looked at so far is an isothermal model where the speed of sound c_0 is a velocity set constant, determined as in (4.11).

Now, what is the reason that the velocity set constant and the speed of sound coincide? Physically, the speed of sound is

$$c_0^2 = \left(\frac{\partial p}{\partial \rho}\right)_{s,0}, \tag{7.1}$$

the derivative being evaluated at the rest state with the entropy s held constant. Denoting the velocity set constant as c_ξ, the macroscopic analysis of the model results in an equation of state $p = c_\xi^2 \rho$, which directly leads to a speed of sound $c_0 = c_\xi$. As a consequence of this, the speed of sound could be changed by changing the equation of state of the LB model.

The chosen equilibrium distribution function $f_i^{(0)}$ determines much of the macroscopic behaviour of the resulting model. The moments of $f_i^{(0)}$ directly determine the behaviour at the Euler level, and indirectly through (4.16c) determine the Navier-Stokes-Fourier level behaviour.

In section 4.1 we found $f_i^{(0)}$ from a Taylor expansion of the Maxwell-Boltzmann distribution (3.18). In the literature, the equilibrium distribution is sometimes given as a power series in $\boldsymbol{u}$ with series coefficients containing unknowns. These unknowns are subsequently chosen to fulfil some particular purpose, which is typically to have macroscopic equations corresponding to those of fluid mechanics [92, 110, 139–143].

In addition, $f_i^{(0)}$ can be constructed by other methods from the continuous Maxwell-Boltzmann equilibrium distribution (3.18) to get non-isothermal models. One method uses a moment expansion of this distribution in tensor Hermite polynomials [144]. However, the equilibrium distribution $f_i^{(0)}$ that directly results from this process is not necessarily stable for all velocity sets [144]. Indeed, there is a complicated connection between the stability of LB simulations and the chosen equilibrium distribution.

Chopard et al. [143] proposed an equilibrium distribution where the function $f_0^{(0)}$ is defined differently to the other functions $f_i^{(0)}$, so that the portion of zero-velocity particles at equilibrium is adjustable. This leads to an adjustable coefficient c_i in the equation of state $p = c_\mathrm{i}^2 \rho$. If the

Isothm. speed of sound, c_i If a medium with speed of sound c_0 were made isothermal (i.e. $\gamma = 1$), the sound speed would become $c_\mathrm{i} = c_0/\sqrt{\gamma}$

coefficient c_i is held constant, then $c_0 = c_\mathrm{i}$, meaning c_i can be seen as an *isothermal speed of sound*. In this model, a larger proportion of zero-velocity particles leads to a lower speed of sound, which is physically meaningful as this corresponds to a lower pressure/density ratio and that the ideal gas speed of sound is $c_0 = \sqrt{\gamma p_0/\rho_0}$.

Similar models have also been presented previously [141, 144–147], though most of these do not reduce to the equilibrium distribution (4.2) given by the Taylor expanded Maxwell-Boltzmann distribution if $c_\mathrm{i} = c_{\tilde{\xi}}$. However, the model by Chopard et al. represents an extension instead of a replacement of the basic equilibrium distribution (3.18) used previously in this thesis, in addition to being explicit for any velocity set. This seems likely to be an important advantage, as that basic equilibrium distribution has been suggested to be the optimally stable polynomial equilibrium for an isothermal equation of state [75]. In addition, the equilibrium by Chopard et al. can be directly applied to any velocity set, unlike those of [144] and [147], which are given only for D2Q9 and D3Q19, respectively.* We will therefore choose to consider this particular method in the following sections.

A strength of these models is that the coefficient c_i is not necessarily constant. Consequently, the equation of state $p = c_\mathrm{i}^2\rho$ is quite flexible; c_i can be chosen e.g. as a function of the local state variables and their history.

As we shall see, a corresponding downside of such models is that they lead to a c_i-dependent bulk viscosity and extra terms in the momentum equation that only disappear if $c_\mathrm{i} = c_{\tilde{\xi}}$. To control the bulk viscosity, we use Lätt's adaptation [76, Ch. 3] of Dellar's bulk viscosity modification method [77].† Most of the other extra terms turn out to be negligible under similar assumptions to those used in section 2.3.5 for the equations of nonlinear acoustics. The single non-negligible extra term contributes to the bulk viscosity when p is a function of ρ. Its contribution is shown to be physically reasonable for $c_\mathrm{i} \approx c_{\tilde{\xi}}$ and an isentropic equation of state.

There also exist other LB models for variable speed of sound [111, 127], which include body force terms of the form $\boldsymbol{F} = \alpha\nabla\rho$ to augment the pressure gradient term in the momentum equation from $c_{\tilde{\xi}}^2\nabla\rho$ to $(c_{\tilde{\xi}}^2 - \alpha)\nabla\rho$. Here, α is a constant and the density gradient is estimated using finite differences. The result is an equation of state $p = (c_{\tilde{\xi}}^2 - \alpha)\rho$, and a speed of sound $c_0 = \sqrt{c_{\tilde{\xi}}^2 - \alpha}$. This method does not seem to cause any error terms in the macroscopic equations. However, the method introduces its own errors and difficulties by using a finite difference approximation,

*It does not follow that this equilibrium is *stable* in all velocity sets, though we will see in section 7.2.2 that it is equivalent for D2Q9 to the provably stable equilibrium derived in [144].

†The two methods are equivalent and the only difference lies in their formulation: The first uses a source term while the second redefines $f_i^{(0)}$.

such as the additional difficulty of dealing with boundaries. Also, less importantly, the artificial forcing term has no physical interpretation.

In this chapter we will analyse the model with modified $f_i^{(0)}$ and a bulk viscosity correction term, using the same techniques as used previously in this thesis. Subsequently, its applications will be demonstrated by recreating the isentropic equation of state (2.23) for a nonlinear acoustics simulation in section 7.2, and by recreating the relaxational equation of state (2.50) in section 7.3 to simulate the effect of slow energy transfer between translational and inner molecular degrees of freedom.

7.1 The extended model

The core of the model is a extension of the equilibrium distribution $f_i^{(0)}$. Unlike the previously used distribution (4.2), $f_0^{(0)}$ and $f_{i\neq 0}^{(0)}$ are defined differently,

$$\boxed{\begin{aligned} f_i^{(0)} &= \rho w_i \left(\frac{c_\mathrm{i}^2}{c_\xi^2} + \frac{\xi_{i\alpha} u_\alpha}{c_\xi^2} + \frac{\xi_{i\alpha}\xi_{i\beta} u_\alpha u_\beta}{2c_\xi^4} - \frac{u_\alpha u_\alpha}{2c_\xi^2} \right) \quad \text{for } i \neq 0, \\ f_0^{(0)} &= \rho w_0 \left(\frac{c_\mathrm{i}^2}{c_\xi^2} + \frac{1}{w_0}\left[1 - \frac{c_\mathrm{i}^2}{c_\xi^2}\right] - \frac{u_\alpha u_\alpha}{2c_\xi^2} \right). \end{aligned}} \tag{7.2}$$

This distribution makes use of both the velocity set constant c_ξ and the isothermal speed of sound c_i. If $c_\mathrm{i} = c_\xi$, this equilibrium distribution reduces to (4.2), with a speed of sound $c_0 = c_\xi$. For $c_\mathrm{i} < c_\xi$, a larger proportion of particles are present in the zero-velocity distribution. For $c_\mathrm{i} > c_\xi$, the proportion is smaller.

In section 4.3 and [82] it was argued that there is a link between negative values of f_i and instability. In the linear limit, the conditions of non-negativity of the extended equilibrium distribution (7.2) are

$$\frac{|\boldsymbol{u}|}{2} \max_i |\boldsymbol{\xi}_i| \leq c_\mathrm{i}^2 \leq \frac{c_\xi^2}{1 - w_0}. \tag{7.3}$$

Note however that non-negativity is unproblematic in linearised LBEs where only the fluctuation f_i' is tracked, as the density fluctuation ρ' is not used for normalising when finding the momentum fluctuation $\rho_0 u_\alpha' = \sum_i \xi_{i\alpha} f_i'$.

The lattice Boltzmann equation gains a term,

$$f_i(\boldsymbol{x} + \boldsymbol{\xi}_i, t+1) - f_i(\boldsymbol{x}, t) = -\frac{1}{\tau}\left[f_i(\boldsymbol{x}, t) - f_i^{(0)}(\boldsymbol{x}, t)\right] + \mathcal{B}_i(\boldsymbol{x}, t). \tag{7.4}$$

This is a bulk viscosity correction term, defined as

$$\boxed{\mathcal{B}_i = \frac{w_i(\xi_{i\alpha}\xi_{i\beta} - c_\xi^2\delta_{\alpha\beta})}{2c_\xi^4} b\Gamma_{\alpha\beta},} \tag{7.5}$$

where the bulk vicsosity correction constant b and the bulk viscosity correction tensor $\Gamma_{\alpha\beta}$ are yet to be specified. As we shall see in the next section, the moments of this correction term are very simple.

7.1.1 Moments and constraints

As shown in section 4.1, the moments of the equilibrium distribution play a major role in determining the macroscopic behaviour of the model. In that section it was required that the moments of the discrete-velocity equilibrium distribution $f_i^{(0)}$ were as similar as possible to the moments of the continuous equilibrium distribution $f^{(0)}$.

A similar procedure must be carried out for the extended model in order to find its macroscopic behaviour. Since the derivation is very similar to the one in section 4.1.1, we will skip the details here and go straight to the results.

The derivation results in a set of constraints on the velocity set,

$$\sum_i w_i = 1, \tag{7.6a}$$

$$\sum_i w_i\xi_{i\alpha} = 0, \tag{7.6b}$$

$$\sum_i w_i\xi_{i\alpha}\xi_{i\beta} = c_\xi^2\delta_{\alpha\beta}, \tag{7.6c}$$

$$\sum_i w_i\xi_{i\alpha}\xi_{i\beta}\xi_{i\gamma} = 0, \tag{7.6d}$$

$$\sum_i w_i\xi_{i\alpha}\xi_{i\beta}\xi_{i\gamma}\xi_{i\delta} = c_\xi^4\left(\delta_{\alpha\beta}\delta_{\gamma\delta} + \delta_{\alpha\gamma}\delta_{\beta\delta} + \delta_{\alpha\delta}\delta_{\beta\gamma}\right), \tag{7.6e}$$

$$\sum_i w_i\xi_{i\alpha}\xi_{i\beta}\xi_{i\gamma}\xi_{i\delta}\xi_{i\epsilon} = 0, \tag{7.6f}$$

so that the moments of $f_i^{(0)}$ are

$$\breve{I}I_0^{(0)} = \sum_i f_i^{(0)} = \rho, \tag{7.7a}$$

$$\breve{I}I_\alpha^{(0)} = \sum_i \xi_{i\alpha} f_i^{(0)} = \rho u_\alpha, \tag{7.7b}$$

$$\breve{I}I_{\alpha\beta}^{(0)} = \sum_i \xi_{i\alpha}\xi_{i\beta} f_i^{(0)} = c_i^2\rho\delta_{\alpha\beta} + \rho u_\alpha u_\beta, \tag{7.7c}$$

$$\breve{I}I_{\alpha\beta\gamma}^{(0)} = \sum_i \xi_{i\alpha}\xi_{i\beta}\xi_{i\gamma} f_i^{(0)} = c_\xi^2\rho\left(u_\alpha\delta_{\beta\gamma} + u_\beta\delta_{\alpha\gamma} + u_\gamma\delta_{\alpha\beta}\right). \tag{7.7d}$$

As the constraints are the same as previously, the same velocity sets as before can be used for this model.

Comparing these moments with those of the continuous equilibrium distribution $f^{(0)}$, we find an inconsistent pressure. In the second order moment, the pressure is $c_{\mathrm{i}}^2\rho$ while it is $c_{\xi}^2\rho$ in the third order moment. Due to this inconsistency, we may expect some errors later in the derivation for $c_{\mathrm{i}} \neq c_{\xi}$. This inconsistency can only be resolved by a different third-order equilibrium moment $\check{\Pi}^{(0)}_{\alpha\beta\gamma}$. However, as discussed in section 5.2.5, moments such as $\check{\Pi}_{xxx}$ and $\check{\Pi}_{yyy}$ may be linearly dependent on lower-order moments such as $\check{\Pi}_x$ and $\check{\Pi}_y$. This particular dependency is present for all the velocity sets presented in section 4.1.3, where $\xi_{i\alpha} \in \{-1, 0, 1\}$. Therefore, resolving the inconsistency requires using extended lattices with more and higher velocities.

From the constraints (7.6), the moments of the bulk viscosity correction term are

$$\sum_i \mathcal{B}_i = 0, \qquad \sum_i \xi_{i\alpha}\mathcal{B}_i = 0, \qquad \sum_i \xi_{i\alpha}\xi_{i\beta}\mathcal{B}_i = b\Gamma_{\alpha\beta}. \tag{7.8}$$

Thus we see that the slightly complicated definition (7.5) of $\mathcal{B}_i$ ensures that the "payload" $b\Gamma_{\alpha\beta}$ is only released in the second order moment equation.

7.1.2 Macroscopic equations

To determine the macroscopic behaviour of this model, we must again perform a Taylor-Chapman-Enskog analysis. We have previously in section 6.2.1 performed such an analysis for the LBE with another source term, and the initial derivation is very similar, resulting in

$$\mathcal{O}(\epsilon): \qquad \left(\frac{\partial}{\partial t_1} + \xi_{i\alpha}\frac{\partial}{\partial x_\alpha}\right) f_i^{(0)} = -\frac{1}{\tau} f_i^{(1)} + \mathcal{B}_i, \tag{7.9a}$$

$$\begin{aligned}\mathcal{O}(\epsilon^2): \qquad & \frac{\partial f_i^{(0)}}{\partial t_2} + \left(\frac{\partial}{\partial t_1} + \xi_{i\alpha}\frac{\partial}{\partial x_\alpha}\right)\left(1 - \frac{1}{2\tau}\right) f_i^{(1)} \\ & \qquad = -\frac{1}{\tau} f_i^{(2)} - \frac{1}{2}\left(\frac{\partial}{\partial t_1} + \xi_{i\alpha}\frac{\partial}{\partial x_\alpha}\right)\mathcal{B}_i.\end{aligned} \tag{7.9b}$$

From this point on, the derivations diverge. We now need to consider the aforementioned pressure inconsistency and that c_{i}^2 is not necessarily constant.

The first and second order moments of (7.9a) and (7.9b) can be recombined to find the macroscopic mass and momentum conservation

equations

$$\frac{\partial \rho}{\partial t} + \frac{\partial \rho u_\alpha}{\partial x_\alpha} = 0, \tag{7.10a}$$

$$\frac{\partial \rho u_\alpha}{\partial t} + \frac{\partial \rho u_\alpha u_\beta}{\partial x_\beta} = -\frac{\partial \rho c_{\mathrm{i}}^2}{\partial x_\alpha} - \frac{\partial}{\partial x_\beta}\epsilon\left[(1-\tfrac{1}{2\tau})\breve{I\!I}^{(1)}_{\alpha\beta} + \tfrac{1}{2} b\Gamma_{\alpha\beta}\right], \tag{7.10b}$$

where $\breve{I\!I}^{(1)}_{\alpha\beta}$ and $b\Gamma_{\alpha\beta}$ are yet to be determined.

The unknown $\breve{I\!I}^{(1)}_{\alpha\beta}$ is as usual found through the third moment of (7.9a),

$$\frac{\partial \breve{I\!I}^{(0)}_{\alpha\beta}}{\partial t_1} + \frac{\partial \breve{I\!I}^{(0)}_{\alpha\beta\gamma}}{\partial x_\gamma} = -\frac{1}{\tau}\breve{I\!I}^{(1)}_{\alpha\beta} + b\Gamma_{\alpha\beta}. \tag{7.11a}$$

Leaving out the details, which are more or less as before, the time derivative term is

$$\begin{aligned}\frac{\partial \breve{I\!I}^{(0)}_{\alpha\beta}}{\partial t_1} &= \delta_{\alpha\beta}\frac{\partial c_{\mathrm{i}}^2 \rho}{\partial t_1} + \frac{\partial \rho u_\alpha u_\beta}{\partial t_1} \\ &= -c_{\mathrm{i}}^2\left(u_\alpha\frac{\partial}{\partial x_\beta} + u_\beta\frac{\partial}{\partial x_\alpha} + \delta_{\alpha\beta}u_\gamma\frac{\partial}{\partial x_\gamma}\right)\rho - c_{\mathrm{i}}^2\rho\delta_{\alpha\beta}\frac{\partial u_\gamma}{\partial x_\gamma} \\ &\quad + \rho\delta_{\alpha\beta}\frac{\partial c_{\mathrm{i}}^2}{\partial t_1} - \rho\left(u_\alpha\frac{\partial}{\partial x_\beta}u_\beta\frac{\partial}{\partial x_\alpha}\right)c_{\mathrm{i}}^2 + \frac{\partial \rho u_\alpha u_\beta u_\gamma}{\partial x_\gamma},\end{aligned} \tag{7.11b}$$

and the spatial derivative term is

$$\begin{aligned}\frac{\partial \breve{I\!I}^{(0)}_{\alpha\beta\gamma}}{\partial x_\gamma} &= c_\xi^2\frac{\partial}{\partial x_\gamma}\rho\left(u_\alpha\delta_{\beta\gamma} + u_\beta\delta_{\alpha\gamma} + u_\gamma\delta_{\alpha\beta}\right) \\ &= \rho c_\xi^2\left(\frac{\partial u_\alpha}{\partial x_\beta} + \frac{\partial u_\beta}{\partial x_\alpha} + \delta_{\alpha\beta}\frac{\partial u_\gamma}{\partial x_\gamma}\right) \\ &\quad + c_\xi^2\left(u_\alpha\frac{\partial}{\partial x_\beta} + u_\beta\frac{\partial}{\partial x_\alpha} + \delta_{\alpha\beta}u_\gamma\frac{\partial}{\partial x_\gamma}\right)\rho.\end{aligned} \tag{7.11c}$$

Putting this together, we find

$$\begin{aligned}\breve{I\!I}^{(1)}_{\alpha\beta} &= -\tau\rho c_\xi^2\left(\frac{\partial u_\alpha}{\partial x_\beta} + \frac{\partial u_\beta}{\partial x_\alpha} + \left[1 - \tfrac{c_{\mathrm{i}}^2}{c_\xi^2}\right]\delta_{\alpha\beta}\frac{\partial u_\gamma}{\partial x_\gamma}\right) + \tau\frac{\partial \rho u_\alpha u_\beta u_\gamma}{\partial x_\gamma} \\ &\quad - \tau c_\xi^2\left(1 - \tfrac{c_{\mathrm{i}}^2}{c_\xi^2}\right)\left(u_\alpha\frac{\partial}{\partial x_\beta} + u_\beta\frac{\partial}{\partial x_\alpha} + \delta_{\alpha\beta}u_\gamma\frac{\partial}{\partial x_\gamma}\right)\rho \\ &\quad + \tau\rho\left(u_\alpha\frac{\partial}{\partial x_\beta} + u_\beta\frac{\partial}{\partial x_\alpha}\right)c_{\mathrm{i}}^2 - \tau\delta_{\alpha\beta}\rho\frac{\partial c_{\mathrm{i}}^2}{\partial t_1} + \tau b\Gamma_{\alpha\beta}.\end{aligned} \tag{7.11d}$$

Compared with (4.22) in the basic model, $\check{\Pi}^{(1)}_{\alpha\beta}$ here contains several additional terms. The first two terms are like those in the basic model, except for a c_i-dependent bulk viscosity. All the other terms vanish for $c_\mathrm{i} = c_{\tilde{\zeta}}$, except for the bulk viscosity correction term.

Several of these terms will be negligible in most cases. Since all terms contain τ, they will be proportional to the viscosity ν in the stress tensor. Furthermore, we assume that the deviations from the constant rest state variables ρ_0, $\boldsymbol{u}_0$, $c_{\mathrm{i}0}$ are small, characterised by a macroscopic smallness parameter ε. Neglecting terms of order $\mathcal{O}(\nu\varepsilon^2)$, similarly to the approximation scheme in the nonlinear acoustics section 2.3.5, the moment perturbation simplifies to

$$\begin{aligned}\check{\Pi}^{(1)}_{\alpha\beta} \simeq -\tau\rho c_{\tilde{\zeta}}^2 \left(\frac{\partial u_\alpha}{\partial x_\beta} + \frac{\partial u_\beta}{\partial x_\alpha} + \left[1 - \tfrac{c_\mathrm{i}^2}{c_{\tilde{\zeta}}^2} \right] \delta_{\alpha\beta} \frac{\partial u_\gamma}{\partial x_\gamma} \right) \\ - \tau\delta_{\alpha\beta}\rho \frac{\partial c_\mathrm{i}^2}{\partial t_1} + \tau b \Gamma_{\alpha\beta}.\end{aligned} \tag{7.12}$$

This approximation scheme is one order more strict than the one for the basic DVBE scheme, where the nonlinear error term of $\mathcal{O}(\nu\varepsilon^3)$ is neglected.

Using this form of $\check{\Pi}^{(1)}_{\alpha\beta}$, the momentum conservation equation finally becomes

$$\frac{\partial \rho u_\alpha}{\partial t} + \frac{\partial \rho u_\alpha u_\beta}{\partial x_\beta} = -\frac{\partial p}{\partial x_\alpha} + \frac{\partial \sigma'_{\alpha\beta}}{\partial x_\beta}, \tag{7.13a}$$

with a deviatoric stress tensor

$$\begin{aligned}\sigma'_{\alpha\beta} = \rho\nu \left(\frac{\partial u_\alpha}{\partial x_\beta} + \frac{\partial u_\beta}{\partial x_\alpha} - \frac{2}{3}\delta_{\alpha\beta} \frac{\partial u_\gamma}{\partial x_\gamma} \right) + \rho\nu \left(\frac{5}{3} - \frac{c_\mathrm{i}^2}{c_{\tilde{\zeta}}^2} \right) \delta_{\alpha\beta} \frac{\partial u_\gamma}{\partial x_\gamma} \\ + \frac{\rho\nu}{c_{\tilde{\zeta}}^2} \delta_{\alpha\beta} \frac{\partial c_\mathrm{i}^2}{\partial t} - \tau b \Gamma_{\alpha\beta}.\end{aligned} \tag{7.13b}$$

For a constant c_i and without the correction term, the resulting pressure and viscosities are

$$p = c_\mathrm{i}^2 \rho, \quad \nu = c_{\tilde{\zeta}}^2 (\tau - 1/2), \quad \nu_\mathrm{B} = \nu(5/3 - c_\mathrm{i}^2/c_{\tilde{\zeta}}^2). \tag{7.13c}$$

7.1.3 Bulk viscosity correction

It is undesirable and unphysical that the bulk viscosity should depend on the ratio $c_\mathrm{i}^2/c_{\tilde{\zeta}}^2$. Additionally, we will see later that the $\partial c_\mathrm{i}^2/\partial t$ term may also contribute to the bulk viscosity.

To get the bulk viscosity of the model under control, we must determine the bulk viscosity correction constant b and tensor $\Gamma_{\alpha\beta}$. To make this

derivation independent of the rest of the model, we assume a general form for the moment perturbation

$$\breve{\Pi}^{(1)}_{\alpha\beta} = \tau b \Gamma_{\alpha\beta} - \tau\rho c_\xi^2 \left(\frac{\partial u_\alpha}{\partial x_\beta} + \frac{\partial u_\beta}{\partial x_\alpha} - \frac{2}{3}\delta_{\alpha\beta}\frac{\partial u_\gamma}{\partial x_\gamma} \right) - \frac{\tau}{\tau - 1/2}\rho\nu'_{\mathrm{B}}\delta_{\alpha\beta}\frac{\partial u_\gamma}{\partial x_\gamma} \tag{7.14}$$

and the corresponding deviatoric stress tensor

$$\sigma'_{\alpha\beta} = \rho\nu \left(\frac{\partial u_\alpha}{\partial x_\beta} + \frac{\partial u_\beta}{\partial x_\alpha} - \frac{2}{3}\delta_{\alpha\beta}\frac{\partial u_\gamma}{\partial x_\gamma} \right) + \rho\nu'_{\mathrm{B}}\delta_{\alpha\beta}\frac{\partial u_\gamma}{\partial x_\gamma} - \tau b\Gamma_{\alpha\beta}. \tag{7.15}$$

Here, ν'_{B} is the unmodified c_{i}-dependent bulk viscosity which we wish to replace with a desired bulk viscosity ν_{B}.

To replace the unmodified bulk viscosity with the desired one, we require that

$$\tau b\Gamma_{\alpha\beta} = \rho\left(\nu'_{\mathrm{B}} - \nu_{\mathrm{B}}\right)\delta_{\alpha\beta}\frac{\partial u_\gamma}{\partial x_\gamma}. \tag{7.16}$$

How can we get the correction term on this form? Two different methods have been described previously [76, Ch. 3]. The first is relatively simple and clean, whereas the second is computationally more efficient but more complicated. Both choose $\Gamma_{\alpha\beta} \propto \delta_{\alpha\beta}\partial u_\gamma/\partial x_\gamma$, and the two methods are equivalent for $c_{\mathrm{i}} = c_\xi$ or for the D1Q3 velocity set.

Correction using $\breve{\Pi}^{(1)}_{\gamma\gamma}$

One choice that results in $\Gamma_{\alpha\beta} \propto \delta_{\alpha\beta}\partial u_\gamma/\partial x_\gamma$ is

$$\boxed{\begin{aligned} \Gamma_{\alpha\beta} &= \frac{\delta_{\alpha\beta}}{d}\breve{\Pi}^{(1)}_{\gamma\gamma}, \qquad \text{with} \\ \breve{\Pi}^{(1)}_{\gamma\gamma} &\simeq \breve{\Pi}^{\mathrm{neq}}_{\gamma\gamma} = \sum_i \xi_{i\gamma}\xi_{i\gamma}(f_i - f_i^{(0)}), \end{aligned}} \tag{7.17}$$

d being the number of spatial dimensions spanned by the velocity set. With this choice, we have $\Gamma_{\gamma\gamma} = \breve{\Pi}^{(1)}_{\gamma\gamma}$.

The explicit form of the correction term, calculated from the approximated form (7.12) for $\breve{\Pi}^{(1)}_{\alpha\beta}$ is consequently

$$\begin{aligned} \tau b\Gamma_{\alpha\beta} &= \frac{\tau b\delta_{\alpha\beta}}{d}\left[\tau b\Gamma_{\gamma\gamma} - \tau\rho c_\xi^2\left(2 - \frac{2d}{3}\right) - \frac{d\tau\rho\nu'_{\mathrm{B}}}{\tau - 1/2}\right]\frac{\partial u_\gamma}{\partial x_\gamma} \\ &= -\frac{\tau^2 b}{1 - \tau b}\left[\rho c_\xi^2\left(\frac{2}{d} - \frac{2}{3}\right) + \frac{\rho\nu'_{\mathrm{B}}}{\tau - 1/2}\right]\delta_{\alpha\beta}\frac{\partial u_\gamma}{\partial x_\gamma}. \end{aligned} \tag{7.18}$$

Combining this with the requirement (7.16) on the bulk viscosity correction term and solving for b, we find

$$\boxed{b = \left[\tau + \tau^2 \frac{c_\xi^2(2/d - 2/3) + \nu_\mathrm{B}'/(\tau - 1/2)}{\nu_\mathrm{B} - \nu_\mathrm{B}'}\right]^{-1}}. \tag{7.19}$$

Thus, with $\Gamma_{\alpha\beta}$ given by (7.17) and b given by (7.19), the resulting stress tensor becomes as desired,

$$\sigma'_{\alpha\beta} = \rho\nu\left(\frac{\partial u_\alpha}{\partial x_\beta} + \frac{\partial u_\beta}{\partial x_\alpha} - \frac{2}{3}\delta_{\alpha\beta}\frac{\partial u_\gamma}{\partial x_\gamma}\right) + \rho\nu_\mathrm{B}\delta_{\alpha\beta}\frac{\partial u_\gamma}{\partial x_\gamma}.$$

A closer look at this choice of bulk viscosity correction reveals a kinship to MRT methods. If we regard the entire right hand side of the lattice Boltzmann equation (7.4) as a collision operator and take its second-order moment, we find

$$\sum_i \xi_{i\alpha}\xi_{i\beta}\Omega_i = \sum_i \xi_{i\alpha}\xi_{i\beta}\left(-\frac{1}{\tau}f_i^\mathrm{neq} + \mathcal{B}_i\right) = -\frac{1}{\tau}\check{\Pi}_{\alpha\beta}^\mathrm{neq} + \frac{b}{d}\delta_{\alpha\beta}\check{\Pi}_{\gamma\gamma}^\mathrm{neq}. \tag{7.20a}$$

The different possible combinations of α and β for a two-dimensional velocity set give

$$\sum_i \xi_{ix}\xi_{ix}\Omega_i = \left(-\frac{1}{\tau} + \frac{b}{d}\right)\check{\Pi}_{xx}^\mathrm{neq} + \frac{b}{d}\check{\Pi}_{yy}^\mathrm{neq}, \tag{7.20b}$$

$$\sum_i \xi_{ix}\xi_{iy}\Omega_i = -\frac{1}{\tau}\check{\Pi}_{xy}^\mathrm{neq}, \tag{7.20c}$$

$$\sum_i \xi_{iy}\xi_{iy}\Omega_i = \left(-\frac{1}{\tau} + \frac{b}{d}\right)\check{\Pi}_{yy}^\mathrm{neq} + \frac{b}{d}\check{\Pi}_{xx}^\mathrm{neq}. \tag{7.20d}$$

This shows us that this choice of $\Gamma_{\alpha\beta}$ is equivalent to an MRT scheme somewhat unlike those in section 4.3.1. In that section, the relaxation matrix $\boldsymbol{T}$ was diagonal, meaning that the relaxation of each moment was determined *only* by its own nonequilibrium part. Here, however, the relaxation of the moments $\check{\Pi}_{xx}$ and $\check{\Pi}_{yy}$ depend on each other. To reproduce this using the MRT formalism the relaxation matrix $\boldsymbol{T}$ must have additional components outside the diagonal, as in [83, Ch. 4].

Correction using $f_0^{(1)}$

As a more computationally efficient, though more complicated, alternative to the previous method, the bulk viscosity correction tensor $\Gamma_{\alpha\beta}$ can be chosen as proportional to

$$f_0^{(1)} \simeq f_0 - f_0^{(0)}.$$

To show how this would work, we must first find $f_0^{(1)}$ explicitly from the first-order smallness terms (7.9a) of the Chapman-Enskog expansion,

$$f_0^{(1)} = -\tau\left(\frac{\partial f_0^{(0)}}{\partial t_1} - \mathcal{B}_0\right). \tag{7.21}$$

From the previous expressions (7.5) and (7.2), we have

$$\mathcal{B}_0 = -\frac{w_0}{2c_\xi^2} b\Gamma_{\gamma\gamma}, \tag{7.22a}$$

$$f_0^{(0)} = \rho w_0\left[\frac{c_\mathrm{i}^2}{c_\xi^2} + \frac{1}{w_0}\left(1 - \frac{c_\mathrm{i}^2}{c_\xi^2}\right)\right] - \frac{w_0}{2c_\xi^2}\rho u_\gamma u_\gamma. \tag{7.22b}$$

Using the moments of (7.9a), the t_1 derivative of $f_i^{(0)}$ can be expressed as

$$\begin{aligned}\frac{\partial f_0^{(0)}}{\partial t_1} = &-w_0\left[\frac{c_\mathrm{i}^2}{c_\xi^2} + \frac{1}{w_0}\left(1 - \frac{c_\mathrm{i}^2}{c_\xi^2}\right)\right]\frac{\partial \rho u_\gamma}{\partial x_\gamma} - \frac{1-w_0}{c_\xi^2}\rho\frac{\partial c_\mathrm{i}^2}{\partial t_1} \\ &+ \frac{w_0}{c_\xi^2}\left[u_\alpha\frac{\partial}{\partial x_\beta}\left(\delta_{\alpha\beta}\rho c_\mathrm{i}^2 + \rho u_\alpha u_\beta\right) + \frac{1}{2}u_\gamma u_\gamma\frac{\partial \rho}{\partial t_1}\right].\end{aligned} \tag{7.23}$$

This can be simplified by applying the same approximation scheme as previously and removing terms that will end up above the order $\mathcal{O}(\nu\varepsilon)$ in the stress tensor. Thus, the explicit, form of $f_0^{(1)}$ with these small terms neglected is

$$f_0^{(1)} = -\frac{w_0}{2c_\xi^2}\tau b\Gamma_{\gamma\gamma} + \tau\rho w_0\left[\frac{c_\mathrm{i}^2}{c_\xi^2} + \frac{1}{w_0}\left(1 - \frac{c_\mathrm{i}^2}{c_\xi^2}\right)\right]\frac{\partial u_\gamma}{\partial x_\gamma} + \tau\rho\frac{1-w_0}{c_\xi^2}\frac{\partial c_\mathrm{i}^2}{\partial t}. \tag{7.24}$$

Choosing the bulk viscosity correction tensor as

$$\boxed{\Gamma_{\alpha\beta} = -\frac{\delta_{\alpha\beta}}{d}\frac{2c_\xi^2}{w_0}f_0^{(1)} \simeq -\frac{\delta_{\alpha\beta}}{d}\frac{2c_\xi^2}{w_0}\left(f_0 - f_0^{(0)}\right)} \tag{7.25}$$

and using ν_B''/ν to denote the coefficients in front of $\tau\rho\frac{\partial u_\gamma}{\partial x_\gamma}$, including any possible contributions from the $\frac{\partial c_\mathrm{i}^2}{\partial t}$ term, we find

$$\tau b\Gamma_{\alpha\beta} = -\frac{\delta_{\alpha\beta}}{d}\frac{2c_\xi^2}{w_0}\frac{\tau^2 b}{1-\tau b}\frac{\rho\nu_\mathrm{B}''}{\nu}. \tag{7.26}$$

Equating this with the requirement (7.16) on $\tau b\Gamma_{\alpha\beta}$, we can solve for b and find

$$\boxed{b = \left[\tau + \tau^2\frac{2c_\xi^2}{dw_0}\frac{\nu_\mathrm{B}''/\nu}{\nu_\mathrm{B} - \nu_\mathrm{B}'}\right]^{-1}.} \tag{7.27}$$

Thus, by choosing $\Gamma_{\alpha\beta}$ as (7.25) and b as (7.27), we may freely choose the bulk viscosity ν_B of the model.

This method is more computationally efficient than the previous method, since calculating $\check{\Pi}_{\alpha\beta} - \check{\Pi}^{(0)}_{\alpha\beta}$ requires more operations than calculating $f_0 - f_0^{(0)}$, especially with large multidimensional velocity sets.

For the LBE with unmodified equation of state, the two correction methods are equivalent [76, Ch. 3]. This does not hold in general for this model, but for the D1Q3 velocity set it can be shown that $\check{\Pi}^{(1)}_{\gamma\gamma} = \check{\Pi}^{(1)}_{xx} = -f_0^{(1)}$. Thus, the two definitions for $\Gamma_{\alpha\beta}$ are equivalent because $w_0/2c_\xi^2 = 1$ in the D1Q3 velocity set. Note that this does *not* generally hold for other velocity sets.

7.1.4 General equilibrium requirements

From the derivation of the model's macroscopic behaviour in section 7.1.2, it is possible to deduce some common aspects of *all* equilibrium functions $f_i^{(0)}$ with variable equation of state. Their moments must fulfil certain criteria, namely the zeroth to second order moments in (7.7), to get the correct Euler-level equations.

To avoid some of the undesired terms in the resulting $\check{\Pi}^{(1)}_{\alpha\beta}$ (7.11d), we would need to have a third order moment proportional to $c_i^2\rho$ instead of $c_\xi^2\rho$. However, this criterion is not possible to fulfil for any of the simple velocity sets described in section 4.1.3 as all have third order moments dependencies such as $\check{\Pi}_{xxx} = \check{\Pi}_x$. To avoid these dependencies, extended velocity sets must be used, though these cause the computational burden to increase and make boundary conditions more difficult to handle.

For simple velocity sets, then, the third order equilibrium moments are not all independent. For isotropy reasons, these moments must therefore all be given as (7.7d). Consequently, these undesired $\mathcal{O}(\nu\varepsilon^2)$ terms are unavoidable for simple velocity sets.

Fourth order and higher moments, such as the single independent fourth order moment $\check{\Pi}_{xxyy}$ in the D2Q9 velocity set, are in principle freely adjustable. The Chapman-Enskog analysis shows that the Navier-Stokes level mass and momentum conservation equations do not depend on them. However, these equilibrium moments may affect the stability of the model [144], which we will discuss briefly into in section 7.2.2.

Regardless, since the zeroth to second moments are fixed by Euler-level considerations, every possible equilibrium distribution with variable equation of state in simple lattices must be equivalent when projected to D1Q3. The reason is that no other independent equilibrium moments than these *exist* for the D1Q3 velocity set; these three fully determine the equilibrium distribution. In fact, we can construct this D1Q3 equilibrium

directly by inverting the matrix in (4.55b),

$$\begin{bmatrix} f_-^{(0)} \\ f_0^{(0)} \\ f_+^{(0)} \end{bmatrix} = \begin{bmatrix} 0 & -\frac{1}{2} & \frac{1}{2} \\ 1 & 0 & -1 \\ 0 & \frac{1}{2} & \frac{1}{2} \end{bmatrix} \begin{bmatrix} \rho \\ \rho u \\ \breve{\Pi}_{xx}^{(0)} \end{bmatrix}. \tag{7.28}$$

With the second order equilibrium moment given by $\breve{\Pi}_{xx}^{(0)} = p + \rho uu$, the resulting D1Q3 equilibrium distribution is

$$f_i^{(0)} = \tfrac{1}{2}\left(p + \rho u \xi_i + \rho uu\right) \quad \text{for } i \neq 0, \tag{7.29a}$$

$$f_0^{(0)} = \rho - p - \rho uu. \tag{7.29b}$$

By evaluating the constants of the extended equilibrium distribution (7.2) for the D1Q3 velocity set, we can confirm that it simplifies to exactly this.

7.1.5 Linearisation analysis

In section 5.3, a linearisation analysis was carried out to determine the sound propagation properties of the basic LB model. Since the extended model described in this section is characterised by a different equilibrium distribution $f_i^{(0)}$ and uses a bulk viscosity correction, another brief linearisation analysis must be performed to determine its sound propagation properties.

From the arguments of section 7.1.4, all LB equilibria $f_i^{(0)}$ that alter the equation of state are equal for the D1Q3 velocity set. It follows that the following D1Q3 linearisation analysis holds for *all* such models, not only the equilibrium (7.2) by Chopard et al.

Since the parameter c_i is not necessarily constant but may be a function of e.g. ρ, we must consider how to linearise the equation of state $p = c_\mathrm{i}^2 \rho$. A general linearised form of this is

$$p = p_0 + \left(\frac{\partial p}{\partial \rho}\right)_{s,0} \rho' = p_0 + c_0^2 \rho'. \tag{7.30}$$

Here, p_0 and c_0 may still depend on underlying variables such as a rest state temperature T_0.

Again, we assume the solution to be on the linearised form

$$\hat{f}_i(x,t) = F_i^{(0)} + \hat{f}_i'(x,t) = F_i^{(0)} + \hat{f}_i^\star \, \mathrm{e}^{\mathrm{i}(\hat{\omega} t - \hat{k} x)}.$$

The two components are a constant rest state distribution $F_i^{(0)}$ and a fluctuation distribution $\hat{f}_i'$ which is assumed to be so small that any terms nonlinear in it may be neglected. Using the general D1Q3 equilibrium

distribution (7.29) and the linearised equation of state (7.30), the equilibria of the two components are

$$F_0^{(0)} = \rho_0 - p_0, \qquad F_\pm^{(0)} = \frac{1}{2} p_0, \tag{7.31a}$$

$$f_0^{\star(0)} = \left(1 - c_0^2\right) \hat{\rho}^\star, \qquad f_\pm^{\star(0)} = \frac{1}{2}\left(c_0^2 \hat{\rho}^\star \pm \rho_0 \hat{u}^\star\right). \tag{7.31b}$$

Using the $\check{I\!I}_{\gamma\gamma}^{(1)}$ method for the bulk viscosity correction term, we have

$$\mathring{I\!I}_{\gamma\gamma}^{\star(1)} \simeq \mathring{I\!I}_{\gamma\gamma}^{\star} - \mathring{I\!I}_{\gamma\gamma}^{\star(0)} \simeq \hat{f}_+^\star + \hat{f}_-^\star - c_0^2 \hat{\rho}^\star = -\hat{f}_0^\star + (1 - c_0^2)\hat{\rho}^\star.$$

Subtracting the rest state and inserting D1Q3 constants, we have the harmonic linearised extended LBE

$$\begin{aligned} \hat{f}_i^\star(\boldsymbol{x} + \xi_i, t+1) = \hat{f}_i^\star - \frac{1}{\tau}\left(\hat{f}_i^\star - \hat{f}_i^{\star(0)}\right) \\ - \tfrac{9}{2} b w_i \left(\xi_i^2 - \tfrac{1}{3}\right)\left[\hat{f}_0^\star - \hat{\rho}^\star(1 - c_0^2)\right]. \end{aligned} \tag{7.32}$$

Proceeding as previously done in section 5.3.1, we end up with another eigenvalue problem of the form

$$\hat{\boldsymbol{A}} \hat{\boldsymbol{f}}^\star = \mathrm{e}^{\mathrm{i}\hat{\omega}} \hat{\boldsymbol{f}}^\star \tag{7.33a}$$

with the eigenvector $\hat{\boldsymbol{f}}^\star = \begin{bmatrix} \hat{f}_-^\star & \hat{f}_0^\star & \hat{f}_+^\star \end{bmatrix}^{\mathrm{T}}$ and the matrix

$$\hat{\boldsymbol{A}} = \begin{bmatrix} \left(1 + \frac{(1-c_0^2)(b-1/\tau)}{2}\right)\mathrm{e}^{-\mathrm{i}\hat{k}} & \left(\frac{c_0^2(1/\tau - b)}{2}\right)\mathrm{e}^{-\mathrm{i}\hat{k}} & \left(\frac{(1-c_0^2)(b-1/\tau)}{2}\right)\mathrm{e}^{-\mathrm{i}\hat{k}} \\ (1-c_0^2)(1/\tau - b) & 1 + c_0^2(b - 1/\tau) & (1-c_0^2)(1/\tau - b) \\ \left(\frac{(1-c_0^2)(b-1/\tau)}{2}\right)\mathrm{e}^{\mathrm{i}\hat{k}} & \left(\frac{c_0^2(1/\tau - b)}{2}\right)\mathrm{e}^{\mathrm{i}\hat{k}} & \left(1 + \frac{(1-c_0^2)(b-1/\tau)}{2}\right)\mathrm{e}^{\mathrm{i}\hat{k}} \end{bmatrix}. \tag{7.33b}$$

As before, we can find the properties of both forced and free waves from the dispersion relation

$$\det(\hat{\boldsymbol{A}} - \boldsymbol{I}\,\mathrm{e}^{\mathrm{i}\hat{\omega}}) = g(\hat{\omega}, \hat{k}, c_0, \tau_\nu) = 0. \tag{7.34}$$

While this relation is again too bulky to write out, it is worth noting that it is not a function of b except through the resulting bulk viscosity ν in τ_ν. This shows that the bulk viscosity correction works perfectly in the linearised limit, with no undesired side-effects.

The fact that the bulk viscosity correction works perfectly for D1Q3 should not be surprising. The viscosity appears in the matrix $\hat{\boldsymbol{A}}$ only in the combination $-1/\tau + b$, as we would expect from considering what (7.20b) would become in a one-dimensional situation. In a sense, all this bulk viscosity correction does for D1Q3 is to increase the relaxation parameter for $\check{I\!I}_{xx}$ from $-1/\tau$ to $-1/\tau + b$. We could have found the same result simply by changing τ, as the relaxation time of the conserved moments ρ and ρu_x do not matter for the end result.

Forced waves

Assuming $\hat{\omega} = \omega_0$ and solving for $\hat{k}$, we find two solutions. These are significantly more bulky than before,* and we'll therefore restrict ourselves to the series expansion of the $+x$-propagating solution,

$$\begin{aligned}\frac{\hat{k}}{k_0} = 1 &+ \tfrac{\omega_0^2}{24}\left(\tfrac{1}{c_0^2} - 1\right) + \tfrac{\omega_0^4}{1920}\left(\tfrac{9}{c_0^4} - \tfrac{10}{c_0^2} + 1\right) + \mathcal{O}(\omega_0^6) \\ &- \mathrm{i}\tfrac{1}{2}X\left[1 + \tfrac{\omega_0^2}{24}\left(\tfrac{3}{c_0^2} + 1\right) + \mathcal{O}(\omega_0^4)\right] \\ &- X^2\left[\tfrac{1}{8}\tfrac{c_0^2+3}{1-c_0^2} + \mathcal{O}(\omega_0^2)\right] + \mathcal{O}(X^3).\end{aligned} \tag{7.35}$$

As before, the acoustic viscosity number X represents the effects of the physical DVBE model and ω_0 represents the numerical resolution. Setting $c_0^2 = c_\xi^2 = 1/3$, this equation is equivalent with (5.63) for the basic model.

At $\mathcal{O}(X^0)$ and $\mathcal{O}(X^1)$, only the discretisation error terms are dependent on c_0. However, at $\mathcal{O}(X^2)$, even the discretisation error independent $\mathcal{O}(\omega_0^0)$ term is dependent on c_0. In fact, this term goes to infinity as $c_0 \to 1$. That high-order dispersion should be dependent on c_0 is plausible since the D1Q3 sound speed ceiling is $c = 1$, as shown in section 5.2.4.

The exact expression for $\hat{k}$ can be evaluated numerically, and the dispersion and absorption that it predicts is plotted as function of discretisation error in Figure 7.1. The figure shows that the effect of discretisation error is decreased if c_0 is increased. However, the undesired c_0-dependent dispersion at $\mathcal{O}(X^2)$ is also visible in the dispersion figure, as the dispersion is markedly altered at $k_0 = 0$ for $X = 0.1$ when c_0 is varied.

Free waves

As before, there are three free wave solutions: Two propagating and one diffusive. The series expansion of the $+x$-propagating solution is

$$\begin{aligned}\frac{\hat{\omega}}{\omega_0} = 1 &- \tfrac{k_0^2}{24}\left(1 - c_0^2\right) + \tfrac{k_0^4}{1920}\left(1 - 10c_0^2 + 9c_0^4\right) + \mathcal{O}(k_0^6) \\ &+ \mathrm{i}\tfrac{1}{2}X\left[1 + \tfrac{k_0^2}{12}\left(3c_0^2 - 1\right) + \mathcal{O}(k_0^4)\right] \\ &+ X^2\left[\tfrac{1}{8}\tfrac{5c_0^2-1}{1-c_0^2} + \mathcal{O}(k_0^2)\right] + \mathcal{O}(X^3).\end{aligned} \tag{7.36}$$

*The large number of terms and sheer complicatedness of these analytical solutions mean that little could be gained by attempting to write them here. The best way for a reader to reproduce these solutions would be through the same procedure used here; finding them from the characteristic polynomial from the eigenvalue problem (7.33) using a computer algebra system.

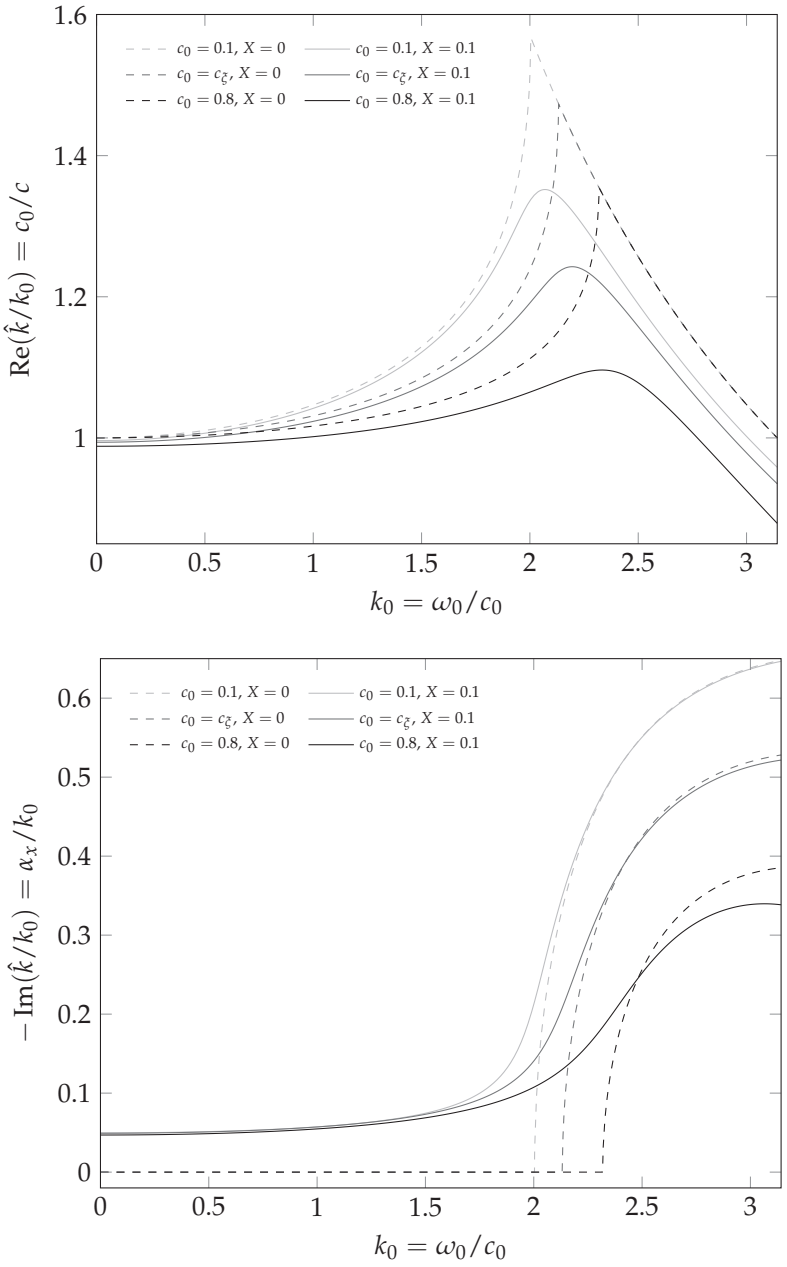

Figure 7.1: The normalised inverse dispersion (upper) and the normalised absorption (lower) of forced waves as functions of the normalised numerical resolution $k_0 = \omega_0/c_0$ for two different values of X and three different values of c_0.

Naturally, this equation is also equivalent with the previous free wave solution (5.64) for $c_0^2 = c_\xi^2 = 1/3$. Like in the forced wave case, the $\mathcal{O}(k_0^0 X^2)$ term is dependent on c_0, and diverges for $c_0 \to 1$.

The exact solution for this mode is plotted in Figure 7.2. Due to a divergence caused by numerical error at very small k_0, very small parts of the graphs are not plotted near $k_0 = 0$. For the dispersion, the higher choice of c_0 leads to a smaller effect from the discretisation error. For the absorption, the lowest discretisation error is found for $c_0^2 = 1/3$, where the $\mathcal{O}(k_0^2 X)$ is zero.

7.2 Isentropic equation of state and nonlinear acoustics

As we have seen, this extended model lets us choose the proportionality coefficient c_i in the equation of state $p = c_\mathrm{i}^2 \rho$. There is no requirement that c_i has to be constant, meaning that we have more freedom in choosing the equation of state.

As described in section 2.3.5, there are two separate mechanisms of nonlinear acoustics. Firstly, the speed of sound increases in sound wave peaks and decreases in troughs due to local changes in $T \propto p/\rho$. Secondly, the local fluid velocity of the sound wave advects peaks and troughs towards and against the sound wave propagation direction, respectively.

Simulations of nonlinear LB acoustics have been performed previously [110]. However, an isothermal LBM was used so that only the second mechanism of self-advection was captured. We will now choose a pseudo-thermal ideal-gas isentropic equation of state

$$p = p_0 \left(\frac{\rho}{\rho_0} \right)^\gamma \tag{7.37}$$

which allows for the first mechanism of nonlinearity to be captured. As seen in section 2.3, this directly leads to the small-signal speed of sound $c_0 = \sqrt{\gamma p_0 / \rho_0}$.

The term *pseudo-thermal* is used here since the model will still not have an independent thermal field, and thermal conduction can consequently not be captured directly by the model. In fact, thermal conduction is incompatible with the isentropic equation of state as it causes entropy to increase as discussed in section 2.3.2. However, the local temperature is related to the density and pressure through the isentropic relations

$$\left(\frac{T}{T_0} \right) = \left(\frac{\rho}{\rho_0} \right)^{\gamma - 1} = \left(\frac{p}{p_0} \right)^{\frac{\gamma - 1}{\gamma}}.$$

LB models with variable adiabatic index γ have been proposed previously [133, 148]. While their resulting macroscopic equations are error-free, these models are more cumbersome and require extended velocity

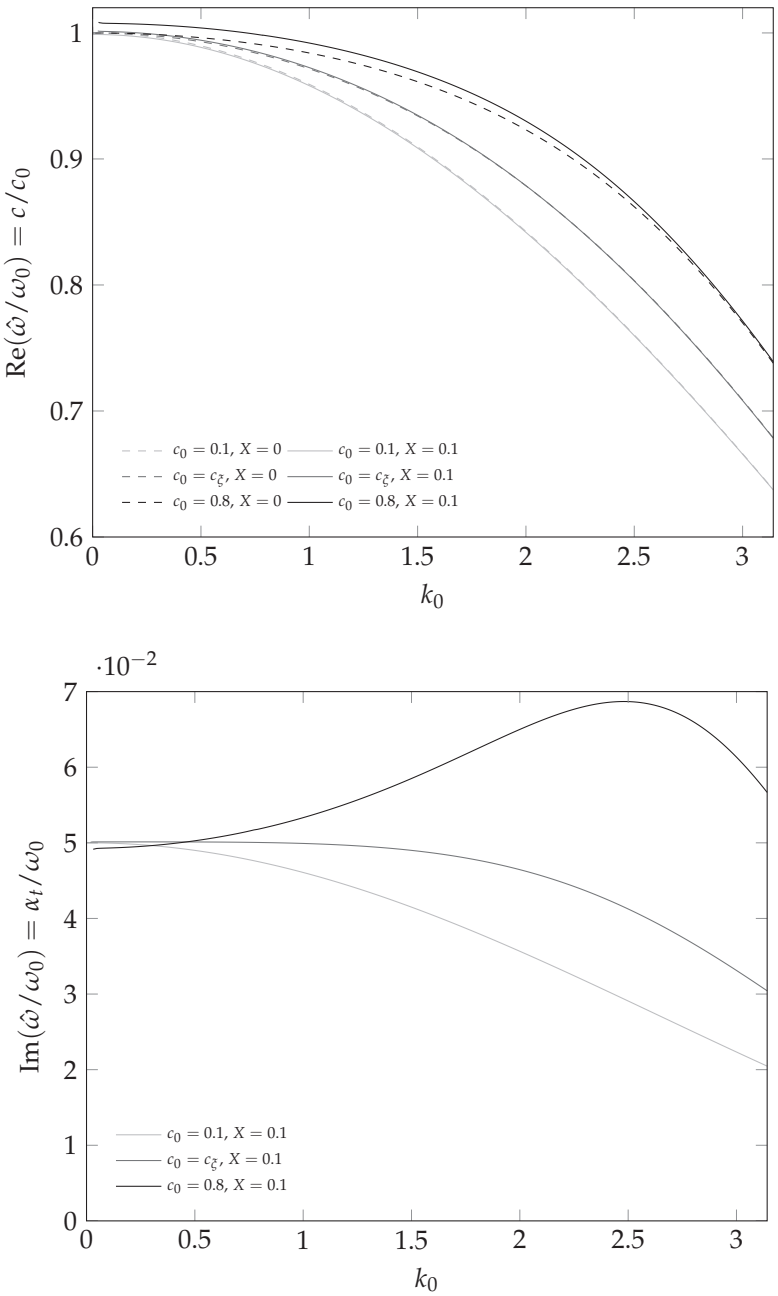

Figure 7.2: The normalised dispersion (upper) and the normalised absorption (lower) of free waves as functions of the normalised numerical resolution $k_0 = \omega_0/c_0$ for two different values of X and three different values of c_0.

sets. The model presented here only requires altering the equilibrium distribution by making c_i a local function of ρ, and adding a source term $\mathcal{B}_i$ to the LBE. Even so, this method has downsides, and while we will see no effect of the neglected $\mathcal{O}(\nu\varepsilon^2)$ error terms in the following application to nonlinear acoustics, these error terms may be more significant in other cases.

7.2.1 The isentropic lattice Boltzmann model

To reproduce the isentropic equation of state (7.37), we must choose

$$\boxed{c_\mathrm{i}^2 = \frac{p}{\rho} = \frac{c_0^2}{\gamma}\left(\frac{\rho}{\rho_0}\right)^{\gamma-1},} \tag{7.38a}$$

where the small-signal (i.e. $\rho \simeq \rho_0$) speed of sound is

$$c_0 = c_\mathrm{i}\sqrt{\gamma}. \tag{7.38b}$$

In order to make the error terms proportional to $1 - c_\mathrm{i}^2/c_\xi^2$ disappear, we could also choose c_i so that $c_\mathrm{i} = c_\xi$ in the rest state and $c_0 = c_\xi\sqrt{\gamma}$.

CFL condition
A stability condition in numerical mathematics. For hyperbolic equations it states that information must not propagate in the simulation more slowly than the characteristics of the solution (e.g. the speed of sound).

Since the speed of sound c_0 is now higher than c_i, the *Courant-Friedrichs-Lewy condition* [104, Ch. 10] poses another stability constraint in addition to (7.3) on the parameter c_i. If the model's speed of sound exceeds the information propagation speed, i.e. the particle speed, of the model, the simulation will necessarily be unstable. Therefore, we must require that $c_0 = c_\mathrm{i}\sqrt{\gamma} < 1$, with an additional margin of safety to account for the nonlinear increase of the speed of sound. In fact, this requirement is even stricter in higher dimensions; we will see in section 7.2.2 that the stability limit for the D2Q9 velocity set is $c_0 > 1/\sqrt{2}$.

Since the parameter c_i is no longer constant, the $\partial c_\mathrm{i}^2/\partial t$ term in the stress tensor will not disappear. Using the chain rule, this time derivative is resolved to

$$\begin{aligned}\frac{\partial c_\mathrm{i}^2}{\partial t} &= \frac{c_0^2}{\gamma}\frac{\partial\rho}{\partial t}\frac{\partial}{\partial\rho}\left(\frac{\rho}{\rho_0}\right)^{\gamma-1} = -\frac{c_0^2}{\rho}\frac{\gamma-1}{\gamma}\left(\frac{\rho}{\rho_0}\right)^{\gamma-1}\frac{\partial\rho u_\gamma}{\partial x_\gamma} \\ &\simeq -c_\mathrm{i}^2(\gamma-1)\frac{\partial u_\gamma}{\partial x_\gamma}.\end{aligned} \tag{7.39}$$

Thus, this term represents an additional contribution to the bulk viscosity.

Inserting this into the extended model's stress tensor (7.13b) and comparing with the generalised stress tensor (7.15), we find that the resulting unmodified bulk viscosity is

$$\nu_\mathrm{B}' = \nu\left(\frac{5}{3} - \gamma\frac{c_\mathrm{i}^2}{c_\xi^2}\right). \tag{7.40}$$

Interestingly, for $c_\mathrm{i} \simeq c_\xi$, this bulk viscosity is the same as found in section (6.1.1) and elsewhere in the literature [55, 133] for instant equilibration of energy between the different molecular degrees of freedom. This would suggest that the $\partial c_\mathrm{i}^2/\partial t$ term in the stress tensor is be physically relevant and not an error term.

Thus, by choosing c_i^2 as in (7.38a), choosing $\Gamma_{\alpha\beta} = \delta_{\alpha\beta}\breve{I\!I}^{\mathrm{neq}}_{\gamma\gamma}/d$, and setting the bulk viscosity correction coefficient to

$$\boxed{b = \left[\tau + \tau^2 \frac{(1+2/d)c_\xi^2 - \gamma c_\mathrm{i}^2}{\nu_\mathrm{B} - \nu(5/3 - \gamma c_\mathrm{i}^2/c_\xi^2)}\right]^{-1}} \tag{7.41}$$

the LB model with isentropic equation of state is complete.

7.2.2 D2Q9 stability: Comparison to another model

With this choice of c_i^2, the resulting equilibrium $f_i^{(0)}$ for D2Q9 equals what we get by similarly specialising the equilibrium $f_i^{(0)}$ derived by Dellar in [144]. Dellar's model in general assumes only that the pressure $p(\rho)$ is a function only of density. We will now show this equivalence.

If we assume for the extended model that the c_i is similarly only a function of density, the exact momentum flux tensor perturbation (7.11d) can be simplified without approximation to

$$\begin{aligned}\breve{I\!I}^{(1)}_{\alpha\beta} = &-\tau\rho c_\xi^2 \left(\frac{\partial u_\alpha}{\partial x_\beta} + \frac{\partial u_\alpha}{\partial x_\beta} + \frac{1}{c_\xi^2}\left[c_\xi^2 - \frac{\partial \rho c_\mathrm{i}^2}{\partial \rho}\right]\delta_{\alpha\beta}\frac{\partial u_\gamma}{\partial x_\gamma}\right) \\ &- \tau\left(c_\xi^2 - \frac{\partial \rho c_\mathrm{i}^2}{\partial \rho}\right)\left(u_\alpha\frac{\partial}{\partial x_\beta} + u_\beta\frac{\partial}{\partial x_\alpha} + \delta_{\alpha\beta}u_\gamma\frac{\partial}{\partial x_\gamma}\right)\rho \\ &+ \tau\frac{\partial \rho u_\alpha u_\beta u_\gamma}{\partial x_\gamma} + \tau b\Gamma_{\alpha\beta},\end{aligned} \tag{7.42}$$

by applying the chain rule for derivatives of $c_\mathrm{i}^2(\rho)$ and the mass conservation equation.

Disregarding the term $\tau b\Gamma_{\alpha\beta}$ term which does not come from the equilibrium distribution, this equation is equal to what is given in [144]. Consequently, the equilibrium moments $\breve{I\!I}^{(0)}_0$, $\breve{I\!I}^{(0)}_\alpha$, $\breve{I\!I}^{(0)}_{\alpha\beta}$, and $\breve{I\!I}^{(0)}_{\alpha\beta\gamma}$ that $\breve{I\!I}^{(1)}_{\alpha\beta}$ determine the macroscopic equations must be equal for the two equilbrium distributions.

For the D2Q9 velocity set for which Dellar's model is derived, this means that eight out of the nine independent equilibrium moments are equal, as can be seen from Figure 5.7. An independent moment, which

we can choose as our ninth, was chosen by Dellar as

$$N^{(0)} = \sum_i g_i f_i^{(0)},$$

with $g_i = (1, -2, -2, -2, -2, 4, 4, 4, 4)$. Furthermore, Dellar showed that a source of potential instability is eliminated if this moment is

$$N^{(0)} = \rho - 3p.$$

Consequently, the D2Q9 equilibrium is fully determined by constraints related to the macroscopic equations and stability.

Taking this moment of (7.2), we do indeed find that $N^{(0)} = \rho - 3p$, meaning that this equilibrium does not suffer the D2Q9 stability issues described in [144]. Also, as all nine independent equilibrium moments are equal for the equilbrium distributions in (7.2) and in [144], it follows that the two equilibria are equal if c_i^2 is a function only of density.

Note however that the fact that this equilibrium distribution is stable for D1Q3 and D2Q9 does not necessarily mean that it is stable for other velocity sets. This stability must either be determined for each velocity set using complex derivations as in [144], or through numerical experiments.

An experiment was carried out to verify the stability of the isentropic model in the D2Q9 velocity set, using a simulation setup similar to that in section 6.3.2, with a monopole point source in the middle of the simulation domain. The high density gradients around the point source make for a demanding stability test. The simulation was performed with the previously used MRT operator which instantly relaxes nonhydrodynamic moments, $\gamma = 5/3$ and $\gamma = 1$, and zero viscosity. With $c_0 < 1/\sqrt{2}$ the simulation appears stable, but instabilities eventually develop at the source if c_0 is chosen to be larger.

This instability can likely be connected to the results of section 5.2.5. In that section, it was shown for the D2Q9 DVBE that the speed of sound in the direction of the diagonal velocities $|\boldsymbol{\xi}_{i\in\{5\text{–}8\}}|$ goes towards $1/\sqrt{2}$ due to the effects of viscous dispersion. This is in contrast to the axial direction where it increases to $|\boldsymbol{\xi}_{i\in\{1\text{–}3\}}| = 1$. This suggests that $1/\sqrt{2}$ is the information propagation speed in the diagonal directions, and not $|\boldsymbol{\xi}_{i\in\{5\text{–}8\}}| = \sqrt{2}$ as could be expected. If this is correct, then increasing the speed of sound above this limit will violate the CFL condition, explaining the instability.

7.2.3 Physical nonlinear acoustics case

With this isentropic model it is possible to capture both mechanisms of nonlinear acoustics. To verify this we will perform a free wave simulation as in [110]. Adapting the Burgers equation from section 2.3.5, which

describes nonlinear sound propagation, from forced waves to free waves, it becomes

$$\frac{\partial \tilde{p}}{\partial \tilde{t}} = \tilde{p}\frac{\partial \tilde{p}}{\partial \tilde{t_\mathrm{r}}} + \tilde{\alpha}_t \frac{\partial^2 \tilde{p}}{\partial \tilde{t_\mathrm{r}}^2}, \tag{7.43a}$$

where the tildes denote nondimensionalised parameters,

$$\tilde{p} = p'/p^\star, \quad \tilde{t} = t/t_\mathrm{shock}, \quad \tilde{t_\mathrm{r}} = k_0 c_0 t_\mathrm{r}, \quad \tilde{\alpha}_t = \alpha_t t_\mathrm{shock}. \tag{7.43b}$$

Here, t_shock is the shock formation time, i.e. the time it takes for the peak to catch up to the trough for a plane wave in a lossless medium,

$$t_\mathrm{shock} = \frac{\rho_0 c_0}{p^\star \beta k_0} = \frac{\gamma}{\beta \omega_0}\frac{p_0}{p^\star}, \tag{7.43c}$$

$\beta = (\gamma+1)/2$ being the coefficient of nonlinearity. In a thermoviscous fluid, the free wave absorption coefficient is

$$\alpha_t \simeq \frac{k_0^2}{2}\nu\left(\frac{4}{3} + \frac{\nu_\mathrm{B}}{\nu} + \frac{\gamma-1}{Pr}\right), \tag{7.44}$$

with the effect of molecular relaxation assumed to be either not present or absorbed into the bulk viscosity.

The free wave Burgers equation (7.43a) is on the same mathematical form as the forced wave Burgers equation (2.66a), and can be solved numerically in the frequency domain using the exact same method, (2.68), only replacing $\tilde{x}$ with $\tilde{t}$.

For the test case we choose a monatomic gas, which is purely thermoviscous and has no molecular relaxation. Monatomic gases have an adiabatic index of $\gamma = 5/3$ and zero bulk viscosity, as found in Chapter 3. Their Prandtl number is $Pr \simeq 2/3$ [58, Ch. II].

More specifically, the monatomic gas is chosen as neon at standard conditions, $p_0 = 1.013 \times 10^5\,\mathrm{Pa}$ and $T_0 = 300\,\mathrm{K}$. The ideal gas law gives a corresponding density of $\rho_0 = 0.820\,\mathrm{kg/m^3}$. The speed of sound as found from (2.24) to be $c_0 = 454\,\mathrm{m/s}$. The final material parameter is the viscosity, $\nu = 3.89 \times 10^{-5}\,\mathrm{m^2/s}$ [149].

The sound wave's frequency is chosen as 10 kHz, and its amplitude as $p^\star/p_0 = \gamma\rho^\star/\rho_0 = 10^{-2}$, corresponding to a *sound pressure level* of 151 dB re 20 µPa. This corresponds to a peak Mach number of

Sound pressure level
A logarithmic measure of RMS sound pressure p'_rms relative to a reference value (typically $p_\mathrm{ref} = 20\,\mu\mathrm{Pa}$), found as $20\log(p'_\mathrm{rms}/p_\mathrm{ref})$ [24, Ch. 5]

$$Ma = \frac{u^\star}{c_0} \simeq \frac{p^\star}{\rho_0 c_0^2} = \frac{p^\star}{\gamma p_0} = 6 \times 10^{-3}.$$

Inserting the constants, we find a shock formation time of $t_\mathrm{shock} = 1.99 \times 10^{-3}\,\mathrm{s}$, a shock formation distance of $x_\mathrm{shock} = c_0 t_\mathrm{shock} = 0.903\,\mathrm{m}$, and a nondimensionalised absorption $\tilde{\alpha}_t = 1.73 \times 10^{-3}$. While it is not directly relevant to the simulation, the acoustic viscosity number is $X = 1.58 \times 10^{-5}$ for the fundamental frequency.

7.2.4 Nonlinear acoustics simulation

As the problem is one-dimensional, it is appropriate to use the D1Q3 velocity set. Similarly to section 5.3.3 the free wave will be initialised as one wavelength spanning a periodic system, using the eigenvector of the eigenvalue problem (7.33), which can be found numerically directly from the matrix $\hat{A}$.

However, the linearisation analysis underlying the eigenvalue problem was performed under two assumptions. Firstly, that $\hat{f}_i^\star$ is a very small fluctuation on top of $F_i^{(0)}$. Secondly, that the speed of sound is a constant. These assumptions do not fully hold for a strongly excited wave and a nonlinear equation of state. By initialising in this way, amplitude oscillations such as those seen in Figure 5.16 can be reduced though not eliminated since the initialisation is no longer exact.

The number of timesteps required for shock formation can be found from the time resolution (4.45b) and the physical shock formation time (7.43c),

$$\frac{t_{\text{shock}}}{\Delta t} = \frac{2\gamma}{\gamma+1}\frac{p_0}{p^\star}\frac{c_{0,\text{ph}}^2}{\omega_{0,\text{ph}}\nu_{\text{ph}}}\frac{\nu_{\text{la}}}{c_{0,\text{la}}^2}. \tag{7.45a}$$

Similarly, the number of nodes per wavelength, which determines the system width, is found from the spatial resolution (4.45a) as

$$\frac{\lambda_{\text{ph}}}{\Delta x} = \frac{2\pi c_{0,\text{ph}}^2}{\omega_{0,\text{ph}}\nu_{\text{ph}}}\frac{\nu_{\text{la}}}{c_{0,\text{la}}}. \tag{7.45b}$$

Note how we have *two* adjustable parameters that determine the the resolution, ν_{la} and $c_{0,\text{la}}$. In the basic model with $c_0 = c_\xi$, only the parameter ν_{la} would be adjustable, and the number of time steps and nodes required could only be decreased by decreasing τ.

To get as few time steps and nodes as possible, meaning a quicker simulation, we desire to have a low numerical viscosity and a high lattice speed of sound. On the other hand, in dispersive numerical methods such as this, numerical dispersion causes a Gibbs-like phenomenon at the shock [150, 151]. A high simulation resolution, corresponding to a small k_0, is necessary to ensure that this phenomenon does not get out of hand before the shock formation occurs. Additionally, (7.36) and Figure 7.2 indicate that a higher value of c_{i} corresponds to a smaller numerical dispersion from discretisation error.

The numerical parameters were chosen as $\tau = 0.51$, $c_{0,\text{la}} = 0.9$. This leads to resolutions $\Delta x = 2.31 \times 10^{-5}$ m and $\Delta t = 4.59 \times 10^{-8}$ s, a lattice shock formation time of $t_{\text{shock}}/\Delta t \approx 43380$ time steps, and a system width of $\lambda_{\text{ph}}/\Delta x = 1962$ nodes.

While there is no bulk viscosity in a monatomic dilute gas and no heat conduction in the simulation, the bulk viscosity in the simulation was set

to $\nu_B = 3\nu(\gamma - 1)/2$ in order to emulate the effect of thermal conduction on acoustic absorption.

Various aspects of the simulation results are shown in Figure 7.3.

Figure 7.3(a) shows that the LB and Burgers equation solutions agree to plotting accuracy up to at least $\tilde{t} = 1$. At $\tilde{t} = 1.5$ the solutions no longer fully agree around the shock, and a spurious oscillation has formed at the upper edge of the shock due to the numerical dispersion of the LB scheme. Since the Burgers equation is solved numerically by a set of ODEs for the frequency components, that solution is not affected by numerical dispersion and such spurious oscillations.

As the shock develops, the different frequency components evolve: Higher harmonics feed on the lower ones, but are more heavily affected by absorption. The magnitude of each harmonic at time $\tilde{t}$ can be found by taking the spatial Fourier transform of the LB solution. The evolution of the first six frequency components in the LB and Burgers equation solutions are compared in Figure 7.3(b), showing excellent agreement.

Strangely, the agreement between the two methods shown here is significantly better than in the previously published article on using LB to simulate isothermal nonlinear acoustic shock formation [110]. However, as explained in that article, the imperfect agreement shown there may be connected to the method of determining the harmonic magnitudes, which involved averaging in time.

Figure 7.3(c) shows the magnitudes of the different harmonics at $\tilde{t} = 1$. While the agreement is excellent at low frequencies, the magnitudes of the higher LB harmonics are lower than those of the Burgers equation solution. It would be tempting to attribute this to numerical absorption, since (7.36) and Figure 7.2 shows that discretisation error causes extra absorption at high frequencies when c_0 is large. However, such a discrepancy also occurs between the two solutions when the simulation is performed using the basic LB model ($\gamma = 1$, $c_i = c_\xi = c_0$) where this is not the case as discretisation error causes a *decrease* in absorption. This indicates that the effect is not rooted in numerical absorption, and may be caused by differences in the two models' behaviour at high acoustic viscosity numbers X: Firstly, terms of $\mathcal{O}(X^2)$ and higher are neglected when deriving the Burgers equation from the Navier-Stokes-Fourier conservation equations. Secondly, we found in section 5.2.4 that the DVBE model's acoustic absorption is slightly higher for free waves than that of the Navier-Stokes-Fourier model.

All in all, the simulation results match very well, showing that the isentropic LB model works as intended and that the nonlinear errors in the extended LB model are negligible even for practical cases in nonlinear acoustics.

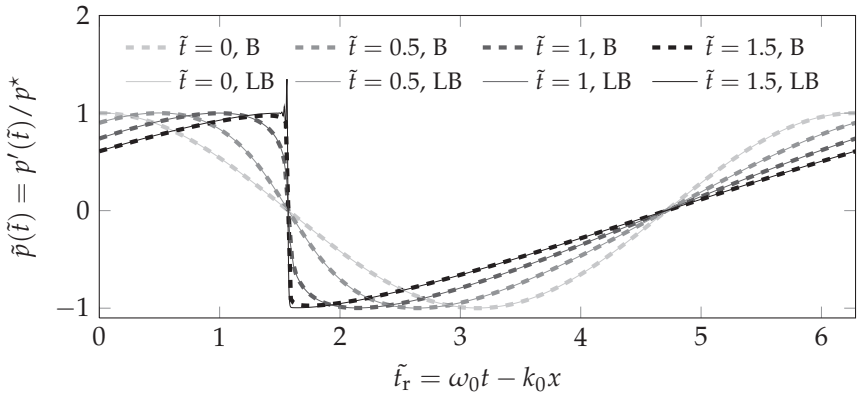

(a) Burgers' equation (B) and lattice Boltzmann (LB) solutions at different times

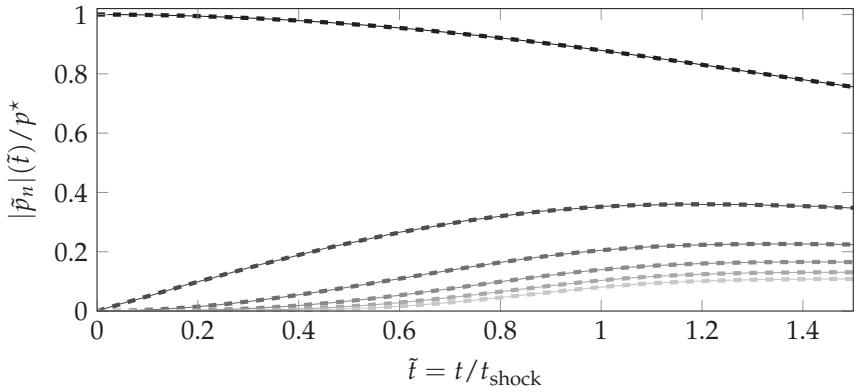

(b) Evolution of magnitude of frequency components $n = 1$ (upper, darkest) to $n = 6$ (lower, lightest), for Burgers (dashed) and LB (solid) solutions

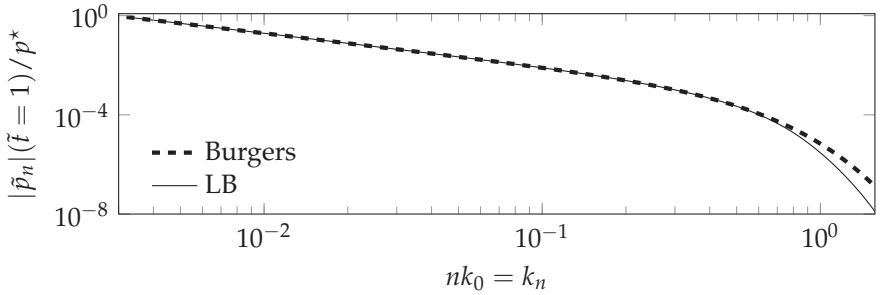

(c) Distribution of harmonic magnitude at $\tilde{t} = 1$ as function of components' numerical LB wavenumber

Figure 7.3: Comparison of different aspects of nonlinear acoustic shock wave formation, for both the Burgers equation and the lattice Boltzmann method.

7.3 Molecular relaxation

We will now utilise the extended LB model to reproduce the effect of slow molecular relaxation on sound propagation, as discussed in section 2.3.3, in a LB simulation. Unfortunately, due to time constraints, the work in this section could not be as fully realised as it should have been. Even so, to the author's knowledge no similar LB work has previously been published.

To reproduce the effect of a single relaxation process, i.e. the transfer of energy in and out of a single internal degree of freedom, we use the relaxation equation of state

$$\tau_\mathrm{m} \frac{\partial}{\partial t} \left(p' - c_\infty^2 \rho' \right) + \left(p' - c_0^2 \rho' \right) = 0, \tag{7.46}$$

where c_0 is the ideal, low-frequency speed of sound and c_∞ is the speed of sound for frequencies so high that the internal degree of freedom is no longer active. From (2.49), the ratio c_∞ / c_0 is determined solely by the excitation fraction of the inner degree of freedom, d_i.

For a general pressure and density fluctuation, the time derivative must be estimated using finite differences or similar. However, if we restrict ourselves to monofrequency sound with a frequency $\hat{\omega}$, we can replace the time derivative as $\partial / \partial t \to \mathrm{i}\hat{\omega}$, which results in the equation of state

$$p' = \frac{c_0^2 + \mathrm{i}\hat{\omega}\tau_\mathrm{m} c_\infty^2}{1 + \mathrm{i}\hat{\omega}\tau_\mathrm{m}} \rho'. \tag{7.47a}$$

For forced waves, this is fulfilled if

$$c_\mathrm{i}^2 = \frac{c_0^2 + \mathrm{i}X_\mathrm{m} c_\infty^2}{1 + \mathrm{i}X_\mathrm{m}} = \frac{c_0^2 + X_\mathrm{m}^2 c_\infty^2}{1 + X_\mathrm{m}^2} + \mathrm{i}\frac{X_\mathrm{m}(c_\infty^2 - c_0^2)}{1 + X_\mathrm{m}^2}, \tag{7.47b}$$

where we have used the *acoustic relaxation number* X_m, defined analogously to the acoustic viscosity number X as

Acoustic relaxation number, X_m
A dimensionless number indicating the effect of molecular relaxation on sound propagation

$$X_\mathrm{m} = \omega_0 \tau_\mathrm{m}. \tag{7.48}$$

Since this choice of c_i is a constant, we do not have to take the extended model's $\partial c_\mathrm{i}^2 / \partial t$ term into consideration. Also, c_i is now complex, meaning that there is a phase shift between the pressure and the density components of the wave.

The derivation in section 2.3.3 on the effect of relaxation on absorption and dispersion was performed with the Euler model, and did therefore not include any thermoviscous absorption. Combining the relaxation equation of state with the Navier-Stokes-Fourier and neglecting $\mathcal{O}(X^2)$ effects, the total absorption is given by addition of the effects of relaxation, viscosity, and heat conduction [28]. Thus, for weak relaxation processes (i.e. small d_i,

or equivalently, small $c_\infty^2/c_0^2 - 1$) and small acoustic viscosity numbers X, the dispersion and absorption for forced waves in an isothermal relaxing fluid are given by

$$c = c_0 \sqrt{\frac{1 + X_\mathrm{m}^2 (c_\infty/c_0)^4}{1 + X_\mathrm{m}^2 (c_\infty/c_0)^2}}, \tag{7.49a}$$

$$\frac{\alpha_x}{k} = \frac{1}{2}\left(\frac{c_\infty^2}{c_0^2} - 1\right) \frac{X_\mathrm{m}}{1 + X_\mathrm{m}^2} + \frac{\omega_0}{2c^2}\left(\frac{4}{3}\nu + \nu_\mathrm{B}\right). \tag{7.49b}$$

The second absorption term is close to $X/2$, but is given by a general speed of sound c instead of the ideal speed of sound c_0. In other words, the dispersion of molecular relaxation affects the thermoviscous absorption.

This change of the speed of sound in the viscous absorption indicates that the acoustic viscosity number should be redefined in this case. Since the expressions above are only valid to $\mathcal{O}(X)$, i.e. not to $\mathcal{O}(X^2)$ where viscous dispersion occurs, and since the viscous effect on absorption is typically only relevant for $X_\mathrm{m} \gg 1$ where $c = c_\infty$, we redefine X from (5.8b) to

$$X = \frac{\omega_0}{c_\infty^2}\left(\frac{4}{3}\nu + \nu_\mathrm{B}\right). \tag{7.50}$$

7.3.1 Verification by simulation

To determine whether the suggested model works, a simulation must be performed. To find the dispersion and absorption expressions (7.49), it is assumed that $X \ll 1$ and that $c_\infty^2/c_0^2 - 1 \ll 1$. For the simulation we choose $c_0 = 0.57$ and $c_\infty = 0.58$, corresponding from (2.49) to an excitation fraction of the inner degree of freedom of $d_\mathrm{i} = 0.176$. To be consistent with the assumption of only one inner degree of freedom, the bulk viscosity is chosen as $\nu_\mathrm{B} = 0$.

The simulation was performed for a linearised LBE, like the inviscid plane forced wave simulations in section 6.3.1, using the same source term,

$$\hat{f}_i(x,t) = -\mathrm{i}w_i\, \mathrm{e}^{\mathrm{i}\omega_0 t} W(t)\delta(x). \tag{7.51}$$

The window function is necessary here in order to ensure sufficient stability. The topic of stability will be discussed later.

The acoustic molecular relaxation number was chosen as $X_\mathrm{m} = 10^4 X$, so that a wide range of values of X_m could be simulated while still keeping $X \ll 1$. Simulations were performed for values in the range $10^{-2} \leq X_\mathrm{m} \leq 10^3$, $10^{-6} \leq X \leq 10^{-1}$. To achieve these values, a constant frequency $\omega_0 = 0.007569$ was chosen in order to have a low but consistent numerical error, and the relaxation time was varied in the interval $0.5001 \leq \tau \leq 10.5$. With these choices, $\tau = 0.51$ corresponds to $X_\mathrm{m} = 1$.

In each simulation, the speed of sound c and the normalised absorption coefficients $\alpha_x/k = \alpha_x/(\omega_0/c)$ were measured from the solution as

$$c = -\frac{\omega_0}{\partial(\arg\hat{\rho}')/\partial x}, \qquad \alpha_x = -\frac{\partial \ln|\hat{\rho}'|}{\partial x}. \tag{7.52}$$

The results of the simulations are shown in Figure 7.4. The measured speed of sound agrees excellently with (7.49a) until the neglected $\mathcal{O}(X^2)$ viscous dispersion terms start making their presence known at around $X = 10^{-2}$. The measured absorption also agrees well, with a very minor disagreement of unknown origin in the crossover zone between the two types of absorption.

It should be noted that these simulations have some stability problems. For simultaneously sufficiently high values of ω_0 and sufficiently low values of τ, spurious high-frequency oscillations appear in the simulation, typically near the first wavefront, with amplitudes that increase in time. The effect is especially pronounced around $X_\mathrm{m} = 1$ and if the window function $W(t)$ is not used.

The origin of these stability issues is likely the choice of a complex c_i; at $X_\mathrm{m} \approx 1$, the instability is most prominent and the imaginary part of c_i is at its largest. In the derivation of (7.47b), the fluctuation was assumed to have a single frequency ω_0. As discussed in section 6.3.1, the signal contains other frequencies due to spectral leakage caused by the source being turned on. It could be that the complex speed of sound c_i causes a negative absorption coefficient α_x for one or more of these frequencies. This is supported by the effect of the window function $W(t)$ which reduces the spectral leakage and has a strong positive effect on stability in the simulations.

If this is the true origin of the instability in the simulation, then stability could be improved by estimating the time derivatives in the equation of state directly using finite differences or similar methods. This would lead to a consistent estimate of the local time derivative instead of the current assumption that the field varies with $\mathrm{e}^{\mathrm{i}\omega_0}$ everywhere, and would also lead to a real-valued and time-varying c_i instead of the complex and constant c_i used here.

Regardless of stability issues, this is a proof of concept showing that it is possible to model molecular relaxation in lattice Boltzmann simulations with accurate results.

7.4 Summary and discussion

Since the speed of sound is a direct consequence of the equation of state, *any* lattice Boltzmann model which allows adjusting the speed of sound must also allow adjusting the equation of state.

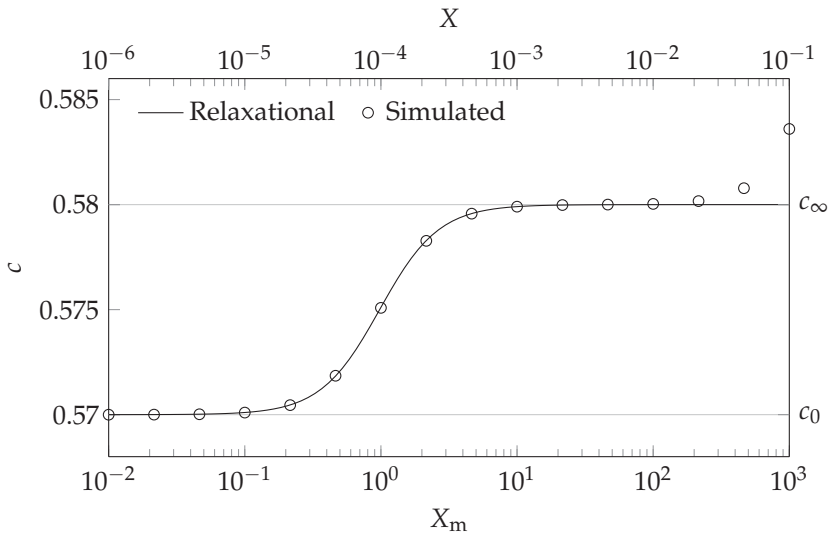

(a) Relaxational and simulated speed of sound as function of X_m and X. The right-hand discrepancy is due to $\mathcal{O}(X^2)$ viscous dispersion which was neglected in (7.49a).

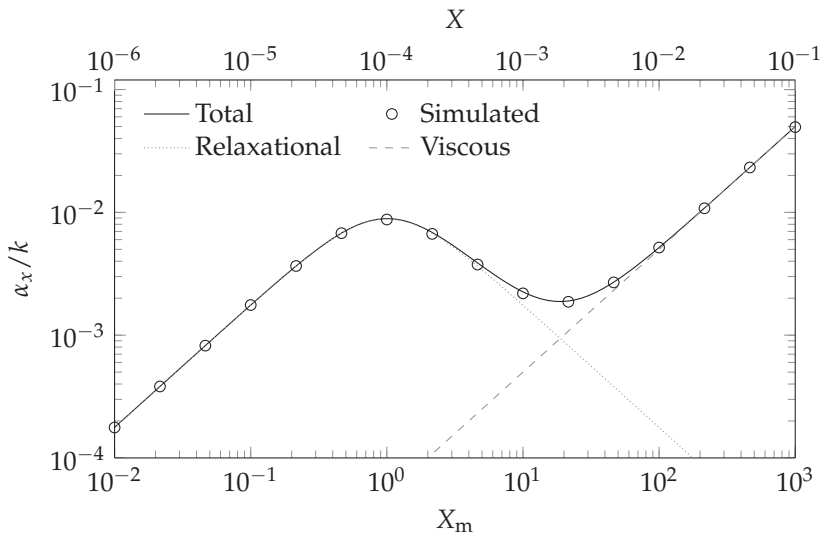

(b) Total and simulated absorption as function of X_m and X. Also plotted are the contributions of the individual terms in (7.49b).

Figure 7.4: Simulated speed of sound and absorption, compared with analytical expressions from (7.49).

Several models have been published where the speed of sound, and consequently the equation of state, are altered by altering the equilibrium distribution $f_i^{(0)}$. While a specific model by Chopard et al. was picked out in this chapter, all such models necessarily have much in common as the zeroth to second moments of their equilibrium distributions must be the same. If such models are used with non-extended velocity sets, they inevitably gain undesired terms in their macroscopic stress tensor.

Most of these undesired terms are negligible even for non-vanishing Mach numbers, as was shown in this chapter by an accurate simulation of nonlinear acoustics. However, some of these terms unphysically affect the bulk viscosity of the model and should be compensated for through a bulk viscosity correction method.

In the D1Q3 velocity set, there are as many constraints on the moments of the equilibrium distribution as there are independent moments. For that reason, all models that implement a variable equation of state through the equilibrium distribution must be equivalent for D1Q3. As a consequence, the linearisation analysis in section 7.1.5 is valid for all such models.

It is surprisingly difficult to construct such equilibria which are stable for other velocity sets than D1Q3. The Chopard et al. equilibrium used throughout this chapter has been shown to be equivalent for D2Q9 to another provably stable equilibrium from [144]. Even so, instabilities develop for the D2Q9 velocity set when $c_0 > 1/\sqrt{2}$. This may be because such a high speed of sound breaks some CFL condition as suggested by the results of Chapter 5. However, it is not given that the Chopard et al. equilibrium given here gives stable results for the simple three-dimensional velocity sets. This must be studied further.

Ideally, we would like to have an equilibrium distribution on a simple mathematical form which is explicit for every velocity set like (7.2), which is also provably stable in every simple velocity set. Considering the difficulty of constructing such an equilibrium which is stable in D2Q9 [144], this may not neccessarily be possible to attain, and individual equilibria specific to each velocity set may have to be constructed.

The relevancy of variable equations of state should not be in doubt. While the basic equation of state $p' = c_\xi^2 \rho'$ (neglecting the rest pressure p_0 which has no effect in the mass and momentum conservation equations) is surprisingly versatile, some physics cannot be captured with this constant and linear relationship between p' and ρ'. A variable equation of state is necessary to capture nonlinearity, slow equilibration (as in the case of molecular relaxation), and the effect of underlying variables such as a varying temperature field or the concentration of solutes.

In this chapter, a nonlinear equation of state was used to capture fully nonlinear acoustics in a simulation. The result has a very good correspondence to the Burgers equation reference solution up to some

time after the shock is formed and numerical dispersion causes a spurious oscillation near the shock. This would also happen for other dispersive numerical schemes.

The effect of molecular relaxation was also recreated, though the mono-frequency assumption underlying that particular simulation is likely the root of an instability which was observed when $X_{\mathrm{m}} \sim 1$. By implementing the relaxation equation of state in its original, time dependent form, this instability could perhaps be removed. Regardless of stability issues, the measured absorption and dispersion matches the corresponding theoretical predictions very well.

It may also be possible to capture multiple molecular relaxation directly in a simulation, without resorting to model equations of state. This might be done by defining underlying variables for the inner and translational energies, all evolved by an advection-diffusion-reaction process. The translational energy would have to be increased and decreased by compression and rarefaction, and directly affect the equation of state as temperature. The relaxation, or equilibration between the degrees of freedom, could be captured by a relaxation process between the energies in the different degrees of freedom. However, such complicated physics would inevitably result in a quite complicated numerical scheme.

8 Discussion and conclusion

The three research chapters in this thesis cover three separate topics of lattice Boltzmann acoustics. Simply put, Chapter 5 details the propagation of free and forced sound waves, Chapter 6 describes a method to generate sound waves in LB simulations, and Chapter 7 describes a method to change the equation of state of the simulated medium. Each chapter ends with a separate summary and discussion of its content, which will not be repeated here.

Of the three research chapters, Chapter 5 is the most fundamental, dealing with the propagation of sound itself. The wavenumber predicted in that chapter for forced waves accurately described the propagation of cylindrical waves from multipole point sources in Chapter 6. A similar sound propagation analysis was also performed for a more general model in Chapter 7.

One essential point that should be emphasised is the difference between free waves, which are absorbed with time, and forced waves, which are absorbed with the distance to their source. We have found that the LB sound propagation for these two types of wave differ at $\mathcal{O}(k_0^4)$, $\mathcal{O}(Xk_0^2)$, $\mathcal{O}(X^2)$, and higher orders. Here, k_0 represents the numerical resolution and X represents the effect of viscosity on sound propagation. Consequently, the order of disagreement between these two types of wave in LB simulations is nearly* the same as their order of disagreement with sound propagation in the Navier-Stokes fluid model.

As explained in the beginning of section 5.3, the thorough work that has previously been done by other authors to describe sound propagation in the LBM has only considered free waves, which is unfortunate since free sound waves do not occur in nature; sound requires a source. Similarly thorough work should therefore also be carried out for forced waves. While it has proven its usefulness in this thesis, the D1Q3 analysis in Chapter 5 does not take into account the possibility of an underlying flow, the anisotropy of higher-dimensional velocity sets, or the effect of more general collision operators. Such aspects should be taken into account in a later analysis.

*The non-numerical Navier-Stokes fluid model naturally has no numerical dispersion, so the disagreement happens at $\mathcal{O}(k_0^2)$. Forced and free LB waves are equally numerically dispersive at $\mathcal{O}(k_0^2)$, even with a variable equation of state, so they do not disagree with each other before $\mathcal{O}(k_0^4)$.

Acoustic boundary conditions must also be examined further. The commonly used pressure and velocity boundary conditions reflect sound waves, which subsequently pollute the pressure field of the simulation [95]. A number of boundary conditions which do not reflect sound waves have been developed, and these are briefly described and referred to in section 4.4. However, it is difficult to know how these methods compare since most of them have not been benchmarked against each other. A new review article containing a comparative analysis of non-reflecting BCs and their capabilities would be very welcome.

In the literature, it is often emphasised that the LBM cannot simulate fully compressible flows. It contains an $\mathcal{O}(u^3)$ error term that limits its range of applicability to "weakly compressible" flows; simulations of trans- and supersonic flow would not be accurate. Even so, this error term is insignificant for acoustics, even for nonlinear acoustics simulations such as the one shown in section 7.2.4.

This author's Master's thesis [9] concluded from time and space resolution equations like (4.45) that LB acoustics simulations are limited to very fine resolutions in space and time, meaning very small values of Δx and Δt. In contrast with LB incompressible flow simulations where the speed of sound is not physically relevant and puts no constraints on the physical resolution, this limitation makes it very computationally expensive to simulate systems of tangible physical size. The reason for this problem is that the only way to significantly increase the space and time steps Δx and Δt is to decrease the viscosity in the simulation. Decreasing the viscosity too far may cause problems with simulations' accuracy and stability.

While the reasoning behind it is sound, this conclusion must still be amended. Using other collision operators than the simplest BGK operator can give significantly better results for low numerical viscosity. In fact, stable and accurate simulations of sound wave generation and propagation at *zero* viscosity were shown in section 6.3. In particular, Figure 6.8 shows the difference between using the BGK collision operator and a particular choice of MRT collision operator: The BGK results are dominated by jagged errors while the MRT results remain smooth and accurate.

In recent years, several articles have been published on using LB for direct aeroacoustics simulations of physical systems of tangible size [43, 44, 46–48, 50, 114], though some do simulate a fluid more viscous than air in order to make the simulations more feasible. The simulations *do* take a very long time to perform, which typically limits the simulated real-world timespan to around a second [47, 48] or even less [43, 44, 46, 50, 114]. However, even such short timespans may be sufficient for simulated aeroacoustic systems to reach a steady state.

Beyond decreasing the lattice viscosity, some special techniques may

be applied to increase the simulation speed. In particular, grid refinement may be used for areas where a finer numerical resolution is desired for accuracy or for stability.* While we have not gone into grid refinement in this thesis, an overview of the available literature can be found in [152].

In some three-dimensional cases with axisymmetric geometries such as pipes, ducts, and loudspeaker drivers, simulations can be simplified by using axisymmetric LB models [131, 132]. These models let us essentially reduce the number of simulated dimensions from three to two, with a consequent decrease in number of nodes and an increase in simulation speed.

In closing, let us consider the usefulness of the lattice Boltzmann method for acoustics.

Due to the aforementioned limitations placed by considering both the viscosity and the speed of sound to be physically relevant phenomena in the simulation, it would be prohibitively computationally expensive to use the LBM for acoustic simulations of sound propagation in large domains such as rooms and outdoors. Interestingly, it is possible to simplify LB by discarding nonlinearity and viscosity [153] so that it becomes identical to the simpler transmission-line matrix (TLM) method [126]. In TLM simulations, there is no effective limit on the physical resolution and the size of simulated systems. Indeed, the TLM method has been used to simulate long-range outdoor sound propagation [154].

Where in acoustics, then, *would* the LBM be more useful for than other methods? Its key acoustic capability is simultaneously simulating fluid flow and sound in complex geometries while remaining simple to implement. Therefore, the LBM is very relevant as a simple compressible Navier-Stokes solver for cases where there is an interaction between the flow field and the acoustic field; in other words, for *direct aeroacoustics*.

Incompressible Navier-Stokes solvers can also be used to simulate the generation of sound, through the approach of *hybrid aeroacoustics*: After a steady state incompressible flow is found, its areas of turbulence can be analysed to determine their acoustic source strength. The far-field sound radiation can subsequently be determined using another computational method. Indeed, the LBM is fully capable of being used as the incompressible flow solver in a hybrid aeroacoustics approach [49], like many other such solvers.

In cases where the simulated system is large, where there is negligible feedback from the sound field on the flow field, and where the far-field sound radiation is the desired result, hybrid aeroacoustics is the best approach since compressible Navier-Stokes simulations are more demanding than incompressible ones. In other cases where there is a feedback from the generated sound field onto the flow field, such as

*In LB acoustics simulations, finer resolution is linked with higher τ, which is linked with improved stability.

the problem of singing risers in the natural gas industry [38–42], hybrid aeroacoustics cannot work and direct aeroacoustics must be used.

This is where the lattice Boltzmann method comes in: It is a simpler tool than the alternatives for simulating weakly compressible flow, and would therefore seem to be an excellent fit for direct aeroacoustics.

Bibliography

[1] J. Hardy, Y. Pomeau, and O. de Pazzis, "Time evolution of a two-dimensional model system. I. Invariant states and time correlation functions," *Journal of Mathematical Physics*, vol. 14, no. 12, pp. 1746–1759, 1973.

[2] U. Frisch, B. Hasslacher, and Y. Pomeau, "Lattice-gas automata for the Navier-Stokes equation," *Physical Review Letters*, vol. 56, no. 14, pp. 1505–1508, 1986.

[3] G. McNamara and G. Zanetti, "Use of the Boltzmann equation to simulate lattice-gas automata," *Physical Review Letters*, vol. 61, no. 20, pp. 2332–2335, 1988.

[4] L. Axner, J. Bernsdorf, T. Zeiser, P. Lammers, J. Linxweiler, and A. G. Hoekstra, "Performance evaluation of a parallel sparse lattice Boltzmann solver," *Journal of Computational Physics*, vol. 227, no. 10, pp. 4895–4911, 2008.

[5] M. Born and H. S. Green, "A general kinetic theory of liquids. I. The molecular distribution functions," *Proceedings of the Royal Society of London. Series A*, vol. 188, no. 1012, pp. 10–18, 1947.

[6] D. d'Humières and P. Lallemand, "Lattice gas automata for fluid mechanics," *Physica A*, vol. 140, no. 1–2, pp. 326–335, 1986.

[7] D. d'Humières and P. Lallemand, "Numerical simulations of hydrodynamics with lattice gas automata in two dimensions," *Complex Systems*, vol. 1, no. 4, pp. 599–632, 1987.

[8] F. J. Higuera, S. Succi, and R. Benzi, "Lattice gas dynamics with enhanced collisions," *Europhysics Letters*, vol. 9, no. 4, pp. 345–349, 1989.

[9] E. M. Viggen, "The lattice Boltzmann method with applications in acoustics," Master's thesis, Norwegian University of Science and Technology (NTNU), 2009.

[10] E. M. Viggen, "The lattice Boltzmann method in acoustics," in *Proceedings of the 33rd Scandinavian Symposium on Physical Acoustics*, 2010.

[11] E. M. Viggen, "Viscously damped acoustic waves with the lattice Boltzmann method," *Philosophical Transactions of the Royal Society A*, vol. 369, no. 1944, pp. 2246–2254, 2011.

[12] E. M. Viggen, "Sound propagation properties of the discrete-velocity Boltzmann equation," *Communications in Computational Physics*, vol. 13, no. 3, pp. 671–684, 2013.

[13] E. M. Viggen, "Acoustic multipole sources for the lattice Boltzmann method," *Physical Review E*, vol. 87, no. 2, p. 023306, 2013.

[14] E. M. Viggen, "Acoustic multipole sources from the Boltzmann equation," in *Proceedings of the 36th Scandinavian Symposium on Physical Acoustics*, 2013.

[15] E. M. Viggen, "Acoustic multipole sources from the Boltzmann equation." arXiv:1302.3764, 2013.

[16] Lord Rayleigh, *The theory of sound, Volume II*. Macmillan and Co., 1st ed., 1878.

[17] H. Lamb, *Hydrodynamics*. Cambridge University Press, 1st ed., 1895.

[18] A. Einstein, "Die Grundlage der allgemeinen Relativitätstheorie," *Annalen der Physik*, vol. 354, no. 7, pp. 769–822, 1916.

[19] P. A. Thompson, *Compressible-fluid dynamics*. McGraw-Hill, 1972.

[20] L. Euler, "Principes généraux du mouvement des fluides," *Mémoires de l'académie des sciences de Berlin*, vol. 11, pp. 274–315, 1757.

[21] G. G. Stokes, "On the theories of the internal friction of fluids in motion, and of the equilibrium and motion of elastic solids," *Transactions of the Cambridge Philosophical Society*, vol. 8, pp. 287–319, 1845.

[22] W. E. Meador, G. A. Miner, and L. W. Townsend, "Bulk viscosity as a relaxation parameter: Fact or fiction?," *Physics of Fluids*, vol. 8, no. 1, pp. 258–261, 1996.

[23] C. Pozrikidis, *Fluid Dynamics – Theory, Computation, and Numerical Simulation*. Springer, 2nd ed., 2009.

[24] L. E. Kinsler, A. R. Frey, A. B. Coppens, and J. V. Sanders, *Fundamentals of acoustics*. John Wiley & Sons Inc., 4th ed., 2000.

[25] D. T. Blackstock, *Fundamentals of physical acoustics*. John Wiley & Sons Inc., 2000.

[26] C. Truesdell, "Precise theory of the absorption and dispersion of forced plane infinitesimal waves according to the Navier–Stokes equations," *Journal of Rational Mechanics and Analysis*, vol. 2, no. 4, pp. 643–730, 1953.

[27] M. Greenspan, "Transmission of sound waves in gases at very low pressures," in *Physical Acoustics* (W. P. Mason, ed.), vol. IIA, ch. 1, pp. 1–45, Academic Press, 1965.

[28] M. J. Lighthill, "Viscosity effects in sound waves of finite amplitude," in *Surveys in Mechanics* (G. K. Batchelor and R. M. Davies, eds.), pp. 250–351, Cambridge University Press, 1956.

[29] H. O. Kneser, "Relaxation processes in gases," in *Physical Acoustics* (W. P. Mason, ed.), vol. IIA, ch. 3, pp. 133–202, Academic Press, 1965.

[30] H.-J. Bauer, "Phenomenological theory of the relaxation phenomenon in gases," in *Physical Acoustics* (W. P. Mason, ed.), vol. IIA, ch. 2, pp. 47–131, Academic Press, 1965.

[31] N. H. Johannesen and J. P. Hodgson, "The physics of weak waves in gases," *Reports on Progress in Physics*, vol. 42, pp. 629–676, 1979.

[32] ISO 9613-1:1993(E). Acoustics — Attenuation of sound during propagation outdoors — Part 1: Calculation of the absorption of sound by the atmosphere.

[33] S. Temkin, *Elements of acoustics*. John Wiley & Sons, 1981.

[34] A. D. Pierce, *Acoustics*. The Acoustical Society of America, 1989.

[35] M. S. Howe, *Theory of vortex sound*. Cambridge University Press, 2003.

[36] P. M. Morse and K. U. Ingard, *Theoretical acoustics*. McGraw-Hill Book Company, 1968.

[37] M. J. Lighthill, "On sound generated aerodynamically. I. General theory," *Proceedings of the Royal Society of London. Series A, Mathematical and Physical Sciences*, vol. 211, no. 1107, pp. 564–587, 1952.

[38] U. R. Kristiansen and G. A. Wiik, "Experiments on sound generation in corrugated pipes with flow," *Journal of the Acoustical Society of America*, vol. 121, no. 3, pp. 1337–1344, 2007.

[39] M. Popescu and S. T. Johansen, "Modelling of aero-acoustic wave propagation in low Mach number corrugated pipe flow," *Progress in Computational Fluid Dynamics*, vol. 9, no. 6–7, pp. 417–425, 2009.

[40] M. Popescu, S. T. Johansen, and W. Shyy, "Flow-induced acoustics in corrugated pipes," *Communications in Computational Physics*, vol. 10, no. 1, pp. 120–139, 2011.

[41] U. R. Kristiansen, P.-O. Mattei, C. Pinhede, and M. Amielh, "Experimental study of the influence of low frequency flow modulation on the whistling behavior of a corrugated pipe," *Journal of the Acoustical Society of America*, vol. 130, no. 4, pp. 1851–1855, 2011.

[42] U. R. Kristiansen, D. Mazzoni, and A. B. Krogvig, "Aeroacoustic investigation of a flow pipe with a small cavity using the lattice Boltzmann method," in *Proceedings of the 35th Scandinavian Symposium on Physical Acoustics*, 2012.

[43] H. Kühnelt, "Simulating the mechanism of sound generation in flutes using the lattice Boltzmann method," in *Proceedings of the Stockholm Music Acoustics Conference*, pp. 401–404, 2003.

[44] A. Wilde, "Calculation of sound generation and radiation from instationary flows," *Computers & Fluids*, vol. 35, pp. 986–993, 2006.

[45] M. Hasert, J. Bernsdorf, and S. Roller, "Towards aeroacoustic sound generation by flow through porous media," *Philosophical Transactions of the Royal Society A*, vol. 369, no. 1945, pp. 2467–2475, 2011.

[46] H. Kühnelt, "Aero-acoustic source characterization for flow-driven resonators using Helmholtz vector field decomposition," in *Proceedings of Numerical Analysis and Applied Mathematics ICNAAM 2011*, pp. 131–134, 2011.

[47] F. A. van Herpe, S. Vergne, and E. Gaudard, "Wavenumber-frequency analysis of the wall pressure fluctuations in the wake of a rear view mirror using a lattice Boltzmann model," in *Proceedings of the Acoustics 2012 Nantes Conference*, pp. 1845–1850, 2012. Available at `http://hal.archives-ouvertes.fr/hal-00810780`.

[48] H. Machrouki, D. Ricot, and O. Coste, "Lattice Boltzmann aeroacoustics modelling of flow around obstacles," in *Proceedings of the Acoustics 2012 Nantes Conference*, pp. 1291–1295, 2012. Available at `http://hal.archives-ouvertes.fr/hal-00811101`.

[49] G. A. Brès, D. Freed, M. Wessels, S. Noelting, and F. Pérot, "Flow and noise predictions for the tandem cylinder aeroacoustic benchmark," *Physics of Fluids*, vol. 24, no. 3, p. 036101, 2012.

[50] A. T. de Jong, H. Bijl, A. Hazir, and J. Wiedemann, "Aeroacoustic simulation of slender partially covered cavities using a lattice Boltzmann method," *Journal of Sound and Vibration*, vol. 332, no. 7, pp. 1687–1703, 2012.

[51] M. F. Hamilton and C. L. Morfey, "Model equations," in *Nonlinear acoustics* (M. F. Hamilton and D. T. Blackstock, eds.), ch. 3, pp. 41–63, Academic Press, 1998.

[52] J. H. Ginsberg and M. F. Hamilton, "Computational methods," in *Nonlinear acoustics* (M. F. Hamilton and D. T. Blackstock, eds.), ch. 11, pp. 309–341, Academic Press, 1998.

[53] H. Grad, "On the kinetic theory of rarefied gases," *Communications on Pure and Applied Mathematics*, vol. 2, no. 4, pp. 331–407, 1949.

[54] C. S. Wang Chang and G. E. Uhlenbeck, "Transport phenomena in polyatomic gases," Tech. Rep. M604-6, University of Michigan, 1951.

[55] T. F. Morse, "Kinetic model for gases with internal degrees of freedom," *Physics of Fluids*, vol. 7, no. 2, pp. 159–169, 1964.

[56] F. B. Hanson and T. F. Morse, "Kinetic models for a gas with internal structure," *Physics of Fluids*, vol. 10, no. 2, pp. 345–353, 1967.

[57] S. Chapman and T. G. Cowling, *The mathematical theory of non-uniform gases*. Cambridge University Press, 3rd ed., 1970.

[58] C. Cercignani, *The Boltzmann equation and its applications*. Springer-Verlag, 1988.

[59] A. S. J. Suiker and C. S. Chang, "Application of higher-order tensor theory for formulating enhanced continuum models," *Acta Mechanica*, vol. 142, no. 1–4, pp. 223–234, 2000.

[60] P. L. Bhatnagar, E. P. Gross, and M. Krook, "A model for collision processes in gases. I. Small amplitude processes in charged and neutral one-component systems," *Physical Review*, vol. 94, no. 3, pp. 511–525, 1954.

[61] D. Hänel, *Molekulare Gasdynamik*. Springer-Verlag, 2004.

[62] J. D. Foch and G. E. Uhlenbeck, "Propagation of sound in monatomic gases," *Physical Review Letters*, vol. 19, no. 18, pp. 1025–1027, 1967.

[63] E. Meyer and G. Sessler, "Schallausbreitung in Gasen bei hohen Frequenzen und sehr niedrigen Drucken," *Zeitschrift für Physik*, vol. 149, pp. 15–39, 1957.

[64] C. S. Wang Chang and G. E. Uhlenbeck, "On the propagation of sound in monatomic gases," Tech. Rep. M999, University of Michigan, 1952.

[65] C. S. Wang Chang and G. E. Uhlenbeck, "The kinetic theory of gases," in *Studies in statistical mechanics*, vol. V, North-Holland Publishing Company, 1970.

[66] J. D. Foch and M. F. Losa, "Improved kinetic theory of sound propagation," *Physical Review Letters*, vol. 28, no. 20, pp. 1315–1317, 1972.

[67] H. Grad, "Asymptotic theory of the Boltzmann equation," *Physics of Fluids*, vol. 6, no. 2, pp. 147–181, 1963.

[68] P. J. Dellar, "Macroscopic descriptions of rarefied gases from the elimination of fast variables," *Physics of Fluids*, vol. 19, no. 10, p. 107101, 2007.

[69] E. T. Jaynes, "Gibbs vs Boltzmann entropies," *American Journal of Physics*, vol. 33, no. 5, pp. 391–398, 1965.

[70] E. H. Hauge, "Exact and Chapman-Enskog solutions of the Boltzmann equation for the Lorentz model," *Physics of Fluids*, vol. 13, no. 5, pp. 1201–1208, 1970.

[71] H. Grad, "Note on N-dimensional Hermite polynomials," *Communications on Pure and Applied Mathematics*, vol. 2, no. 4, pp. 325–330, 1949.

[72] X. Shan, X.-F. Yuan, and H. Chen, "Kinetic theory representation of hydrodynamics: a way beyond the Navier–Stokes equation," *Journal of Fluid Mechanics*, vol. 550, pp. 413–441, 2006.

[73] X. He and L.-S. Luo, "Theory of the lattice Boltzmann method: From the Boltzmann equation to the lattice Boltzmann equation," *Physical Review E*, vol. 56, no. 6, pp. 6811–6817, 1997.

[74] Y. H. Qian, D. d'Humières, and P. Lallemand, "Lattice BGK models for Navier-Stokes equation," *Europhysics Letters*, vol. 17, no. 6, pp. 479–484, 1992.

[75] S. Ansumali, I. V. Karlin, and H. C. Öttinger, "Minimal entropic kinetic models for hydrodynamics," *Europhysics Letters*, vol. 63, no. 6, pp. 798–804, 2003.

[76] J. Lätt, *Hydrodynamic limit of lattice Boltzmann equations*. PhD thesis, University of Geneva, 2007.

[77] P. J. Dellar, "Bulk and shear viscosities in lattice Boltzmann equations," *Physical Review E*, vol. 64, no. 3, p. 031203, 2001.

[78] S. Succi, *The lattice Boltzmann equation for fluid dynamics and beyond*. Oxford University Press, 2001.

[79] C. M. Bender and S. A. Orszag, *Advanced mathematical methods for scientists and engineers*. McGraw-Hill, 1978.

[80] X. He, S. Chen, and G. D. Doolen, "A novel thermal model for the lattice Boltzmann method in incompressible limit," *Journal of Computational Physics*, vol. 146, pp. 282–300, 1998.

[81] J. Lätt, "Choice of units in lattice Boltzmann simulations." Freely available online at `http://wiki.palabos.org/_media/howtos:lbunits.pdf`, April 2008.

[82] B. M. Boghosian, J. Yepez, P. V. Coveney, and A. Wagner, "Entropic lattice Boltzmann methods," *Proceedings of the Royal Society A*, vol. 457, pp. 717–766, 2001.

[83] S. Bennett, *A lattice Boltzmann model for diffusion of binary gas mixtures*. PhD thesis, King's College, Cambridge, 2010.

[84] P. Lallemand and L.-S. Luo, "Theory of the lattice Boltzmann method: Dispersion, dissipation, isotropy, Galilean invariance, and stability," *Physical Review E*, vol. 61, no. 6, pp. 6546–6562, 2000.

[85] P. J. Dellar, "Incompressible limits of lattice Boltzmann equations using multiple relaxation times," *Journal of Computational Physics*, vol. 190, no. 2, pp. 351–370, 2003.

[86] H. Xu and P. Sagaut, "Optimal low-dispersion low-dissipation LBM schemes for computational aeroacoustics," *Journal of Computational Physics*, vol. 230, no. 13, pp. 5353–5382, 2011.

[87] P. Asinari and I. V. Karlin, "Generalized Maxwell state and H theorem for computing fluid flows using the lattice Boltzmann method," *Physical Review E*, vol. 79, no. 3, p. 36703, 2009.

[88] J. Lätt and B. Chopard, "Lattice Boltzmann Method with regularized non-equilibrium distribution functions." arXiv:physics/0506157, 2005.

[89] J. Lätt and B. Chopard, "Lattice Boltzmann method with regularized pre-collision distribution functions," *Mathematics and Computers in Simulation*, vol. 72, no. 2–6, pp. 165–168, 2006.

[90] A. J. C. Ladd and R. Verberg, "Lattice-Boltzmann simulations of particle-fluid suspensions," *Journal of Statistical Physics*, vol. 104, no. 5/6, pp. 1191–1251, 2001.

[91] H. Chen, R. Zhang, I. Staroselsky, and M. Jhon, "Recovery of full rotational invariance in lattice Boltzmann formulations for high Knudsen number flows," *Physica A*, vol. 362, pp. 125–131, 2006.

[92] S. Chen and G. D. Doolen, "Lattice Boltzmann method for fluid flows," *Annual Review of Fluid Mechanics*, vol. 30, pp. 329–364, 1998.

[93] J. Lätt, B. Chopard, O. Malaspinas, M. Deville, and A. Michler, "Straight velocity boundaries in the lattice Boltzmann method," *Physical Review E*, vol. 77, no. 5, p. 056703, 2008.

[94] Q. Zou and X. He, "On pressure and velocity boundary conditions for the lattice Boltzmann BGK model," *Physics of Fluids*, vol. 9, no. 7, pp. 1591–1598, 1997.

[95] S. Izquierdo, P. Martínez-Lera, and N. Fueyo, "Analysis of open boundary effects in unsteady lattice Boltzmann simulations," *Computers and Mathematics with Applications*, vol. 58, no. 5, pp. 914–921, 2009.

[96] M. M. Tekitek, M. Bouzidi, F. Dubois, and P. Lallemand, "Towards perfectly matching layers for lattice Boltzmann equation," *Computers and Mathematics with Applications*, vol. 58, no. 5, pp. 903–913, 2009.

[97] A. Najafi-Yazdi and L. Mongeau, "An absorbing boundary condition for the lattice Boltzmann method based on the perfectly matched layer," *Computers & Fluids*, vol. 68, pp. 203–218, 2012.

[98] E. Vergnault, O. Malaspinas, and P. Sagaut, "A lattice Boltzmann method for nonlinear disturbances around an arbitrary base flow," *Journal of Computational Physics*, vol. 231, no. 24, pp. 8070–8082, 2012.

[99] E. Vergnault, O. Malaspinas, and P. Sagaut, "Noise source identification with the lattice Boltzmann method," *Journal of the Acoustical Society of America*, vol. 133, no. 3, pp. 1293–1305, 2013.

[100] S. Izquierdo and N. Fueyo, "Characteristic nonreflecting boundary conditions for open boundaries in lattice Boltzmann methods," *Physical Review E*, vol. 78, no. 4, p. 046707, 2008.

[101] D. Heubes, A. Bartel, and M. Ehrhardt, "Characteristic boundary conditions in the lattice Boltzmann method for fluid and gas dynamics." Submitted to Journal of Computational and Applied Mathematics, preprint available at `http://www.imacm.uni-wuppertal.de/fileadmin/imacm/preprints/2012/imacm_12_32.pdf`.

[102] E. W. S. Kam, R. M. C. So, and R. C. K. Leung, "Lattice Boltzmann method simulation of aeroacoustics and nonreflecting boundary conditions," *AIAA journal*, vol. 45, no. 7, pp. 1703–1712, 2007.

[103] F. M. White, *Viscous fluid flow*. McGraw-Hill, 3rd ed., 2006.

[104] R. J. LeVeque, *Finite difference methods for ordinary and partial differential equations*. Society for Industrial and Applied Mathematics, 2007.

[105] J. J. Markham, R. T. Beyer, and R. B. Lindsay, "Absorption of sound in fluids," *Reviews of Modern Physics*, vol. 23, no. 4, pp. 353–411, 1951.

[106] J. D. Sterling and S. Chen, "Stability analysis of lattice Boltzmann methods," *Journal of Computational Physics*, vol. 123, no. 1, pp. 196–206, 1996.

[107] T. Reis and T. N. Phillips, "Alternative approach to the solution of the dispersion relation for a generalized lattice Boltzmann equation," *Physical Review E*, vol. 77, no. 2, p. 026702, 2008.

[108] S. Marié, D. Ricot, and P. Sagaut, "Comparison between lattice Boltzmann method and Navier-Stokes high order schemes for computational aeroacoustics," *Journal of Computational Physics*, vol. 228, no. 4, pp. 1056–1070, 2009.

[109] J. M. Buick, C. A. Greated, and D. M. Campbell, "Lattice BGK simulation of sound waves," *Europhysics Letters*, vol. 43, no. 3, pp. 235–240, 1998.

[110] J. M. Buick, C. L. Buckley, C. A. Greated, and J. Gilbert, "Lattice Boltzmann BGK simulation of nonlinear sound waves: the development of a shock front," *Journal of Physics A*, vol. 33, pp. 3917–3928, 2000.

[111] J. M. Buick and J. A. Cosgrove, "Investigation of a lattice Boltzmann model with a variable speed of sound," *Journal of Physics A*, vol. 39, no. 44, pp. 13807–13815, 2006.

[112] D. Haydock and J. M. Yeomans, "Lattice Boltzmann simulations of acoustic streaming," *Journal of Physics A*, vol. 34, pp. 5201–5213, 2001.

[113] S. Mallick, R. Shock, and V. Yakhot, "Numerical simulation of the excitation of a Helmholtz resonator by a grazing flow," *Journal of the Acoustical Society of America*, vol. 114, no. 4, pp. 1833–1840, 2003.

[114] H. Kühnelt, "Simulation and analysis of the flow-acoustic interactions in the mouth of flute-like instruments," in *Proceedings of Forum Acusticum*, pp. 417–422, 2005.

[115] A. R. da Silva, G. P. Scavone, and M. van Walstijn, "Numerical simulations of fluid-structure interactions in single-reed mouthpieces," *Journal of the Acoustical Society of America*, vol. 122, no. 3, pp. 1798–1809, 2007.

[116] M. Tsutahara, T. Kataoka, K. Shikata, and N. Takada, "New model and scheme for compressible fluids of the finite difference lattice Boltzmann method and direct simulations of aerodynamic sound," *Computers & Fluids*, vol. 37, no. 1, pp. 79–89, 2008.

[117] J. M. Buick, M. Atig, D. J. Skulina, D. M. Campbell, J. P. Dalmont, and J. Gilbert, "Investigation of non-linear acoustic losses at the open end of a tube," *Journal of the Acoustical Society of America*, vol. 129, no. 3, pp. 1261–1272, 2011.

[118] X. M. Li, R. M. C. So, and R. C. K. Leung, "Propagation speed, internal energy, and direct aeroacoustics simulation using lattice Boltzmann method," *AIAA Journal*, vol. 44, no. 12, pp. 2896–2903, 2006.

[119] X. M. Li, R. C. K. Leung, and R. M. C. So, "One-step aeroacoustics simulation using lattice Boltzmann method," *AIAA Journal*, vol. 44, no. 1, pp. 78–89, 2006.

[120] A. R. da Silva and G. P. Scavone, "Lattice Boltzmann simulations of the acoustic radiation from waveguides," *Journal of Physics A*, vol. 40, no. 3, pp. 397–408, 2007.

[121] D. Haydock and J. M. Yeomans, "Lattice Boltzmann simulations of attenuation-driven acoustic streaming," *Journal of Physics A*, vol. 36, pp. 5683–5694, 2003.

[122] J. A. Cosgrove, J. M. Buick, D. M. Campbell, and C. A. Greated, "Numerical simulation of particle motion in an ultrasound field using the lattice Boltzmann model," *Ultrasonics*, vol. 43, pp. 21–25, 2004.

[123] A. R. da Silva, G. P. Scavone, and A. Lefebvre, "Sound reflection at the open end of axisymmetric ducts issuing a subsonic mean flow: A numerical study," *Journal of Sound and Vibration*, vol. 327, pp. 507–528, 2009.

[124] B. Chopard, P. O. Luthi, and J.-F. Wagen, "Lattice Boltzmann method for wave propagation in urban microcells," *IEE Proceedings: Microwaves, Antennas and Propagation*, vol. 144, no. 4, pp. 251–255, 1997.

[125] W. J. R. Hoefer, "The transmission-line matrix method—Theory and applications," *IEEE Transactions on Microwave Theory and Techniques*, vol. 33, no. 10, pp. 882–893, 1985.

[126] Y. Kagawa, T. Tsuchiya, B. Fujii, and K. Fujioka, "Discrete Huygens' model approach to sound wave propagation," *Journal of Sound and Vibration*, vol. 218, no. 3, pp. 419–444, 1998.

[127] H. Yu and K. Zhao, "Lattice Boltzmann method for compressible flows with high mach numbers," *Physical Review E*, vol. 61, no. 4, pp. 3867–3870, 2000.

[128] S. Ha, N. Ku, and K.-Y. Lee, "Lattice Boltzmann approach to acoustic propagation for underwater warfare simulation," in *Proceedings of the 2012 Symposium on Theory of Modeling and Simulation*, 2012.

[129] H. Xu, O. Malaspinas, and P. Sagaut, "Sensitivity analysis and determination of free relaxation parameters for the weakly-compressible MRT-LBM schemes," *Journal of Computational Physics*, vol. 231, no. 21, pp. 7335–7367, 2012.

[130] Z. Guo, C. Zheng, and B. Shi, "Discrete lattice effects on the forcing term in the lattice Boltzmann method," *Physical Review E*, vol. 65, no. 4, p. 046308, 2002.

[131] I. Halliday, L. Hammond, C. Care, K. Good, and A. Stevens, "Lattice Boltzmann equation hydrodynamics," *Physical Review E*, vol. 64, no. 1, p. 011208, 2001.

[132] T. Reis and T. N. Phillips, "Modified lattice Boltzmann model for axisymmetric flows," *Physical Review E*, vol. 75, no. 5, p. 056703, 2007.

[133] P. J. Dellar, "Two routes from the Boltzmann equation to compressible flow of polyatomic gases," *Progress in Computational Fluid Dynamics*, vol. 8, no. 1/2/3/4, pp. 84–96, 2008.

[134] D. T. Blackstock, "Transient solution for sound radiated into a viscous fluid," *Journal of the Acoustical Society of America*, vol. 41, no. 5, pp. 1312–1319, 1967.

[135] J. G. Proakis and D. G. Manolakis, *Digital Signal Processing*. Pearson Prentice Hall, 4th ed., 2007.

[136] H. B. Ju and K.-Y. Fung, "Time-domain simulation of acoustic sources over an impedance plane," *Journal of Computational Acoustics*, vol. 10, no. 3, pp. 311–329, 2002.

[137] W. P. Graebel, *Advanced Fluid Mechanics*. Academic Press, 2007.

[138] J. L. Butler, A. L. Butler, and J. A. Rice, "A tri-modal directional transducer," *Journal of the Acoustical Society of America*, vol. 115, no. 2, pp. 658–665, 2004.

[139] H. Chen, S. Chen, and W. H. Matthaeus, "Recovery of the Navier-Stokes equations using a lattice-gas Boltzmann method," *Physical Review A*, vol. 45, no. 8, pp. 5339–5342, 1992.

[140] P. A. Skordos, "Initial and boundary conditions for the lattice Boltzmann method," *Physical Review E*, vol. 48, no. 6, pp. 4823–4842, 1993.

[141] X. Shan and H. Chen, "Simulation of nonideal gases and liquid-gas phase transitions by the lattice Boltzmann equation," *Physical Review E*, vol. 49, no. 4, pp. 2941–2948, 1994.

[142] B. Chopard and M. Droz, *Cellular automata modeling of physical systems*. Cambridge University Press, 1998.

[143] B. Chopard, A. Dupuis, A. Masselot, and P. O. Luthi, "Cellular automata and lattice Boltzmann techniques: An approach to model and simulate complex systems," *Advances in complex systems*, vol. 5, no. 2 & 3, pp. 103–246, 2002.

[144] P. J. Dellar, "Nonhydrodynamic modes and a priori construction of shallow water lattice Boltzmann equations," *Physical Review E*, vol. 65, no. 3, p. 036309, 2002.

[145] F. J. Alexander, H. Chen, S. Chen, and G. D. Doolen, "Lattice Boltzmann model for compressible fluids," *Physical Review A*, vol. 46, no. 4, pp. 1967–1970, 1992.

[146] B. J. Palmer and D. R. Rector, "Lattice Boltzmann algorithm for simulating thermal flow in compressible fluids," *Journal of Computational Physics*, vol. 161, pp. 1–20, 2000.

[147] J. Tölke, M. Krafczyk, M. Schulz, and E. Rank, "Lattice Boltzmann simulations of binary fluid flow through porous media," *Philosophical Transactions of the Royal Society of London A*, vol. 360, no. 1792, pp. 535–545, 2002.

[148] T. Kataoka and M. Tsutahara, "Lattice Boltzmann model for the compressible Navier-Stokes equations with flexible specific-heat ratio," *Physical Review E*, vol. 69, no. 3, p. 035701, 2004.

[149] E. Bich, J. Millat, and E. Vogel, "The viscosity and thermal conductivity of pure monatomic gases from their normal boiling point up to 5000 K in the limit of zero density and at 0.101325 MPa," *Journal of Physical and Chemical Reference Data*, vol. 19, no. 6, pp. 1289–1305, 1990.

[150] C. D. Levermore and J.-G. Liu, "Large oscillations arising in a dispersive numerical scheme," *Physica D*, vol. 99, no. 2, pp. 191–216, 1996.

[151] J. Levesley, A. N. Gorban, and D. Packwood, "A numerical analyst's view of the lattice Boltzmann method," in *Approximation algorithms for complex systems* (E. H. Georgoulis, A. Iske, and J. Levesley, eds.), pp. 127–150, Springer, 2011.

[152] D. Lagrava, *Revisiting Grid Refinement Algorithms For The Lattice Boltzmann Method*. PhD thesis, University of Geneva, 2012.

[153] B. Chopard and P. O. Luthi, "Lattice Boltzmann computations and applications to physics," *Theoretical Computer Science*, vol. 217, no. 1, pp. 115–130, 1999.

[154] P. Aumond, G. Guillaume, B. Gauvreau, C. Lac, V. Masson, and M. Bérengier, "Application of the Transmission Line Matrix method for outdoor sound propagation modelling – Part 2: Experimental validation using meteorological data derived from the meso-scale model Meso-NH," *Applied Acoustics*, vol. 76, pp. 107–112, 2014.